Mechanisms and Time-scales

in

Breakup of ^{6,7}Li

A thesis submitted for the degree of
Doctor of Philosophy
of The Australian National University

Lương Đức Huy

July 6, 2012

Kính tặng mẹ,

người với bao hy sinh, nhẫn nại, và lòng yêu thương vô bờ.

Abstract

The current and near future of nuclear physics is being directed by the availability of radioactive ion beams and exotic nuclei near the neutron drip line. Reactions with the weakly-bound but stable ^{6}Li and ^{7}Li nuclei were thus studied as a testbed for relating nuclear structure of weakly-bound and unstable nuclei to nuclear reaction outcomes within a coherent framework, an important goal in nuclear reaction theory.

Coincidence measurements of charged fragments produced from the reactions of ^{6,7}Li with high-Z targets were carried out, at sub-barrier energies, using a large-area position sensitive detector array at back-angles. The wide and continuous angular coverage of the detector, and the choice of sub-barrier energies, were crucial in obtaining clear conclusions. For the reactions with ^{6}Li, the observed $\alpha + d$ and $\alpha + p$ coincidences show direct cluster breakup (^{6}Li $\rightarrow \alpha + d$), but also large yields of breakup triggered by n-transfer (^{6}Li $\rightarrow {}^5$Li $\rightarrow \alpha + p$). Coincidences between $\alpha + \alpha$ were also observed indicating breakup triggered by d-transfer (^{6}Li $\rightarrow {}^8$Be $\rightarrow \alpha + \alpha$). For the ^{7}Li-induced reactions, direct cluster breakup (^{7}Li $\rightarrow \alpha + t$) was observed, but more probable was p-pickup by the projectile resulting in $\alpha + \alpha$ coincidences (^{7}Li $\rightarrow {}^8$Be $\rightarrow \alpha + \alpha$). The measured relative energy gives an indication of the time-scales for each breakup mode, allowing a comparison with the time-scales for direct nuclear reactions and fusion.

These measurements demonstrate that the reaction dynamics and outcomes are determined not only by the properties of the two colliding nuclei, but also by the ground-state and excited state properties of their neighbours. This is a key insight for understanding and predicting reactions of weakly-bound nuclei near the limits of nuclear existence. Furthermore, the results suggest that in sub-barrier collisions of ^{6}Li and ^{7}Li with all but the lightest nuclei, the most likely nuclear reactions will lead to breakup of the projectile-like nucleus, forming elements lighter than Li. This needs to be tested experimentally for collisions with much lighter nuclei, and possible implications for lithium abundances in cosmological processes investigated.

Preface

This thesis details the study of sub-barrier reactions induced by ^{6}Li and ^{7}Li. Beams of accelerated lithium nuclei were provided by the 14UD Pelletron accelerator of the Heavy Ion Accelerator Facility at the Australian National University in Canberra, Australia. All measurements were carried out with the assistance of the nuclear reaction dynamics group and the nuclear physics technical staff.

This project was motivated by Prof. M. Dasgupta and Prof. D. J. Hinde, with measurements performed using a large-area position sensitive detector array. The detector array and the associated electronics were set up by the author with assistance from Dr. R. Rafiei, Dr. C. J. Lin, and Dr. P. Davidson. All data analysis was done by the author using customised scripts written by himself for the `ROOT` framework. The author also used a routine library written by Dr. R. du Rietz, and worked closely with Dr. R. Rafiei in extracting experimental data.

The following publications are directly related to the work in this thesis, and have been or will be published:

1. *Sub-barrier breakup of ^{6,7}Li and its effects on fusion at above-barrier energies,*
   D. H. Luong, M. Dasgupta, D. J. Hinde, R. du Rietz, R. Rafiei, M. Evers,
   To be submitted.
2. *Insights into the mechanisms and time-scales of breakup of ^{6,7}Li,*
   D. H. Luong, M. Dasgupta, D. J. Hinde, R. du Rietz, R. Rafiei, C. J. Lin, M. Evers,
   A. Diaz-Torres, Phys. Lett. B**695**, 105 (2011).

The author was closely involved with the following work, which was done using the same detector array as used by the author

1. *Mechanisms and systematics of breakup in reactions of ^{9}Be at near-barrier energies,*
   R. Rafiei, R. du Rietz, **D. H. Luong**, D. J. Hinde, M. Dasgupta, M. Evers,
   A. Diaz-Torres, Phys. Rev. C**81**, 024601 (2010).

The work detailed in this thesis has also been presented in several international conferences with the following papers have been published in their proceedings:

1. *Time-scales and mechanisms of breakup influencing fusion*, M. Dasgupta, **D.H. Luong**, D.J. Hinde, R. Rafiei, M. Evers, R. du Rietz, AIP Conf. Proc. **1423**, 81 (2012).
2. *A complete picture of the breakup in* ^{6,7}*Li-induced reactions*, **D.H. Luong**, D.J. Hinde, M. Dasgupta, M. Evers, R. Rafiei, R. du Rietz, EPJ Web of Conf. **17**, 03002 (2011).
3. *Reaction dynamics of weakly bound nuclei at near-barrier energies*, M. Dasgupta, L.R. Gasques, **D. H. Luong**, R. du Rietz, R. Rafiei, D.J. Hinde, C.J. Lin, M. Evers, and A. Diaz-Torres, Nucl. Phys. A**834**, 147c (2010).

No part of this thesis has been submitted for a degree at any other university.

Duc H. Luong

Canberra, July 2011

I am indebted to my father for living,
but to my teacher for living well.
Alexander of Macedon

Acknowledgements

For suggesting this project, the continual support and encouragement and most of all, for holding the light to the bigger picture, I am greatly indebted to Prof. Mahananda Dasgupta and Prof. David J. Hinde. They have both been very attentive to my personal and academic life, well beyond anything expected of a supervisor. For all that and more I offer my heartfelt thanks.

To my good friends and colleagues Dr. Maurits Evers, Dr. Ramin Rafiei, Dr. Rickard du Rietz and Mr. Aditya Wakhle, thanks are in order for without them "Fusion Boys" would just be boys. Their opinions, and some had plenty, and perspectives certainly did not fall on deaf ears. The rico_cxx.so library lives on.

Special thanks go to Dr. Alexis Diaz-Torres for his help with `PLATYPUS` and Prof. Jeff Tostevin for his discussions on the structure of ^{6,7}Li. Thanks to Dr. Chengjian Lin, detector noise chaser extraordinaire, and Mr. Ian Carter with the night-shifts.

I also wish to thank Dr. Elizabeth Williams for reading my draft chapters, giving a fresh perspective on things. Thanks to Dr. Maurits Evers, again, for critical reading of my final draft. Thanks to the delightful Ms. Petra Rickman for making life at the department feels like home, to Mr. Tom Kitchen for being an awesome mate, and a roundhouse applause (Chuck Norris style) to the technical staff and the entire Nuclear Physics Department.

For their help and support during my undergraduate years at the Royal Melbourne Institute of Technology, I would like to thank Assoc. Prof. Philip Wilksch and Dr. Ken McGregor.

Contents

> *We have a habit in writing articles published in scientific journals to make the work as finished as possible, to cover all the tracks, to not worry about the blind alleys or to describe how you had the wrong idea first, and so on. So there isn't any place to publish, in a dignified manner, what you actually did in order to get to do the work.*
>
> R. Feynman (1918-1988)

1

A study of broken pieces

Nuclear physics began just a century ago with the formulation of the Rutherford model of the atom, but mankind's endeavour to understand the building blocks of the physical universe probably began with a question: "If one was to cut a piece of wood into smaller pieces, how fine could one cut before it becomes uncuttable?" This question led ancient Greek philosophers like Democritus into coining the term *atomos* meaning "uncuttable" or "the smallest indivisible particle of matter". And as sharper knives and surer hands are required to cut things into ever finer parts, the nucleus of the atom itself becomes one of the sharpest knives, and the particle accelerator the surest hand.

Because nuclei contain protons and neutrons, held together by the short-range attractive nuclear force, they have a net positive charge which repel other nuclei though the long-range repulsive Coulomb force. If brought close enough, the combination of the attractive and repulsive forces results in many possible outcomes, including elastic and inelastic scattering, nucleon transfer, fusion, and even nuclear fragmentation, depending on how much kinetic energy is available. With the availability of powerful particle accelerators, nuclei have been accelerated to ever greater velocities, and smashed together to study the outcomes – the "broken pieces".

In continuing the quest to understand the physical universe, this thesis is an account of what transpired, including the right ideas, and a few blind alleys that were followed, from a study of the broken pieces that result when nuclei of ^{6,7}Li are brought close to other nuclei much heavier than lithium. This thesis work came out of a desire to investigate the pressing matter of understanding the different breakup mechanisms of ^{6,7}Li, and how coupling to states that lead to breakup affects the reaction dynamics. Such understanding is essential in relating the internal nuclear structure, e.g. nucleon clustering and low threshold for cluster-breakup, to the reaction outcomes, e.g. fusion, nucleon transfer, breakup, and incomplete fusion. The current and near future of nuclear physics is being directed by the availability of radioactive ion beams (RIBs) and exotic nuclei near and at the neutron and proton drip lines (the limits of the existence of bound nuclei). Therefore relating nuclear structure of weakly-bound and unstable nuclei to nuclear reaction outcomes within a coherent framework has became an important goal in reaction theory. The stable but weakly-bound nuclei ^{6,7}Li have a low threshold against breakup, a characteristic they share with light radioactive nuclei near the drip-lines. With ^{6,7}Li being more accessible, while offering similar characteristics (namely nucleon clustering and low breakup threshold), studying the former presents a great opportunity to understand and predict the behaviour of their much less accessible but more exotic nuclei.

In this chapter, we'll set the scene with a short historical overview of the nucleon clustering phenomenon that helps explain some of the more particular properties of ^{6,7}Li. This is followed by a review of what is known from previous breakup studies, the importance of investigating their breakup, and the remaining questions that necessitated the current study.

Clustering in nuclei: an historical overview

The correlation of neutrons and protons into small clusters, particularly α-particles, has a long and fascinating history. Well before the discovery of the neutron, Rutherford in 1921 pictured the nitrogen nucleus as composed of three α-particles and a proton [88]. Gamow then used α-clustering in the nucleus to formulate his model of α-decay through quantum tunnelling [41]. This idea was further developed by Wheeler [125], who proposed that nucleons in the nucleus may cluster together and are continually being broken up and reformed in all possible combinations. Since then, clustering has remained a consistent feature of models of the structure of the nucleus, arising spontaneously from many different theoretical approaches [38, 39, 44, 82, 114, 123].

The likelihood of the formation of a particular cluster depends on its binding energy: the higher the binding energy the more likely it is to form a cluster. From the binding energies of some of the smaller possible clusters, 2.224 MeV for a deuteron, 8.481 MeV for a triton, and 28.300 MeV for an α-particle, clustering into the latter should thus be the most likely. This α-clustering hypothesis is by no means just a theoretical construct without physical consequences. Its existence is well established by α-decay of heavy nuclei [16], the strong selective excitations in cluster transfer [12, 19, 53, 65, 84], knockout reactions [87, 119], and resonance structure in elastic and inelastic scattering [64, 74]. Further evidence for clustering in ^{6,7}Li was observed in cluster breakup of ^{6,7}Li, into $\alpha+d$ and $\alpha+t$ respectively, in the field of high-Z targets [46, 76]. The picture of $\alpha + residue$ clustering in ^{6,7}Li nuclei is now widely accepted, both theoretically and experimentally [1, 112, 113].

Previous works on the breakup of ^{6,7}Li

In the early 1960s, several stellar nucleosynthesis theories [8, 37] were presented to explain the stellar abundance of lighter elements. The abundance ratio of the isotopes of lithium (^{7}Li/^{6}Li) was, and still is, one of several constraints [102] that severely test these theories. Understanding the abundance of lithium observed on the surface of some magnetic stars [47], and old metal-poor halo dwarfs [2], is also important in gaining information on stellar evolution. Since nucleosynthesis in stars involves radiative capture reactions at extremely low energies, its duplication in the laboratory is extremely difficult. It was proposed [6, 117] that experimental studies of Coulomb disintegration of light nuclei, especially the mechanism of Coulomb dissociation, is potentially of great astrophysical interest, allowing determination of the radiative capture cross sections for the inverse process.

Expecting binary dissociation, from α+*residue* cluster breakup, fragments produced from reactions with ^{6,7}Li were captured in coincidence by Disdier *et al.* [34] and Québert *et al.* [85]. Two different breakup modes were observed. The first breakup mode was *sequential* (resonant) breakup. Here breakup proceeds sequentially, firstly though Coulomb excitation of the nuclei to a resonant state, which then dissociate into $\alpha + residue$ cluster fragments [34, 48, 85, 92].

The second breakup mode was *direct* (non-resonant) breakup, observed to be prominent in ^{7}Li → $\alpha + t$ breakup. For this breakup mode, the application of Coulomb breakup theory by Thompson *et al.* [111] yielded cross-sections much larger than the cross-sections observed experimentally by Shotter *et al.* [93]. It was believed that nuclear forces may be the dominant contributor and a proper treatment of the effects of the Coulomb forces remains an open question [111]. Subsequent studies by Davinson *et al.* [29] and Shotter *et al.* [95]

showed that the Coulomb interaction became increasingly dominant at lower energies, allowing both breakup modes to be reasonably described by Coulomb disintegration theory [34, 45, 70].

Criticisms were raised [49, 94] against Coulomb breakup measurements as tools for probing the radiative capture cross sections, since nuclear interactions may still play a role well beyond the energy regime (or separation distance between the reacting nuclei) where Coulomb excitation was thought to dominate. Also, the observation of distinctly different anisotropies, in the direction of the coincident particles with respect to the beam, between the sequential and direct $\alpha+deuteron$ breakup components in ^{6}Li [48] showed that Coulomb dissociation cannot be related in a straightforward manner to the astrophysically relevant $\alpha(d,\gamma)^{6}$Li capture reaction. This also raised questions about whether excitation and breakup can be treated independently, or whether they proceed rather on comparable time-scales so that three-body kinematics and dynamics come into play.

When the total cross-section of all breakup fragments of ^{6,7}Li were measured in singles, however, other possible breakup mechanisms emerged. The yields of α-particles were found to be more than triple the deuteron yields in reactions with ^{6}Li [79], where protons were also observed, and up to an order of magnitude more than triton yields in reactions with ^{7}Li [46]. These observations showed a breakup mechanism incompatible with the Coulomb breakup process, rather suggesting the presence of other more complex α-particle production processes such as nucleon(s) transfer leading to breakup of the projectile-like nuclei. From the energy range of the α-particles, Pfeiffer *et al.* [83] concluded that there was a definite contribution from the α-unstable ^{5}He and ^{5}Li, which are the projectile-like products of the transfer of either a proton or a neutron from ^{6}Li, or a deuteron or two neutrons from ^{7}Li.

In 1973, Ost *et al.* [78] performed one of the very first kinematically complete breakup experiment for ^{6}Li on ^{208}Pb. Nucleon transfer leading to breakup was observed. Strong correlations between the energies of the coincident α + *proton*, α + *deuteron*, and $\alpha+\alpha$ breakup fragments, as can be seen in *Figure 1.1*, showed that these fragments originated from breakup of ^{5}Li, ^{6}Li, and ^{8}Be respectively. This confirmed that nucleon transfer, both single nucleon and cluster, may make an important contribution to breakup in reactions of weakly-bound nuclei. Fast forward to the mid 1980s, the discovery of exotic neutron-rich halo nuclei [108, 109] became one of the motivations for the development of intense

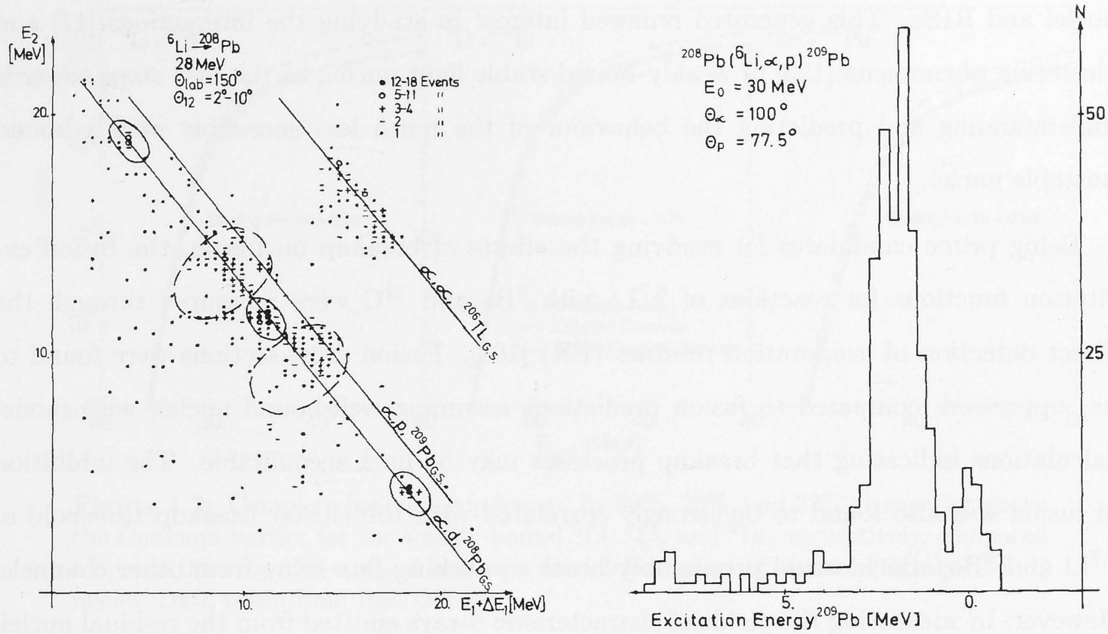

Figure 1.1: Results from an early kinematically complete breakup measurement for ^{6}Li on ^{208}Pb at 28 MeV bombarding energy by Ost *et al.* [78]. (left panel) Two-dimensional display of coincidence events. Events due to the two step reaction ^{208}Pb(^{6}Li,^{6}Li*)^{208}Pb; ^{6}Li* $\rightarrow \alpha + d$ are circled by a solid line. Events due to the reaction ^{208}Pb(^{6}Li,^{5}Li)^{209}Pb; ^{5}Li$\rightarrow$ $\alpha + p$ are circled by dashed lines. Higher energy events are due to the reaction ^{208}Pb(^{6}Li,^{8}Be$_{gs}$)^{206}Tl; ^{8}Be$_{gs}$ $\rightarrow 2\alpha$. (right panel) Projection of α+p events onto a line perpendicular to the kinematical curve corresponding to the excitation energy spectrum of ^{209}Pb produced following the neutron transfer reaction ^{208}Pb(^{6}Li,^{5}Li)^{209}Pb.

RIBs facilities around the globe. The availability of neutron-rich nuclei will allow reaction and structure studies on nuclei far from stability, and provide direct data for use in the calculations of the rapid neutron capture process (r-process) [60].

As it turns out, the theoretical models that work well for reactions of tightly-bound nuclei, where the fusion process can be described to a great degree of precision using a model involving just the radial distance between the centre of mass of the two nuclei and channel coupling effects [91], do not work well in reactions involving weakly-bound and/or neutron-rich nuclei [17]. Neutron-rich nuclei may have extremely weakly-bound nucleons, resulting in quantum-mechanical tunnelling to large distances well beyond the tightly bound core, forming a diffuse neutron cloud or halo [50]. It was predicted that fusion cross-sections would be enhanced for certain neutron-rich halo nuclei due to coupling of the soft dipole mode of excitation which lowers the fusion barrier [28, 106]. Being weakly-bound, however, these nuclei may breakup leading to suggestions that fusion cross-sections would instead be suppressed [56, 105] for more short-lived and unstable halo nuclei and RIBs. This generated renewed interest in studying the interactions [17] and clustering phenomena [123] of weakly-bound stable light nuclei, as the first steps towards understanding and predicting the behaviour of the much less accessible weakly-bound unstable nuclei.

Being prime candidates for studying the effects of breakup on fusion, the fusion excitation functions for reactions of ^{6,7}Li with ^{9}Be and ^{12}C were measured through the direct detection of evaporation residues (ER) [104]. Fusion cross-sections were found to be suppressed, compared to fusion predictions assuming well-bound nuclei, with model calculations indicating that breakup processes may be held accountable. The inhibition of fusion was also found to be strongly correlated with the cluster breakup threshold of ^{6,7}Li and ^{9}Be, which would presumably break up, taking flux away from other channels. However, by measuring the yields of characteristic γ-rays emitted from the residual nuclei, other groups reported no fusion suppression in the reaction of ^{6,7}Li with ^{12,13}C [69, 67] and ^{6,7}Li with ^{16}O [68]. Further measurements for the reaction of ^{7}Li with ^{12}C by detecting the ER [66], and α-particle angular distributions [80], have reconciled these differences, with the conclusion that the suppression of fusion is not significant for these reactions.

For weakly-bound nuclei however, it is important to make a distinction between complete fusion, where the weakly-bound nucleus is captured as a whole, and incomplete fusion where only a part of the weakly-bound nucleus is captured. In the fusion reactions discussed above, such a distinction is not possible and thus the sum of complete and incomplete fusion is identified as fusion (referred to as total fusion in the literature). The distinction between complete and incomplete fusion can be made more easily in reactions of weakly-bound nuclei with heavy nuclei.

With this aim, the complete fusion for the reactions of ^{9}Be with ^{208}Pb, and ^{6,7}Li with ^{209}Bi, were studied by Dasgupta *et al.* [24, 25, 26] at energies below and above the fusion-barrier energy. Complete fusion could be separated from incomplete fusion by detecting the α-decay of the fusion products. The measured complete fusion cross-sections are shown in *Figure 1.2*, which at above-barrier energies are suppressed by $\sim$30% compared to calculations assuming no breakup (dashed lines). Results from the reactions of ^{9,10,11}Be with ^{209}Bi [51, 97, 98, 100] also showed complete fusion being suppressed at energies above the fusion-barrier energy. By studying the α-particles produced at energies below the fusion-barrier energy, in singles [52] and in coincidence [86], the breakup probability

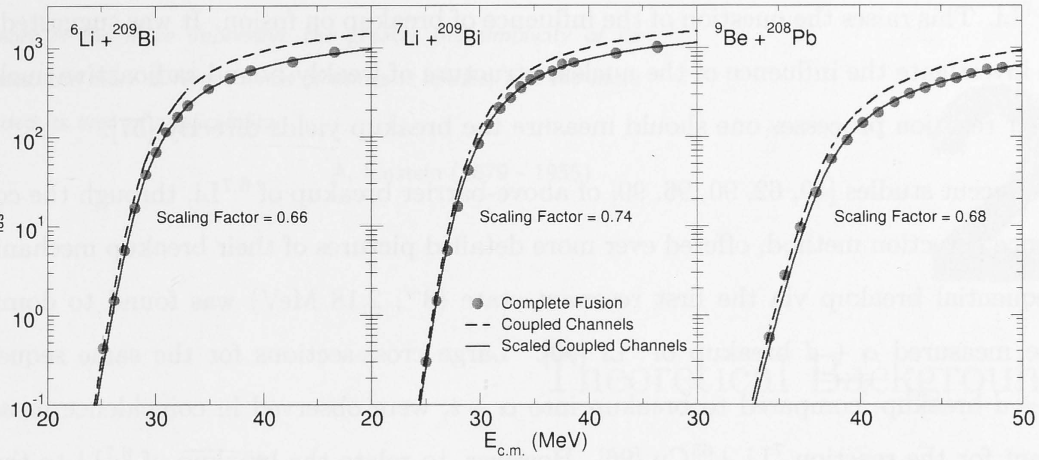

Figure 1.2: Complete fusion is suppressed by 34%, 26%, and 32% at energies above the Coulomb barrier for the weakly-bound ^{6}Li, ^{7}Li, and ^{9}Be, respectively, compared to predictions by the coupled channels model for fusion of normal (tightly-bound) nuclei. Data taken from Ref. [25, 26]

of ^{9}Be on ^{208,nat}Pb was found to vary exponentially with the distance of closest approach. This below-barrier breakup of the weakly-bound projectile was successfully mapped to the above-barrier suppression of complete fusion through a three-dimensional classical stochastic breakup model developed by Diaz-Torres *et al.* [32]. Further evidence that breakup competes with complete fusion was observed in the form of a correlation between incomplete fusion and the breakup threshold of the weakly-bound nuclei [42].

The involvement of weakly-bound nuclei, as discussed above, clearly modifies the simplistic yet successful model of fusion of tightly-bound nuclei. Any new model of nuclear reactions of weakly-bound nuclei must incorporate internal cluster structures, the effect of breakup, and must be capable of calculating complete and incomplete fusion. Early attempts at describing breakup by separating the Coulomb and nuclear effects have been questioned [48, 55] as many real world mechanisms need to be considered: Coulomb nuclear interference, higher-order multipoles of the Coulomb field, and multi-step effects. And this is even before the relationship between breakup and incomplete and complete fusion is considered.

Attempts at describing fusion of weakly-bound nuclei achieved moderate success. The experimental total fusion cross-sections, obtained using the characteristic γ-ray method, were observed to be essentially identical [68] for the two reactions ^{6}Li $+^{16}$O and ^{7}Li $+^{16}$O. These total fusion cross-sections agreed well with CDCC calculations [57], the same calculation in which the predicted total breakup cross section for ^{6}Li is more than 50 times that of ^{7}Li. This raises the question of the influence of breakup on fusion. It was suggested that to investigate the influence of the nuclear structure of weakly-bound radioactive nuclei on their reaction processes one should measure the breakup yields directly [57].

Recent studies [49, 62, 90, 96, 99] of above-barrier breakup of ^{6,7}Li, through the coincidence detection method, offered ever more detailed pictures of their breakup mechanisms. Sequential breakup via the first resonant state (3^+, 2.18 MeV) was found to dominate the measured $\alpha + d$ breakup of ^{6}Li [90]. Large cross-sections for the same sequential $\alpha + d$ breakup, compared to breakup into $\alpha + t$, were observed in coincidence measurement for the reaction ^{7}Li $+^{65}$Cu [96]. However, to relate the breakup of ^{6,7}Li to the observed [24, 26, 104] above-barrier suppression of complete fusion, requires more complete pictures of their reaction mechanisms at sub-barrier energies.

Summary of this work and thesis structure

In this work, the breakup of ^{6}Li and ^{7}Li was studied with unprecedented completeness by making coincidence measurements of breakup fragments. The major difference to previous work was that breakup was measured using a position sensitive detector array with wide and continuous angular coverage, at energies *below* that of the fusion-barrier energy. The choice of below barrier energies, which minimises absorption of breakup fragment by the target nucleus, was crucial in obtaining clear conclusions. For the first time, all the major breakup channels could be identified along with their respective breakup time-scales.

The results obtained in this work allow many previously unresolved questions regarding reactions induced by ^{6,7}Li to be answered. They also provide critical information for development of reaction models involving weakly-bound nuclei. These measurements, together with a recently developed classical trajectory model, already allow below-barrier breakup to be related to the observed suppression of complete fusion at above barrier energies.

Details of the thesis work are presented as follows: Chapter 2 gives the theoretical concepts relating to this work; Chapter 3 details the experimental apparatus and experimental methods; results on the mechanism and time-scales of breakup of ^{6,7}Li are given in Chapter 4; the cross-sections for breakup and incomplete fusion are presented in Chapter 5; and an outlook for future work is given in Chapter 6.

> *A theory is the more impressive the greater the simplicity of its premises, the more different kinds of things it relates, and the more extended its area of applicability.*
>
> A. Einstein (1879 - 1955)

2

Theoretical Background

The interactions between the protons and neutrons, driven by the strong nuclear force, give rise to the different structures in nuclei. One on hand nuclear collisions are affected by the structure, whilst on the other, collisions disturb the motion and interaction of nucleons in each of the colliding nuclei. Thus reaction outcomes are intimately connected to the structure of the colliding nuclei.

In this Chapter, cluster models for the ^{6,7}Li nuclei are discussed in Section 2.1. A classical picture of nuclear collisions is given in Section 2.2. Finally, Section 2.3 is dedicated to describing `PLATYPUS`, a classical dynamical model that is used in this thesis to simulate the trajectories of charged breakup fragments in their mutual Coulomb field.

2.1 Properties of ^{6,7}Li nuclei

The experimentally determined energy levels of ^{7}Li are shown in *Figure 2.1a* by the solid lines, and the dashed line shows the threshold energy $E_{\mathrm{B.U.}} = 2.467$ MeV for the $^7\mathrm{Li} \to \alpha + t$ breakup. The arrangement of nucleons inside the ^{7}Li nucleus can be described either in terms of independent protons and neutrons (multi-nucleon model) or as a system made up of clusters of an α-particle and a triton (cluster model). In the former, the ^{7}Li nucleus can be analysed within the shell model, where the configuration of the ground-state is shown in *Figure 2.1b*. The unpaired $1p_{3/2}$ proton gives rise to the $J^\pi = \frac{3}{2}^-$ ground-state of ^{7}Li. Spin-orbit splitting of the $1p$-shell results in the next level being $1p_{1/2}$ and its occupation by the unpaired proton results in the first excited state being the $\frac{1}{2}^-$ state (*Figure 2.1c*).

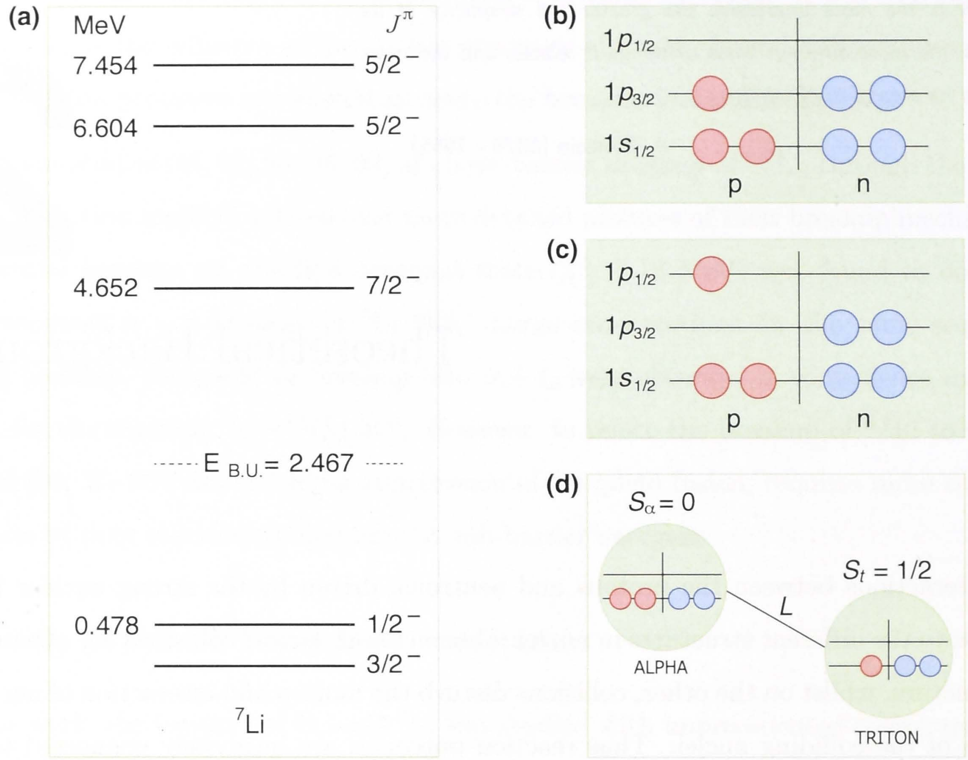

Figure 2.1: (a) Experimentally defined energy levels for ^{7}Li. The dashed line shows the threshold for breakup into $\alpha + t$. Shell model configurations of (b) the ground-state and (c) the first excited-state of ^{7}Li. (d) Equivalent $\alpha + t$ cluster model for ^{7}Li with relative momentum L between the clusters.

The nuclear cluster model of ^{7}Li, thought to provide a convenient and essentially correct description of its structure [126, 115], is illustrated in *Figure 2.1d*. Here, the ^{7}Li nucleus can be associated with an α-particle core and a valence *triton*, which can have relative motion between them. Couplings of the spins and angular momenta of the two clusters should reproduce all the observed energy levels in ^{7}Li. The α-particle and the *triton* both have positive parity with a ground-state 0^+ and $\frac{1}{2}^+$ respectively. Extra energy is provided by spins and angular momenta couplings of the two cluster ($S_\alpha + S_t + L = \frac{3}{2}^-$) where the final negative parity dictates an odd L. For $L = 1$, coupling of the 1p-state and the S_t reproduces the the expected $\frac{3}{2}^-$ and $\frac{1}{2}^-$ states.

For ^{6}Li, the experimentally determined energy levels are shown in *Figure 2.2a*. The energy threshold for $\alpha + d$ breakup is 1.474 MeV. In the multi-nucleon model of the ^{6}Li nucleus (*Figure 2.2b*), spin coupling of the unpaired $p_{3/2}$ proton and neutron results in the 1^+ ground-state and the 3^+ excited-state at 2.186 MeV . The equivalent $\alpha+d$ cluster model

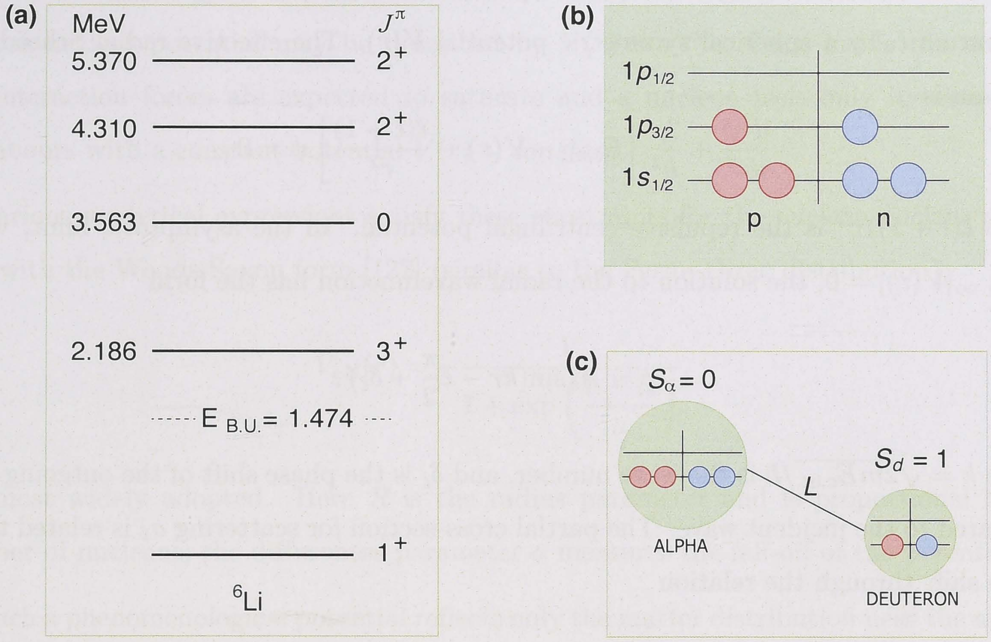

Figure 2.2: (a) Energy levels for ^{6}Li. (b) Shell model configuration for the ground-state of ^{6}Li. (c) Equivalent $\alpha + d$ cluster model for ^{6}Li with relative momentum L between the clusters.

is shown in *Figure 2.2c*. With the α-cluster having a 0^+ ground-state and the deuteron with a 1^+ ground-state, reproduction of the positive parity in the states in ^{6}Li requires coupling of the two $\alpha + d$ clusters with even angular momenta (i.e. $L = 0$, 2, 4... etc). Other cluster models of ^{6}Li includes the three bodies α-n-p [22, 21].

For both ^{6,7}Li, the energy levels show states with energies higher than their respective breakup thresholds. These are not long-lived as the nuclei would break-up into their respective $\alpha + t$ and $\alpha + d$ clusters. Through the cluster model, these quasi-bound states can be thought of as resonant cluster states in the cluster-cluster potential, and are seen as resonances in measured nuclear collision cross-sections.

Resonance or scattering states

In considering the ^{6,7}Li nuclei as comprising interacting clusters, e.g. $\alpha + residue$, at certain resonance energies the two clusters are trapped for a time, delayed and resonating during their relative motion. Quantum-mechanically, resonance states can be interpreted as a large amplitude of the wave function near the origin of the potential well as follows.

Consider the scattering of a spinless particle of mass μ, energy $E_{\text{c.m.}}$ and angular momentum ℓ, by a spherical symmetric potential $V(r)$. The effective radial Schrödinger equation is

$$\frac{d^2\psi}{dr^2} + \frac{2\mu}{\hbar^2}\left[E_{\text{c.m.}} - V(r) - \frac{\ell(\ell+1)}{r^2}\right]\psi = 0\,, \tag{2.1}$$

where $\ell(\ell+1)/r^2$ is the repulsive centrifugal potential. In the asymptotic limit, where $\lim_{r\to\infty}[V(r)] = 0$, the solution to the radial wavefunction has the form

$$\psi \sim A_\ell \sin(kr - \ell\frac{\pi}{2} + \delta_\ell)\,, \tag{2.2}$$

where $k = \sqrt{2mE_{\text{c.m.}}}/\hbar$ is the wave number, and δ_ℓ is the phase shift of the outgoing wave compared to the incident wave. The partial cross-section for scattering σ_ℓ is related to the phase shift through the relation

$$\sigma_\ell = \frac{4\pi}{k^2}(2\ell+1)\sin^2\delta_\ell\,, \tag{2.3}$$

and is at a maximum when δ_ℓ passes through $\pi/2$. When δ_ℓ changes rapidly over a small energy (or k) interval, the partial wave ℓ is at resonance with the scattering potential, describing the formation of an effective bond between the two colliding nuclei before re-separating.

Phase-shift analyses of elastic scattering of *deuterons* by α-particles [40] and of α-particles by *tritons* [101] have shown that the *α-residue* cluster model of ^{6,7}Li is equivalent to the shell model, and allows correct assignment of parity and angular momenta to most low energy states in these light nuclei.

2.2 Classical picture of nuclear collisions

The interaction potential between two colliding nuclei is the sum of the attractive nuclear potential $V_N(r)$, the repulsive Coulomb potential $V_C(r)$ and the repulsive centrifugal potential $V_\ell(r)$:

$$V(r) = V_N(r) + V_C(r) + V_\ell(r)\,. \tag{2.4}$$

Here r is the centre to centre separation of the colliding nuclei. The nuclear potential $V_{\text{N}}(r)$ arises from the individual nucleon-nucleon interactions. The interaction forces between the nucleons is short ranged and decreases exponentially as a function of r. Interactions between a nucleon and a nucleus will then be a sum of the former interactions, and the nucleon-nucleus potential may be described by $V(r) \sim e^{-\alpha r}$. Once inside the nucleus, the interaction forces are expected to saturate and a nucleon feels only its immediate neighbours with a constant potential $V(r) \sim constant$.

Various analytical expressions satisfy these constraints for the nucleon-nucleus potential, with the Woods-Saxon form [127] (similar to the Fermi-Dirac distribution),

$$V_{\mathrm{nN}}(r) = -\frac{V}{1+\exp\left(\dfrac{r-R}{a}\right)} \tag{2.5}$$

the most widely adopted. Here R is the radius parameter and is proportional to the number of nucleons; the diffuseness parameter a measures the fall-off of the potential.

Such a phenomenological potential reflects only the matter distribution near the nuclear surface, with nuclear matter inside the nucleus considered incompressible. The nucleus-nucleus potential often takes the same form, since during the collision of two nuclei, the peripheral inter-nuclear interaction is dictated by nucleons on the surface of both nuclei. Thus the inter-nuclear potential $V_{\mathrm{N}}(r)$ in equation (2.4) is parameterised as

$$V_{\mathrm{N}}(r) = -\frac{V_0}{1+\exp\left(\dfrac{r-R_0}{a_0}\right)}, \tag{2.6}$$

where $R_0 = r_0(A_1^{1/3} + A_2^{1/3})$, and A_i are the mass number of the colliding nuclei, V_0 is the potential depth, and a_0 is the surface diffuseness. These parameters are often determined by fitting experimental scattering data, e.g. fits to elastic-scattering angular distributions [81, 120]. Double folding model calculations of the inter-nuclear potential [43] confirm that a Woods-Saxon form gives a good representation for inter-nuclear separations down to just inside the fusion barrier radius.

The repulsive Coulomb potential $V_{\mathrm{C}}(r)$ in equation (2.4) is usually expressed in terms of the potential between a point-like particle and a charged sphere of finite radius r_c through:

$$V_C(r) = \begin{cases} \dfrac{Z_1 Z_2 e^2}{r} & \text{for } r > r_c \\[2ex] \dfrac{Z_1 Z_2 e^2}{2}\dfrac{3r_c^2 - r^2}{r_c^3} & \text{for } r \leq r_c\,, \end{cases} \tag{2.7}$$

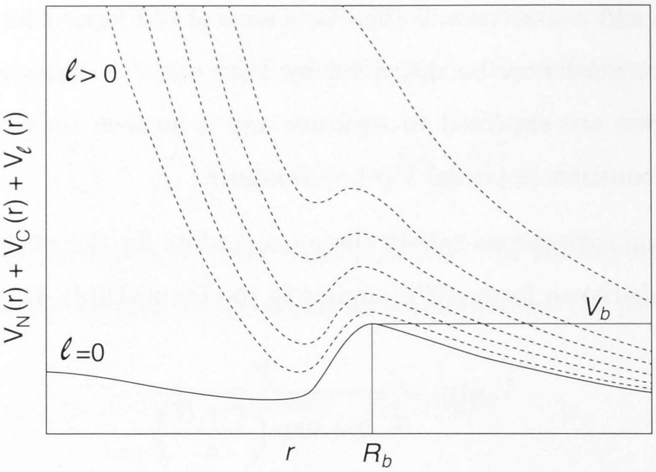

Figure 2.3: Sum of Woods-Saxon nuclear, Coulomb, and centrifugal potentials gives a series of potentials that depend on ℓ. The energy V_b is the fusion-barrier energy for a head-on collision.

where e^2 =1.44 MeVfm and $Z_{1,2}$ are the atomic numbers of the participants. The centrifugal potential is given by

$$V_\ell(r) = \frac{\ell(\ell+1)\hbar^2}{2\mu r^2} . \tag{2.8}$$

The sum of the nuclear, Coulomb, and centrifugal potentials gives a series of potentials that depend on ℓ as shown qualitatively in *Figure 2.3.* For each ℓ-dependant potential, the local maximum, e.g. at V_b for $\ell = 0$, is the barrier to fusion. For head-on collisions ($\ell = 0$) the radial separation R_b of this maximum is the barrier radius.

Classically speaking, the interaction potential determines the orbits during the interaction. The type of interaction between the nuclei is dependent on the orbital angular momentum ℓ as illustrated in *Figure 2.4*, since this determines the distance of closest approach of the two nuclei. For a nuclear interaction to take place, the energy of the incident particle needs to be near or above the fusion barrier. At energies well below the fusion barrier, the nucleus can interact only through the Coulomb field, resulting in Rutherford scattering and possibly inelastic scattering through Coulomb excitation. With increasing energies, the two nuclei get closer to each other. In order of decreasing separation, this can result in direct reactions (reactions where only a few degrees of freedom are involved) such as few-nucleon transfer, followed by multi-nucleon transfer, deep inelastic collisions with dissipation of kinetic energy, and finally fusion with the formation of a compound nucleus.

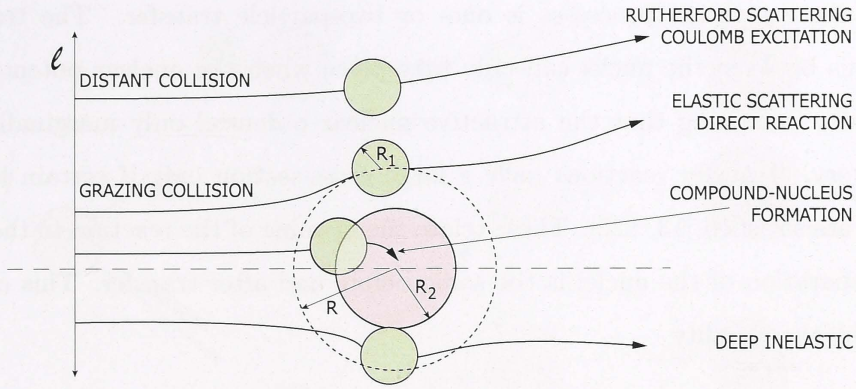

Figure 2.4: Classical picture of nuclear collisions showing the ℓ-dependent trajectories and the corresponding reaction outcomes. R_i denotes the radius of nucleus i and R is the sum of the radii of the colliding nuclei. Figure adapted from Ref. [73].

2.2.1 Scattering and nucleon-transfer

At energies well below the barrier, the scattering is dominated by the Coulomb potential. In this case, the point of closest approach R_{min} between the colliding nuclei, the impact parameter b, and the centre-of-mass scattering angle θ are related by

$$R_{\mathrm{min}} = \frac{Z_1 Z_2 e^2}{2E_{\mathrm{c.m.}}}\left(1 + \frac{1}{\sin\frac{\theta}{2}}\right) \tag{2.9}$$

and

$$b = \frac{Z_1 Z_2 e^2}{2E_{\mathrm{c.m.}}}\cos\frac{\theta}{2}\,. \tag{2.10}$$

Since the differential cross-section for scattering through an angle θ is

$$\frac{d\sigma}{d\Omega} = \frac{b}{\sin\theta}\frac{db}{d\theta}\,, \tag{2.11}$$

we get the Rutherford scattering formula

$$\left(\frac{d\sigma}{d\Omega}\right)_{Ruth.} = \left(\frac{Z_1 Z_2 e^2}{4E_{\mathrm{c.m.}}}\right)^2 \left(\frac{1}{\sin\frac{\theta}{2}}\right)^4 . \tag{2.12}$$

With increasing energy $E_{\mathrm{c.m.}}$, the distance R_{min} decreases and the nuclei can get closer to each other to feel the attractive as well as the repulsive potentials of equation (2.4). The differential cross-section then deviates from that for pure Rutherford scattering, equation (2.12), due to Coulomb-nuclear interference [36] and the onset of competing processes other than elastic scattering.

One of these reaction processes is one- or two-particle transfer. The transfer of a few nucleons between the nuclei can only take place when the nuclear potential is small but non-zero, indicating that the attractive nuclear potential only marginally perturbs the trajectory. Transfer reactions have a large cross-section only if certain kinematical conditions are satisfied [13, 122]. These relate the Q-value of the reaction to the condition that the separation of the nuclei is the same before and after transfer. This condition is described by the equality

$$\frac{Z_1 Z_2 e^2}{2E_{\mathrm{c.m}}}\left(1+\frac{1}{\sin\frac{\theta}{2}}\right)=\frac{Z_1' Z_2' e^2}{2E'_{\mathrm{c.m}}}\left(1+\frac{1}{\sin\frac{\theta'}{2}}\right), \tag{2.13}$$

where Z_{i} is the initial charge of the nucleus i, $E_{\mathrm{c.m.}}$ and θ are the energy and the scattering angle, and the superscript $'$ denotes the corresponding properties after transfer. For the same trajectory $\theta \approx \theta'$, the optimum Q-value for the transfer reaction is [5]

$$Q_{\mathrm{opt}} = -E_{\mathrm{c.m.}}\left(1-\frac{Z_1' Z_2'}{Z_1 Z_2}\right). \tag{2.14}$$

This means for one-proton transfer, Q_{opt} is positive for pickup and negative for stripping. The p-pickup reaction ^{208}Pb(^{7}Li,^{8}Be)^{207}Tl, having $Q_{\mathrm{opt}} \approx 8.90$ MeV at an incident beam energy of 29 MeV, is thus favoured having a ground-state Q-value of 9.25 MeV. Neutron(s)-transfer reactions, where Z_{i} does not change, are favoured when the reaction Q-value is $\sim$0. It should be noted that the matching conditions described here are energy matching, relying on a classical orbit description of reaction kinematics. Further matching conditions such as angular momentum could also be applied as shown by Brink [13].

2.2.2 Fusion and breakup of weakly-bound nuclei

For collisions at and around the fusion-barrier energy, multi-nucleon transfer, deep inelastic collisions (with dissipation of kinetic energy) and fusion all compete with each other. For the latter, extensive theoretical works (see review by Birkelund and Huizenga [11] and references therein) ranging from a classical potential model [4] to empirical descriptions of fusion cross sections [54, 63] have been developed to analyse experimental data on heavy-ion fusion with varying success.

In a simplistic classical picture that assumes that fusion occurs when two nuclei touch each other ($R \approx R_1 + R_2$), the cross-section is given by

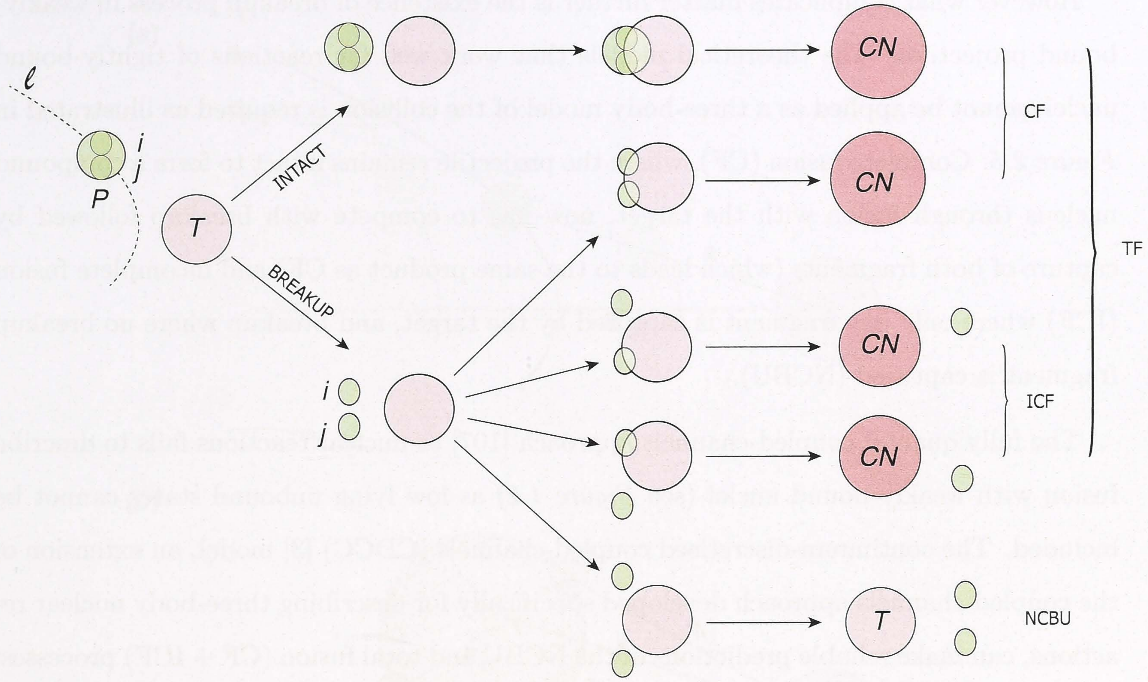

Figure 2.5: Schematic representation of all possible reaction pathways for collisions of a two-cluster (i, j) weakly-bound nuclei P with a target nucleus T. The formation of a new compound nucleus (CN) is possible when P penetrates the P-T barrier radius (when P survives intact at the barrier), or when P breaks up and either or both fragments i, j penetrates the i, j-T barrier radii. The former is called complete fusion (CF) while for the latter, incomplete fusion (ICF) occurs if either i or j, but not both, is captured by the target. If both fragments are captured then it is also called complete fusion. The sum of complete and incomplete fusion is called total fusion (TF). Reactions where both breakup fragments i, j are not captured by the target are called no-capture breakup (NCBU).

$$\sigma_{\mathrm{CF}}(E_{\mathrm{c.m.}}) = \pi R^2[1 - V(R)/E_{c.m}]\,. \tag{2.15}$$

This is an over-simplification of the fusion process where factors including the internal degrees of freedom of the participants, quantum-mechanical effects, and competing reaction channels are not included.

Going beyond this simplified picture are quantum models, that include quantum tunnelling as well as coupling to excited states in the colliding nuclei (e.g. coupled channels model [107]). A significant consequence of the latter is that the single fusion barrier, discussed above, is effectively “split” into many barriers [124], some lower in energy and some higher than the single fusion barrier. This has the most dramatic effect in fusion reactions.

However what complicates matter further is the existence of breakup process in weakly-bound projectiles. The theoretical models that work well for reactions of tightly-bound nuclei cannot be applied as a three-body model of the collision is required as illustrated in *Figure 2.5*. Complete fusion (CF), where the projectile remains intact to form a compound nucleus through fusion with the target, now has to compete with breakup followed by capture of both fragments (which leads to the same product as CF) and incomplete fusion (ICF) where only one fragment is captured by the target, and breakup where no breakup fragment is captured (NCBU).

The fully quantal coupled-channels approach [107] to nuclear reactions fails to describe fusion with weakly-bound nuclei (see *Figure 1.2*) as low lying unbound states cannot be included. The continuum-discretised coupled-channels (CDCC) [3] model, an extension of the coupled-channels approach developed specifically for describing three-body nuclear reactions, can make reliable predictions of the NCBU and total fusion (CF + ICF) processes. This approach and other existing quantum models, however, cannot distinguish between the ICF and CF processes [33]. Furthermore, after the formation of incomplete fusion products, CDCC models do not follow the evolution of the surviving breakup fragment(s) since ICF results in the depletion of the total few-body wave-function.

The angular and energy distributions of the breakup fragments may be obtained from CDCC results [116] through post processing, however, multi-step processes such as transfer leading to breakup are more challenging. Progress is being made for more elaborate three-body quantal calculations* using hyper-spherical coordinates [71] (the hyper-radius and the so-called hyper-angles).

An alternative for solving the problem of breakup and incomplete fusion of weakly-bound projectiles is the development of classical dynamical approaches based on the concept of a classical trajectory with stochastic breakup [32]. This three-dimensional model allows a consistent calculation of breakup, incomplete, and complete fusion cross sections and has been successfully applied [86] to predict the above-barrier suppression of complete fusion for reactions of ^{9}Be. In the next section, this classical trajectory model, developed into the computer code `PLATYPUS`, will be discussed.

---

*Private communication with A. Moro, University of Sevilla (Spain)

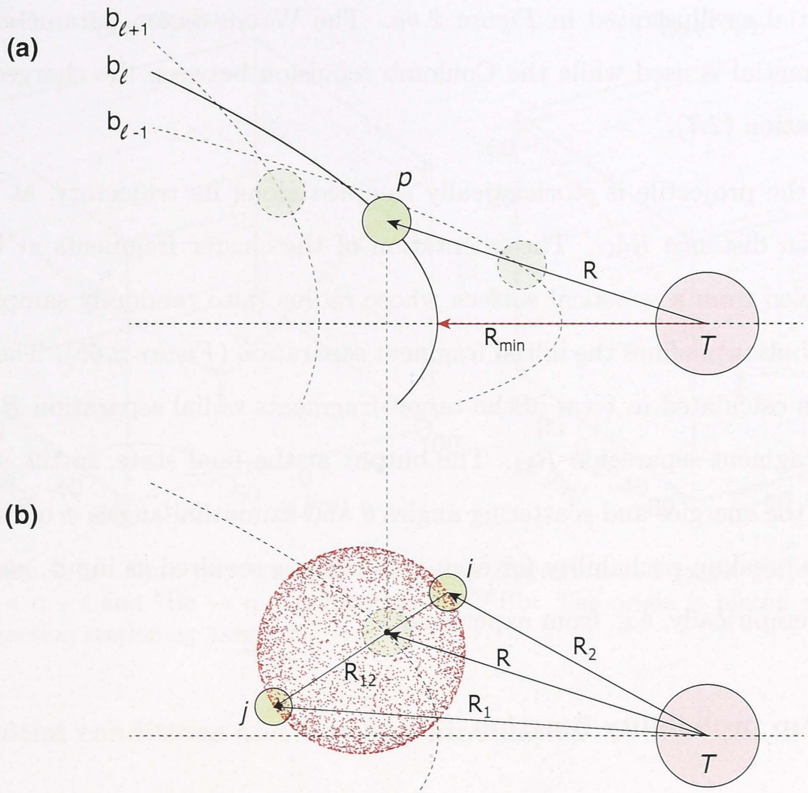

Figure 2.6: Illustrations of trajectory calculations performed by `PLATYPUS`. (a) Coulomb trajectories of the projectile for the ℓ^{th} partial wave. (b) The orientations of the fragments at breakup, with respect to the target, are randomly sampled on a spherical surface with radius defined by the fragments separation, which is also randomly sampled using a Gaussian distribution.

2.3 `PLATYPUS`: A classical dynamical model for breakup

In this work, quantifying the breakup results relies heavily on a three-dimensional classical trajectory model incorporating stochastic breakup developed for the calculation of breakup, incomplete, and complete fusion cross sections in reactions of weakly-bound projectiles. The physics is encoded within the the computer program `PLATYPUS` [31], and is described in Ref. [32]. Here a review of the main concepts behind this model will be presented.

`PLATYPUS` considers a weakly-bound projectile P as a two-body cluster $i + j$, separated by an initial separation distance. Simulation of the breakup of projectile P when it interacts with a target T thus requires four different sets of potentials P-T, i-T, j-T, and i-j. For a given incident energy, and a range of partial waves ℓ as specified by the user to include in the calculation, Coulomb trajectories of the projectile are calculated using the P-T potential as illustrated in *Figure 2.6a.* The Woods-Saxon parameterisation of the nuclear potential is used while the Coulomb repulsion between the charged particles is given by equation (2.7).

Breakup of the projectile is stochastically sampled along its trajectory, at projectile-target separation distance R_{BU}. The orientation of the cluster fragments at breakup is randomly sampled from a spherical surface whose radius (also randomly sampled from a Gaussian distribution) defines the initial fragment separation (*Figure 2.6b*). The evolution of the system is calculated in term of the target-fragments radial separation R_1, R_2, and the fragment-fragment separation R_{12}. The output at the final state, in the asymptotic region, include the energies and scattering angles θ and azimuthal angles ϕ of the breakup fragments. The breakup probability for each trajectory is required as input, and needs to be determined empirically, e.g. from experiments.

2.3.1 Breakup probability function

The breakup probability for a projectile can be described [32] in terms of a local breakup probability $P_{\mathrm{BU},\ell}(R)$, corresponding to a trajectory with angular momentum ℓ. The function $P_{\mathrm{BU},\ell}(R)$ is such that $P_{\mathrm{BU},\ell}(R)dR$ is the probability of breakup on the interval R to $R+dR$. More importantly, experimental data [52] indicate that the integral of this breakup probability along a given classical orbit is an exponential function of its distance of closest approach R_{min},

$$P_{\mathrm{BU}}(R_{\mathrm{min}}) = 2\int_{R_{\mathrm{min}}}^{\infty} P_{\mathrm{BU},\ell}(R)dR = e^{(\nu-\mu R_{\mathrm{min}})}\,. \tag{2.16}$$

Here, the exponential weighting places most breakup in the vicinity of R_{min} and the factor 2 accounts for the fact that in a classical picture, breakup may occur on the incoming (as it approaches the target nuclei) or outgoing branch (as it recedes from the nucleus) of the trajectory. Strictly speaking the probability on the way out is not equal to that on the way in as the projectile have a finite lifetime, and may lead to possible over estimation of incomplete fusion (see Section 5.6). The quantity $P_{\mathrm{BU},\ell}$ is a crucial quantity that is used as input in `PLATYPUS` calculations and, as can be deduced from equation (2.16), has the same exponential behaviour as $P_{\mathrm{BU}}(R_{\mathrm{min}})$. The latter quantity is deduced from experimental measurements, but it is the former that is used in breakup and incomplete fusion calculations.

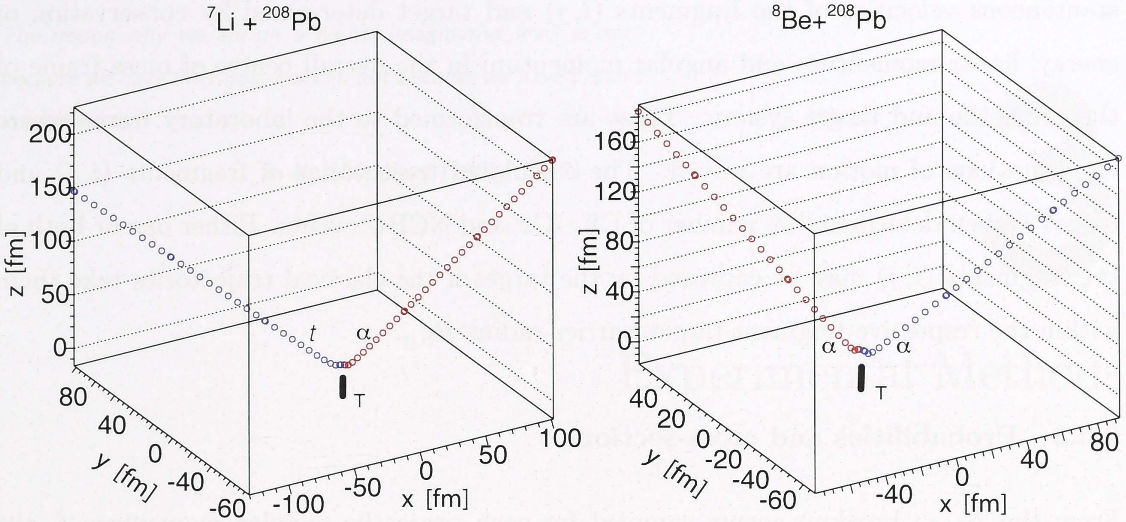

Figure 2.7: Time step tracking of breakup fragments and target trajectories for ^{7}Li $\rightarrow \alpha + t$ and ^{8}Be $\rightarrow \alpha + \alpha$ breakup on ^{208}Pb. The origin is placed at the pre-interaction stationary target.

2.3.2 Initial conditions and breakup kinematics

The initial conditions for each breakup event are obtained through a Monte Carlo sampling approach. For each trajectory with angular momentum ℓ, the position of breakup on this orbit is determined by sampling a breakup radius $R_{\rm BU}$ in the interval $[R_{\rm min}, \infty]$ for both breakup before (incoming branch) and after scattering (outgoing branch). The exponential weighting of $P_{{\rm BU},\ell}$ will clearly place most breakup in the vicinity of $R_{\rm min}$ (i.e. $R_{\rm BU} \approx R_{\rm min}$). For a trajectory with angular momentum ℓ less than that of the critical partial wave ℓ_{cr} for projectile fusion, $R_{\rm min}$ is less than the barrier radius $R_{\rm b}$ and breakup is confined to the incoming branch only, with $R_{\rm BU}$ being sampled only in the interval $[R_{\rm b}, \infty]$ as $R_{\rm min}$ is set to $R_{\rm b}$.

Having chosen $R_{\rm BU}$, and the orientation of the clusters i and j, the projectile is broken up instantaneously. Then the three-body interactions between fragments-target and fragment-fragment through the specified potentials come into play. All dynamical variables including the total internal energy and angular momentum are Monte Carlo sampled. The initial separations between the fragments are Gaussian distributed in their classically allowed region to mimic the radial probability distribution of the projectile ground-state [30]. The internal energy of the fragments is sampled in the interval of $[V_{\rm b,ij}, E_{\rm max}]$ where $V_{\rm b,ij}$ is the barrier energy between the fragments and $E_{\rm max}$ is some chosen input.

The positions of the three nuclei are propagated in time (*Figure 2.7*), with the instantaneous velocities of the fragments (i, j) and target determined by conservation of energy, linear momentum and angular momentum in the overall centre of mass frame of the projectile and target system. These are transformed to the laboratory frame where the equations of motion are solved. The calculated trajectories of fragments (i, j) and target T then determine the number of CF, ICF and NCBU events. Either one or both of the fragments (i, j) may be captured by the target if the classical trajectories take them within the respective fragment-target barrier radius $R_{\mathrm{b,ij}}$.

2.3.3 Probabilities and cross-sections

From the $N_{i+j,\ell}$ breakup events sampled for each projectile angular momentum ℓ, the number of events for no-capture breakup $(N_{\mathrm{NCBU},\ell})$, incomplete fusion due to capture of one fragment $(N_{\mathrm{ICF},\ell})$ and complete fusion due to breakup and capture of both breakup fragments and fusion of projectile that survives breakup $(N_{\mathrm{CF},\ell})$ determine the relative yields $\hat{P}_i = N_{i,\ell}/N_\ell$ with $\hat{P}_{\mathrm{NCBU}} + \hat{P}_{\mathrm{ICF}} + \hat{P}_{\mathrm{CF}} = 1$. The absolute probabilities of each processes are given [30] by

$$\begin{aligned}
P_{\mathrm{NCBU}}(E,\ell) &= P_{\mathrm{BU}}(R_{\mathrm{min}})\hat{P}_{\mathrm{NCBU}} \\
P_{\mathrm{ICF}}(E,\ell) &= P_{\mathrm{BU}}(R_{\mathrm{min}})\hat{P}_{\mathrm{ICF}} \\
P_{\mathrm{CF}}(E,\ell) &= [1 - P_{\mathrm{BU}}(R_{\mathrm{min}})]H(\ell_{cr} - \ell) + P_{\mathrm{BU}}(R_{\mathrm{min}})\hat{P}_{\mathrm{CF}}
\end{aligned} \tag{2.17}$$

where $H(x)$ is the Heaviside step function. The cross-sections are calculated using

$$\sigma_i(E) = \pi\lambda^2 \sum_\ell (2\ell + 1)P_i(E,\ell)\,, \tag{2.18}$$

where $\lambda^2 = \hbar^2/(2m_p E_{\mathrm{c.m.}})$ and m_p is the projectile mass. The other observables, such as the angle, kinetic energy and relative energy distributions of the fragments from N_{NCBU} events, are calculated by tracking their trajectories (*Figure 2.7*) to a large distance from the target.

The reliability of `PLATYPUS` has been verified elsewhere [32, 86], and also in Section 5.3.3 where the simulated quantities were compared to experimental observables. In the next chapter, the experimental methods used for the measurements made in this work are described.

The reason why we are on a higher imaginative level is not because we have finer imagination, but because we have better instruments.

A. N. Whitehead (1861 - 1947)

3

Experimental Methods

To characterise the breakup of ^{6,7}Li, charged fragments produced from their reactions with high-Z targets were required to be detected. A large-area position sensitive detector array was used to detect charged fragments at back-angles. Its large angular coverage also allowed measurement of the angular distribution of the fragments. Experiments were performed with lithium and beryllium beams provided by the 14UD Pelletron accelerator [14] at the Australian National University, Australia. The beam energies were defined by the field in the analysing magnet, measured with a nuclear magnetic resonance probe.

In this Chapter, beam production and energy selection is described in Section 3.1. The target and beam energy combinations used are listed in Section 3.2. The detector setup and electronics, together with data collection and offline post-processing methods, are presented in Section 3.3. The operation of the detector array is detailed in Section 3.4. A summary of measurements made in all the experimental runs, together with general measurement practice in all experiments, is given in Section 3.5.

3.1 Beam production

In stand-alone operation since 1973, the 14UD is a NEC* 14UD Pelletron accelerator capable of maintaining terminal voltages up to 15.5 million volts [77]. The operational principle of the 14UD involves subjecting charged particles to an electrostatic potential, accelerating them to the required energies. As a tandem accelerator, the 14UD requires negatively charged ions to be injected.

---

*National Electrostatics Corporation, Middleton, Wisconsin, USA.

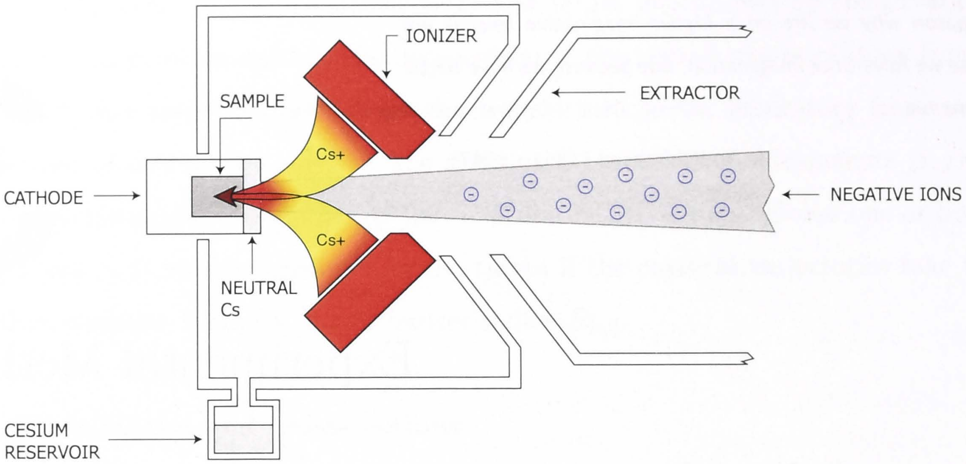

Figure 3.1: Schematic layout of SNICS. Positively charged caesium ions converge on the cathode, sputtering the sample material on impact. Sputtered atoms pick up an electron while passing through the neutral caesium on the surface of the cathode, forming a beam of negatively charged ions.

3.1.1 Ion source

A negatively charged atom or molecule (negative ion) is obtained by adding an electron to that particle. This is accomplished using a NEC Source of Negative Ions by Caesium Sputtering (SNICS), shown schematically in *Figure 3.1.* Caesium in a reservoir is heated to typically 115°C, forming vapour. This vapour rises from the reservoir to an enclosed region between the cathode and the ionizer. The cathode, housing a cylinder containing the source sample, is cooled to a temperature $\sim 18 - 20°$C. Some of the caesium vapour condenses onto the cool surface of the cathode, forming a neutral layer of caesium atoms, while some of the caesium comes in contact with the surface of the ioniser.

The ioniser is usually made of tungsten or molybdenum, as both elements have greater electron affinity than caesium, and is heated to a temperature of $\sim$ 1000°C. Caesium vapour that comes in contact with the ioniser is immediately "boiled away", but not before leaving behind an electron. The singly charged positive caesium ions that emerge from the ioniser are accelerated towards the cathode, sputtering source material from the cathode on impact. Some of the sputtered material picks up an electron in passing through the neutral caesium layer and forms a beam of negatively charged ions. The negative ions are drawn out of the SNICS by the positively biased extractor electrode.

Both Li and Be are extracted as hydride ions, achieved by introducing oxygen and ammonia (NH_3) respectively into the volume around the sample.

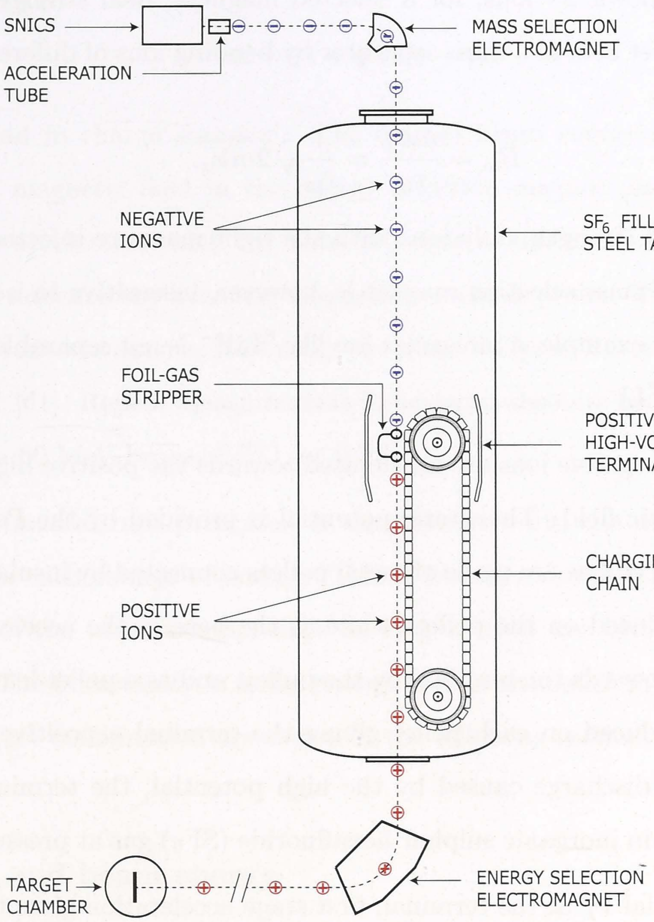

Figure 3.2: A simplified schematic layout of the 14UD accelerator, adapted from Ref. [77]. Negative ions produced in the SNICS are injected into the accelerator after deflection in the mass selection magnet. The singly charged ions are accelerated toward the positive terminal and enter the stripper foil, in which more than one electron is stripped. The ions are now positively charged and are accelerated a second time towards the ground potential.

3.1.2 Mass selection and beam acceleration

The negative ions, upon leaving the SNICS, are accelerated though a potential V_a by the acceleration tube as seen in *Figure 3.2*. With mass m and charge $q = 1$, the ions then enter the mass selection electromagnet with velocity, $v_\perp = \sqrt{2V_a/m}$, perpendicular to the magnetic field B of the latter. This magnetic field exerts a force, the Lorentz force $F = v_\perp B$, on the moving ions, providing a centripetal force resulting in uniform circular motion with radius r,

$$v_\perp B = \frac{mv_\perp^2}{r}. \tag{3.1}$$

Since there are no known 2^- ions, for a selected magnetic field strength B_m, the mass selection electromagnet acts as a mass separator by bending ions of different mass through different radius r_m

$$B_\mathrm{m} = \frac{mv_\perp}{r_\mathrm{m}} = \frac{1}{r_\mathrm{m}}\sqrt{2mV_a}. \tag{3.2}$$

By adjusting the field strength, only ions with the right mass are injected into the 14UD for acceleration. The mass selection magnet is, however, insensitive to isobaric variations of the beam ions. For example, a molecular ion like $^6\mathrm{LiH}^-$ is not separable from its atomic isobaric counterpart $^7\mathrm{Li}^-$.

Inside the 14UD, negative ions are accelerated towards the positive high voltage terminal by the electrostatic field. This static potential is provided by the Pelletron charging system. The charging chains are made of metal pellets connected by insulating nylon links. Positive charge is induced on the pellets while at the base of the accelerator tube. The chain is then pulled towards the terminal by the pulley, and as a pellet leaves the terminal, negative charge is induced on each pellet giving the terminal a positive net charge. To prevent electrostatic discharge caused by the high potential, the terminal and charging system are immersed in inorganic sulphur hexafluoride (SF_6) gas at pressure of ~700 kPa.

For a given potential V_T at the terminal, first stage acceleration gives the negative ions an energy of

$$E = V_T + V_a \tag{3.3}$$

upon reaching the terminal. Once there, the negative ions pass through a carbon stripper foil, or alternately a gas stripper. Collisions with the stripper atoms remove electrons from the ions, resulting in a distribution of positively charged ions. The charge state distribution $\bar{q}$ is given by the semi-empirical formula for particles passing through solids [72]

$$\bar{q} = Z\left[1 + Z^{0.75}\left(3.86\sqrt{\frac{E}{A}}\right)^{-1.67}\right]^{-0.6}, \tag{3.4}$$

where E is the ion-energy in MeV, Z is the atomic number, and A is the mass number of the passing ion. The foil stripper also breaks up all molecular ions to make elemental ions, e.g. the molecule $^6\mathrm{LiH}^-$ now becomes $^6\mathrm{Li}^{x+}$ and H^+.

All the ions are now positively charged and are subjected to the second stage of acceleration away from the positive terminal. The beam now has a spread of well-defined energies according to

$$E = \left(1 + q'\right) V_T + V_a \tag{3.5}$$

due to the spread in charge states q'. The desired beam energy is selected by setting the appropriate magnetic field in the energy selection magnet (see *Figure 3.2*), as the beam leaves the accelerator, with the same principle as outlined by equation (3.2). This magnetic field is measured by a nuclear magnetic resonance probe. The latest calibration of the magnet constant was done in 2004 using the same ^{12}C$(p, \alpha)^9$Be resonance at 14.23 MeV described in Ref. [61]. Repeat measurements indicate an absolute beam energy uncertainty of ±60 keV for a 60 MeV beam of ^{16}O, or 0.1%.

For all experimental runs presented in the current work, the magnetic field was not recycled between each change of energy. This is because absolute accuracy in the beam energies is not of the utmost importance as long as they are below that of the fusion-barrier energy. The uncertainty in beam energy is thus estimated to be ±0.3%. The beam energies and target combination are shown in the following section.

3.2 Targets and beam energy

The combination of targets and projectiles studied, and the range of energies, is listed in Table 3.1. The targets were prepared by evaporation of the target materials onto carbon backing foils of ~20 μg/cm^2, except for ^{197}Au and the thicker ^{209}Bi which were self-supporting targets. For the lead targets, the isotopic enrichments were ^{204}Pb (99%), ^{207}Pb (99%), and ^{208}Pb (99%). Sulphides of ^{207}Pb and ^{208}Pb were used as PbS has a much higher melting point than elemental Pb (1114°C for PbS versus 327°C for Pb), allowing them to better withstand exposure to the incident beam without degradation.

During experimental runs, all targets with carbon backings were oriented with the carbon backings facing downstream relative to the beam so as to eliminate energy loss of both the original projectile and the back-scattered reaction products. Apart from the sulphur, and the carbon backing, other light impurities may well be present in the targets, as materials may change chemical composition over time. Reactions between ^{6,7}Li and these light impurities are above-barrier for the measured beam energies, resulting in fusion evaporation residues travelling in the forward direction, thus giving little or no contribution to coincidence fragments at backward angles.

Table 3.1: The range of beam energies for the projectile/target combinations used in these experiments and the areal densities of the targets. All targets, apart from ^{nat}C, ^{197}Au and the thickest ^{209}Bi, have carbon backings with an areal density ~20 μg/cm^2.

Projectile	Target	Areal density [μg/cm^2]	Beam energies [MeV]
^{6}Li	^{207}PbS	70	26.4 to 29.0
	^{208}PbS	170	26.5 to 29.0
	^{209}Bi	130	26.5 to 29.0
^{7}Li	^{nat}C	20	28.0 to 39.0
	^{197}Au	150	20.0 to 39.0
		200 – 250	21.5 to 29.0
	^{207}PbS	70	21.5 to 29.0
	^{208}PbS	170	21.5 to 29.0
	^{209}Bi	130	21.5 to 29.0
		480	28.0 to 39.0
^{9}Be	^{nat}C	20	37.0 to 46.0
	^{204}Pb	400	37.0 to 46.0

It should also be noted that the above-barrier measurements were carried out for the reactions of ^{7}Li with ^{197}Au and ^{209}Bi, and ^{9}Be with ^{204}Pb to characterise the lampshade array and certain aspects of breakup.

3.3 Experimental setup

Charged break-up fragments were detected using a large-area position sensitive detector array consisting of four double-sided silicon strip detectors (DSSD) as shown in *Figure 3.3*. With low-current signals expected, the preamplifiers were placed as close as possible to the DSSDs, inside the target vacuum chamber, to reduce capacitive input load which introduces noise and distorts signals.

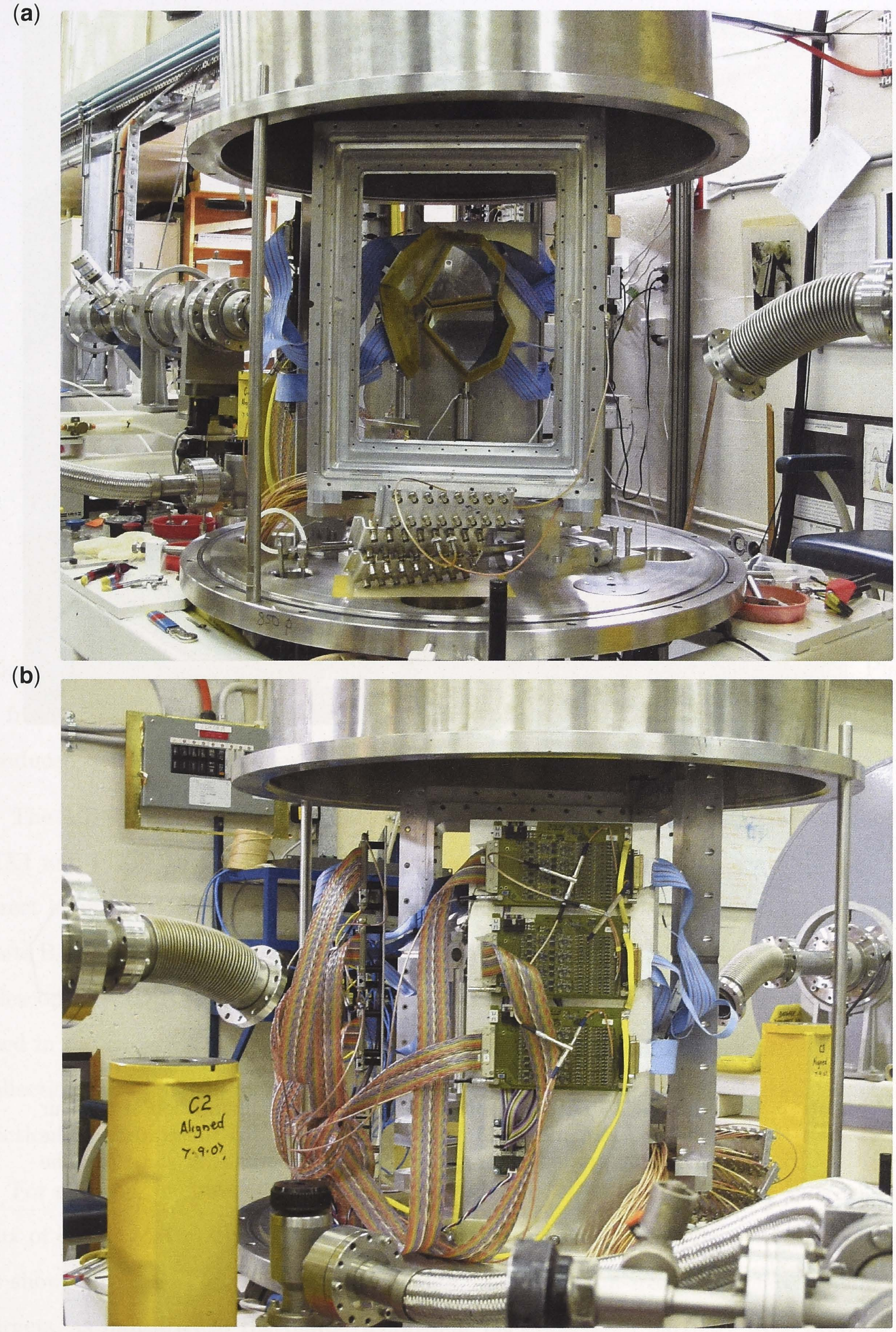

Figure 3.3: Photos of the experimental setup inside the opened vacuum chamber showing (a) the breakup detector array and (b) the pre-amplifiers and cabling.

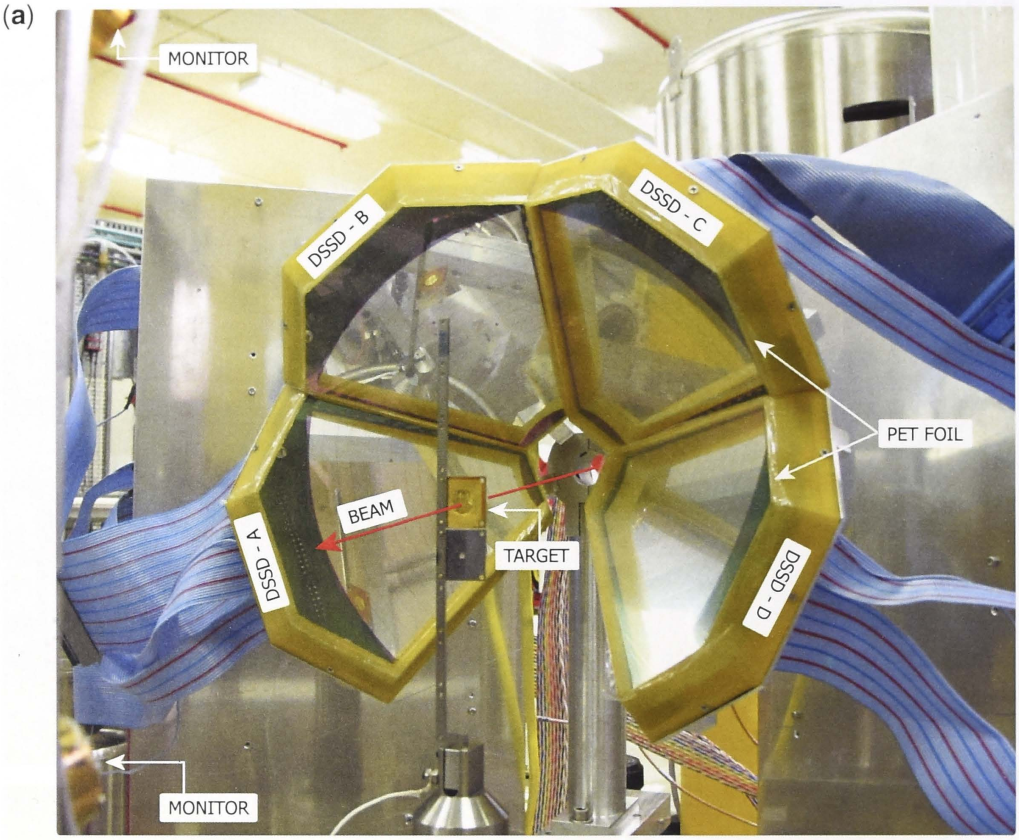

A|B|C|D
NON-TELESCOPIC CONFIGURATION

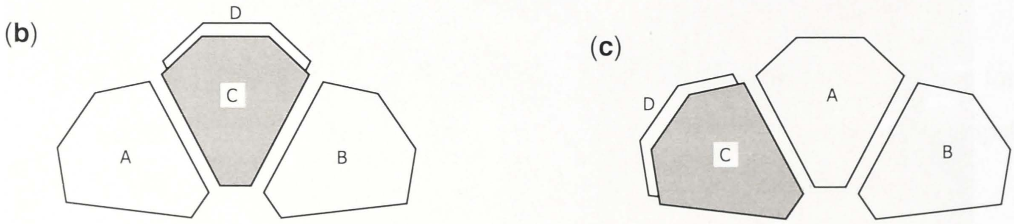

A|C-D|B
TELESCOPIC CONFIGURATION

C-D|A|B
TELESCOPIC CONFIGURATION

Figure 3.4: (a) Photograph of the A|B|C|D non-telescopic configuration of the four DSSDs as used in the LIX1 and LIX4 experimental runs. (b) Illustration of the A|C-D|B telescopic configuration as used in the LIX3 experimental run. (c) The C-D|A|B telescopic configuration used in the LIX2 experimental run.

3.3.1 Detector arrangement

The four DSSDs*, labelled A to D, are mounted on a hub in a "lampshade" annular arrangement all angled at 45°, with respect to their bisector, towards the focal point of the hub as shown in *Figure 3.4a*. All four DSSDs are 400 μm thick, with units A, B and D

---

*manufactured according to user specifications by Micron Semiconductor Limited, Sussex, UK

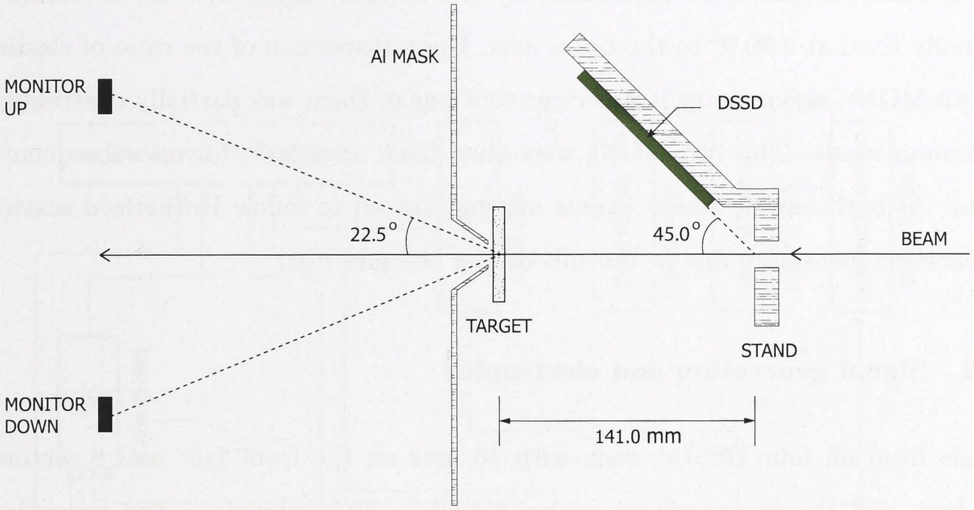

Figure 3.5: Cross-sectional view of the experimental setup showing only one of the four DSSDs. The aluminium mask is in place during experiments to stop back-scattered particles from downstream of the target.

taking −90 V of bias for full depletion, while unit C is fully depleted with −40 V. Placed in front of each DSSD is a PET* foil of 0.7 μm thickness to stop the low energy electrons produced by the interaction of the beam and the target during operation.

The A|B|C|D configuration (*Figure 3.4a*) was used in the two experimental runs labelled LIX1 and LIX4. In this configuration, there was no overlapping of the DSSDs and thus direct identification of particles was not possible. In the experimental run labelled LIX3, units B and C traded places, with unit D placed behind unit C creating a $\Delta E - E$ detector telescope A|C-D|B (*Figure 3.4b*). The telescopic arrangement C-D|A|B (*Figure 3.4c*) was used in the experimental run labelled LIX2. Details on the operation of the DSSDs, data collection, and particle identification by the $\Delta E - E$ telescope are described in detail in Section 3.4.

For all experimental runs, the entire array was placed at back angles, to avoid the high flux of elastic scattering at forward angles, and was aligned coaxially with the beam axis as shown in *Figure 3.5*. During experiments, an aluminium mask was placed behind the targets, as indicated in the figure, to prevent back-scattered particles from downstream reaching the detectors. The distance between the array and the target is adjustable resulting in different angular coverage between different experimental runs (see *Figure 3.9*).

---

[*] Polyethylene terephthalate, free sample of 3 km length from Toray Plastics, Japan.

Experimental data were normalised by two surface-barrier monitor detectors (MON) originally fixed at ±30.0° to the beam axis. Upon inspection of the ratio of elastic counts in both MONs, assymmetry it was clear that one of them was partially obstructed by the aluminium mask. The two MONs were then fixed at ±22.5° for all subsequent experiments. At both angles, elastic events are guaranteed to follow Rutherford scattering for all reactions measured, due to the sub-barrier energies used.

3.3.2 Signal generation and electronics

Signals from all four DSSDs, each with 16 arcs on the front face and 8 sectors in the rear face, and the two monitors are processed by an electronics setup consisting of six `MPR-16`[*] preamplifiers, six `STM-16+`[†] amplifiers, three `CAEN V785`[‡] analog-to-digital converters, a `CAEN V1190B`[‡] time-to-digital converters, an `ORTEC RD 2000`[§] rate divider, an `ORTEC 416A`[§] gate and delay generator, an `ORTEC CF 8000`[§] octal constant fraction discriminator, and a `LeCroy 4616`[¶] ECL-to-NIM-to-ECL converter, as shown in *Figure 3.6*.

All six `MPR-16` preamplifiers were grounded to clean earth separated from that of the main power line. Negative bias to the DSSDs were supplied by an `ORTEC 710 QUAD`[§] power supply. The detector dark currents range from 0.8 – 1.9 μA. Differential mode signals, to minimise electromagnetic interference and crosstalk coupling, are used at the pre-amplifying stage, between the DSSDs and the `MPR-16` preamplifiers, and the amplifying stage between the `MPR-16` and the shaping and timing filter amplifier `STM-16+`.

Signals from the arcs were amplified in four `STM-16+`s. Their multiplicity outputs were chained, allowing for hardware-based multiplicity selection across all the DSSDs. Each channel above the threshold contributes to a multiplicity level and a trigger is generated depending on the chosen multiplicity threshold. The coincidence time interval in defining multiplicity is also adjustable from 40 to 150 ns. Once the trigger condition is satisfied, the `STM-16+` energy and time output signals are digitised, by the `CAEN V785` and `CAEN V1190B` respectively, and sent to the data acquisition system. The `ORTEC RD 2000`, `ORTEC 416A`, and `LeCroy 4616` are used to incorporate auxiliary signals, including signals from the MONs and pulsers, for collection with signal from the lampshade detector array.

---

[*] mesytec GmbH & Co. KG, Putzbrunn, Germany.

[†] Differential version, mesytec GmbH & Co. KG.

[‡] Costruzioni Apparecchiature Elettroniche Nucleari S.p.A, Viareggio, Italy.

[§] Advanced Measurement Technology, Inc, Oak Ridge, Tennessee, USA

[¶] LeCroy Corporation, Chestnut Ridge, New York, USA.

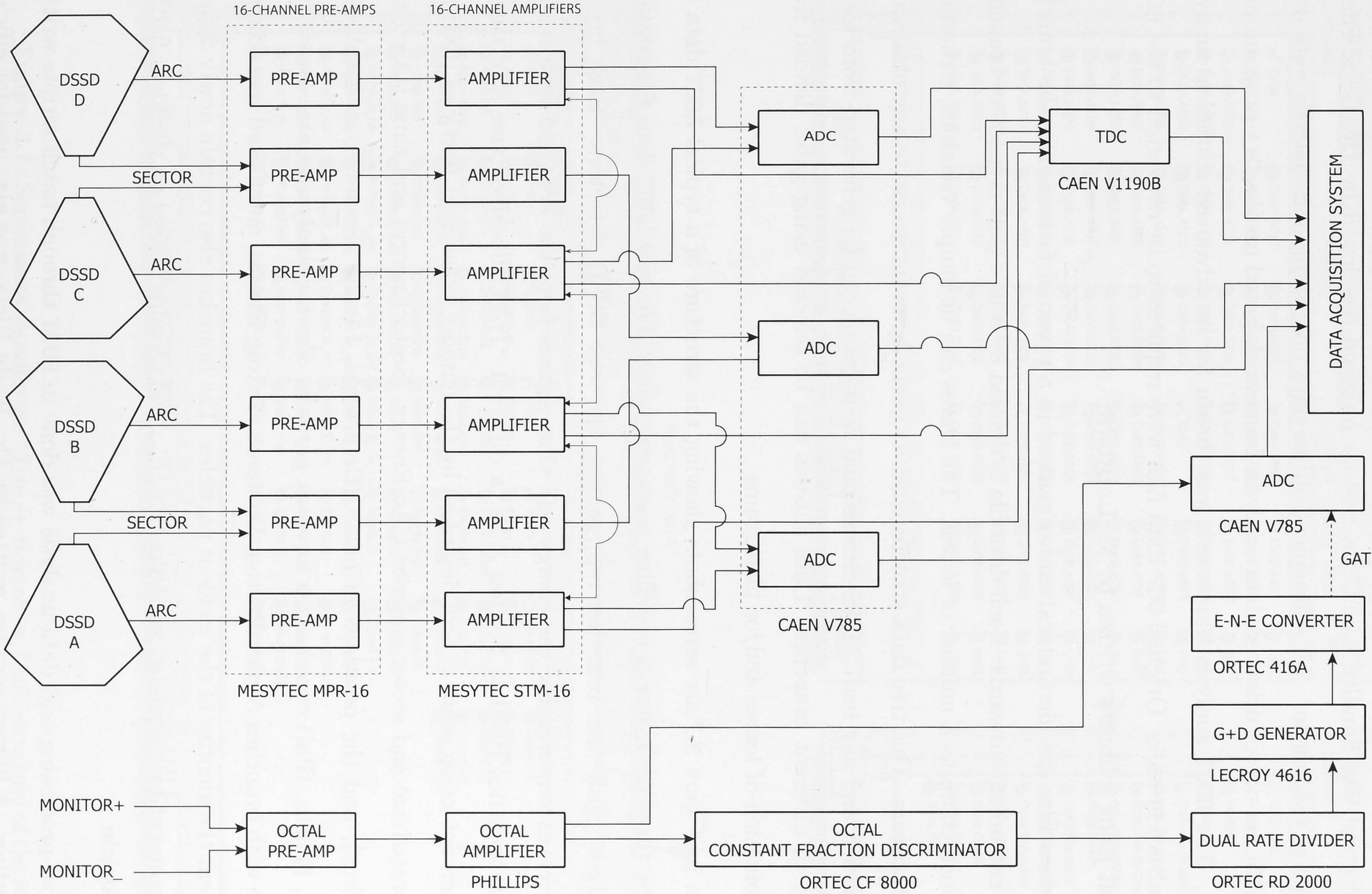

Figure 3.6: Electronics setup for signal processing.

3.3.3 Data collection and post-processing

Data collection was handled by `DCP`, a custom program developed by Dr. G. S. Foote, running on a VMScluster. All subsequent offline data processing and analysis were done in `ROOT` [15], an object oriented data analysis framework based on the `C++` programming language. The `ROOT` analysis framework was chosen for its advanced statistical analysis and visualisation tools. Original `DCP` data files were required to be converted to the `ROOT` file format using a library written by M. L. Brown.

`ROOT` data files are hierarchical and organised in a pyramid fashion, like the branches of a tree extending outwards. Each data file is defined by a tree that is made of branches. Each branch contains a number of leaves. The leaves can be simple variables, structures, arrays or objects. This tree data structure allows event-by-event access to any observable in any branch and any leaf. Multi-dimensional histograms can be generated from leaves belonging to different branches. Data subsets can be selected using gates defined from any combination of leaves and/or histograms.

Shown in *Figure 3.7* are screenshots showing the structure of a typical `ROOT` data file during the three main stages of offline post-processing. The raw `ROOT` data file contains a "CubeTree" with four branches representing the four DSSD detectors. Each branch contains leaves representing the energy and time signals from the arcs and sectors. After calibration, described in Section 3.4.4, a different "TreeCalibrated" tree structure is used. Each detection event is now described by the number of incident particles (fNHits), the calibrated arc and sector energies (fArcEnergy, fSectorEnergy) and time (fArcTime, fSectorTime), and the positions in pixel (fDetectorId, fArcId, fSectorId) and spherical (fRadius, fTheta, fPhi) coordinates for each particle. For the analysed data, a new tree structure with branches Alpha, Proton, Deuteron, Triton, Elastic, and Coord was adopted to represent the identity of the incident particles. The branches also contain newly defined leaves, representing calculated variables (e.g. E_{rel} and Q-value) based on the identified incident particle.

All post-processing and data analysis was done in `ROOT` through batch scripts written by the author. A library routine, written by Dr. R. du Rietz, was also used for efficient access and storage of data variables. Quick access to the `ROOT` data files was done via the `ROOT` graphical user interface.

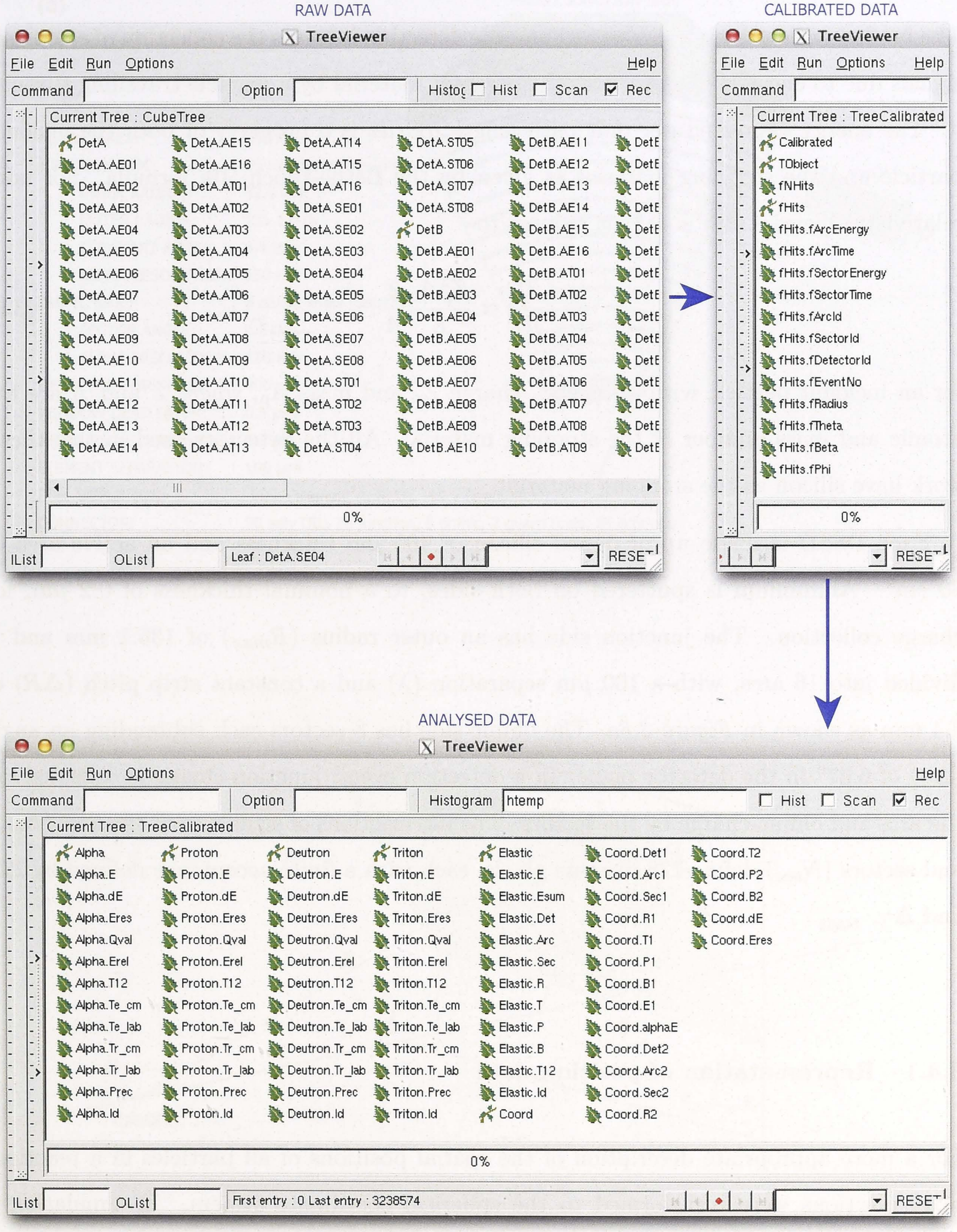

Figure 3.7: Screenshots showing the "*Tree* → *Branch* → *Leaf*" structure of the `ROOT` data files during the three main stages of offline post-processing.

3.4 The position sensitive DSSD array

The fundamental principle of charged particle detection involves the collection of electronic signals due to energy deposited into the detector material by a particle travelling through it. The energy deposited per unit path length dE/dx is a property of both the incident particle and the stopping material as given by the Bethe-Bloch [10] formula. For non-relativistic energies ($v/c < 0.1$) it reduces to

$$-\frac{dE}{dx} \propto \frac{Z_p^2 A_p}{E} \frac{Z}{A}, \tag{3.6}$$

for an incident particle with energy E, charge Z_p and mass A_p, where Z and A are the atomic and mass number of the stopping material. All the detectors used in this thesis work have silicon as the stopping material.

Each DSSD is made up of doped silicon of 400 μm thickness and an active area of 80 cm^2. Aluminium is sputtered on both sides, to a nominal thickness of 0.2 μm, for charge collection. The junction side has an outer radius (R_{max}) of 135.1 mm and is divided into 16 arcs, with a 100 μm separation (λ) and a constant strip pitch (ΔR) of 6.4 mm as shown in *Figure 3.8a*. The ohmic side has 8 sectors each subtending an angle ($\Delta\gamma$) of 6.67° in the detector plane. In a detection event, junction-charge is collected via the arcs and ohmic-charge by the sectors. The intersections of signals from the arcs (N_{arc}) and sectors (N_{sec}) define 128 discrete pixels, each with a finite acceptance defined by ΔR and $\Delta\gamma$.

3.4.1 Representation of position data

For a more appropriate description of the spatial positions of all particles in a reaction, pixel positions were transformed to the spherical coordinate system. In simulating a continuous position spectrum, the discrete (N_{arc}, N_{sec}) position information on the DSSD plane is first converted to a continuous local coordinate (R, γ),

$$\begin{aligned} R &= R_{max} - (16 - N_{arc})\Delta R - \lambda(16 - N_{arc} - 1) + \delta_R \\ \gamma &= N_{arc}\Delta\gamma - \lambda\Delta\gamma - \delta_\gamma \end{aligned} \tag{3.7}$$

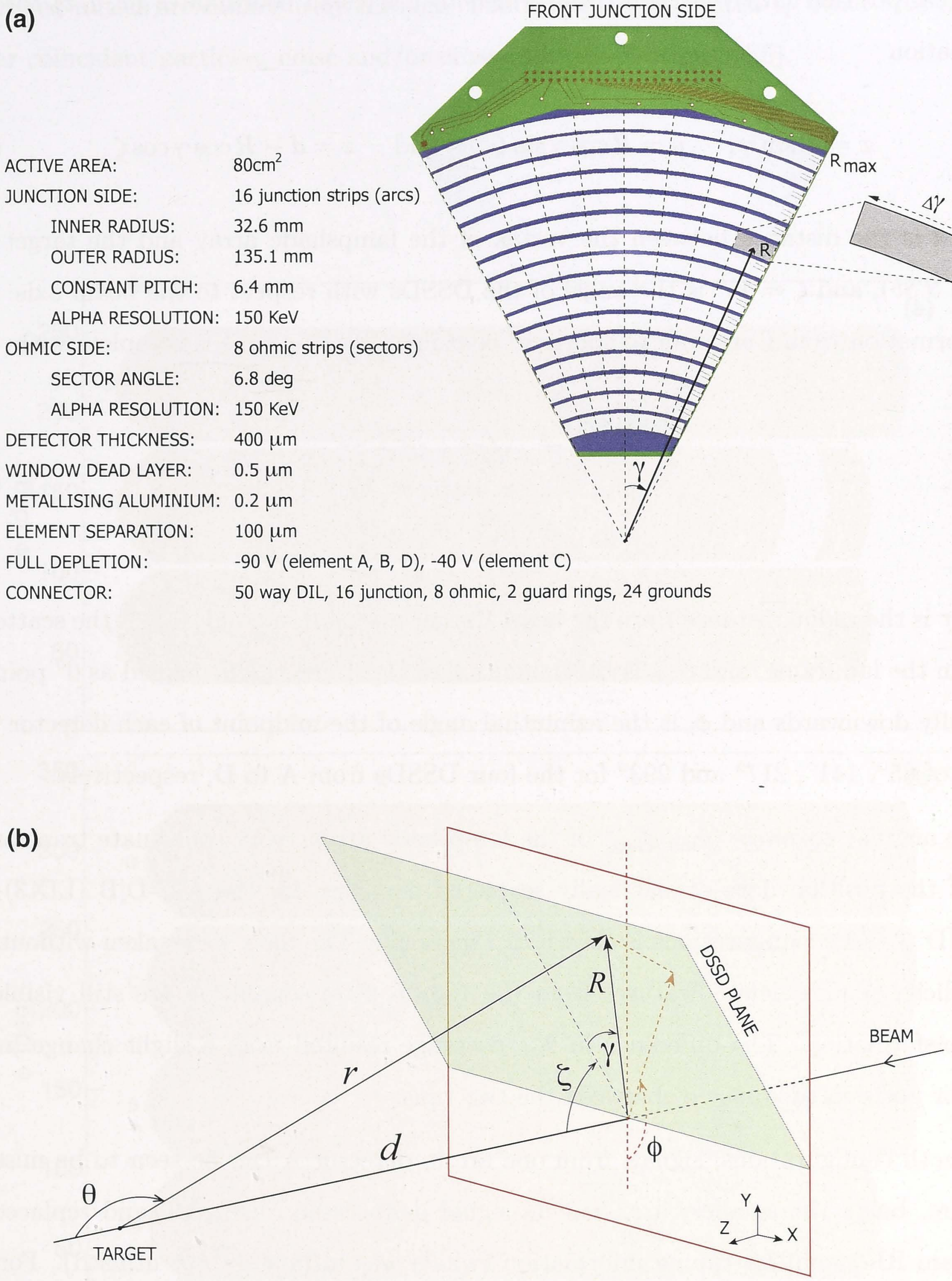

ACTIVE AREA:	80cm^2
JUNCTION SIDE:	16 junction strips (arcs)
INNER RADIUS:	32.6 mm
OUTER RADIUS:	135.1 mm
CONSTANT PITCH:	6.4 mm
ALPHA RESOLUTION:	150 KeV
OHMIC SIDE:	8 ohmic strips (sectors)
SECTOR ANGLE:	6.8 deg
ALPHA RESOLUTION:	150 KeV
DETECTOR THICKNESS:	400 μm
WINDOW DEAD LAYER:	0.5 μm
METALLISING ALUMINIUM:	0.2 μm
ELEMENT SEPARATION:	100 μm
FULL DEPLETION:	-90 V (element A, B, D), -40 V (element C)
CONNECTOR:	50 way DIL, 16 junction, 8 ohmic, 2 guard rings, 24 grounds

Figure 3.8: (a) Manufacturer specifications for the DSSDs. (b) Schematic illustration of the coordinate transformation. The local DSSD coordinate (R, γ), on a plane leaning towards the beam at $\zeta = 45°$, is randomised within the confines of the pixel $(\Delta R, \Delta\gamma)$ and transformed into spherical coordinates with origin at the beam/target interaction point.

where δ_R and δ_γ are uniformly randomly distributed from 0 to ΔR and 0 to $\Delta\gamma$ respectively. The local position (R, γ) is then transformed to Cartesian coordinates (x, y, z) through the relation

$$x = R \sin\gamma \,, \qquad y = R\cos\gamma\sin\zeta \,, \qquad \text{and} \qquad z = d - R\cos\gamma\cos\zeta \,, \tag{3.8}$$

where d is the distance between the vertex of the lampshade array and the target (see *Figure 3.8b*), and $\zeta = 45°$ is the angle of the DSSDs with respect to the beam axis. The transformation from Cartesian to spherical coordinate (r,θ_{lab},ϕ_{lab}) is complete with

$$\begin{aligned} r &= \sqrt{x^2 + y^2 + z^2} \\ \theta_{\text{lab}} &= \pi - \arccos(\tfrac{z}{r}) \\ \phi_{\text{lab}} &= \phi_{\text{i}} + \arctan(\tfrac{x}{y}) \end{aligned} \tag{3.9}$$

where r is the radial distance from the beam/target interaction point, θ_{lab} is the scattering angle in the lab frame, and ϕ_{lab} is the azimuthal angle. Here ϕ_{lab} is defined as 0° pointing vertically downwards and ϕ_{i} is the azimuthal angle of the midpoint of each detector with values of 65°, 141°, 217° and 293° for the four DSSDs from A to D, respectively.

The angular coverage (θ_{lab},ϕ_{lab}) of the lampshade array, from coordinate transformation of the position data of elastically scattered particles, for the A|C-D|B (LIX3) and A|B|C|D (LIX4) configurations is shown in *Figure 3.9.* The data were taken without any multiplicity requirement. Features from the 100μm pixel separation are still visible after transformation. The difference in θ_{lab} coverage resulted from a slight change in the detector position (distance d) between the two runs.

In both configurations, signals from one arc in detector A can be seen to be missing. This arc, being the smallest arc, had its signal deliberately discarded and replaced by the beam RF signal for timing information (which was ultimately not utilised). For the telescopic A|C-D|B configuration (*Figure 3.9a*), signals from the first and third arc from detector C were also discarded because they were found to duplicate each other. A fault in the wiring, where two exposed wires carrying the signals from the two arcs may have come into contact, is believed to be the cause. This problem was rectified when the lampshade array was reconfigured to the non-telescopic A|B|C|D configuration (*Figure 3.9b*). In this configuration, the low number of events registered at θ_{lab} ~156° from detector B is believed to be caused by the electronic unit not generating a trigger when this arc fired. Particles registered in this arc came purely through chance triggers generated by other arcs through either coincident particles, noise and/or cross-talk (see Section 3.4.6).

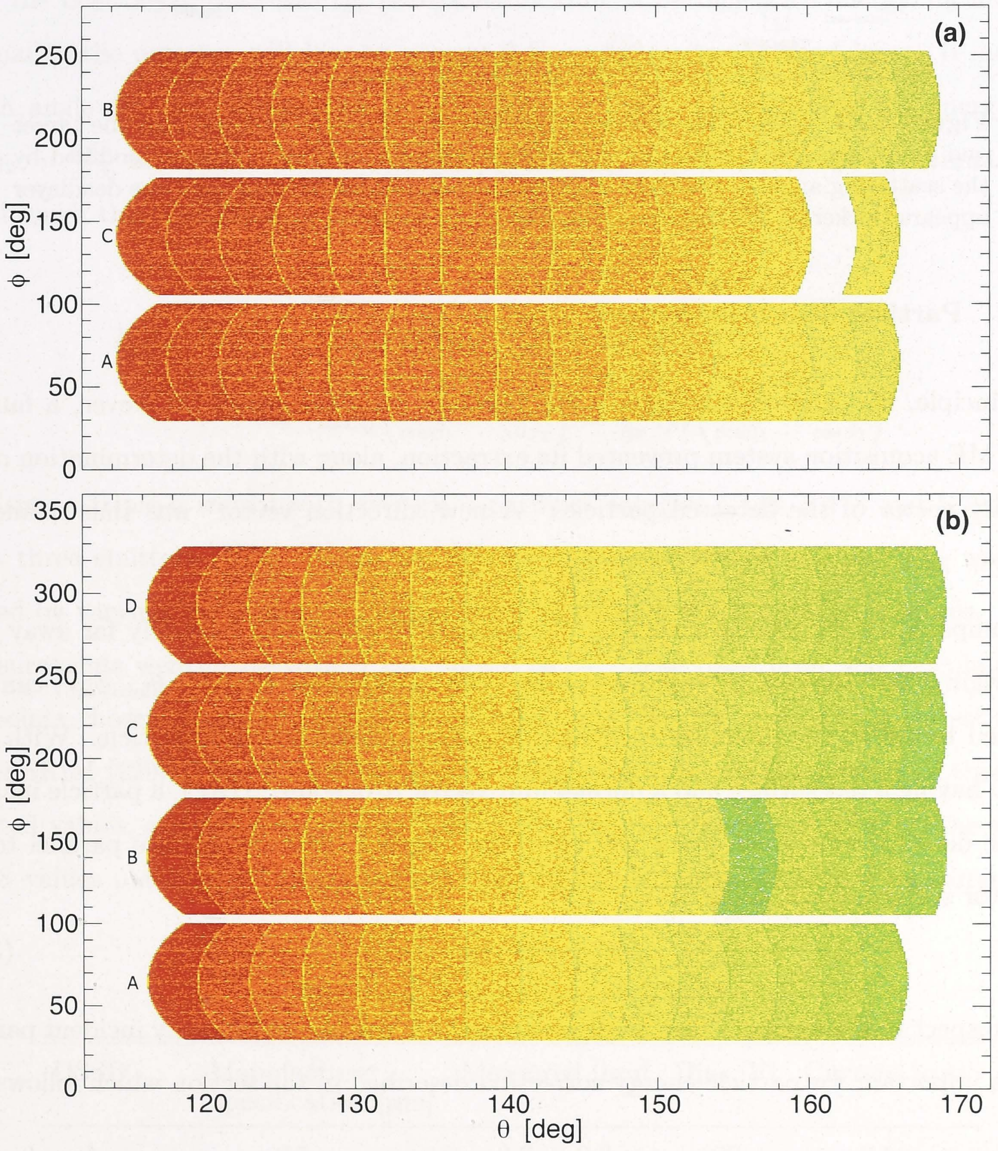

Figure 3.9: Coordinate transformation of the position data of elastically scattered particles showing the angular coverage (θ_{lab},ϕ_{lab}) of the lampshade detector array in (a) the telescopic A|C-D|B configuration used in the LIX3 experimental run, and (b) the non-telescopic A|B|C|D configuration used in the LIX4 experimental run.

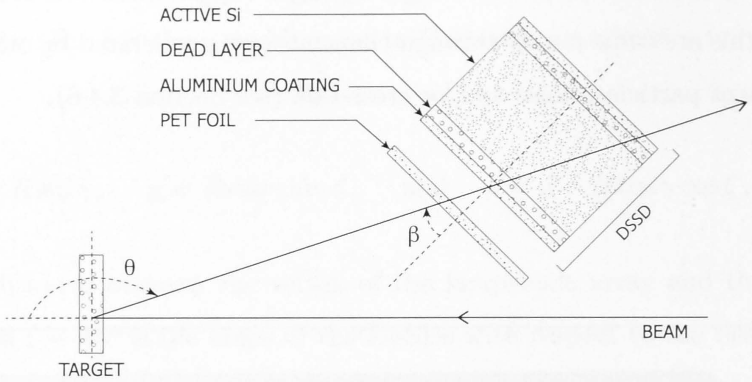

Figure 3.10: Illustration of energy loss after the particle emerges from the target and enters the DSSD detector. The apparent thickness of the target is modified by the scattering angle θ, while the PET foil, the aluminium coating, and the deadlayer appears thicker to the particle depending on its incidence angle β.

3.4.2 Particle direction vector

In principle, the time information of the particles were measured. However, a fault in the VME acquisition system prevented its extraction, along with the determination of the velocity vector of the detected particles. A new "direction vector" was thus defined as follows.

Compared to the size of a nucleus, the detector is effectively infinitely far away from the origin where the nuclear reactions occur. The spatial coordinates (r,θ_{lab},ϕ_{lab}) can thus be used to define the direction vector $\boldsymbol{v}(r,\theta_{\text{lab}},\phi_{\text{lab}})$ of the detected particle. With each DSSD having a flat surface and a normal unit vector $\hat{\boldsymbol{n}}(0, -\sin\zeta, \cos\zeta)$, a particle incident on the detector at a given point will enter the detector, and any surface parallel to the detector surface, at an angle

$$\beta = \pi - \arccos\left(\frac{\hat{\boldsymbol{n}}.\boldsymbol{v}}{v}\right) \tag{3.10}$$

with respect to the normal. This angle of incidence is calculated for every incident particle and is important for particle energy correction described in the section which follows.

3.4.3 Dead layer measurement

The dead layer is an unresponsive layer in the detector, lying close to the detector surface, where energy deposition does not result in detector signal (*Figure 3.10*). Many factors contribute to its presence and its thickness. In solid state detectors, these factors include oxidation of the active area in the detector fabrication process. Any particle incident on the detector must first traverse this layer, losing energy in doing so, before reaching the active charge-collecting region of the detector. The recorded energy of the particle is thus smaller than its true energy. Knowing the thickness of this dead layer allows correction for the true energy of the particle from the recorded energy signal.

Assuming the charge collection efficiency is not a function of angle of incidence β, and that the dead layer thickness t_{Si} is reasonably thin, a particle with energy E_0 incident normal to the detector will lose an energy $\Delta E_0 = \frac{dE_0}{dx} t_{Si}$ to the dead layer. If incident at an angle β_1, the ion loses an amount $\Delta E_{\beta 1} = \frac{\Delta E_0}{cos\beta_1}$. By knowing the energy loss $\Delta E_{\beta 2} = \frac{\Delta E_0}{cos\beta_2}$ at another incidence angle β_2, the angle method [35] allows estimation of t_{Si} through the relation

$$\begin{aligned} E_{\beta 2} - E_{\beta 1} &= (E_0 - \Delta E_{\beta 1}) - (E_0 - \Delta E_{\beta 2}) \\ &= \Delta E_0 \left(\frac{1}{cos\beta_1} - \frac{1}{cos\beta_2} \right) = \frac{dE_0}{dx} t_{Si} \left(\frac{1}{cos\beta_1} - \frac{1}{cos\beta_2} \right) . \end{aligned} \tag{3.11}$$

Using a triple-α source with average α-particles energies 5.148, 5.478 and 5.794 MeV from three emitters ^{239}Pu, ^{241}Am and ^{244}Cm, the energy losses $E_{\beta 1}$ and $E_{\beta 2}$ were obtained by varying the distance of the detector array with respect to the α source. Three measurements were made with β varying up to 24°. The dead layer was calculated for 16 points chosen diagonally across each DSSD with $\frac{dE_0}{dx}$ for each α particle estimated using SRIM [129]*. The final dead layer thickness was taken as the average of these calculated values, and are presented in Table 3.2. The uncertainties come from the spread in 48 values obtained (3 measurements with 16 values per detector per measurement).

Table 3.2: Dead layer for each DSSD

DSSD	Manufacturer specification [μm]	Measured [μm]	Bias [V]	Current [μA]
A	0.5	2.7 ± 0.3	90	0.90
B	0.5	2.4 ± 0.2	90	0.90
C	0.5	0.6 ± 0.1	40	1.70
D	0.5	2.3 ± 0.2	90	0.90

---

* J.F. Ziegler, `http://srim.org`

3.4.4 Energy calibration

At the end of each experimental run, the DSSDs were irradiated with α-particles of known energy, from the aforementioned triple-α source. These α-energies along with the energies of the elastically scattered beam particles, at all measured energies, were used in calibrating all 96 arcs and sectors individually. In reaching the active (charge collecting) area of the DSSDs, however, a particle would have suffered successive energy loss while traversing through the target, the PET foil, the aluminium coating, and the dead layer as illustrated in *Figure 3.10.* The energy loss to each layer is given by

$$\Delta E_{\mathrm{i}} = \frac{dE_{\mathrm{i}}}{dx} t_{\mathrm{i}} \frac{1}{\cos\beta}. \tag{3.12}$$

where dE_{i}/dx is dependent on both the identity and energy of the incident particle, as seen from the non-relativistic Bethe-Bloch equation (equation (3.6)), t_{i} is the known thickness of each layer, and β is the incident angle given by equation (3.10). The elastically scattered particles and α-particles, of energy E_{elas} and E_α respectively, upon reaching the active layer of the DSSDs will thus have energies E_{elas_f} and E_{α_f} respectively, calculable as

$$\begin{aligned} E_{\mathrm{elas}\_f} &= E_{\mathrm{elas}} - \Delta E_{\mathrm{tgt}} - \Delta E_{\mathrm{foil}} - \Delta E_{\mathrm{Al}} - \Delta E_{\mathrm{dlayer}} \\ E_{\alpha\_f} &= E_\alpha - \Delta E_{\mathrm{foil}} - \Delta E_{\mathrm{Al}} - \Delta E_{\mathrm{dlayer}} \end{aligned} \tag{3.13}$$

With E_{elas} given by `CATKIN`*, dE_{i}/dx given by `SRIM-2008`, and E_α known, the energies E_{elas_f} and E_{α_f} expected at the position of the 96 chosen pixels were calculated and used in the calibration of the DSSDs.

For a detected particle w, the calibrated energy E_{w_f} is then the energy it deposited in the active area of the DSSDs, not the true energy E_w it has when leaving the beam-target interaction point. To obtain the latter, the successive energy losses ΔE_{i}, which depend on the identity and energy of the particle, need to be corrected iteratively. This energy correction process was done event-by-event, during the determination of Q-values and E_{rel} as shown in Chapter 4, after the identification of the incident particles. The effect this energy correction has on the particle final energy is shown in *Figure 3.11* for protons (red), deuterons (magenta), tritons (blue), and α-particles (green).

---

[*] W.N. Catford, University of Surrey, `http://personal.ph.surrey.ac.uk/~phs1wc/kinematics/`

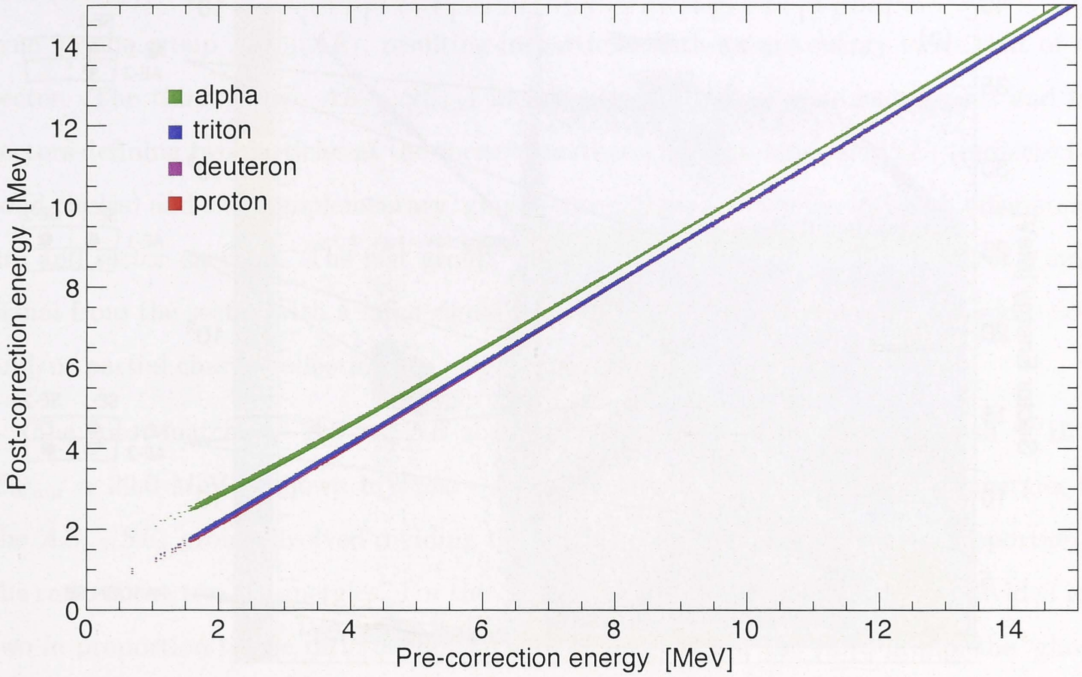

Figure 3.11: The effect of energy correction on protons (red), deuterons (magenta), tritons (blue), and α-particles (green), for energy loss while the particle traverses the dead-layer, the aluminium coating and the PET foil.

Pixel identification

As described in Section 3.4.1, intersections of signals from the arcs and sectors from the same DSSD define the position of the detected particles. However, because multiple particles may have been incident on a DSSD at different arcs but same sector, and vice versa, matching of the calibrated arc energy (AE) and sector energy (SE) is required to define the correct energies and positions for the detected particles.

The "pre-matching" AE vs. SE scatterplot from the reaction of ^{7}Li with ^{209}Bi at $E_{\mathrm{beam}} = 29.0$ MeV is shown in *Figure 3.12a*. This measurement was taken with a multiplicity-2 requirement, meaning data collection is triggered only when at least 2 arcs are fired. The plot shows all possible arc and sector correlations (both correct and incorrect), to illustrate the criteria used to determine the correct arc and sector correlation.

Groups of particles with badly mismatched arc and sector energies may be explained as follows. The group comprising particles with an arc energy half of that of the sector $AE_{1,2}|SE_1$ (illustrated in *Figure 3.12a right panel*) involves events where two coincident particles were incident in such a way that the junction-charge was collected by two

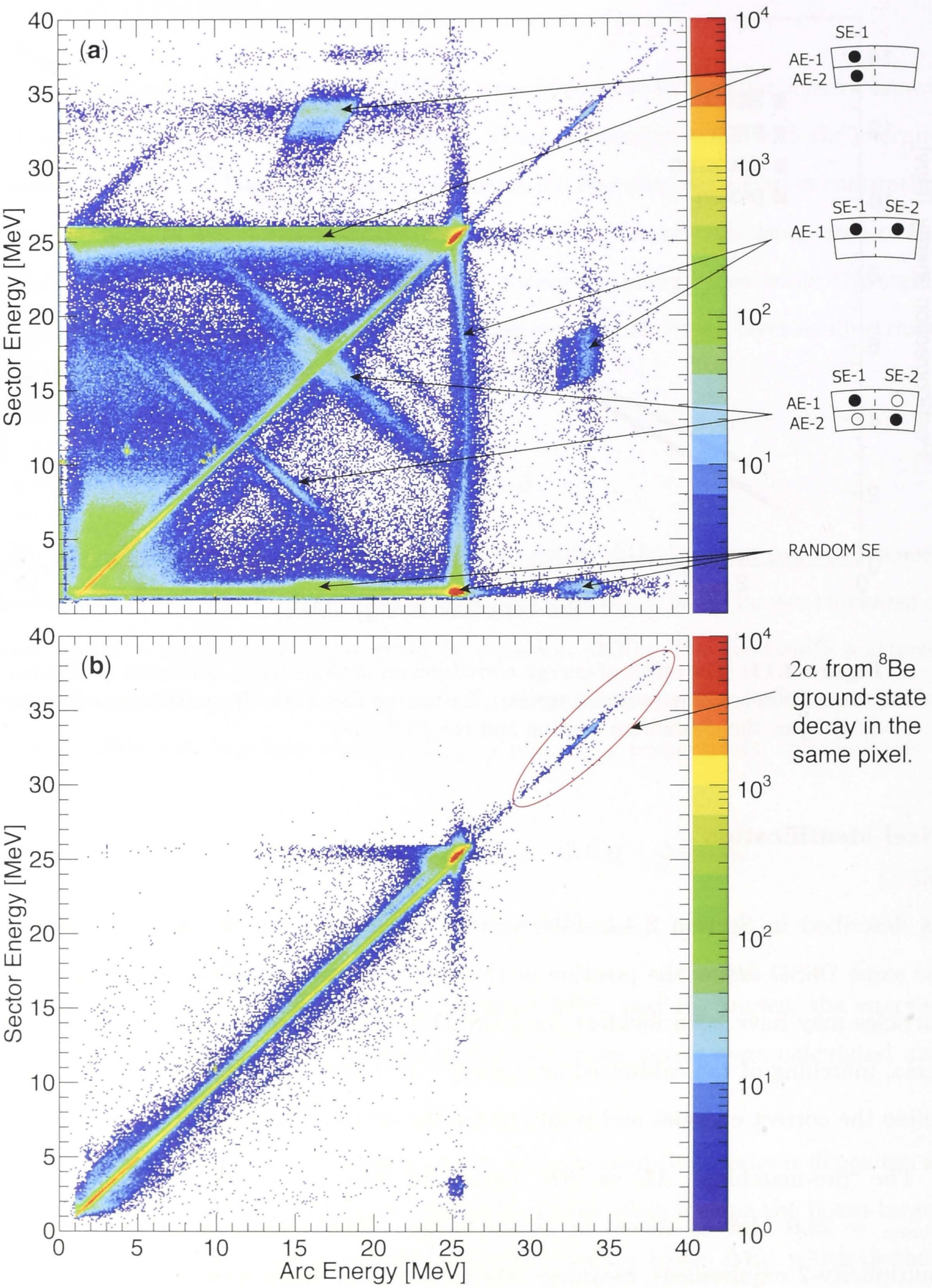

Figure 3.12: Calibrated arc and sector energy for the reaction of ^{7}Li with ^{209}Bi at E_{beam} = 29.0 MeV, from the LIX3 experimental run. (a) AE vs. SE scatterplot showing all possible arc and sector correlations. Reasons for mismatching of AE and SE are explained by illustrations and described in the body text. Here *AE-i* and *SE-i* stand for i number of calibrated arc energy and sector energy respectively. (b) The same plot as in (a) but with correct energy assignment after post-processing.

arcs ($AE_{1,2}$), while the ohmic-charge was collected from one sector (SE_1). The reverse is true for the group $SE_{1,2}|AE_1$, resulting in particles with an arc energy twice that of the sector. The third group, $AE_{1,2}|SE_{1,2}$, includes events with signals in two arcs and two sectors defining two particles at the correct location with matching $AE_1|SE_1$ (indicated by solid circles) and two complementary "ghost" correlations (hollow circles) with mismatched arc and sector energies. The last group, random SE, involves an intersection of a small signal from the sector with a large signal from the arc. This was caused by random noise and/or partial charge collection via neighbouring sectors.

The "post-matching" AE vs. SE scatterplot the same reaction of ^{7}Li with ^{209}Bi at $E_{\text{beam}} = 29.0$ MeV is shown in *Figure 3.12b.* Resolving the mismatching of energies for the $AE_{1,2}|SE_1$ group involved dividing the single sector energy into two, in proportion to the ratio of the two arc energies. For the $SE_{1,2}|AE_1$ group, the arc energy was divided into two in proportion to the ratio of the two sector energies. For the third group, the "ghost" correlations were removed. For the random SE group, the small sector energies were either removed or, when coming from a neighbouring sector, added to the larger sector energy of that same event. Particles with an energy greater than the beam energy (circled by red line in the figure) corresponds to^{8}Be, produced in the p-pickup reaction ^{209}Bi(^{7}Li,^{8}Be)^{208}Pb, where the 2α from the ground-state decay were incident in the same pixel. The small fraction of off-diagonal particles ($< 0.2\%$) come from events with incomplete junction- or ohmic-charge collection.

To verify both the energy calibration, and coordinate transformation of the pixels, a scatterplot of the "post-matching" arc energy against the scattering angle θ_{lab} is shown in *Figure 3.13*, for the reaction of ^{7}Li with ^{209}Bi at $E_{\text{beam}} = 31.5$ MeV for a multiplicity-1 trigger condition. Events belonging to the most intense group at E ~27.5 MeV have decreasing energy with increasing scattering angle, as is expected for elastic scattering. The group at ~25.0 MeV corresponds to n-stripping resulting in ^{6}Li, while the group at ~23.5 MeV corresponds to inelastic scattering of ^{7}Li by excitation of the target. Groups with constant energies independent of angle, between 5 to 10 MeV, consist of α-particles from the α-unstable evaporation residues formed following complete and incomplete fusion (E_{beam} is above the fusion barrier energy). The stability and correct value of these energies confirm both the energy calibration and position representation methods. The group with a broad energy distribution, at about 4/7 of the beam energy, is most likely α-particles from break-up of ^{7}Li with the complementary fragment contributing to the broad distribution seen below 11 MeV.

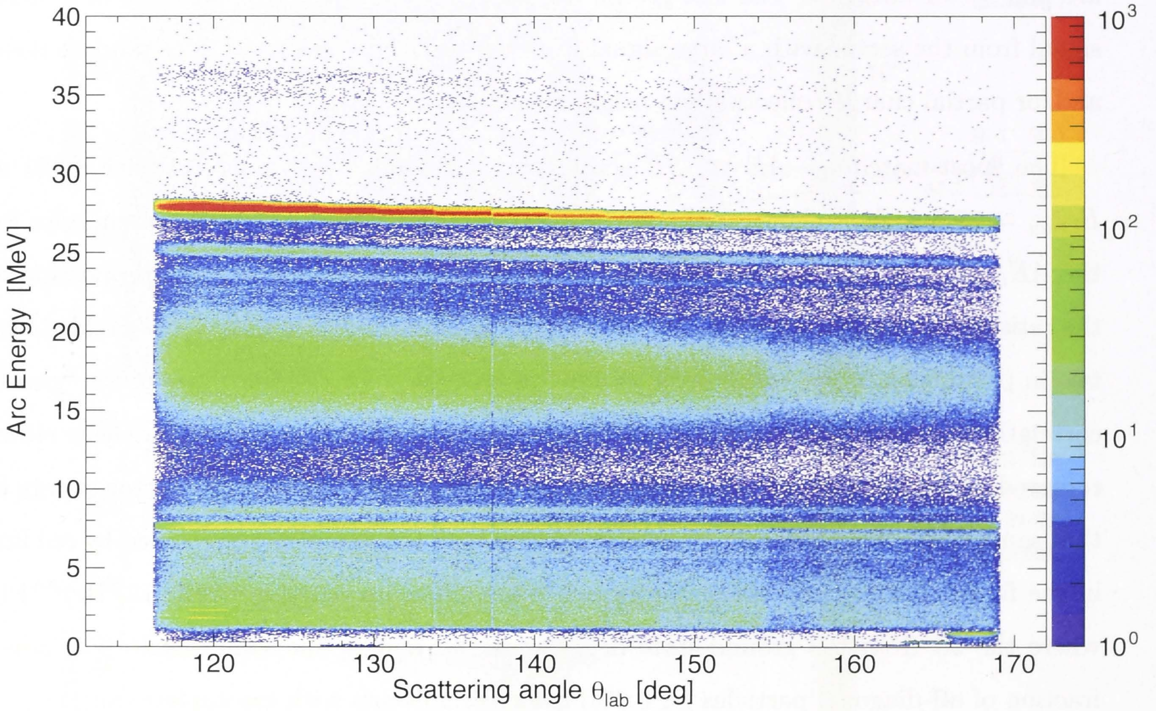

Figure 3.13: AE vs. θ_{lab} scatterplot for particles detected in singles in the reaction of ^{7}Li with ^{209}Bi at $E_{\mathrm{beam}} = 31.5$ MeV.

Arc and sector energy resolution

The difference in the resolution between the calibrated AE and SE is shown in *Figure 3.14* for the DSSD labelled A. This data was taken from the reaction of ^{7}Li with ^{209}Bi at $E_{\mathrm{beam}} = 31.5$ MeV. The AE spectrum can be seen to have a full width at half maximum (FWHM) of $\lesssim$0.1 MeV (*Figure 3.14a*), compared to a FWHM of ~0.30 MeV in the corresponding SE spectrum taken from the same pixel (*Figure 3.14b*). The other DSSD detector showed similar features. For this reason, the calibrated arc energy AE was used for energy determination of the detected particles.

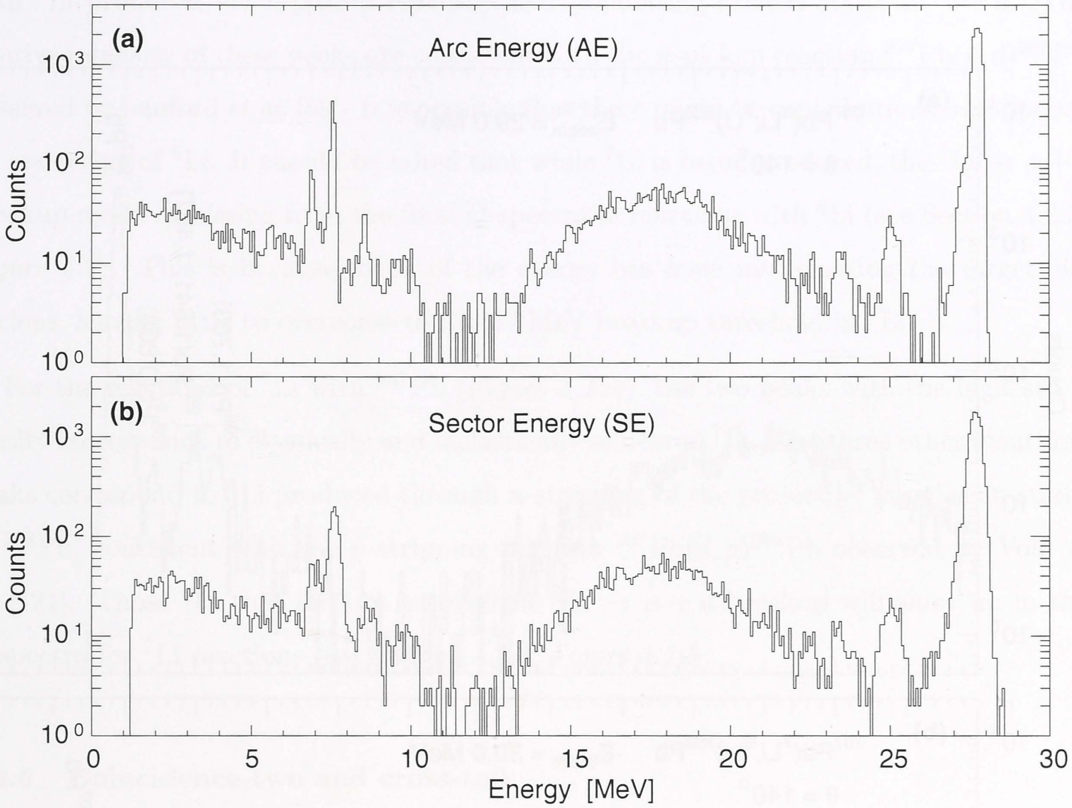

Figure 3.14: The difference in resolution of (a) AE and (b) SE for particles detected in the reaction of ^{7}Li with ^{209}Bi at $E_{beam} = 31.5$ MeV, at a specific pixel in the DSSD labelled A.

3.4.5 Coincidence-one and ground-state transfer

After calibration and resolution of the mismatched arc and sector energies, the "post-matching" data would include both single particle and multiple particles events. This is true for data taken with both hardware-based multiplicity-1 and multiplicity-2 requirements. For the latter, one expects only multi-particle events, however, occasionally random noise will give rise to a signal and satisfy the hardware-based multiplicity level requirement. Events with only one single genuine particle are labelled *coincidence-one*, while those where two particles were determined to be in coincidence are called *coincidence-two*.

The reactions of ^{6,7}Li with ^{207}Pb were measured with a hardware-based multiplicity-1 requirement at $E_{\text{beam}} = 29.0$ and 30.0 MeV respectively. Shown in *Figure 3.15* are the energy spectra for coincidence-one events from these reactions. For the reactions of ^{6}Li with ^{207}Pb (*Figure 3.15a*), the peak at the highest energy, and also with the highest intensity, corresponds to elastically scattered ^{6}Li. The next three peaks are consistent in energy

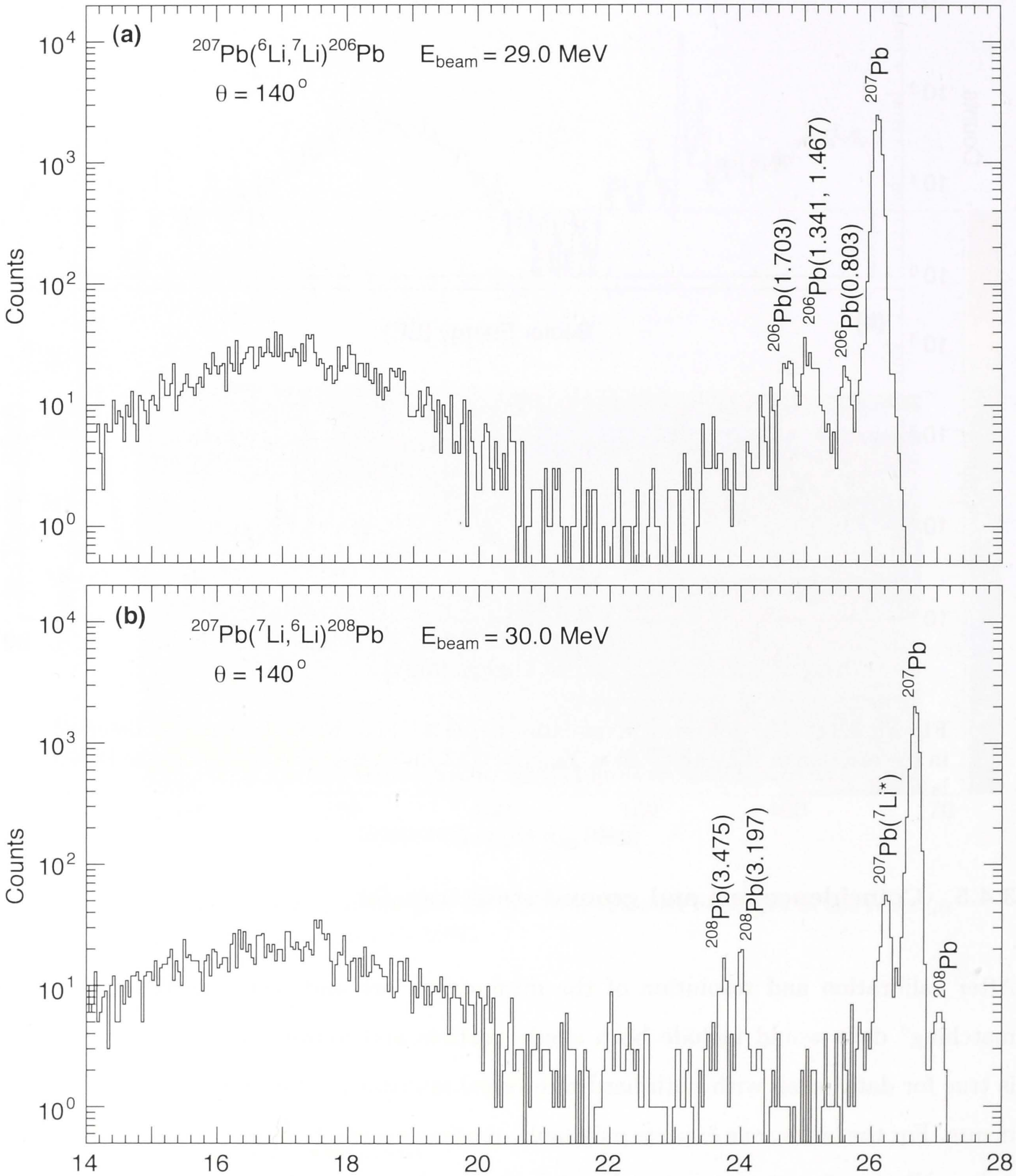

Figure 3.15: Energy spectra for coincidence-one events at scattering angles centered at $\theta_{\rm lab} = 140^\circ$ (with a $\Delta\theta = 5^\circ$ bin width) for the reactions of ^{6,7}Li with ^{207}Pb at the indicated energies. The numbers inside the brackets indicate the excitation energy, in MeV, of the target-like nucleus. (a) The identified peaks correspond to elastic scattering of ^{6}Li, and possible n-pickup channels producing ^{7}Li which populate various states in ^{206}Pb. (b) The identified peaks correspond to the elastic and inelastic scattering of ^{7}Li, and the n-stripping channels populating ^{208}Pb in various states.

with ^{7}Li produced via n-pickup reactions and populating excited states in ^{206}Pb. The relative intensity of these peaks are consistent with the n-pickup reaction $^{207}\mathrm{Pb}(p,d)^{206}\mathrm{Pb}$ observed by Lanford *et al.* [59]. It is possible that there might be contributions from inelastic scattering of ^{6}Li. It should be noted that while ^{7}Li is being produced, the $^{7}\mathrm{Li} \rightarrow \alpha + t$ breakup mode is missing from the final Q-spectra in reactions with ^{6}Li (see Section 4.2.2, *Figure 4.9*). This is because much of the energy has gone into exciting the target-like nucleus, leaving little to overcome the 2.467 MeV breakup threshold in ^{7}Li.

For the reactions of ^{7}Li with ^{207}Pb (*Figure 3.15b*), the two peaks with the highest intensity corresponds to elastically and inelastically scattered ^{7}Li. The three other identified peaks correspond to ^{6}Li produced through n-stripping of the projectile, populating states in ^{208}Pb, consistent with the n-stripping reaction $^{207}\mathrm{Pb}(d,p)^{208}\mathrm{Pb}$ observed by Vold *et al.* [121]. Those ^{6}Li that did not survive the $^{6}\mathrm{Li} \rightarrow \alpha + d$ breakup will show up in the Q-spectra for ^{7}Li reactions (see Section 4.2.3, *Figure 4.10*).

3.4.6 Coincidence-two and cross-talk

For coincidence-two events, the E_1 vs. E_2 scatterplot reveals many interesting features as shown in *Figure 3.16a* for data from the reaction of ^{7}Li with ^{209}Bi at $E_{\mathrm{beam}} = 31.5$ MeV. A few events are found in the horizontal and vertical bands indicating that one of the two particles has an energy equal to that expected of elastically scattered ^{7}Li at the given beam energy. Events comprising these bands must be random coincidences between an elastically scattered ^{7}Li and another fragment at lower energy (or coincidence between two elastically scattered particle for events comprising the intersection of the two bands). Most of the events however, lie on diagonal bands comprising events with a fixed sum energy ($E_1 + E_2$) that defines each band and its label (A to F). The energy correlation between the coincident particles indicates that they are fragments from the same parent-nuclei of energy $E_0 = E_1 + E_2$, i.e. breakup events. Discrete bands then indicate breakup of different parent-nuclei, or parent-nuclei with different kinetic energies.

Not all coincidence-two events with energy correlation (*Figure 3.16a*) are genuine breakup events, however, as can be seen in the E_1 vs. E_2 scatterplot (*Figure 3.16b*) only for events where the two particles were incident on neighbouring pixels of the same DSSD. Given this condition, these correlated events can either be genuine two particles events with small opening angle between them, or a single particle that was incident on

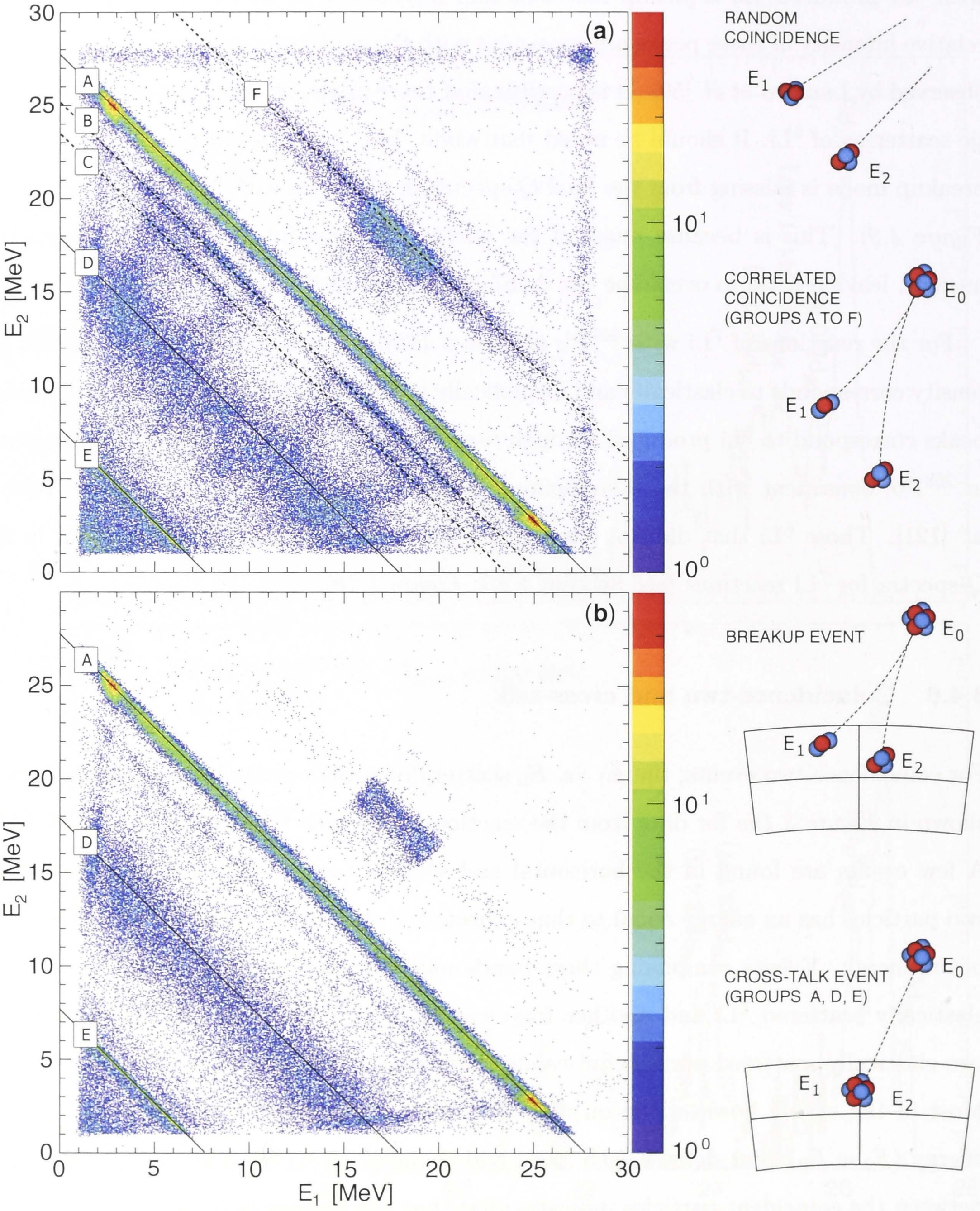

Figure 3.16: (a) E_1 vs. E_2 scatterplot for coincidence-two events in the reaction of ^{7}Li on ^{209}Bi at $E_{\mathrm{beam}} = 31.5$ MeV. Diagonal bands comprise events consisting of fragments originating from the same initial nuclei of energy $E_0 = E_1 + E_2$, i.e. breakup events. (b) Same plot as in (a) but only for events where both fragments were detected in two adjacent pixels of the same DSSD, as illustrated in the right panel. Bands A, D, and E are due to *cross-talk* (a single particle incident on the inter-strip separation simulating a coincidence event, see illustration) of elastically scattered particles, α-particles from breakup of ^{7}Li, and α-particles from the decay of α-unstable evaporation residues, respectively.

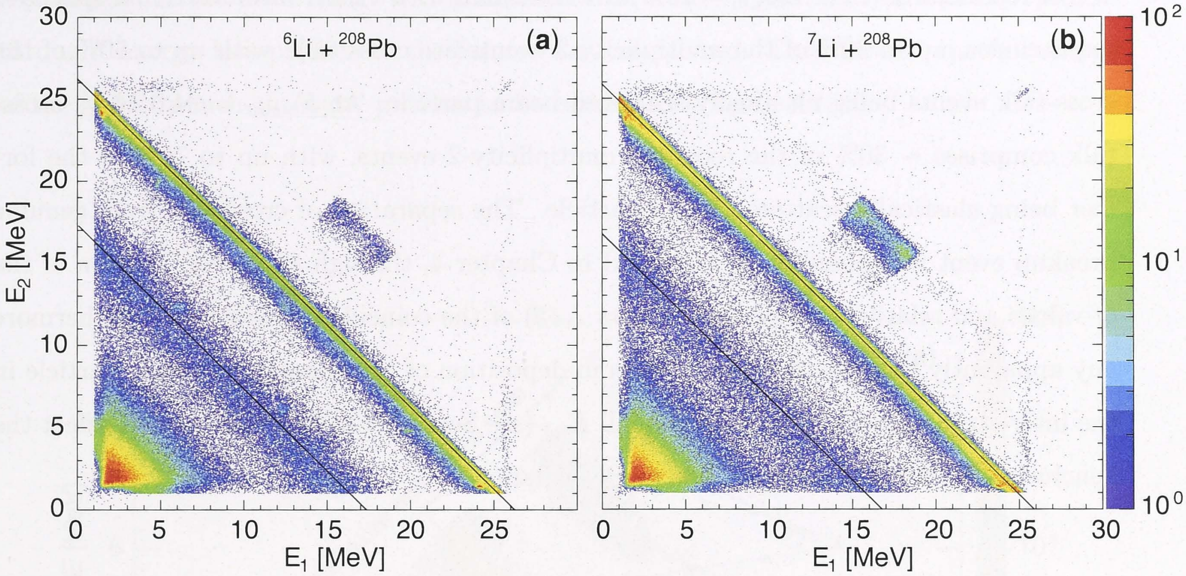

Figure 3.17: E_1 vs. E_2 scatterplots for coincidences where both particles were incident on neighbouring pixels for the indicated reactions at $E_{\text{beam}} = 29.0$ MeV.

the DSSD right at the inter-strip separation causing the junction- or omhic-charge to be collected via two arcs or two sectors. Energy matching during calibration (see Section 3.4.4) then allows these single particle *cross-talk* events to simulate a genuine binary event with correlated energies as illustrated. Here, events comprising bands A and E have sum energy E_0 equal to that expected of an elastically scattered ^{7}Li and α-particles from the α-unstable evaporation residues, respectively. Since breakup of ^{7}Li requires energy expenditure, and there is no breakup mode for ^{7}Li that produces particles with a sum energy at precisely the energy of α-particles from the α-unstable evaporation residues, events comprising these two bands are thus cross-talk events. Similarly, events in band D have a sum energy $\sim$18 MeV, coinciding with particles forming the intense group at about 4/7 of the beam energy (*Figure 3.13*), and thus are most likely due to cross-talk of α-particles from breakup of ^{7}Li where the complementary partner escaped detection.

Further evidence indicating the origin of group E (in *Figures 3.16a,b*) as cross-talk of α-particles is seen in the E_1 vs. E_2 scatterplots (*Figure 3.17*) of coincidence-two events from the reactions of ^{6,7}Li with ^{208}Pb at $E_{\text{beam}} = 29.0$ MeV. Since this energy is sub-barrier for the two systems, there is no significant number of cross-talk events from α-particles from the decay of evaporation residues. Cross-talk of elastic particles and α-particles from breakup remain however, as indicated by the diagonal lines.

For reactions of ^{7}Li at $E_{\text{beam}} = 29.0$ MeV measured with a hardware-based multiplicity-2 requirement, up to 20% of the multiplicity-2 events are cross-talk, with up to 50% of the cross-talk events being elastically scattered beam particle. At $E_{\text{beam}} = 24.0$ MeV, cross-talk comprises $\sim$ 30% of the recorded multiplicity-2 events, with up to 70% of the former being elastically scattered beam particle. The separation of cross-talk from genuine breakup event was possible, as discussed in Chapter 4, through the determination of the Q-values and relative energy E_{rel} (*Figure 4.12*) of the coincident fragments. Furthermore any apparently binary event resulting from deposition of the energy of a single particle in the inter-strip region will have very small E_{rel} (see Section 4.3) and thus cannot affect the conclusion for *prompt* breakup, where E_{rel} is large.

3.4.7 Particle identification

The Bethe-Bloch equation, (3.6), shows that for a charged particle travelling in a material, the energy loss depends *linearly* on the mass of the incident particle but *quadratically* on its charge Q_p. At these velocities, the ions are fully stripped, and thus $Q_p \approx Z_p$, the atomic number of the particle. By measuring first a fraction of energy loss ΔE and the residual energy E, both the mass and charge of the particle can be determined. With the lampshade detector arranged in the A|C-D|B telescopic configuration (*Figure 3.4b*), energetic particles may penetrate the front detector C, registering a ΔE signal, before depositing the remaining energy in the back detector D for an E signal. Since each DSSD detector is 400 μm thick, an α-particle for example will need to have an energy greater than 29.0 MeV to penetrate detector C, and be identified by this particular $\Delta E - E$ setup.

From the reaction of ^{7}Li on ^{207}Pb at $E_{beam} = 29.0$ MeV, the recorded energy ΔE is plotted against the sum energy $E_{total} = \Delta E + E$ in *Figure 3.18a*. Overlaid are `SRIM-2008` predictions, for the energy deposition profiles for protons, deuterons and tritons with incident energy ranging from 7.0 to 20.0 MeV, for the given thickness of the DSSDs. Agreement between data and `SRIM-2008` predictions shows that the $\Delta E - E$ telescope can be used to separate isotopes of hydrogen, but only in a limited energy range of 7.5 to 11.0 MeV for protons, 10.0 to 15.0 MeV for deuterons, and 11.5 to 17.0 MeV for tritons. For hydrogen isotopes with energies higher than their respective ranges, full energy deposition is not possible as the particles will penetrate both DSSDs (punch-through) and the energy loss profiles overlap. From `SRIM-2008` predictions for full energy deposition (*Figure 3.18b*) assuming that the back DSSD was infinitely thick, a direct relation between the "punch-through" energy loss profiles to the former was established. This allowed the full energy of the gated "punch-through" protons to be estimated (*Figure 3.18b*).

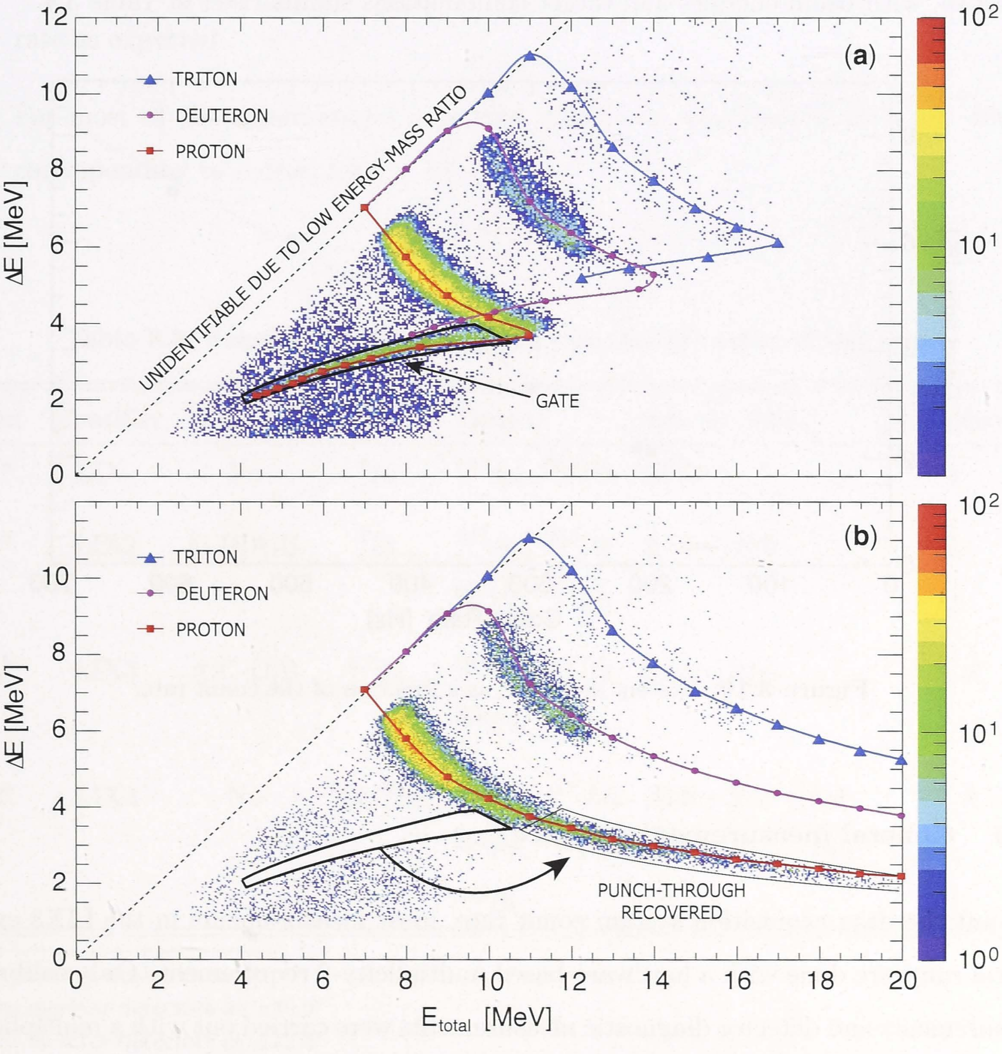

Figure 3.18: (a) A plot of the energy loss ΔE in the front DSSD against the total energy of loss E_{total} in both the front and back DSSDs of the telescope. Overlaid are the `SRIM-2008` predictions of the energy loss in each DSSD for protons, deuterons and tritons of energies from 7 to 20 MeV. The kink in the $\Delta E - E$ profile for proton is due to the proton punching through the back DSSD. (b) Same plot as in (a) but with the energy loss due to punch-though protons recovered. The overlaid `SRIM-2008` calculation now specifically assume the back DSSD is infinitely thick.

3.5 Experimental runs summary

Four experiments were carried out with different detector arrangements and electronics trigger multiplicity levels as summarised in Table 3.3. The first two experiments, LIX and LIX2, were done to test the detector setup, the electronics and to develop analysis software. All results presented in this thesis came from the later two experiments, LIX3 and LIX4, with beam energies and target combinations summarised in Table 3.4.

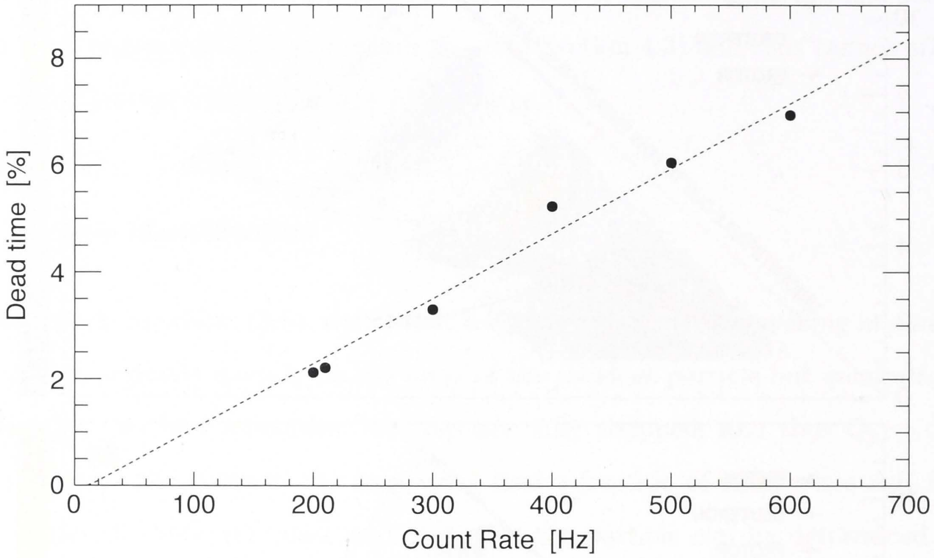

Figure 3.19: System deadtime as a function of the count rate.

3.5.1 General measurement practice

To limit the data acquisition system count rate, most measurements in the LIX3 experimental run were done with a hardware-based multiplicity-2 requirement. Only calibration measurements and detector diagnostic measurements were carried out with a multiplicity-1 requirement (or in other words, no multiplicity requirement) in this experimental run. Generally, the following measurement procedure was followed for all the runs:

- Before each run, the lampshade detector array was always properly aligned, using a telescope, to ensure it is positioned coaxially with the beam.
- The vacuum chamber in which the detector and the entire pre-amp ensemble is housed is generally kept at a pressure of $\sim 1.3\times10^{-5}$ Pa during operation.

- The elastic counts from the monitor detectors, when in use, were usually pre-scaled by a factor of 10 to 100 to limit the count rate. Counts from the elastics were used for normalisation purposes.

- A pulser was sent through to one arc and one sector of each DSSD, triggered by pre-scaled elastic counts in one of the monitor detectors, to monitor the system dead time. The system dead time (*Figure 3.19*) was found to vary linearly with the count rate as expected.

- For most of the experimental runs, the count rate was limited to below 400 Hz, corresponding to a dead time < 6%.

Table 3.3: Summary of all experimental runs over the course of four years.

run	Identifier	$\Delta E - E$	Beam	Targets	Energy [MeV]	Multiplicity
1[a]	LIX	No	^{7}Li	^{197}Au, ^{208}Pb	30.0	1
2[a]	LIX2	C-D|A|B	^{7}Li	^{197}Au, ^{204}Pb	27.5 - 30.0	1
				^{207}Pb, ^{208}Pb		1
3[b]	LIX3	A|C-D|B	^{6,7}Li	^{197}Au, ^{207}Pb	21.5 - 29.0	1, 2
				^{208}Pb, ^{209}Bi		
4[c]	LIX4	No	^{7}Li, ^{9}Be	^{nat}C, ^{197}Au	20.0 - 39.0 (^{7}Li)	1, 2
				^{204}Pb, ^{208}Pb	37.0 - 46.0 (^{9}Be)	1
				^{209}Bi		1

---

[a] No monitor detectors used.
[b] Two monitor detectors at ±30.0°
[c] Two monitor detectors at ±22.5°

Table 3.4: Measurements analysed and presented in this thesis.

Beam	Energy		Target		
	[MeV]	^{197}Au	^{207}Pb	^{208}Pb	^{209}Bi
^{6}Li	26.5		✓	✓	✓
	29.0		✓	✓	✓
^{7}Li	20.0	◇			
	21.5	◇			
	24.0		✓	✓	✓
	26.5		✓		
	29.0		✓	✓	✓
	30.0		●		
	31.5				●

✓ Measurements fully analysed to extract the breakup parameters used in `PLATYPUS`.

◇ Measurements used for detector normalisation.

● Measurements used for detector checks and calibration purposes.

It is important to realise that it is not the one measurement, alone, but its relation to the rest of the sequence that is of interest.

W. E. Deming (1900 - 1993)

4

A complete picture of breakup

Coincidence measurements were carried out at sub-barrier energies for the reactions of ^{6,7}Li with ^{207}Pb, ^{208}Pb and ^{209}Bi. Distinct groups of binary-fragment events are observed having correlated energies. Kinematic reconstruction of these binary fragments allows the determination of reaction Q-values and relative energies E_{rel} between the two fragments. The Q-values and E_{rel} are then utilised to get a complete picture of the reaction mechanism and dynamics that result in the observed binary events.

In this Chapter, results from coincidence measurement of ^{6}Li and ^{7}Li are presented in Section 4.1. Details on the origin of the fragments, as determined through the reaction Q-value are presented in Section 4.2. Information on the reaction time-scale from the relative energy E_{rel} spectra of the coincidence fragments, is discussed in Section 4.3.

4.1 Binary break-up of ^{6,7}Li

With the lampshade detector arranged in the A|C-D|B telescopic configuration (*Figure 3.4*), the reactions of ^{6,7}Li with ^{207}Pb, ^{208}Pb and ^{209}Bi were measured at various sub-barrier energies with a multiplicity-2 requirement. The data were found to include events where (i) a single particle was detected which triggered two detector arcs labelled *coincidence-one* events, and (ii) two particles in coincidence labelled *coincidence-two* events. The presence of coincidence-two events is in line with the expectation that cluster breakup of ^{6,7}Li will produce a maximum of two charged fragments, $\alpha+i$, where i can be either a *proton*, *deuteron*, or *triton*. In the subsections that follow, only coincidence-two data are presented.

4.1.1 ^{6}Li + ^{208}Pb

The individual energies E_1 and E_2 of the two coincident fragments already provide a lot of information. An E_1 vs. E_2 scatterplot is shown in *Figure 4.1a* for mass-unidentified coincidence-two events following the reaction of ^{6}Li with ^{208}Pb at $E_{beam} = 29.0$ MeV. The ordering between the two particles (E_1 or E_2) was randomised, since their identities are unknown, resulting in symmetry about 45°. The structures that emerge from this scatterplot include groups of events forming distinct diagonal bands, as defined by the sum energy $E_1 + E_2$ of the coincident particles, labelled A to D, and horizontal and vertical bands (at E_i ~26 MeV) labelled E.

Events in band E have energies E_1 or $E_2 \sim 26$ MeV, which matches the expected energy of elastically scattered beam particles detected in the detector array. These events are thus random coincidence between two elastically scattered beam particles, or between an elastically scattered particle and another particle of lower energy. As for events comprising the diagonal bands, the energy correlation between the coincident particles showed that the pair have a common origin, making them prime candidates for binary breakup following interaction of ^{6}Li with the target nucleus.

The diagonal band A is seen to be discontinuous between $10 < E_{1,2} < 12.5$ MeV, at which it is replaced by events with different energy correlations forming two arcs. The missing energy at which the band is broken matches exactly with the maximum energy a deuteron can deposit in the 400μm thick DSSD. Events in these arcs thus arise from x-particle + *deuteron* coincidences, where a deuteron with energy greater that 10 MeV was incident on the non-telescopic part of the detector array. The diagonal part of band A have full energy deposition for x-particles with energy >15 MeV, indicating these particles are possibly α-particles. Events forming the diagonal part of this band should therefore be α-particle + deuteron ($\alpha + d$) coincidences.

The two diagonal bands labelled B are also discontinuous at $E_{1,2} > 7.5$ MeV, the energy at which a proton would punch through the DSSD and at which they are joined by events forming arcs. Following the same line of reasoning as for the case of $\alpha + d$ coincidences, events in these arcs should include coincidences of α-particle and a high energy proton, where the latter was incident on the non-telescopic part of the detector. Events forming the diagonal part of band B should therefore be α-particle + proton ($\alpha + p$) coincidences.

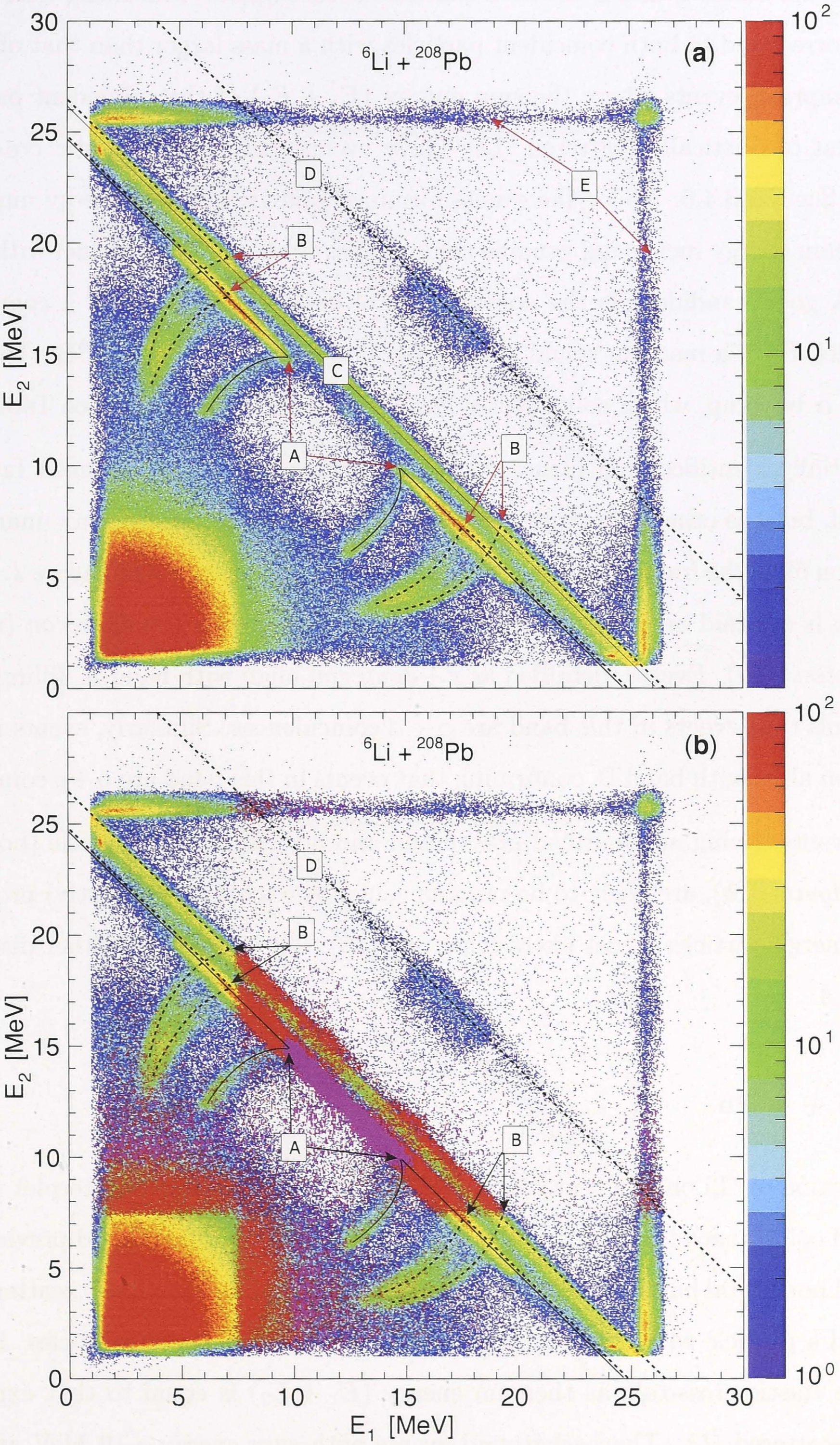

Figure 4.1: (a) E_1 vs. E_2 scatterplot for mass-unidentified coincidence-two events from the reaction of ^{6}Li on ^{208}Pb at E_{beam} = 29.0 MeV. Symmetry about 45° is a result of random ordering of the coincident particles. (b) Same plot as in (a) but overlaid with events where one of the coincident particles was identified by the $\Delta E - E$ telescope as a proton (red) or deuteron (magenta). This colour scheme is independent of the intensity scale for the mass-unidentified events.

The diagonal bands C and D are seen continuous throughout, indicating that events in this band correspond to both coincident particles with a mass larger than that of a triton. Band C comprises events where the sum energy ($E_1 + E_2$) of the coincident particles is equal to that of elastically scattered ^{6}Li. These events can only be elastic *cross-talk* as detailed in Section 3.4.6. As for the events forming band D, the sum energy much larger than the beam energy incidating genuine coincidences from reaction channel with positive Q-value. A good candidate is the coincidences of two α-particles from a common ^{8}Be parent-nuclei. Such a reaction would involve d-pickup by ^{6}Li to produce ^{8}Be, followed by $^8\text{Be} \rightarrow \alpha + \alpha$ breakup, which coincidently has a large positive Q-value (see Table 4.1).

The partially identified coincidence-two events, where one of the fragment (x) is mass unidentified, but the other is identified as a proton or deuteron, provides an unambiguous identification of all the fragments in bands A and B. This is illustrated in *Figure 4.1b*, where *Figure 4.1a* is overlaid on top by coincident events identified as $x + deuteron$ (magenta) and $x + proton$ (red). Events identified as $x + deuteron$ align with band A, filling the gap. This confirms that events in this band are $\alpha + d$ coincidences. Similarly, events identified as $x + proton$ align with band B, confirming that events in this band are $\alpha + p$ coincidences.

Those events having an identified proton and another low energy particle (bottom left corner of *Figure 4.1b*), are likely to be random coincidences between (mostly) protons and other low energy particles (most likely other protons). Their origin is further discussed in Section 4.1.3.

4.1.2 ^{7}Li + ^{208}Pb

For the reaction of ^{7}Li on ^{208}Pb at $E_{beam} = 29.0$ MeV, an E_1 vs. E_2 scatterplot for mass-unidentified coincidence-two events is shown in *Figure 4.2a*. As established previously, the vertical and horizontal bands are due to coincidences between an elastically scattered beam particle and a particle with lower energy, or two elastically scattered particles. Events in band C are elastic cross-talk as the sum energy ($E_1 + E_2$) is equal to that expected of elastically scattered ^{7}Li. The background events with sum energy $\sim$16 MeV are due to cross-talk of α-particles from breakup of ^{7}Li.

Of the events comprising the remaining diagonal bands, labelled A, B and D, discontinuity between $10 < E_{1,2} < 12$ MeV in band A indicates energy losses consistent with that of a deuteron. The drop in intensity in band B at $11 < E_{1,2} < 13$ MeV reflects energy

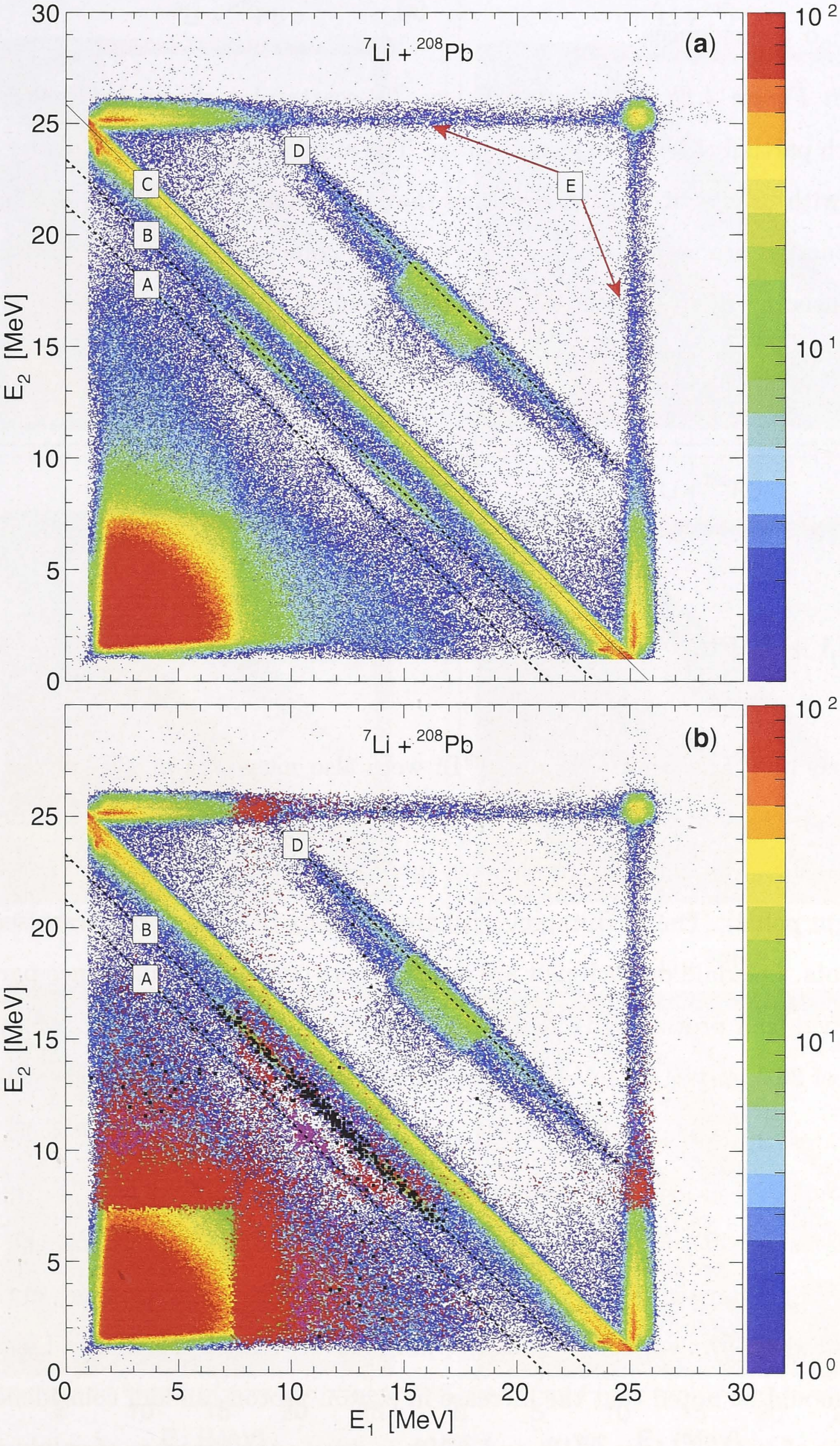

Figure 4.2: (a) E_1 vs. E_2 scatterplot for mass-unidentified coincidence-two events from the reaction of ^{7}Li on ^{208}Pb at $E_{beam} = 29.0$ MeV. Symmetry about 45° is a result of random ordering of the coincident particles. (b) Same plot as in (a) but overlaid with events where one of the coincident particles was identified by the $\Delta E - E$ telescope as a proton (red), deuteron (magenta) or a triton (black). This colour scheme is independent of the intensity scale for the mass-unidentified events.

losses consistent with that of a triton. Band D is seen continuous throughout, identifying these as $\alpha + \alpha$ coincidences.

Shown in *Figure 4.2b* is the same E_1 vs. E_2 scatterplot shown in *Figure 4.2a* but overlaid with partially identified coincidences. The alignment between $x + deuteron$ events (magenta) with events in band A confirms that this band is due to $\alpha + d$ coincidences. Events in band B are seen aligned with $x + triton$ coincidences (black), confirming this band as consisting of $\alpha + triton$ ($\alpha + t$) coincidences. A small number of $x + proton$ coincidences (red) can also be seen, and are identified in Section 4.2.2.

4.1.3 ^{6,7}Li + ^{207}Pb, ^{209}Bi

The reactions of ^{6,7}Li with ^{207}Pb and ^{209}Bi were also measured at sub-barrier energies, with hardware-based multiplicity-2. E_1 vs. E_2 scatterplots of coincidence-two events, measured at $E_{\text{beam}} = 29.0$ MeV, are shown in *Figure 4.3* for reactions of ^{6}Li (left panel) and ^{7}Li (right panel). The ^{209}Bi target with areal density of 130 μgcm^{-2} was used in these measurements. Overlaid on each plot are events where one of the coincidence particles has been identified as a proton (red), deuteron (magenta) and triton (black). Measurements at energies of 26.5 and 24.0 MeV show the same features but with reduced yield.

All features in the scatterplots for the reactions of ^{6,7}Li with ^{207}Pb and ^{209}Bi (*Figures 4.3a,b,d,e*) are similar to those in the reactions of ^{6,7}Li with ^{208}Pb (reproduced here in *Figures 4.3c,d*), which were discussed thoroughly. It emerges that the reactions induced by ^{6}Li (*Figures 4.3a,c,e*) produce $\alpha+\alpha$, $\alpha+p$ and $\alpha+d$ independent of the target; the ^{7}Li-induced reactions (*Figures 4.3b,d,f*) produce $\alpha + \alpha$, $\alpha + p$, $\alpha + d$ and $\alpha + t$ coincidences. It should be noted that the increase in proton-proton random coincidence seen in the reactions of both ^{6,7}Li on ^{207}Pb and ^{208}Pb is due to the presence of sulphur as these are PbS targets. There is also a possible random proton contribution from interactions of ^{6,7}Li with the carbon backing. Further understanding of the origin of coincident particles from the reactions of ^{6,7}Li with ^{207,208}Pb, and ^{209}Bi, requires the Q-value of each event to be determined.

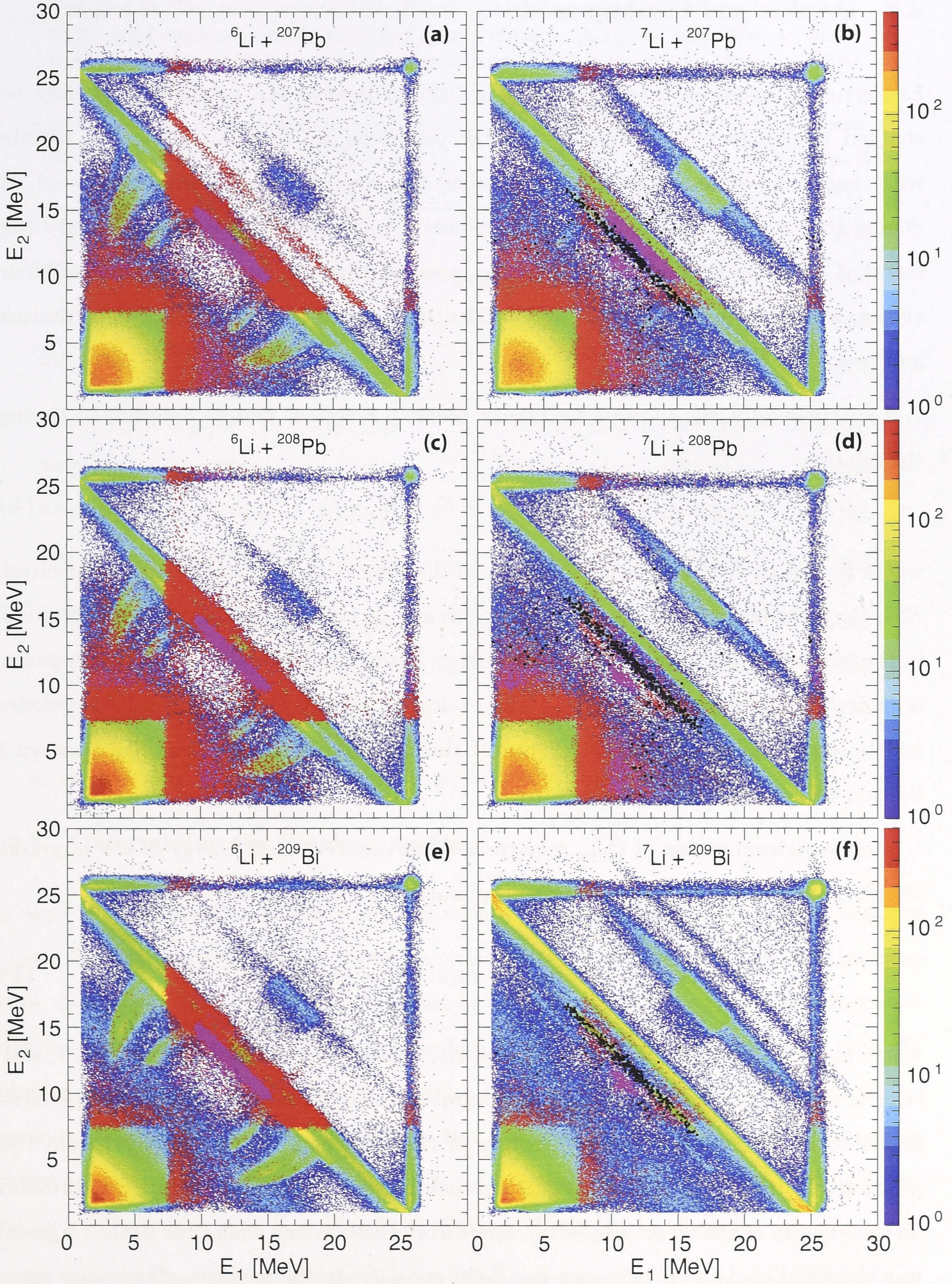

Figure 4.3: E_1 vs. E_2 scatterplots for mass-unidentified coincidence-two events from the indicated reactions at $E_{beam} = 29.0$ MeV. Overlaid are events where one of the coincident particles has been identified as a proton (red), deuteron (magenta) and triton (black). This colour scheme is independent of the intensity scale for the mass-unidentified events. Symmetry about 45° is a result of random ordering of the coincident particles.

4.2 Q-value and breakup mode

Energetically favoured breakup modes of lithium involve the production of only two charged fragments. These favoured charge partitions are listed in Table 4.1, together with the ground-state energy change (Q-value) characteristic of each breakup process. We denote this calculated Q-value by $Q_{[i+j]}$ where i, j are the identities of the binary fragments. Comparison of these calculated $Q_{[i+j]}$ values with the measured Q-value of binary events, where one or both particles are unidentified, allows identification of these particles and hence the breakup mode.

Experimentally, the Q-value for binary breakup reactions can be determined through the relation

$$Q_{i+j} = E_i + E_j + E_r - E_p \tag{4.1}$$

where E_i and E_j are the measured energies of the coincident fragments i and j respectively, E_r is the recoil energy of the target-like nucleus and E_p is the kinetic energy of the projectile in the laboratory frame of reference. As energy lost to excitation of the target-like nucleus is unaccounted for, $Q_{i+j} \leqslant Q_{[i+j]}$. The excitation energy of the projectile-like nucleus will be recovered in the kinetic energy of the breakup fragments, as will be shown in Section 4.3.

Precise determination of Q_{i+j} requires the unmeasured recoil energy of the target-like nuclei E_r to be first determined through momentum conservation

$$m_p \boldsymbol{v}_p + m_t \boldsymbol{v}_t = m_i \boldsymbol{v}_i + m_j \boldsymbol{v}_j + m_r \boldsymbol{v}_r \tag{4.2}$$

where m and $\boldsymbol{v}$ stand for the mass and velocity vector, and the subscripts p, t, r, i, and j refer to the projectile, target, target-like recoil and the coincident fragments respectively. Given their energies, the velocity vectors of the fragments can be obtained from their positions, as described in Section 3.4.1, and their masses. There is generally no information on the identity of the target-like recoil, apart from those events where one of the fragments was identified in $\Delta E - E$ telescope (see Section 3.4.7). In the analysis, all breakup modes ($\alpha + \alpha$, $\alpha + t$, $\alpha + d$, and $\alpha + p$) were considered and thus for every mass-unidentified event, four new parameters $Q_{\alpha+\alpha}$, $Q_{\alpha+t}$, $Q_{\alpha+d}$, and $Q_{\alpha+p}$ were determined concurrently as described below. These newly derived parameters, together with the experimentally measured quantities ($E_{1,2}, \theta_{1,2}, \phi_{1,2}$) then define the event.

Table 4.1: The most energetically favoured breakup modes of lithium incident on each target nucleus and the expected energy change, $Q_{[i+j]}$, for each process where the target or target-like recoil nuclei remain in their lowest energy state, i.e. their ground-state.

Reaction	$Q_{[i+j]}$ [MeV]	Reaction	$Q_{[i+j]}$ [MeV]
^{207}Pb(^{6}Li,$\alpha+\alpha$)^{205}Tl	+10.605	^{207}Pb(^{7}Li,$\alpha+\alpha$)^{206}Tl	+9.860
^{207}Pb(^{6}Li,$\alpha+t$)^{206}Pb	−1.954	^{207}Pb(^{7}Li,$\alpha+t$)^{207}Pb	−2.466
^{207}Pb(^{6}Li,$\alpha+d$)^{207}Pb	−1.474	^{207}Pb(^{7}Li,$\alpha+d$)^{208}Pb	−1.356
^{207}Pb(^{6}Li,$\alpha+p$)^{208}Pb	+3.669	^{207}Pb(^{7}Li,$\alpha+p$)^{209}Pb	+0.357
^{208}Pb(^{6}Li,$\alpha+\alpha$)^{206}Tl	+9.741	^{208}Pb(^{7}Li,$\alpha+\alpha$)^{207}Tl	+9.343
^{208}Pb(^{6}Li,$\alpha+t$)^{207}Pb	−2.584	^{208}Pb(^{7}Li,$\alpha+t$)^{208}Pb	−2.466
^{208}Pb(^{6}Li,$\alpha+d$)^{208}Pb	−1.474	^{208}Pb(^{7}Li,$\alpha+d$)^{209}Pb	−4.786
^{208}Pb(^{6}Li,$\alpha+p$)^{209}Pb	+0.239	^{208}Pb(^{7}Li,$\alpha+p$)^{210}Pb	−1.826
^{209}Bi(^{6}Li,$\alpha+\alpha$)^{207}Pb	+13.430	^{209}Bi(^{7}Li,$\alpha+\alpha$)^{208}Pb	+13.548
^{209}Bi(^{6}Li,$\alpha+t$)^{208}Bi	−2.676	^{209}Bi(^{7}Li,$\alpha+t$)^{209}Bi	−2.466
^{209}Bi(^{6}Li,$\alpha+d$)^{209}Bi	−1.473	^{209}Bi(^{7}Li,$\alpha+d$)^{210}Bi	−4.119
^{209}Bi(^{6}Li,$\alpha+p$)^{210}Bi	+0.906	^{209}Bi(^{7}Li,$\alpha+p$)^{211}Bi	−1.206

4.2.1 Determining the breakup modes

As seen from Table 4.1, at least one α-particle is expected from every binary breakup event. Thus for every coincidence event recorded by the DSSDs, if it is a genuine breakup event then either one or both particles must be an α-particle. For coincidence-two events with one particle identified as either a *proton*, *deuteron*, or *triton*, this means that the complementary unidentified particle must be an α-particle. The determination of the breakup Q-value for these events follows the first pathway shown in the flowchart in *Figure 4.4*, with the appropriate $Q_{\alpha+p_{ID}}$, $Q_{\alpha+d_{ID}}$, and $Q_{\alpha+t_{ID}}$ being determined following energy loss correction and E_{r} calculation using equations (4.1) and (4.2).

For mass-unidentified coincidence events, all breakup modes ($\alpha+p$, $\alpha+d$, $\alpha+t$, and $\alpha+d$) were assumed possible with the greater of the two recorded energies $E_{1,2}$ assigned to the α-particle. The reason for this assignment is as follow. Consider the $\alpha+t$ breakup of ^{7}Li at $E_{\mathrm{beam}} = 29.0$ MeV, which after scattering from the target will have energy ~26 MeV. The breakup Q-value of −2.584 MeV (see Table 4.1) means the sum energy

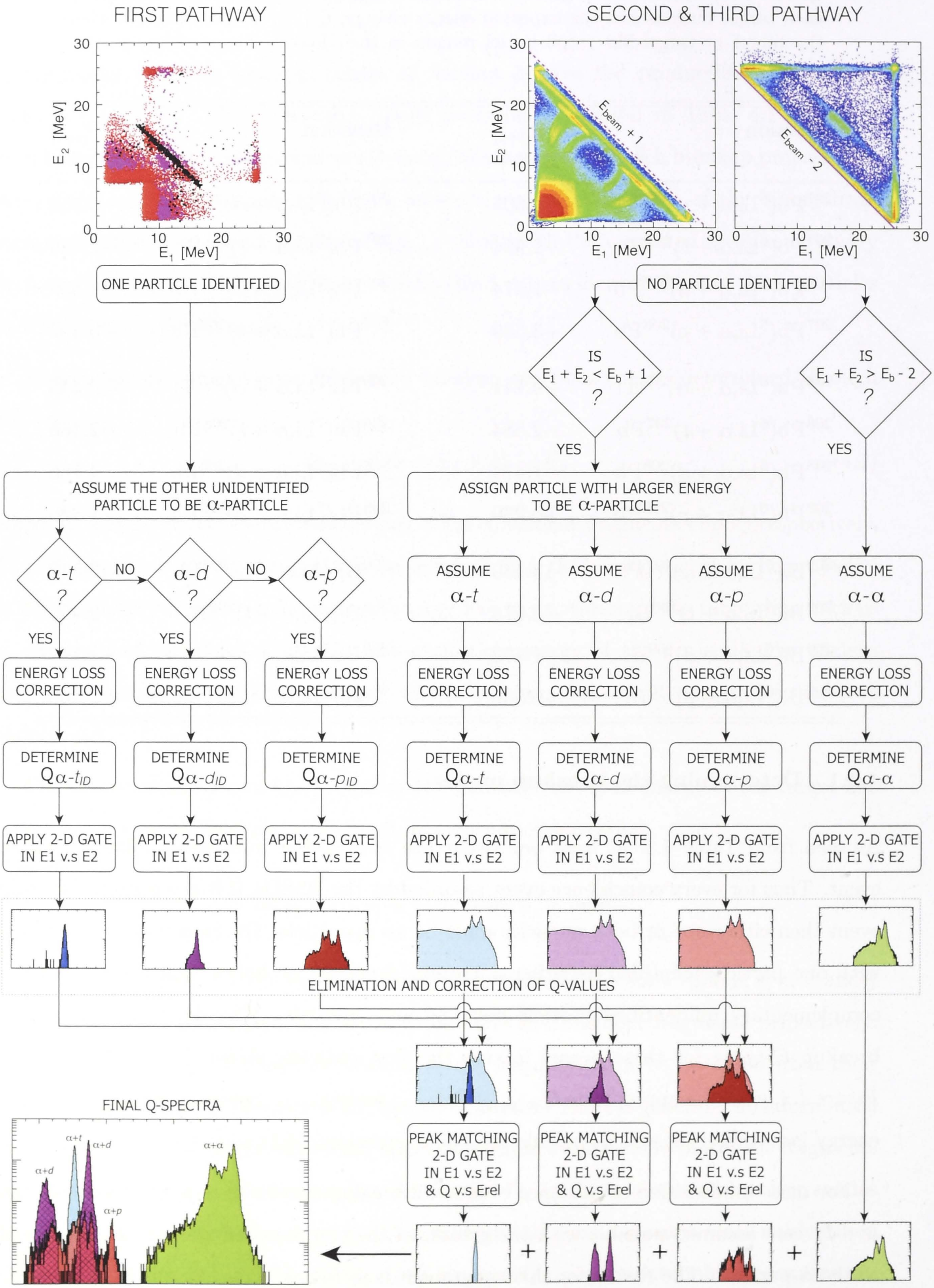

Figure 4.4: Flowchart representing the steps taken to obtain the final Q-spectra.

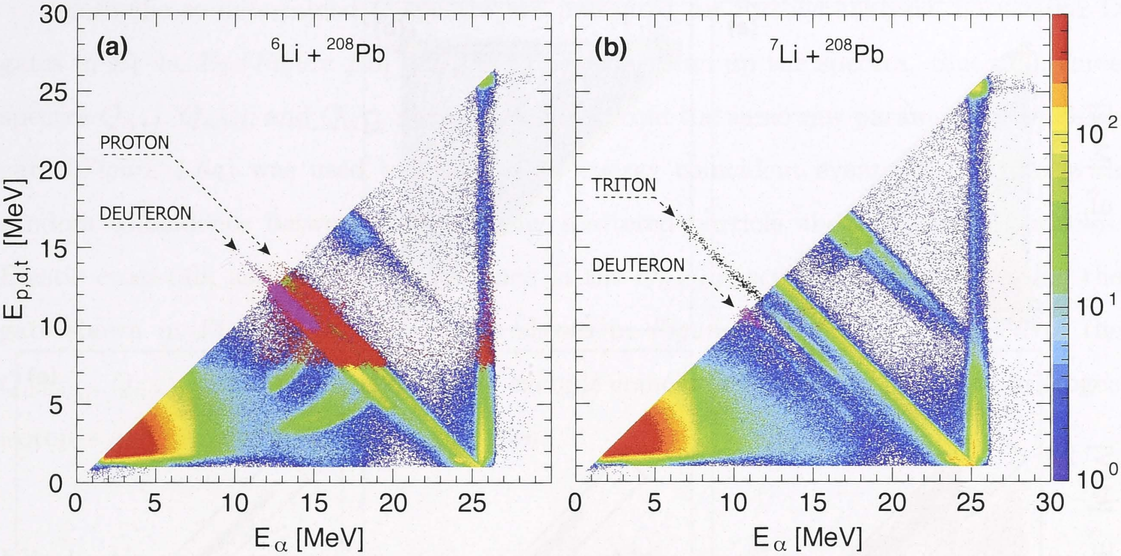

Figure 4.5: E_α vs. E_x scatterplots for $\alpha + x$ coincidences from mass-unidentified coincidence-two events for the indicated reactions at $E_{beam} = 29.0$ MeV. The α-particles were always assigned the greater energy between the two, resulting in the cut off at 45°. Overlaid are $\alpha + p$ (red), $\alpha + d$ (magenta) and $\alpha + t$ (black) coincidence where the energies of the hydrogen isotopes were identified by the $\Delta E - E$ telescope. This colour scheme is independent of the intensity scale for the mass-unidentified events.

$E_1 + E_2 \sim 23.5$ MeV. Given that both particles are unidentified in this breakup event, the *triton* must have an energy less than 11.5 MeV or else it would have been identified by the $\Delta E - E$ telescope (resulting in $Q_{\alpha+t_{ID}}$ being determined instead). The complementary α-particle, carrying the remainder energy, will thus always have a greater energy than that of the *triton*. Similarly, unidentified *deuterons* and *protons* must have an energy less than 10.0 and 7.5 MeV respectively, with the remaining (larger) energy being carried by the complementary α-particle. These points are summarised in the E_1 vs. E_2 scatterplots (*Figure 4.5*) for mass-unidentified coincidence-two events from the reactions of ^{6,7}Li with ^{208}Pb at $E_{\text{beam}} = 29.0$ MeV. The greater of the two energies has been assigned to the α-particle. The overlaid identified $\alpha + p$ (red), $\alpha + d$ (magenta), and $\alpha + t$ (black) events can be seen aligned along the diagonal bands of correlated mass-unidentified events. Even for the most energetic *protons* and *deuterons* which are identified by the $\Delta E - E$ telescope, only a few actually have an energy larger than that of the complementary α-particles. The identified $\alpha + t$ (black) events show that due to their mass being almost equal, coincident *tritons* can have energies much larger than those of the complementary α-particles.

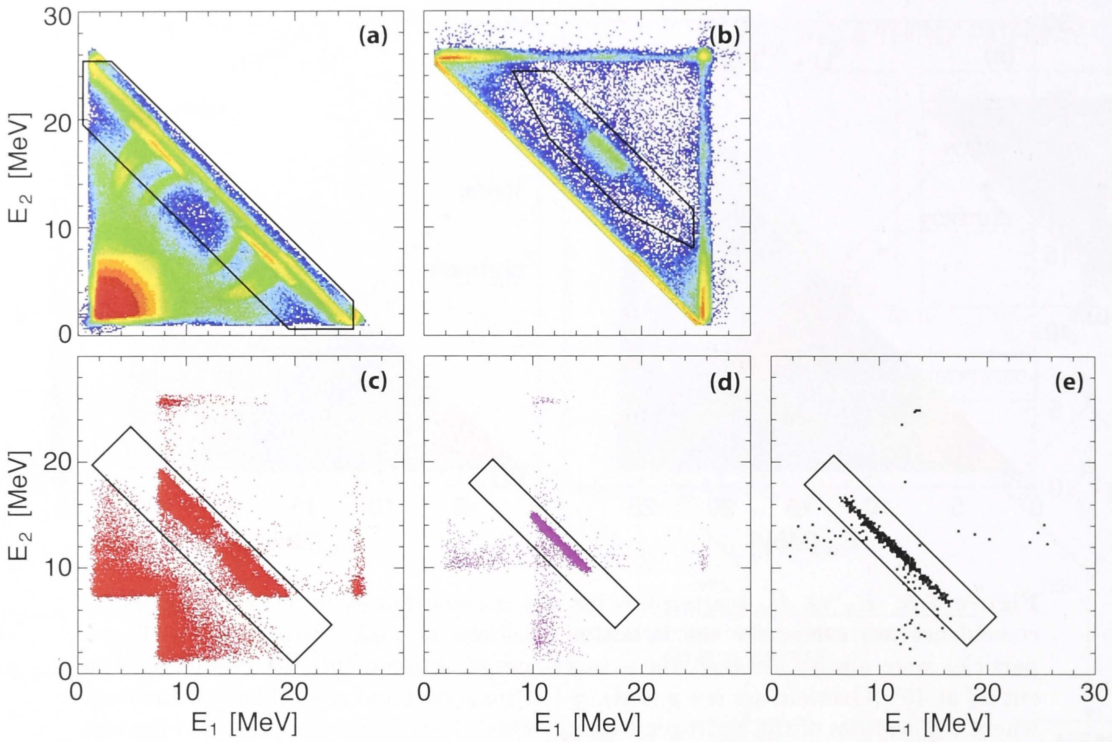

Figure 4.6: The solid black lines define two-dimensional gates in E_1 vs. E_2 that were used to select coincidence events with correlated energies. The Q-spectra from events where $E_{1,2}$ fall within these gates are then presented for further analysis. Shown in (a) is the gate that was used for the $Q_{\alpha+t}$, $Q_{\alpha+d}$, and $Q_{\alpha+p}$ spectra, (b) for the $Q_{\alpha+\alpha}$ spectra, (c) for the $Q_{\alpha+p_{ID}}$ spectra, (d) for the $Q_{\alpha+d_{ID}}$ spectra, and (e) for the $Q_{\alpha+t_{ID}}$ spectra.

Because of the possible overlapping between the $\alpha+d$, $\alpha+p$, $\alpha+t$, and $\alpha+\alpha$ bands (see *Figure 4.3*), each mass-unidentified event could have had four Q-values, determined assuming $\alpha+p$, $\alpha+d$, $\alpha+t$, and $\alpha+\alpha$ coincidences. However, exploiting the fact that $\alpha+p$, $\alpha+d$ and $\alpha+t$ all have $Q_{[i+j]} < 1$ MeV (and $Q_{[\alpha+p]} < 4.0$ MeV for ^{207}Pb(^{6}Li,$\alpha+p$)^{208}Pb), only mass-unidentified events with $E_1+E_2 \leqslant E_{\text{beam}}+1.0$ MeV ($E_1+E_2 \leqslant E_{\text{beam}}+3.0$ MeV for the reaction of ^{6}Li with ^{207}Pb) had the particles with the smaller energy assigned as proton, deuteron, and triton with the appropriate energy loss correction applied. With the corresponding E_{r} calculated for each case, three Q-values ($Q_{\alpha+t}$, $Q_{\alpha+d}$, and $Q_{\alpha+p}$) were determined from the same event as shown in the second pathway in *Figure 4.4*. And since a large positive Q-value, e.g. $Q_{[\alpha+\alpha]} > 9.0$ MeV for all $\alpha+\alpha$ breakup, would result in the sum energy of the fragments exceeding the initial beam energy, events with $E_1 + E_2 \geqslant E_{\text{beam}} - 2.0$ MeV have both particles identified as α-particles (the -2 MeV offset is there to make sure no events were missed). The third pathway in *Figure 4.4* shows the process in determining $Q_{\alpha+\alpha}$.

Before the so-determined Q-spectra are presented for further analysis, however, 2-D gates in E_1 vs. E_2 (*Figure 4.6*) are first applied to clean up the spectra. Since the three spectra $Q_{\alpha+t}$, $Q_{\alpha+d}$, and $Q_{\alpha+p}$ were determined from the same raw parameters, the same gate (*Figure 4.6a*) was used to exclude low energy coincident events, and events with random coincidence between an elastically scattered particle and low energy particles. Elastic cross-talk and random coincidence in the $Q_{\alpha+\alpha}$ spectra were removed using the gate shown in *Figure 4.6b*. The gates shown in *Figures 4.6c,d,e* were applied to the $Q_{\alpha+p_{ID}}$, $Q_{\alpha+d_{ID}}$, and $Q_{\alpha+t_{ID}}$ spectra to exclude coincidences between identified hydrogen isotopes and low energy or elastic particles.

Elimination and correction of Q_{i+j} assumptions for ^{6}Li

Because multiple Q_{i+j} ($Q_{\alpha+p}$, $Q_{\alpha+d}$, and $Q_{\alpha+t}$) were calculated for the same mass-unidentified event (the second pathway shown in *Figure 4.4*), selection of the correct Q_{i+j} is required. This is done by comparing the $Q_{\alpha+p}$, $Q_{\alpha+d}$, and $Q_{\alpha+t}$ spectra to the particle-identified $Q_{\alpha+p_{ID}}$, $Q_{\alpha+d_{ID}}$, and $Q_{\alpha+t_{ID}}$ spectra respectively. Data from all reactions were subjected to the same Q-value selection procedures as will be described; however, only data from the reaction of ^{6,7}Li on ^{208}Pb are shown (*Figure 4.7*) for illustrative purposes.

For the reaction of ^{6}Li with ^{208}Pb, the Q-spectra for mass-unidentified events are presented in *Figure 4.7* (pale colours) with Q_{i+j} values calculated assuming $\alpha+\alpha$, $\alpha+d$, $\alpha+p$ and $\alpha+t$ breakup modes. The position of the calculated ground-state Q-value ($Q_{[i+j]}$, see Table 4.1) is indicated in all figures by vertical broken lines. If there is missing mass due to undetected fragments, one expects the Q-spectra to exhibit broad distributions because energy would be carried away by the missing mass. As seen in *Figure 4.7*, the Q-spectra have distinct narrow peaks meaning that all breakup fragments were detected. This validates the assumption that mass was conserved at all stages of the reaction, with the final breakup being binary. For the assumption of $\alpha+\alpha$ breakup, the resulting $Q_{\alpha+\alpha}$ spectrum (*Figure 4.7a*) shows a sequence of narrow peaks at $Q_{\alpha+\alpha} \leqslant Q_{[\alpha+\alpha]}$. This indicates that this group indeed consists of $\alpha+\alpha$ breakup, populating mainly excited states in the target-like nucleus.

For the $Q_{\alpha+d}$ spectrum (*Figure 4.7b*) calculated for mass-unidentified events, overlaid is the $Q_{\alpha+d_{ID}}$ spectrum from events where one of the coincident fragments was identified as a deuteron. The peak in $Q_{\alpha+d_{ID}}$ coincides with one of the peaks in $Q_{\alpha+d}$, and both match the calculated $Q_{[\alpha+d]}$ (indicated by dashed lines), which shows that these events must come from the $\alpha + d$ breakup mode. For the four other $Q_{\alpha+d}$ peaks, three coincide closely with peaks in the $Q_{\alpha+p_{ID}}$ spectra (*Figure 4.7c*), and are discussed later. The most intense peak at $Q_{\alpha+d} = 0$ MeV comprises breakup events where no energy has been expended to produce the breakup fragments. This does not fit with any identified Q-value. Events comprising this peak must therefore be *cross-talk* of elastically scattered ^{6}Li masquerading as breakup events. These events form the most intense peak in the $Q_{\alpha+t}$ spectra at $Q > 0$ MeV (*Figure 4.7c*), and the most intense peak in the $Q_{\alpha+p}$ spectra nearest to (but less than) $Q = 0$ MeV (*Figure 4.7d*). This is due to the incorrect mass, and thus incorrectly calculated E_{r}, with one nucleon more when assuming $\alpha + t$ coincidences and one nucleon less when assuming $\alpha + p$ coincidences.

For the $Q_{\alpha+p}$ spectrum determined from mass-unidentified events (*Figure 4.7c*), overlaid is the measured $Q_{\alpha+p_{ID}}$ spectrum for event in which one of the coincident particles was identified as a proton. The peak in $Q_{\alpha+p_{ID}}$ (with the highest Q-value) aligns with the peak in $Q_{\alpha+d}$ (also with the highest Q-value), and both coincide with the indicated $Q_{[\alpha+p]}$ (dashed line). Also four other peaks in $Q_{\alpha+p_{ID}}$ coincide with peaks in $Q_{\alpha+p}$ indicating that these events are indeed due to breakup into $\alpha + p$. The peak marked by a red arrow coincides both with peaks in the measured $Q_{\alpha+d_{ID}}$ (*Figure 4.7b*) and the overlaid $Q_{\alpha+p_{ID}}$ spectra. Thus it comprises two contributions; one due to breakup into the $\alpha + d$ partition and the other from the $\alpha + p$ breakup mode. In this case, an isolated peak is identified in the measured $Q_{\alpha+p_{ID}}$ spectrum together with its corresponding peak in the $Q_{\alpha+p}$ spectrum (labelled as reference peaks in *Figure 4.7c*). The raw counts under these respective isolated peaks, $N_{\mathrm{iso\_p}}$ and $N_{\mathrm{iso\_pID}}$, are then obtained and a reference ratio $R_{\mathrm{ref}} = N_{\mathrm{iso\_p}}/N_{\mathrm{iso\_pID}}$ is defined. The number of genuine $\alpha + p$ events in the $Q_{\alpha+p}$ peak that overlap with the $Q_{\alpha+d}$ peak is $N_{\alpha+\mathrm{p}} = R_{\mathrm{ref}}.N_{pID}$ where N_{pID} is the number of events comprising the peak in $Q_{\alpha+p_{ID}}$ that coincides with the $Q_{\alpha+p}$ peak in question. The $N_{\alpha+\mathrm{p}}$ events attributed to $\alpha + p$ breakup by this method form a peak in $Q_{\alpha+p}$, indicated by a blue arrow in *Figure. 4.7c*. It should be noted that the counts $N_{\mathrm{iso\_p}}$ and $N_{\mathrm{iso\_pID}}$ were chosen from peaks as close as possible to the peak in which $N_{\alpha+\mathrm{p}}$ is to be determined. This is because the ratio R_{ref} varies with the efficiencies for $\alpha+p$ and $\alpha+p\_{}_{\mathrm{pID}}$ detections, which in turn vary with the Q-value of the peaks.

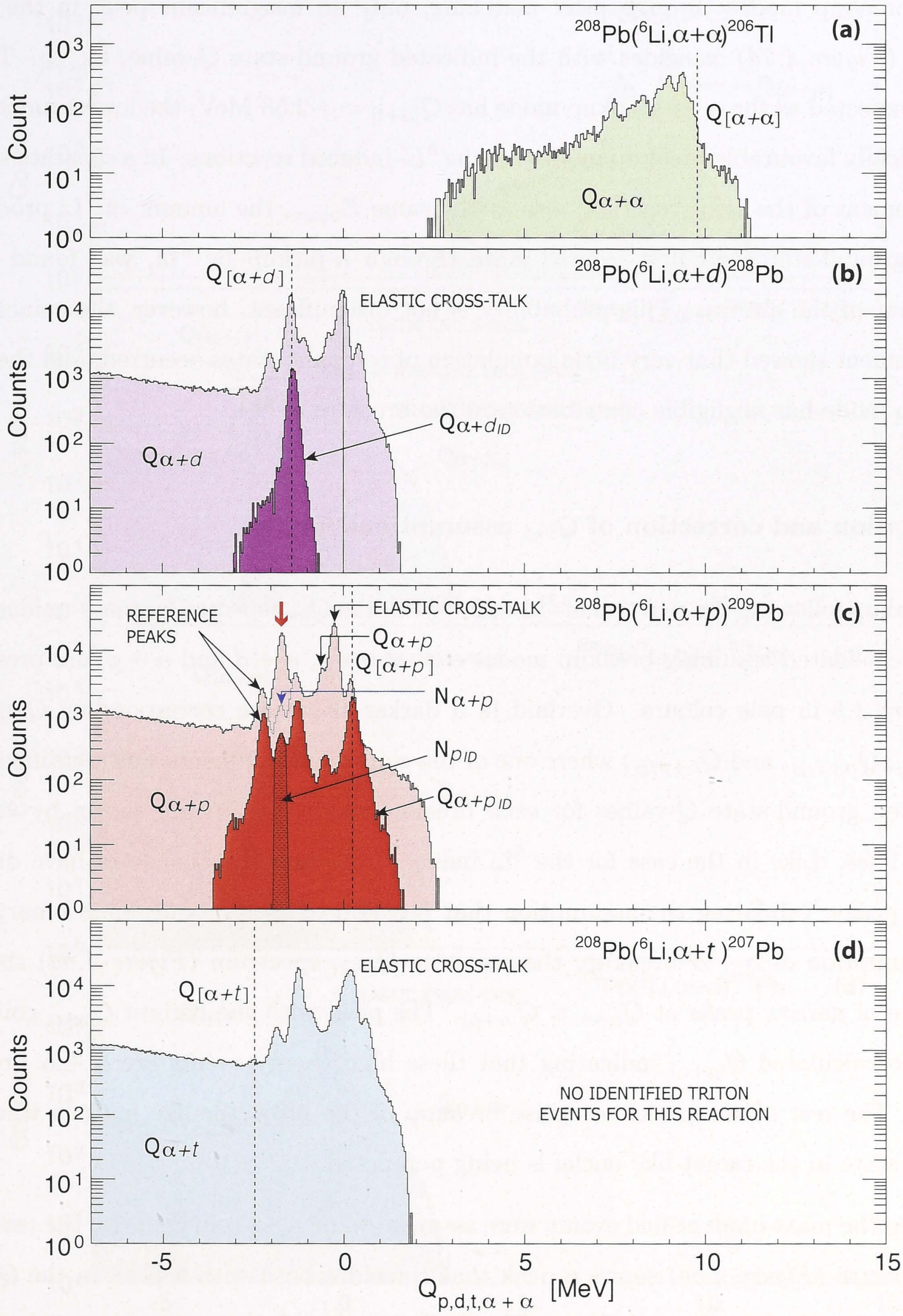

Figure 4.7: Q-spectra from the reaction of ^{6}Li with ^{208}Pb at $E_{\text{beam}} = 29.0$ MeV. In pale colours are Q-spectra for mass-unidentified coincidence events, calculated assuming (a) $\alpha + \alpha$ breakup, (b) $\alpha + d$ breakup, (c) $\alpha + p$ breakup, and (d) $\alpha + t$ breakup. The overlaid $Q_{\alpha+d_{ID}}$ and $Q_{\alpha+p_{ID}}$ (dark colours) in (b) and (c) are Q-spectra for events with an identified deuteron and proton respectively. The vertical dashed lines indicate the ground-state Q-value for the respective breakup processes.

With the majority of the mass-unidentified events assigned to either the $\alpha + d$ or $\alpha + p$ breakup modes through peak matching, only an insignificant peak in the $Q_{\alpha+t}$ spectra (*Figure 4.7d*) coincides with the indicated ground-state Q-value, $Q_{[\alpha+t]}$. This is rather expected as the $\alpha+t$ breakup mode has $Q_{[\alpha+t]} = -2.58$ MeV, the lowest among the energetically favourable breakup modes for the ^{6}Li-induced reactions. In a separate singles measurement of the same reaction, also at the same E_{beam}, the amount of ^{7}Li produced, in the ground-state and first excited state through n-pickup by ^{6}Li, was found to be $\sim$5% that of the elastics. This probability is not insignificant, however, the coincidence measurement showed that very little population of resonant states occurred, and the $\alpha+t$ breakup mode has negligible contribution in the breakup of ^{6}Li.

Elimination and correction of Q_{i+j} assumptions for ^{7}Li

For breakup following the reaction of ^{7}Li with ^{208}Pb, the Q_{i+j} spectra for mass-unidentified events, calculated assuming breakup modes $\alpha + \alpha$, $\alpha + t$, $\alpha + d$ and $\alpha + p$, are presented in *Figure 4.8* in pale colours. Overlaid in a darker shade are corresponding Q-spectra ($Q_{\alpha+t_{ID}}$, $Q_{\alpha+d_{ID}}$, and $Q_{\alpha+p_{ID}}$) where one of the coincident fragments was identified. The calculated ground-state Q-values for each breakup mode, $Q_{[i+j]}$, are shown by vertical dashed lines. Like in the case for the ^{6}Li induced reaction, the Q-spectra have distinct narrow peaks, validating the assumption that breakup in reactions of ^{7}Li is binary. For the assumption of $\alpha + \alpha$ breakup, the resulting $Q_{\alpha+\alpha}$ spectrum (*Figure 4.8a*) shows a sequence of narrow peaks at $Q_{\alpha+\alpha} \leqslant Q_{[\alpha+\alpha]}$. The peak with the highest $Q_{\alpha+\alpha}$ coincides with the calculated $Q_{[\alpha+\alpha]}$ indicating that these high energy events are $\alpha + \alpha$ breakup events. The rest of the peaks comprise breakup of the projectile-like nucleus where an excited state in the target-like nuclei is being populated.

When the mass-unidentified events were assumed to be $\alpha+t$ coincidences, the resultant $Q_{\alpha+t}$ spectra (*Figure 4.8b*) shows a peak that coincides both with a peak in the $Q_{\alpha+t_{ID}}$ spectra and with the indicated $Q_{[\alpha+t]}$. This indicates that these events are $\alpha+t$ breakup. The most intense peak at $Q_{\alpha+t} = 0$ MeV is the expected cross-talk of elastically scattered ^{7}Li, analogous to the peak at $Q_{\alpha+d} = 0$ MeV for ^{6}Li (*Figure 4.7b*). The small shoulder to the left of this peak coincides with cross-talk from inelastic ^{7}Li scattering.

When assuming breakup into $\alpha+p$, the resultant $Q_{\alpha+p}$ spectrum (*Figure 4.8c*) contains one peak that coincides with a peak in the overlaid $Q_{\alpha+p_{ID}}$ spectrum of identified $\alpha + p$

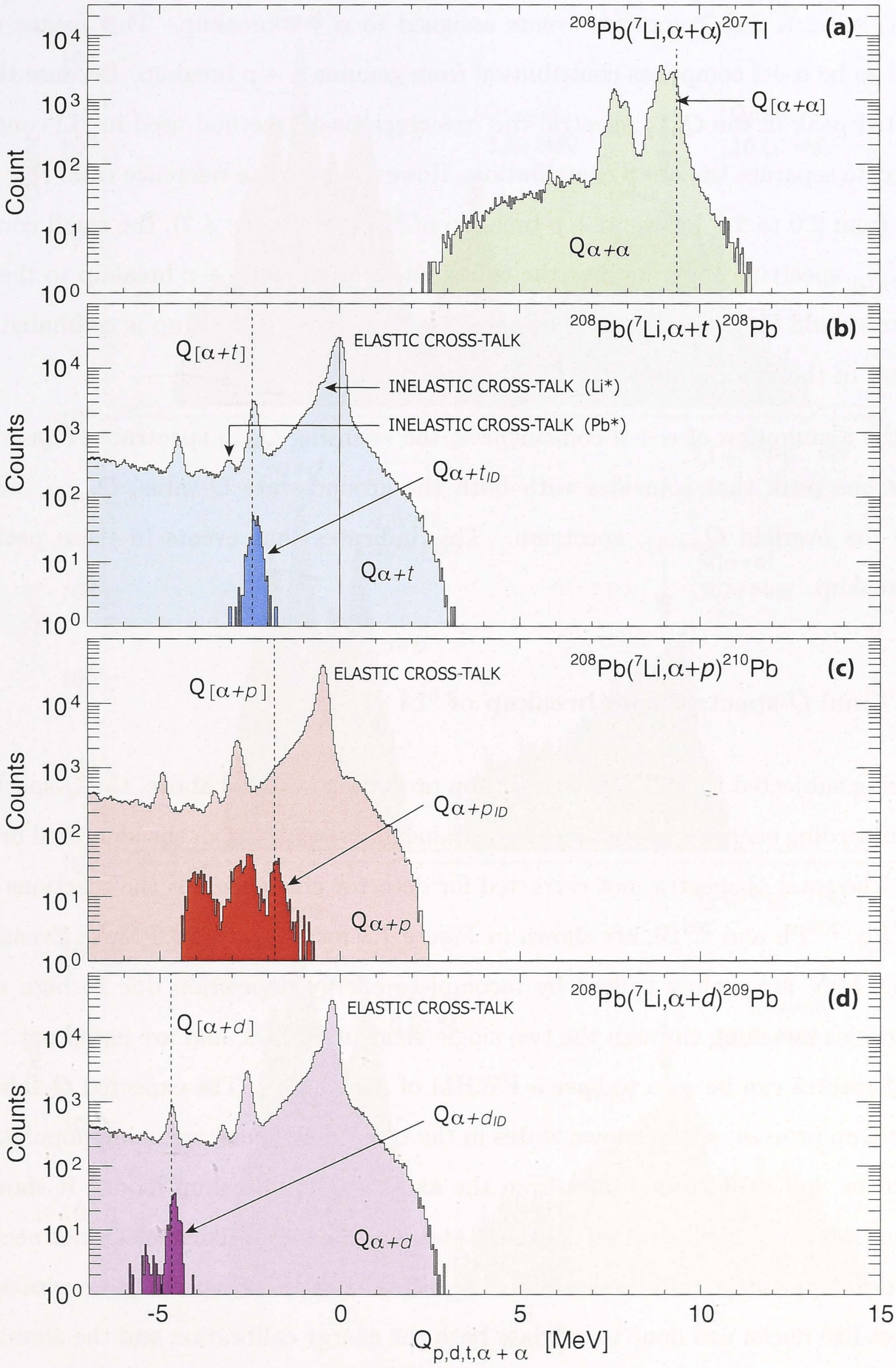

Figure 4.8: Q-spectra for mass-unidentified coincidence events, from the reaction of ^{7}Li with ^{208}Pb at $E_{\mathrm{beam}} = 29.0$ MeV, calculated assuming (a) $\alpha+\alpha$ breakup, (b) $\alpha+t$ breakup, (c) $\alpha+p$ breakup, and (d) $\alpha+d$ breakup. The overlaid dark filled spectra in (b) and (c) and (d) are the $Q_{\alpha+t_{ID}}$, $Q_{\alpha+d_{ID}}$, and $Q_{\alpha+p_{ID}}$ spectra for events with an identified triton, proton, and deuteron respectively. The vertical dashed lines indicate the ground-state Q-value for the respective breakup processes.

breakup triggered by $2n$-stripping of ^{7}Li. These peaks also overlapped with a peak in the $Q_{\alpha+t}$ spectra that comprises events assigned to $\alpha + t$ breakup. This means events assigned to be $\alpha + t$ comprises contribution from genuine $\alpha + p$ breakup. Because there is no isolated peak in the $Q_{\alpha+p}$ spectra, the "reference peak" method used in ^{6}Li cannot be employed to separate the $\alpha + p$ contribution. However, with the reference ratio R_{ref} found varying from 2.0 to 2.5 for the $\alpha + p$ breakup of ^{6}Li (see *Figure 4.7*), the small counts in the $Q_{\alpha+p_{ID}}$ spectrum suggests that the contribution from the $\alpha + p$ breakup to the $Q_{\alpha+t}$ spectrum should be insignificant. The total number of $\alpha + p$ breakup is estimated to be twice that of the raw counts of the $Q_{\alpha+p_{ID}}$ spectrum.

For the assumption of $\alpha + d$ coincidences, the resulting $Q_{\alpha+d}$ spectrum (*Figure 4.8d*) contains one peak that coincides with both the ground-state Q-value, $Q_{[\alpha+d]}$, and the peak in the overlaid $Q_{\alpha+d_{ID}}$ spectrum. This indicates that events in these peaks are $\alpha + d$ breakup.

4.2.2 Final Q-spectra from breakup of ^{6}Li

After being subjected to the Q-value selection procedure outlined above, the Q-spectra for each bombarding energy and reaction was obtained by combining all the identified breakup modes. The total Q-spectra, not corrected for detector efficiency, for the reactions of ^{6}Li with ^{207}Pb, ^{208}Pb and ^{209}Bi, are shown in *Figure 4.9* for $E_{\text{beam}} = 29.0$ MeV. Events with $Q < -5.0$ MeV are mainly caused by incomplete energy deposition due to high energy Z=1 particles punching through the two single element DSSDs, and are gated out. Peaks in the Q-spectra can be seen to have a FWHM of $\approx$0.20 MeV. The expected Q-values for each breakup process, where known states in the target-like nuclei are being populated are indicated by vertical coloured lines from the axis for every breakup mode. It should be noted that while the identification of excited states of the target-like nuclei is not necessary for the development of this thesis, matching of peaks in the Q-spectra to excitations in the target-like nuclei was done to validate both the energy calibration and the assumption of binary breakup.

For the reactions of ^{6}Li (*Figure 4.9*), the most intense peak at $Q \sim 1.45$ MeV, for all targets, corresponds to breakup of excited states of the projectile into its cluster constituents ($\alpha + d$) as might be expected. Other significant contributions, however, come from peaks corresponding to $\alpha + p$ breakup, arising from stripping of a neutron from the projectile

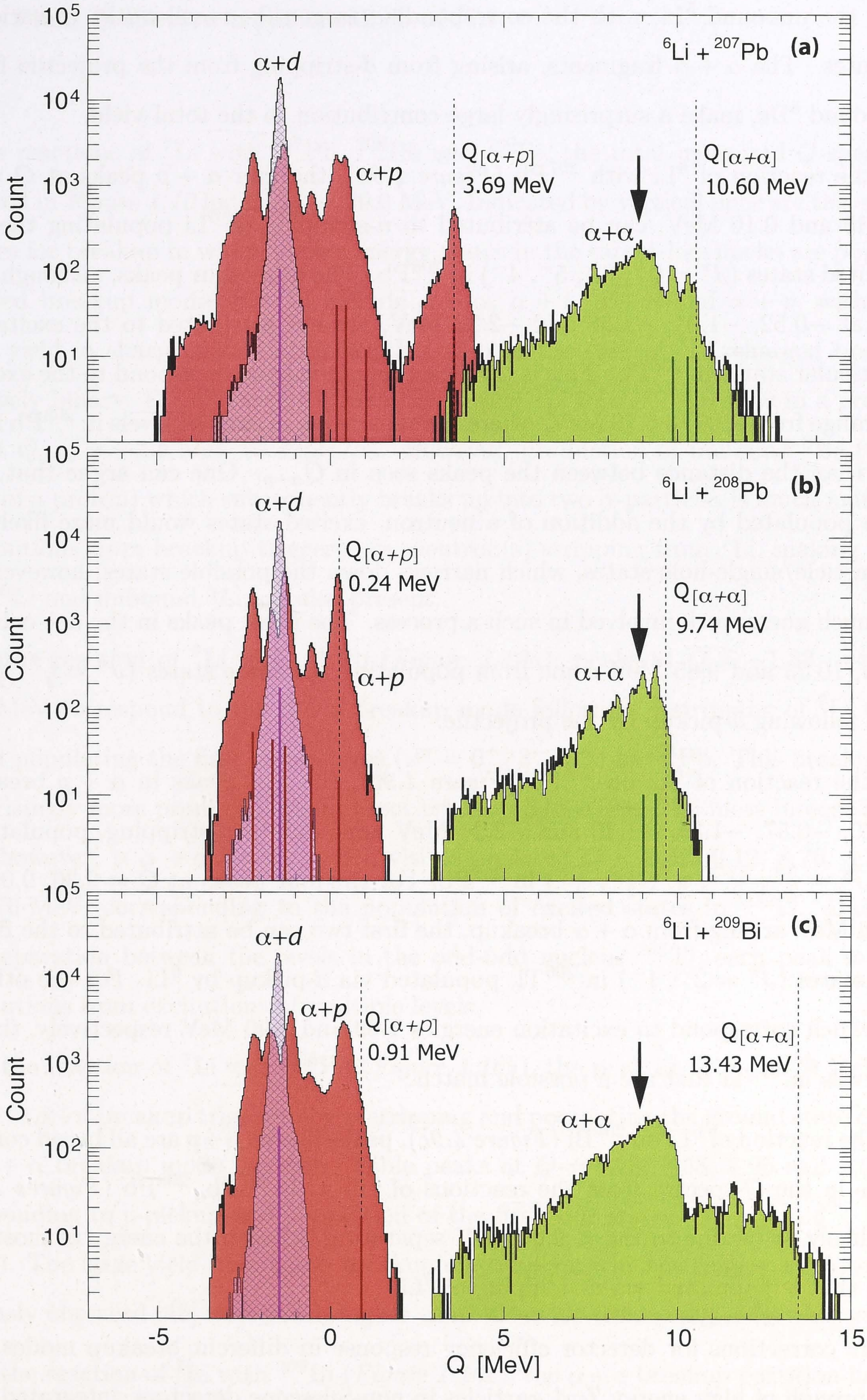

Figure 4.9: Q-spectra determined for the indicated reactions at $E_{\text{beam}} = 29.0$ MeV. Identified breakup modes consist of $\alpha + p$ (red), $\alpha + d$ (magenta with hatching), and $\alpha + \alpha$ (green). The vertical lines, in a darker shade of the colour of the respective breakup mode, indicate Q-values for breakup following the population of known excited states of the target-like nucleus. The arrows indicate the positions of the optimum Q-value, Q_{opt}, for the indicated reactions. Peaks in the Q-spectra without corresponding vertical lines include breakup following the population of excited states of the target-like nuclei where the separation in excited states is much smaller than the width of the peaks and thus they cannot be identified reliably.

forming the unbound ^{5}Li, with the corresponding target-like recoil nuclei in various excited states. The $\alpha + \alpha$ fragments, arising from d-stripping from the projectile forming the unbound ^{8}Be, make a surprisingly large contribution to the total yield.

For the reaction of ^{6}Li with ^{207}Pb (*Figure 4.9a*), the four $\alpha + p$ peaks at $Q = 3.57$, 1.04, 0.45 and 0.16 MeV, can be attributed to n-stripping of ^{6}Li populating the lowest four excited states ($J^{\pi} = 0^{+}, 3^{-}, 5^{-}, 4^{-}$) in ^{208}Pb. The other four peaks, although clearly defined at -0.52, -1.01, -1.38 and -2.22 MeV, are not attributed to the excitation of any particular states in ^{208}Pb. This is because these Q-values correspond to the excitation energy range from 4.09 to 5.79 MeV, where the separation in excited levels in ^{208}Pb is much smaller than the distance between the peaks seen in $Q_{\alpha+p}$. One can argue that, as the ^{208}Pb is populated by the addition of a neutron, excited states would more likely be in single-particle/single-hole states, which narrows down the possible states, however, there is still much guess work involved in such a process. The three peaks in the $\alpha + \alpha$ breakup at 10.55, 10.23 and 9.85 MeV come from populating the three states ($J^{\pi} = \frac{1}{2}^{+}, \frac{3}{2}^{+}, \frac{5}{2}^{+}$) in ^{205}Tl following d-pickup by the projectile.

For the reaction of ^{6}Li on ^{208}Pb (*Figure 4.9b*), the five peaks in $\alpha + p$ breakup at $Q = 0.20$, -0.57, -1.34, -1.70 and -2.24 MeV arise due to n-stripping, populating the states ($J^{\pi} = \frac{9}{2}^{+}, \frac{11}{2}^{+}, \frac{5}{2}^{+}, \frac{1}{2}^{+}, \frac{7}{2}^{+}$) in ^{209}Pb. For the four peaks at $Q = 9.36$, 9.00, 8.27, and 7.46 MeV arising from $\alpha + \alpha$ breakup, the first two can be attributed to the first two excited states ($J^{\pi} = 2^{-}, 1^{-}$) in ^{206}Tl, populated via d-pickup by ^{6}Li. For the other two peaks, which correspond to excitation energies 1.09 and 1.90 MeV respectively, there are many levels in ^{206}Tl that are a possible match.

For the reaction of ^{6}Li on ^{209}Bi (*Figure 4.9c*), peaks due to $\alpha+p$ are all broad compared to peaks in the Q-spectra from the reactions of ^{6}Li with ^{207}Pb, ^{208}Pb (*Figures 4.9a,b*). This is likely to be due to the < 0.05 MeV separation between the energy of most states in ^{210}Bi that is populated via n-stripping of ^{6}Li.

Before corrections for detector efficiency response in different breakup modes, or for punch-through of high energy Z=1 particles in non-telescope detectors, integrated counts show that breakup following n-stripping (leading to $\alpha + p$ fragments) strongly competes with direct breakup of ^{6}Li into $\alpha + d$; indeed it is stronger than $\alpha + d$ breakup in the reactions of ^{6}Li with ^{207}Pb and ^{209}Bi.

4.2.3 Final Q-spectra from breakup of ^{7}Li

For the reactions of ^{7}Li with ^{207}Pb, ^{208}Pb and ^{209}Bi, the total measured Q-spectra are presented in *Figure 4.10* for $E_{\text{beam}} = 29.0$ MeV. Indicated by vertical lines are the expected Q-values for breakup in which known energy states in the target-like nuclei are populated. Identified breakup modes for ^{7}Li include $\alpha + \alpha$, $\alpha + t$, $\alpha + d$ and $\alpha + p$, with almost all the yield in sharp peaks indicating that also in the case of ^{7}Li, charged breakup is exclusively binary. For all targets, direct breakup of ^{7}Li into $\alpha + t$ results in a prominent peak at $Q_{\alpha+t} = -2.5$ MeV as expected. However, production of unbound ^{8}Be (through pickup of a proton) which subsequently breaks up into two α-particles is much more likely. Contributions from breakup triggered by neutron(s)-stripping from ^{7}Li, making the less bound ^{6}Li and unbound ^{5}Li are also present.

For the reaction of ^{7}Li with ^{207}Pb (*Figure 4.10a*), peaks at $Q = -1.33$, -4.00 and -4.46 MeV correspond to the $\alpha + d$ breakup mode following n-stripping of ^{7}Li to make ^{6}Li and populating the first three states ($J^\pi = 0^+, 3^-, 5^-$) in ^{208}Pb. This breakup mode is surprisingly more prominent than direct breakup into $\alpha + t$. The most intense breakup mode, however, is $\alpha + \alpha$ breakup with visible peaks at $Q = 9.47$, 9.12, 8.76, 8.38, 8.08 and 7.76 MeV, corresponding to the population of excited states in ^{206}Tl. Due to the small separation between the levels in the odd-odd nucleus ^{206}Tl, each peak may have contributions from excitations of multiple levels.

For the reaction of ^{7}Li with ^{208}Pb (*Figure 4.10b*), the peak at $Q = -4.70$ MeV corresponds to $\alpha+d$ breakup triggered by n-stripping and populating the ground state of ^{209}Pb. The $\alpha + \alpha$ breakup mode has four visible peaks at $Q = 9.23$, 8.58, 7.95 and 7.61 MeV, corresponding to p-pickup and population of the first four states ($J^\pi = \frac{1}{2}^+, \frac{3}{2}^+, \frac{11}{2}^-, \frac{5}{2}^+$) in ^{207}Tl. The large yield from $\alpha+\alpha$ breakup may explain why the singles α cross-sections previously observed [46] were much higher than those for triton-singles for this reaction.

For the reaction of ^{7}Li with ^{209}Bi (*Figure 4.10c*), the $\alpha+\alpha$ breakup partition has seven visible peaks at $Q = 13.36$, 10.82, 10.20, 9.50, 9.15, 8.30 and 7.97 MeV, corresponding to p-pickup and population of states in ^{208}Pb. The three lowest energy states ($J^\pi = 0^+, 3^-, 5^-$) in ^{208}Pb match the first three peaks in $\alpha + \alpha$ breakup. The rest of the peaks may comprise contributions from many excited states. For the $\alpha + d$ breakup mode, the peak at $Q = -4.50$ MeV indicates n-stripping, possibly populating the $J^\pi = 3^-$ state in ^{210}Bi.

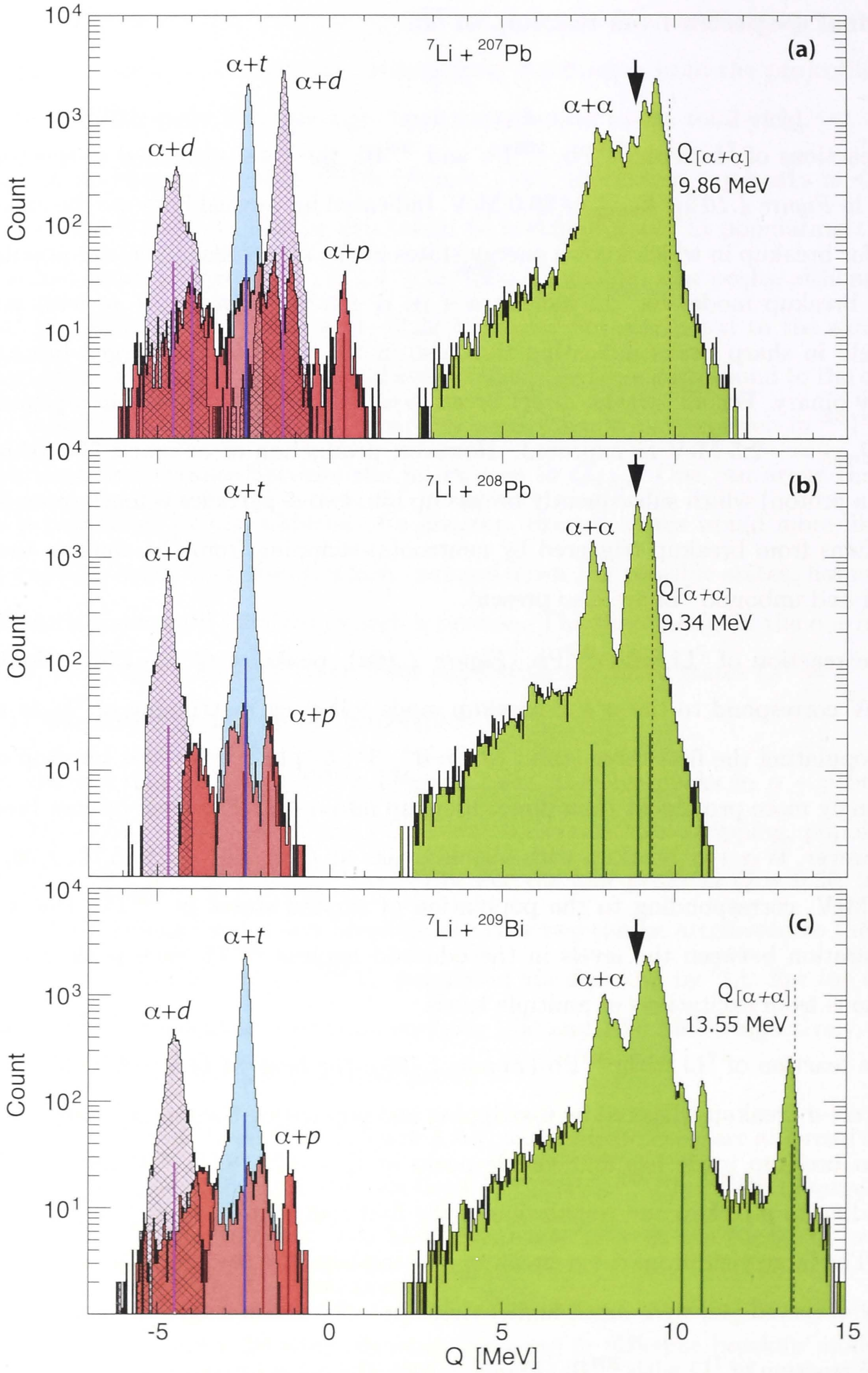

Figure 4.10: Measured Q-spectra for the indicated reactions at $E_{\text{beam}} = 29.0$ MeV. Identified breakup modes consist of $\alpha + p$ (red), $\alpha + d$ (magenta with hatching), $\alpha + t$ (blue), and $\alpha + \alpha$ (green). The vertical lines, of a darker shade of the colour of the respective breakup mode, indicate Q-values for breakup following the population of known excited states of the target-like nucleus. The arrows indicate the position of the optimum Q-values, Q_{opt}, for the indicated reactions. Many peaks in the Q-spectra cannot be aligned to the population of definite states in the target-like nuclei as the separation in excited levels is much smaller than the width of those peaks.

Results from reactions with both ^{6}Li and ^{7}Li show that breakup characteristics depend both on the properties of the initial nucleus and its neighbours (produced via transfer). Identification of breakup modes show preference for breakup triggered by transfer of a proton to ^{7}Li, and a neutron from both ^{6}Li and ^{7}Li. However, identification of the reaction processes leading to breakup is not sufficient to understand the interplay between breakup and the observed suppression of fusion [26, 24]. It is also critical to know the time-scales of these breakup processes as compared to the time-scale associated with fusion.

In a classical picture of fusion, whether the breakup occurs before or after the projectile reaches its point of closest approach to the target nucleus will determine the reaction outcome. For example, although formation of ^{8}Be through proton transfer can only occur close to the target nucleus, its ground-state lifetime [113] is long: $\sim 10^{-16}$s. It will thus decay into two α-particles after receding many thousands of nuclear diameters, and thus its decay can have no effect on fusion. Excited states of ^{8}Be have much shorter lifetimes [113], but the Q-value spectra give no clue to their population. Unlike excited states of the heavy reaction partner, which typically decay by emission of γ-rays in $>10^{-12}$s, breakup of the light partner occurs before γ-ray emission, thus the energy of the excited states appears in the fragment kinetic energies, and so cannot be determined from the Q-spectra. However, this crucial information on excited states and time-scales can be extracted from a second derived variable, the relative energy of the two coincidence particles, as discussed in the next Section.

4.3 Relative energy of breakup fragments and reaction time-scale

Consider nuclear collisions at sub-barrier energies from a classical perspective. We can picture the Coulomb field associated with the target nucleus as a spherical mirror, as illustrated in *Figure 4.11.* A projectile approaching a target nucleus will be excited with excitation energy E_x and, depending on its binding energy, may breakup after reflection (*Figure 4.11a*) far away as it is receding. Such breakup is termed *asymptotic* breakup and, with minimal interaction with the target nucleus following breakup, the relative energy E_rel between the breakup fragments will comprise mainly the reaction Q-value and the excitation energy,

$$E_\mathrm{rel} = E_\mathrm{x} + Q_\mathrm{BU} \,. \tag{4.3}$$

A more weakly-bound projectile may breakup early before reflection (*Figure 4.11b*) termed *prompt* breakup. The charged fragments will then experience different acceleration by the Coulomb field of the target nucleus [7, 62, 9]. Thus the relative energy $E_{\rm rel}$ may differ from that in the asymptotic region. The $E_{\rm rel}$ for prompt breakup will now include an extra term:

$$E_{\rm rel} = E_{\rm x} + Q_{\rm BU} + E_{\rm post\_acc.} \,. \tag{4.4}$$

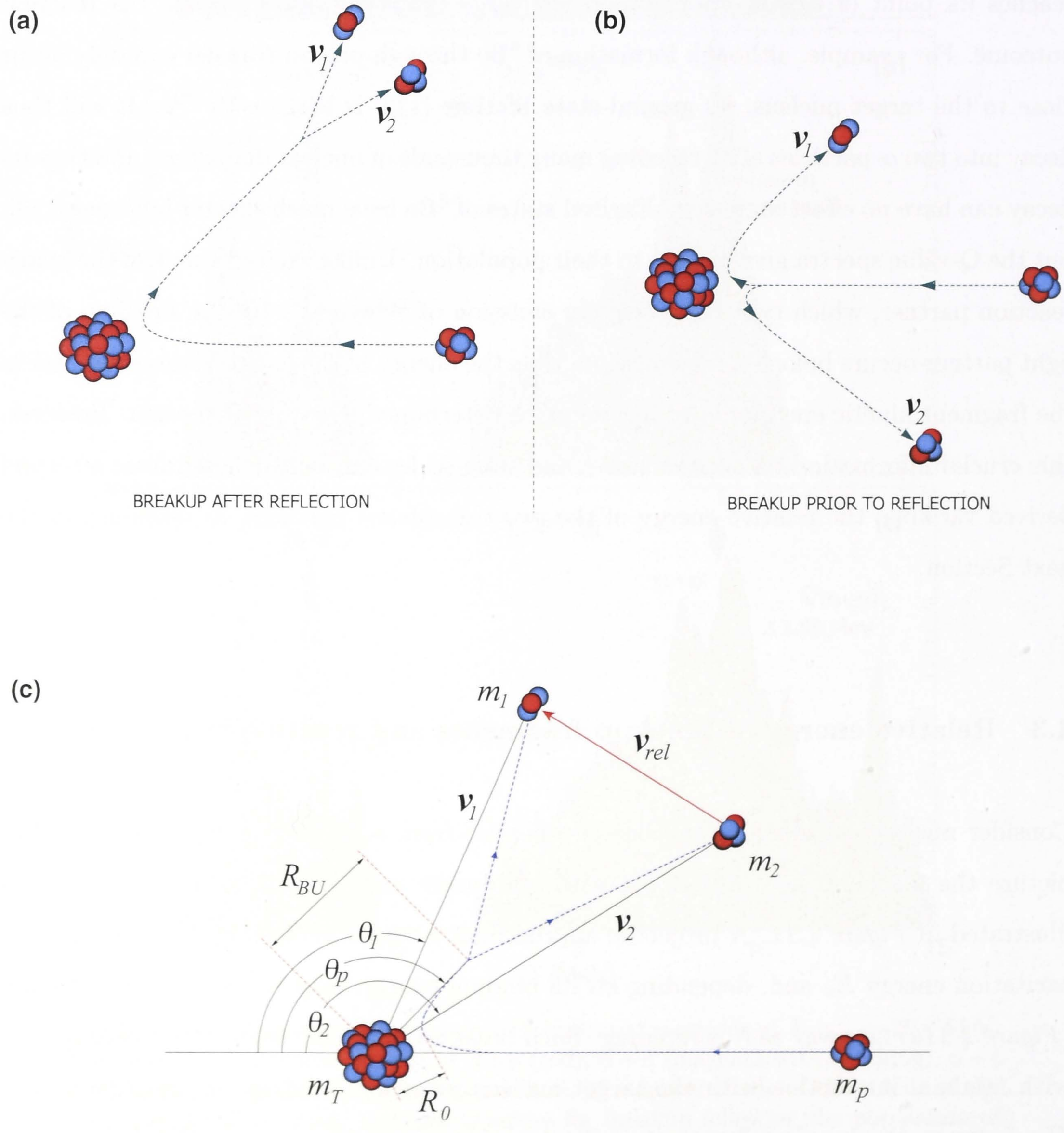

Figure 4.11: (a,b) Illustration of possible breakup trajectories. (c) Coordinates for the determination of the relative velocity of two breakup fragments.

Experimentally, E_{rel} is defined as the sum of the kinetic energies of the two particles in their centre-of-mass frame of reference

$$E_{\mathrm{rel}} = \frac{1}{2}\frac{m_1 m_2}{m_1 + m_2}\boldsymbol{v}_{rel}^2\,, \tag{4.5}$$

where m_1 and m_2 are the fragment masses. For two particles with velocities $\boldsymbol{v}_1$ and $\boldsymbol{v}_2$ (*Figure 4.11c*), their relative velocity $\boldsymbol{v}_{rel}$ is obtained through the cosine law

$$\boldsymbol{v}_{rel}^2 = \boldsymbol{v}_1^2 + \boldsymbol{v}_2^2 - 2\boldsymbol{v}_1\boldsymbol{v}_2\cos\Theta_{12}\,, \tag{4.6}$$

where Θ_{12} is the laboratory opening angle between the two fragments and is related [75] to their spatial positions by

$$\cos\Theta_{12} = \cos\theta_1\cos\theta_2 - \sin\theta_1\sin\theta_2\cos(\phi_1 - \phi_2)\,. \tag{4.7}$$

Here, θ_{i} and ϕ_{i} are the laboratory scattering and azimuthal angles of the fragments with respect to the beam axis, and are obtainable experimentally together with their energies E_{i}. Substitution of equation (4.6) into (4.5) gives

$$E_{\mathrm{rel}} = \frac{m_2E_1 + m_1E_2 - 2\sqrt{m_1E_1m_2E_2}\cos\Theta_{12}}{m_1 + m_2}\,. \tag{4.8}$$

From the coincidence measurements with ^{6,7}Li, breakup events were identified by the energies and positions of the coincidence particles $i+j$, $i(E_i,\theta_i,\phi_i)$ and $j(E_j,\theta_j,\phi_j)$. With the particle identities deduced from the Q-spectra, the experimental E_{rel} for each pair of coincident breakup fragments was determined as described by equations (4.7) and (4.8). By firstly comparing the combined Q vs. E_{rel} information for mass-unidentified events and the Q vs. E_{rel} belonging to events with an identified hydrogen isotope, cross-talk between adjacent detector arcs (see Section 3.4.6) can be separated from genuine breakup events with greater accuracy.

Shown in *Figure 4.12* are scatterplots of $Q_{\alpha+d}$ vs. E_{rel} for mass-unidentified events from the reaction of ^{6}Li with ^{208}Pb. Recall that $Q_{\alpha+d}$ is the Q-value determined assuming an $\alpha + d$ partition. The Q-values of spurious cross-talk events (*Figure 4.12a*) are seen to be extending to lower Q, reaching that of genuine $\alpha+d$ breakup events. If one was to gate for $\alpha+d$ only by Q-value, which is equivalent to a rectangular gate in the $Q_{\alpha+d}$ vs. E_{rel} matrix

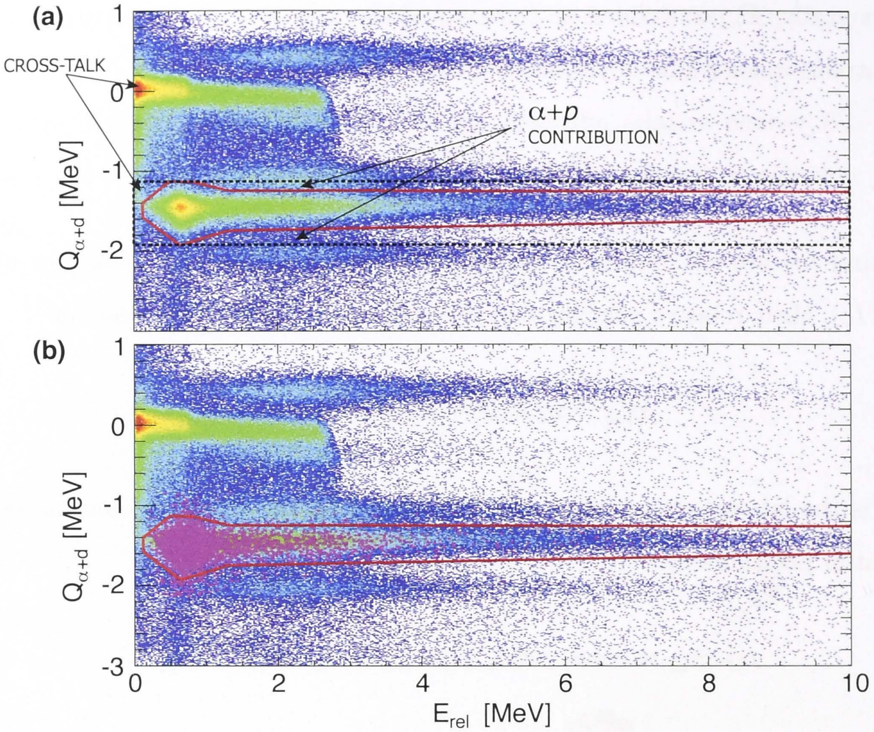

Figure 4.12: (a) 2-D gate (red) in the $E_{\rm rel}$ vs. Q-value applied to select $\alpha+d$ breakup for mass-unidentified events from reactions of ^{6}Li. (b) Same as in (a) but overlaid in magenta are events with one particle identified as a deuteron.

shown by the dashed black lines, then there would be contributions from both (i) cross-talk events that have the right Q-value but wrong $E_{\rm rel}$, and (ii) $\alpha+p$ breakup events with the right Q-value but with the wrong $E_{\rm rel}$. The subtle differences in $E_{\rm rel}$ allows the 2-D gate (shown in red) to be drawn, enabling better separation of these distinct groups. When overlaid with events where a deuteron has been identified (*Figure 4.12b*), the spread of these identified events allows fine tuning of the 2-D gate. This 2-D gating procedure was applied to every breakup mode for all data collected.

4.3.1 Interpretation of the measured $E_{\rm rel}$

Shown in *Figure 4.13* are the measured Q vs. $E_{\rm rel}$ scatterplots for the reactions of ^{6,7}Li with ^{207}Pb, ^{208}Pb and ^{209}Bi, at $E_{\rm beam} = 29.0$ MeV. Genuine breakup events are shown in colours with $\alpha+\alpha$ in green, $\alpha+t$ in blue, $\alpha+d$ in magenta, and $\alpha+p$ in red, while non-genuine events are greyed out. The $E_{\rm rel}$ distributions show narrow peaks at low $E_{\rm rel}$ and broad components extending to high $E_{\rm rel}$. The same breakup mode, even when originating from different projectile-target combinations and/or different preceding processes (e.g. direct

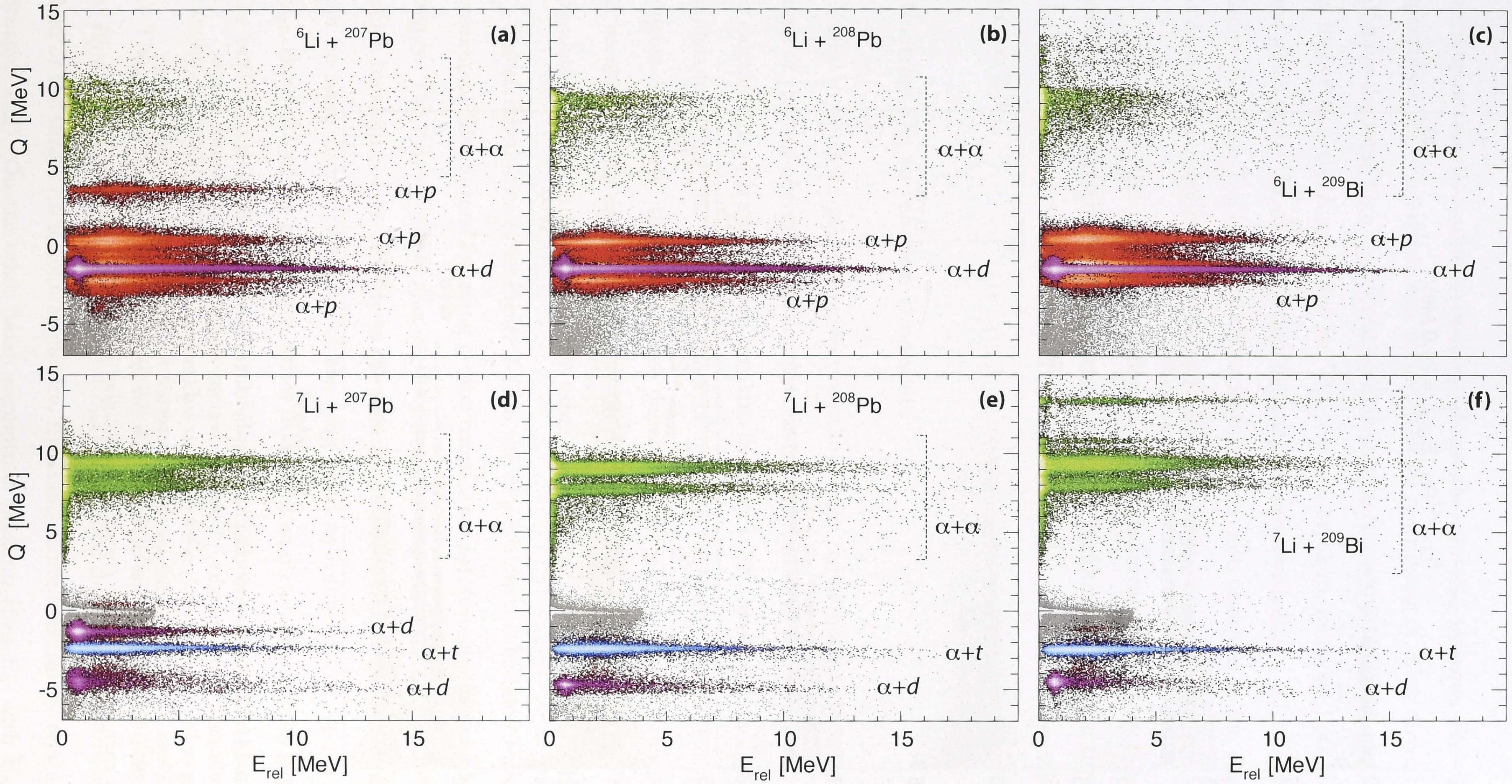

Figure 4.13: Scatterplots of E_{rel} vs. Q-value for the indicated reactions at E_{beam} = 29.0 MeV. Coloured regions shows the gated genuine events belonging to the $\alpha+\alpha$ (green), $\alpha+t$ (blue), $\alpha+d$ (magenta) and $\alpha+p$ (red) breakup modes. These spectra have neither been corrected for punch-though of high energy Z=1 particles in the non-telescope detectors, nor for geometrical efficiency. The paler shade for each breakup mode corresponds to higher intensity.

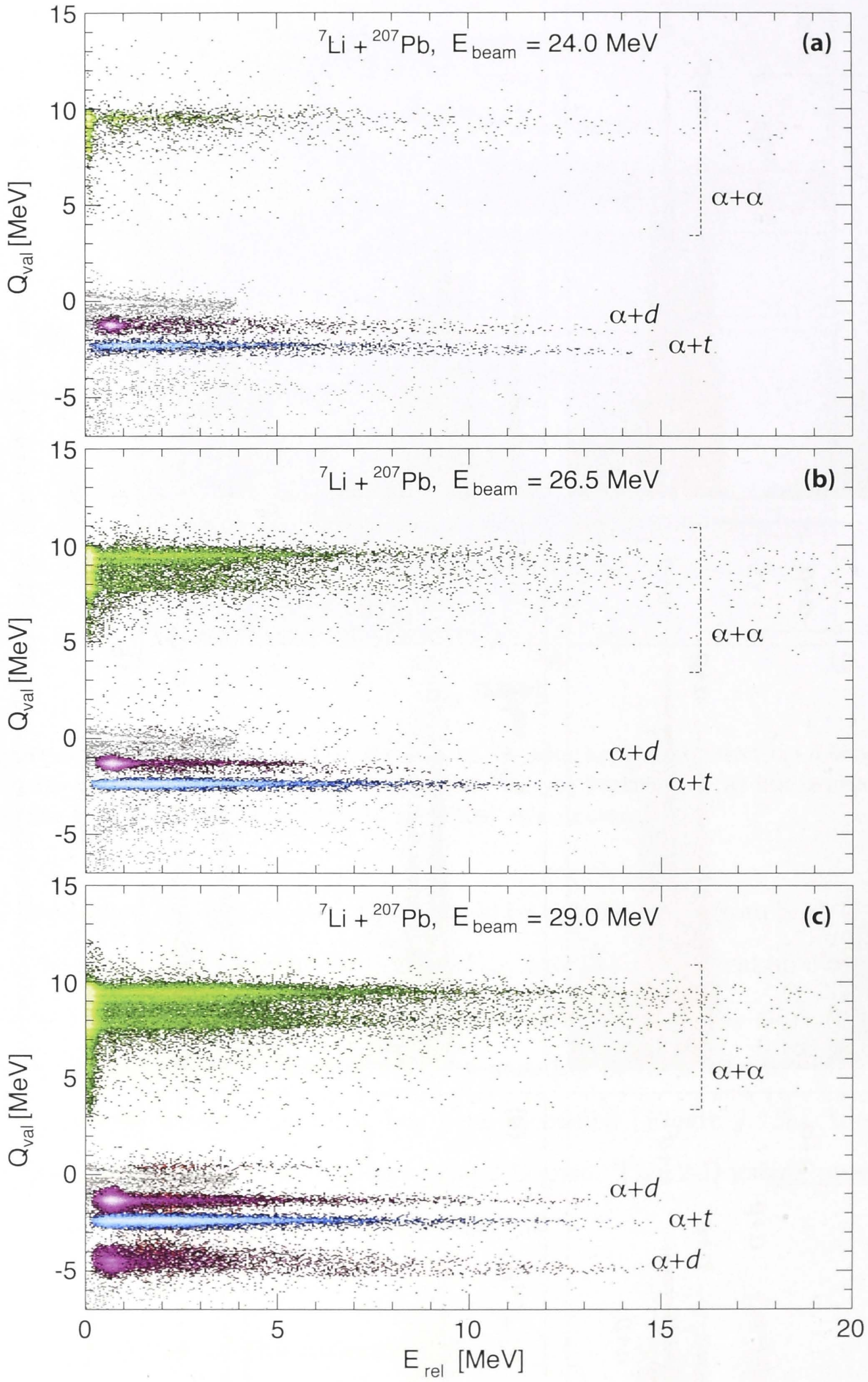

Figure 4.14: Scatterplots of $E_{\rm rel}$ vs. Q-value for the reaction of ^{7}Li with ^{207}Pb at the indicated beam energies. Coloured regions shows the gated genuine events belonging to the $\alpha+\alpha$ (green), $\alpha+t$ (blue), $\alpha+d$ (magenta) and $\alpha+p$ (red) breakup modes. These spectra have neither been corrected for punch-though of high energy Z=1 particles in non-telescope detectors, nor for geometrical efficiency. The paler shade for each breakup mode corresponds to higher intensity.

breakup or transfer leading to breakup) shares the same $E_{\rm rel}$ features. For example the $E_{\rm rel}$ spectra for ^{6}Li $\to \alpha+d$ breakup, following either n-stripping of ^{7}Li or direct breakup of ^{6}Li, all have the same high concentration of events at $E_{\rm rel} = 0.7$ MeV and a broad tail leading to higher $E_{\rm rel}$; the $E_{\rm rel}$ spectra for ^{8}Be $\to \alpha + \alpha$ breakup, following both d-pickup by ^{6}Li and p-pickup by ^{7}Li, all have a high intensity of events with $E_{\rm rel} = 0.1$ MeV and broad tails comprising high $E_{\rm rel}$ events. Similar features were also observed in the $E_{\rm rel}$ distributions at other lower energies, as shown in *Figure 4.14* for the reaction of ^{7}Li with ^{207}Pb.

To interpret the physical significance of the features seen in the $E_{\rm rel}$ distributions, simulation of three-body breakup reactions were performed using the three-dimensional classical model `PLATYPUS` [32, 31]. This classical dynamical model is described in detail in Section 2.3.

Relating $E_{\rm rel}$ to reaction time-scale

Central to the description of nuclear reactions is the radial distance between the centres of mass of the two objects. Reaction processes, from fusion of two many-body systems [17] to calculations of trajectories of breakup fragments [32], have been described reliably by models involving just the radial distance between the centres of mass of the interacting objects. Similarly, the quantitative dependence of $E_{\rm rel}$ on the internuclear separation at breakup, which can be related to the time-scales of the reaction, can be seen in the simulation for $\alpha + \alpha$ breakup of ^{8}Be using the computer code `PLATYPUS` [31].

Shown schematically in *Figure 4.15* is the $E_{\rm rel}$ evolution calculated with `PLATYPUS` for breakup of ^{8}Be (formed following proton transfer to ^{7}Li), from a nominal 2 MeV excitation energy. The dependence of $E_{\rm rel}$ on the projectile-target separation $R_{\rm BU}$ (or time $T_{\rm BU}$) at which breakup occurs, relative to the point of closest approach without breakup R_0 (T_0), can be seen through variation of the pink band as a function of $R_{\rm BU}$. The spread in $E_{\rm rel}$, the width of the pink band, arises from random orientations of the two fragments at the point of breakup, and the range of impact parameters considered (corresponding to angular momenta up to $14\hbar$).

The strong variation of the calculated $E_{\rm rel}$ around R_0 (T_0) indicates that breakup close to R_0 will be characterised by a broad $E_{\rm rel}$ distribution due to acceleration in the Coulomb field of the target (in a quantal picture, the energy-time uncertainty relation will further broaden $E_{\rm rel}$). On the other hand, asymptotic breakup after R_0, with $E_{\rm rel} \sim 2.0$ MeV,

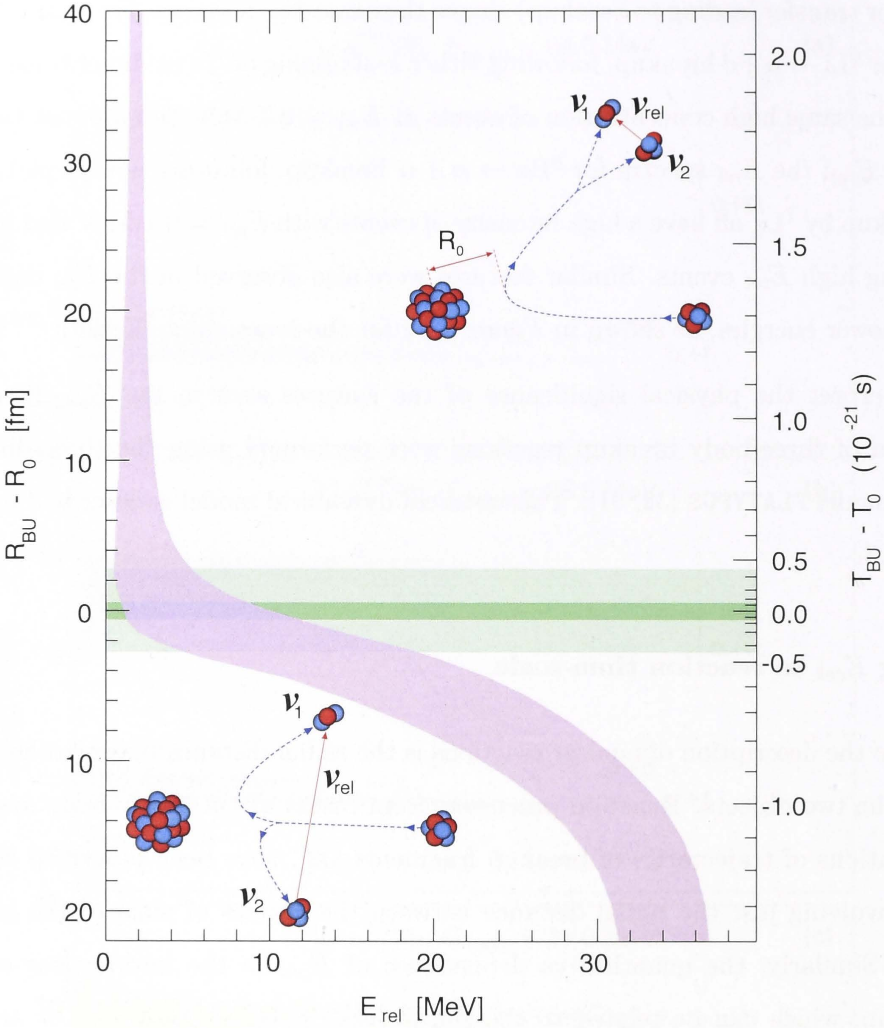

Figure 4.15: The curved pink band shows the classically calculated spread of $E_{\rm rel}$ versus the nuclear separation (left axis) or time (right axis) at which breakup occurs, relative to the point of closest approach (R_0, T_0), for ^{8}Be in the field of a ^{208}Pb nucleus. The spread in $E_{\rm rel}$ arises from the different impact parameters and projectile orientations. Breakup prior to reflection, $(T_{\rm BU} - T_0) < 0$, sketched in the lower inset, results in higher $E_{\rm rel}$ values than breakup after reflection $(T_{\rm BU} - T_0) > 0$ (upper inset). The horizontal bands show the 50% (dark) and 95% (light) probability regions for p-pickup by ^{7}Li to form ^{8}Be (see text).

shows that breakup when moving away from the target will be characterised by a peak at lower $E_{\rm rel}$ in accordance with equation (4.3). The measured $E_{\rm rel}$-spectra are thus expected to show two components. The first consists of peaks at low $E_{\rm rel}$ values, centred at $E_{\rm rel} = E_{\rm x} + Q_{\rm BU}$, where $E_{\rm x}$ is the excitation energy of the state from which breakup occurs and $Q_{\rm BU}$ is the breakup Q-value. These peaks are associated with breakup on the outgoing trajectory, and thus cannot suppress fusion. The second component consists of events extending to high $E_{\rm rel}$, which are associated with breakup close to the target nucleus. It is these breakup events that can be responsible for the suppression of fusion observed at above-barrier energies [24, 26, 128].

The possible population of relatively long-lived resonant states in the projectile-like nuclei means it is crucial to make a clear distinction between the locations (and times) of the processes triggering breakup (e.g. transfer), and those of the breakup itself (which can follow promptly or be delayed if a long-lived state is populated). It has been predicted theoretically [32], and observed experimentally [52, 86], that at energies below the barrier the probability of breakup is well described by an exponential dependence on inter-nuclear separation. For each of the mechanisms observed to trigger breakup, we have determined the exponential slope (see next chapter) from our measurements of the probabilities as a function of beam energy. The probabilities for proton pickup by ^{7}Li, which serves as a trigger for breakup, was found to be strongly peaked around the distance of closest approach R_{BU}, and thus around T_0, with 50% of the yield occurring within $|R_{\mathrm{BU}} - R_0| < 0.7$ fm, and 95% within $|R_{\mathrm{BU}} - R_0| < 2.7$ fm. For fusion to be suppressed, $\alpha + \alpha$ breakup of ^{8}Be must occur before the projectile passes R_0, i.e. before ^{8}Be starts receding from the target-like nucleus. From the mapping between radius and time, we can thus conclude that breakup time-scales of $\sim 10^{-22}$s are required for *prompt breakup* which at higher beam energies will suppress complete fusion.

The relationship described between the E_{rel} spectrum and the time-scales of breakup shows that the experimental E_{rel} spectra indeed give the critical breakup time-scale information. Thus, by plotting Q vs. E_{rel}, the spectra shown in *Figure 4.13* give the first *complete* picture of breakup of ^{6,7}Li. For each breakup event, its Q-value defines the breakup mode, revealing the reaction process triggering breakup and the excitation of the target-like nucleus, while at the same time, the determination of E_{rel} gives the information on the breakup time-scale which, in turn, allows separation between prompt and delayed breakup as further described below.

Time-scales for different breakup modes in ^{6}Li

The E_{rel} spectra for all the major breakup modes of ^{6}Li are shown in *Figure 4.16*, together with the detection efficiency for the $\alpha + d$ and $\alpha + p$ breakup modes as a function of the relative energy between the two fragments. These final E_{rel} spectra are essentially *x-projections* of the Q vs. E_{rel} scatterplots (*Figures 4.13a,b,c*). Losses due to punch-through of high energy Z=1 events and detection efficiency have been accounted for. Details on how the correction for these losses was achieved, and its justifications, are presented in Section 5.4. The E_{rel}-*efficiency* factors (*Figure 4.16a*) cover all θ and ϕ and thus total cross-sections for each breakup mode can be obtained from the integral of the efficiency corrected E_{rel} spectra.

The E_{rel} spectra for $\alpha + d$ breakup of ^{6}Li, on all three targets, shows a peak at 0.7 MeV consistent with asymptotic breakup from 2.17 MeV excitation energy, the sum of E_{rel} (0.7 MeV) and Q_{BU} (-1.47 MeV) for $\alpha + d$ cluster breakup of ^{6}Li according equation (4.3). Breakup events comprising this peak must have come from $\alpha + d$ decay from the 2.18 MeV (3^+) state in ^{6}Li, a resonant state with intrinsic width $\Gamma_{\text{c.m.}} = 0.024$ MeV [112] and a lifetime of 2.7×10^{-20} s. Compared to the 10^{-22} s time-scale for direct reactions and fusion, in reactions at beam energies above the fusion-barrier energy, ^{6}Li nuclei excited to this 3^+ resonant state would have survived intact at the fusion-barrier, and thus would participate in complete fusion as ^{6}Li. Hence, breakup from this resonant state cannot affect complete fusion.

The shaded peak in *Figure 4.16c* is a simulated E_{rel} spectrum for asymptotic breakup of ^{6}Li on ^{208}Pb, from the 3^+ resonance, incorporating the effects of instrumental resolution in E_{rel}. The simulation was carried out using `BUGS` [86], an asymptotic breakup simulation program. Because the program only takes the reaction Q-value as input to calculate the asymptotic E_{rel}, as opposed to the excitation energy E^* and Q_{BU} seen in equation (4.3), an input Q-value of 0.7 MeV was used, corresponding to excitation of the 2.18 MeV resonance state and $Q_{BU} = -1.47$ MeV for $\alpha + d$ cluster breakup of ^{6}Li. The match between the simulated and experimental E_{rel} confirms the observed width ($\sim$ 0.4 MeV FWHM) of the peak in $E_{\text{rel}} = 0.7$ MeV in the latter is an effect of instrumental resolution, which arises largely from the pixel size of the DSSDs.

The E_{rel} spectra for the $\alpha + p$ breakup mode show a broad distribution to high E_{rel}. This reflects the *prompt* nature of the breakup of ^{5}Li, produced by n-stripping from ^{6}Li. The ground-state lifetime of ^{5}Li, 5.3×10^{-22} s [112], is comparable to the time-scale for complete fusion reactions. With such a short decay time-scale, breakup will strongly affect complete fusion at beam energies above the fusion-barrier energy, and contribute to into incomplete fusion via partial capture of charged breakup fragments by the target (this is further discussed in Section 5.6).

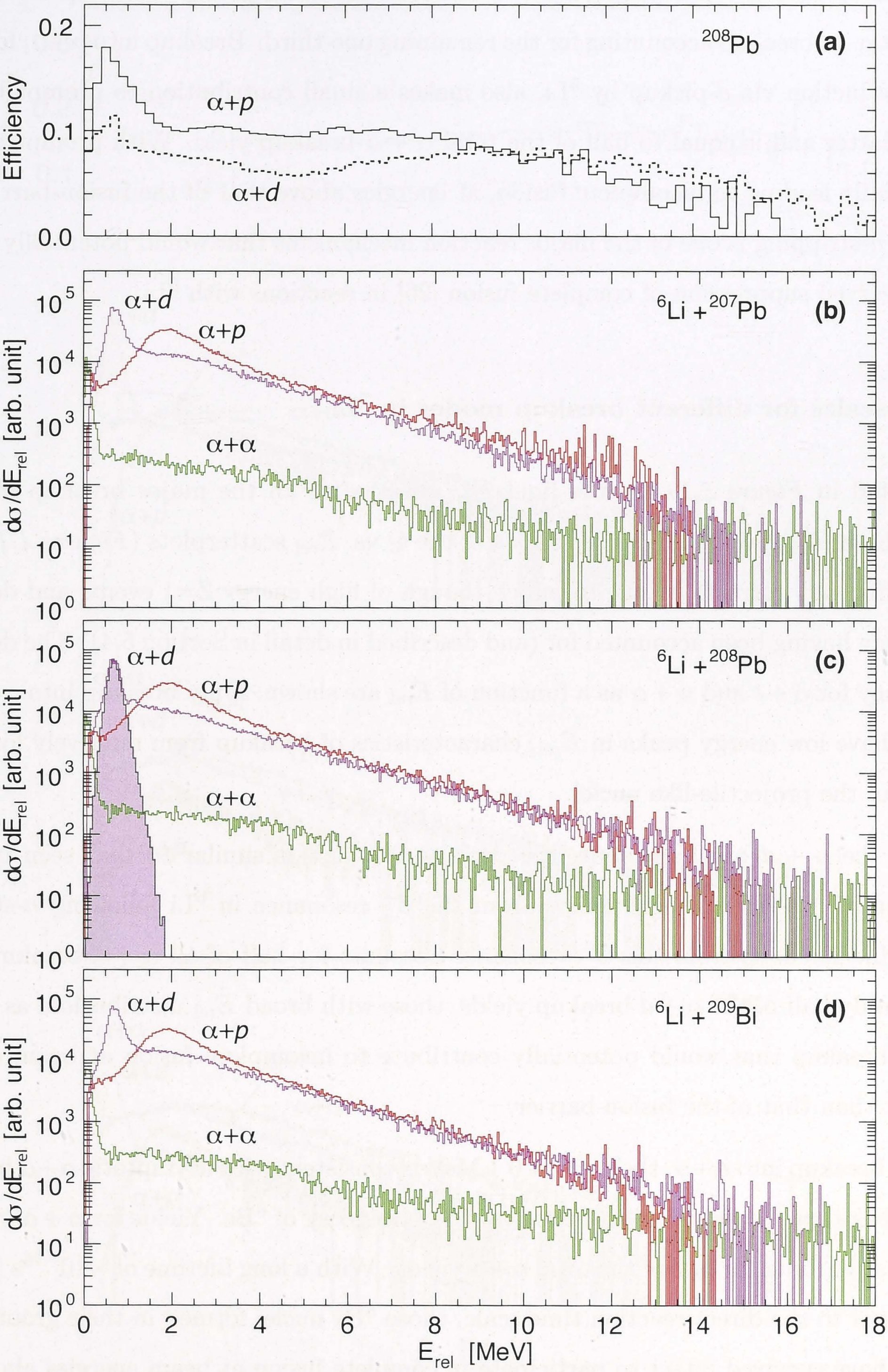

Figure 4.16: (a) Detector efficiency response for indicated breakup modes in the Coulomb field of ^{208}Pb. (b,c,d) E_{rel}-spectra, corrected for punch-through of high energy Z=1 particles in the non-telescope detectors and the detector efficiency shown in (a), for the major breakup partitions for the indicated reactions at $E_{\mathrm{beam}} = 29.0$ MeV. The shaded spectrum in (c) shows a simulation of breakup of ^{6}Li from the first resonant state ($J^\pi = 3^+$) incorporating the effects of instrumental resolution on E_{rel} (see main text).

Breakup into $\alpha + p$ accounts for two-thirds of the total prompt breakup of ^{6}Li, with prompt α+d breakup accounting for the remaining one-third. Breakup into α+α, following ^{8}Be production via d-pickup by ^{6}Li, also makes a small contribution to prompt breakup of the latter and is equal to half of the total $\alpha + \alpha$ breakup yield. With prompt breakup potentially leading to incomplete fusion, at energies above that of the fusion-barrier, this means n-stripping is one of the major reaction mechanisms that would potentially explain the observed suppression of complete fusion [26] in reactions with ^{6}Li.

Time-scales for different breakup modes in ^{7}Li

Presented in *Figure 4.17* are the final E_{rel} spectra for all the major breakup modes of ^{7}Li. These E_{rel} spectra are *x-projections* of the Q vs. E_{rel} scatterplots (*Figures 4.13d,e,f*), with efficiency corrections due to punch-though of high energy Z=1 events and detection efficiency having been accounted for (and described in detail in Section 5.4). The detection efficiency for $\alpha + t$ and $\alpha + \alpha$ as a function of E_{rel} are shown. Only breakup into $\alpha + d$ and $\alpha + \alpha$ have low energy peaks in E_{rel}, characteristics of breakup from relatively long-lived states in the projectile-like nuclei.

For the $\alpha + d$ breakup mode, the peak at 0.7 MeV is similar to that seen in $\alpha + d$ breakup of ^{6}Li, indicating breakup from the 3^+ resonance in ^{6}Li following n-stripping from ^{7}Li. Breakup from this 3^+ resonance accounts for half of all $\alpha + d$ breakup. This leaves only half of the $\alpha + d$ breakup yields, those with broad E_{rel} distribution, as prompt $\alpha + d$ breakup that would potentially contribute to incomplete fusion at beam energies greater than that of the fusion-barrier.

For breakup into α+α, the peak at 0.1 MeV is consistent with asymptotic α+α breakup. This peak thus comprises $\alpha + \alpha$ from ground-state decay of ^{8}Be. Yields for $\alpha + \alpha$ events in this peak account for half of the total α+α yields. With a long lifetime of $\sim 10^{-16}$s [113], as compared to the direct reaction time-scale, those ^{8}Be nuclei formed in their ground-state would have survived intact to participate in complete fusion at beam energies above that of the fusion-barrier energy. Thus the $^8\text{Be}_{\text{g.s}}$ population cannot contribute to incomplete fusion, and suppression of complete fusion. The observed width of the 0.1 MeV peak is also an instrumental effect, as confirmed by the simulated E_{rel} for ground-state decay of ^{8}Be (shaded peak in *Figure 4.17c*). This simulation for $\alpha + \alpha$ breakup of ^{8}Be on ^{208}Pb at $E_{\text{beam}} = 29.0$ MeV, was carried out using `BUGS`.

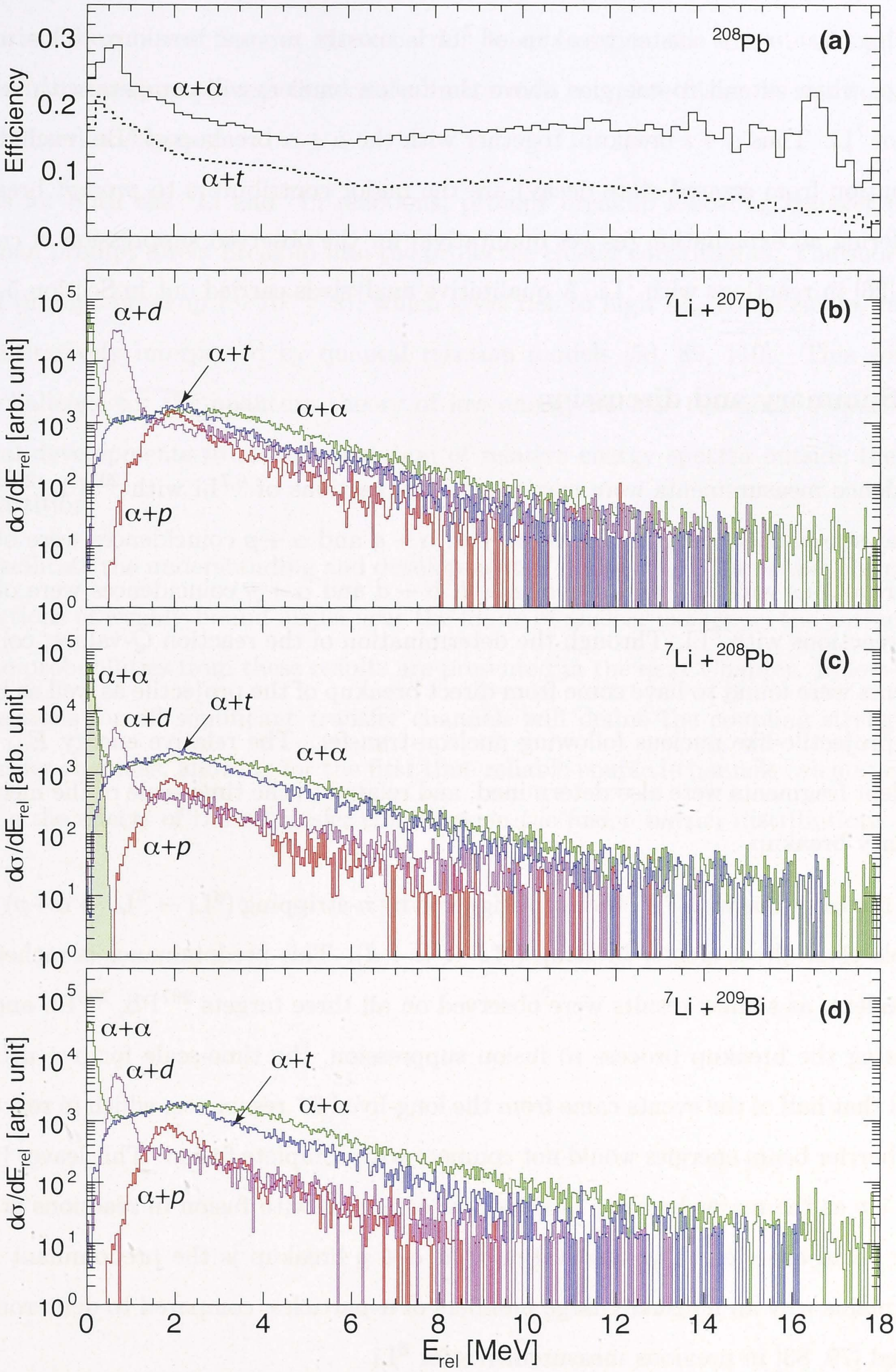

Figure 4.17: (a) Detector efficiency response for the indicated breakup mode in the Coulomb field of ^{208}Pb. (b,c,d) $E_{\rm rel}$-spectra, corrected for punch-through of high energy Z=1 particles in non-telescope detectors and for detector efficiency shown in (a), for the major breakup partitions for the indicated reactions at $E_{\rm beam} = 29.0$ MeV. The shaded spectrum in (c) is from a simulation of ground-state decay of ^{8}Be with decay Q-value of 0.092 MeV incorporating the effects of instrumental resolution on $E_{\rm rel}$.

The E_{rel} spectra for the $\alpha + t$ breakup mode have broad distributions to high E_{rel} indicating that $\alpha + t$ cluster breakup of ^{7}Li is mostly *prompt* breakup. This mode of breakup, when extend to energies above the fusion barrier, will compete with complete fusion of ^{7}Li. Thus $\alpha + t$ breakup, together with the $\alpha + \alpha$ breakup of ^{8}Be (excluding the contribution from ground-state decay) are the major contributors to *prompt* breakup of ^{7}Li, offering an explanation (as yet qualitative) for the observed suppression of complete fusion [26] in reactions with ^{7}Li. A qualitative analysis is carried out in Section 5.6.

4.4 Summary and discussion

Coincidence measurements were carried out for reactions of ^{6,7}Li with ^{207}Pb, ^{208}Pb and ^{209}Bi, at sub-barrier energies. Binary $\alpha + \alpha$, $\alpha + d$ and $\alpha + p$ coincidences were observed in the reactions with ^{6}Li, and $\alpha + \alpha$, $\alpha + t$, $\alpha + d$ and $\alpha + p$ coincidences were observed in the reactions with ^{7}Li. Through the determination of the reaction Q-values, coincident fragments were found to have come from direct breakup of the projectile as well as breakup of the projectile-like nucleus following nucleon-transfer. The relative energy E_{rel} for the coincident fragments were also determined, and related to the time-scale of the mechanism for binary breakup.

For the reactions with ^{6}Li, breakup triggered by n-stripping ($^{6}\text{Li} \rightarrow {}^{5}\text{Li} \rightarrow \alpha + p$) is more probable than direct cluster breakup ($^{6}\text{Li} \rightarrow \alpha + d$). This predominance is rather target independent, as similar results were observed on all three targets ^{207}Pb, ^{208}Pb and ^{209}Bi. In relating the breakup process to fusion suppression, the time-scale for $\alpha + d$ breakup showed that half of the events came from the long-lived 3^{+} resonance, which in reactions at above-barrier beam energies would not compete with complete fusion. This leaves breakup into $\alpha + p$ as the major breakup process that competes with fusion in reactions at above-barrier beam energies. The observation that $\alpha + p$ breakup is the predominant process also explains why an unusually large numbers of α-particles, compared to deuterons, were observed [79, 83] in previous measurements for ^{6}Li.

The ^{7}Li-induced reactions were found to be dominated by p-pickup forming the unbound ^{8}Be that subsequently decays into two α-particles ($^{7}\text{Li} \rightarrow {}^{8}\text{Be} \rightarrow \alpha + \alpha$). This reaction mechanism is also target independent as the same behaviour was observed for all reactions with ^{209}Bi, ^{208}Pb and ^{207}Pb. For the latter, breakup triggered by n-stripping ($^{7}\text{Li} \rightarrow {}^{6}\text{Li} \rightarrow \alpha + d$) was also more prominent than direct cluster breakup ($^{7}\text{Li} \rightarrow \alpha + t$).

Even though half of all the ^{8}Be produced are long-lived, and thus would survive to participate in fusion in reactions at above-barrier beam energies, the short-lived half is still the dominant breakup process that can compete with complete fusion in reactions of ^{7}Li at above-barrier energies.

Thus for both the ^{6}Li and ^{7}Li reactions, prompt breakup following transfer is more likely than prompt direct breakup into the projectile cluster constituents. The short time-scale of prompt breakup ($\sim 10^{-22}$ s), which gives rise to high E_{rel} components, can only be quantitatively interpreted by quantal reaction models [58, 89, 110]. This will be a major challenge for the quantum theory of low energy nuclear reactions, requiring new technical developments to allow calculation of relative energy spectra outside the initial mass-partition.

To facilitate the understanding and development of a theoretical framework for predicting reactions of weakly-bound nuclei near the limits of nuclear existence, the extraction of absolute probabilities from these results are presented in the next Chapter. Below-barrier cross sections for all significant transfer channels will define the coupling strengths for the transfer channels, allowing for the first time reliable coupled-channels calculations and revealing the effects of these transfer couplings on the fusion barrier distributions [27].

> *The problem of physics is how the actual phenomena, as observed with the help of our sense organs aided by instruments, can be reduced to simple notions which are suited for precise measurement and used for the formulation of quantitative laws.*
>
> M. Born (1882 - 1970)

5

Breakup and suppression of complete fusion

Qualitative results presented in the preceding chapter showed that, along with direct breakup into their cluster constituents, breakup triggered by transfer of nucleon(s) is a very important reaction channel in reactions induced by ^{6,7}Li on high-Z targets. To obtain the quantitative contributions of different breakup modes, however, a knowledge of the absolute probability is required. In particular since we are interested in understanding the relationship between prompt breakup and the suppression of complete fusion, we need to determine breakup probabilities as a function of the distance of closest approach. This breakup function can then be fed into the classical trajectory calculations (see Section 2.3) to make predictions of complete and incomplete fusion cross-sections.

The process of converting measured breakup yields into the breakup function involves many steps. Firstly the yields need to be normalised to the elastic scattering cross-sections, as explained in Section 5.1. Following this, Section 5.2 outlines the procedure to determine the distance of closest approach for events that lead to breakup. The normalised breakup yields then need to be corrected for the detection efficiency for coincidence measurements. The determination of this efficiency is not straight forward as it depends on the kinematics of each breakup mode. Details of simulations of breakup kinematics and the breakup detection efficiency are presented in Section 5.3 and 5.4, respectively. From the determined efficiency, the absolute probabilities for each breakup mode were determined and are given in Section 5.5. The predictions for the suppression of complete fusion, based on the determined breakup probabilities, are presented in Section 5.6.

5.1 Solid angle normalisation

In our experiment, the lampshade detector array covers a restricted (though large) range in both θ and ϕ. It is large enough to allow the data to be divided into relatively small bins of width $\Delta\theta_{\text{lab}}$, having the same azimuthal acceptance $\Delta\phi_{\text{lab}}$. For a reaction at beam energy E, the number of particles incident on each bin, centred around the bin mid-angle θ_{lab}, is given by

$$Y(\theta_{\text{lab}}, E) = [I][N]\frac{d\sigma(\theta_{\text{lab}}, E)}{d\Omega_{\text{lab}}} d\Omega_{\theta_{\text{lab}}}, \tag{5.1}$$

where I is the number of incident beam particles, N the number of target nuclei/cm^2, $d\sigma(\theta_{\text{lab}}, E)/d\Omega$ the differential cross-section, and $d\Omega_{\theta_{\text{lab}}}$ the solid angle of the lampshade detector for the given angular bin.

The total yield for elastically scattered beam particles in the two monitor detectors at angle θ_M is $Y_M(\theta_M, E)$, when scattering is purely Rutherford, is given by:

$$Y_M(\theta_M, E) = [I][N]\frac{d\sigma_{Ruth}(\theta_M, E)}{d\Omega_{\text{lab}}} d\Omega_M\,, \tag{5.2}$$

where $d\sigma_{Ruth}(\theta_M, E)/d\Omega$ is the Rutherford scattering differential cross-section and $d\Omega_M$ is the solid angle subtended by the monitor detectors. As the beam current and target thickness are usually not known accurately, their effect can be cancelled out by taking the ratio of equations (5.1) and (5.2):

$$\frac{Y(\theta_{\text{lab}}, E)}{Y_M(\theta_M, E)} = \left[\frac{d\Omega_{\theta_{\text{lab}}}}{d\Omega_M}\right] \frac{d\sigma(\theta_{\text{lab}}, E)/d\Omega}{d\sigma(\theta_M, E)/d\Omega}. \tag{5.3}$$

The quantity $d\Omega_{\theta_{\text{lab}}}/d\Omega_M$ was determined experimentally by measuring Rutherford scattering. This avoids introducing unnecessary uncertainties through having to calculate $d\Omega_M/d\Omega_{\theta_{\text{lab}}}$ from the physical geometry of the detectors. To determine $d\Omega_{\theta_{\text{lab}}}/d\Omega_M$, the energy of the normalisation reaction, E_{cal}, was chosen such that scattering at all angles in the lampshade detector is Rutherford. In practice, this required an energy of ~ 0.7 times that of the fusion barrier. At this energy equation (5.3) can be written as

$$\frac{d\Omega_M}{d\Omega_{\theta_{\text{lab}}}} = \frac{Y_M(\theta_M, E_{\text{cal}})(d\sigma/d\Omega)_{Ruth}(\theta_{\text{lab}}, E_{\text{cal}})}{Y_{\text{el}}(\theta_{\text{lab}}, E_{\text{cal}})(d\sigma/d\Omega)_{Ruth}(\theta_M, E_{\text{cal}})}, \tag{5.4}$$

where Y_{el} (θ_{lab}, E_{cal}) is the elastic yield per bin in the lampshade detector. Then by writing $d\Omega_{\theta_{\text{lab}}} = \sin\theta_{\text{lab}} d\theta_{\text{lab}} \Delta\phi_{\text{lab}}$, equation (5.4) becomes

$$\frac{d\Omega_M}{d\theta_{\text{lab}}} = \sin\theta_{\text{lab}}\Delta\phi_{\text{lab}} \frac{Y_M(\theta_M, E_{\text{cal}})(d\sigma/d\Omega)_{Ruth}(\theta_{\text{lab}}, E_{\text{cal}})}{Y_{\text{el}}(\theta_{\text{lab}}, E_{\text{cal}})(d\sigma/d\Omega)_{Ruth}(\theta_M, E_{\text{cal}})} \,. \tag{5.5}$$

We define the RHS of equation 5.5 as the normalisation constant per bin,

$$A(\theta_{\text{lab}}) = \sin\theta_{\text{lab}}\Delta\phi_{\text{lab}} \frac{Y_M(\theta_M, E_{\text{cal}})(d\sigma/d\Omega)_{Ruth}(\theta_{\text{lab}}, E_{\text{cal}})}{Y_{\text{el}}(\theta_{\text{lab}}, E_{\text{cal}})(d\sigma/d\Omega)_{Ruth}(\theta_M, E_{\text{cal}})} \,. \tag{5.6}$$

The advantage of including $\sin\theta_{\text{lab}}$ and $\Delta\phi_{\text{lab}}$ explicitly in the definition of $A(\theta_{\text{lab}})$ is that the value of $A(\theta_{\text{lab}})$ is expected to be a constant if θ_{lab} and $\Delta\phi_{\text{lab}}$ are correctly determined from the detector geometry. This allows a check of the extracted values of $A(\theta_{\text{lab}})$ from the calibration runs.

The differential cross-section for each breakup mode can be obtained from their respective yields, Y, and the normalisation constant per bin, $A(\theta_{\text{lab}})$, by combining equations (5.3), (5.5) and (5.6):

$$\frac{d\sigma(\theta_{\text{lab}}, E)}{d\Omega} = \left[\frac{A(\theta_{\text{lab}})}{\Delta\phi_{\text{lab}}\sin\theta_{\text{lab}}}\right] \left[\frac{Y(\theta_{\text{lab}}, E)}{Y_M(\theta_M, E)}\right] (d\sigma/d\Omega)_{Ruth}(\theta_M, E) \,. \tag{5.7}$$

The exact angle θ_M of the monitor detectors is not critical since the dependence of $d\sigma(\theta_{\text{lab}}, E)/d\Omega$ on θ_M in equation (5.7) cancels out with the term $(d\sigma/d\Omega)_{Ruth}(\theta_M, E_{\text{cal}})$ in equation (5.5).

5.1.1 Angle bin normalisation

For the two runs LIX3 and LIX4, the normalisation constant $A(\theta_{\text{lab}})$ was determined by elastic scattering of ^{7}Li from ^{197}Au at $E_{\text{beam}} = 21.5$ and 20.0 MeV respectively. The self-supporting Au target ensures that the only scattering observed was from Au. Before determining the constant $A(\theta_{\text{lab}})$, it was checked that scattering was indeed elastic at these energies, over the full angular range (112°-172°) of the lampshade detector. This check was done by plotting the elastic counts per bin $N_{\text{el}}^{\theta_{\text{lab}}}/\sin\theta_{\text{lab}}$ (where the $\sin\theta_{\text{lab}}$ weighting ensures a constant solid angle) against the mid-angle of each bin.

The bin populations in (θ_{lab},ϕ_{lab}) for elastic scattering for the reactions ^{7}Li with ^{197}Au at 21.5 and 20.0 MeV are shown in the top panels of *Figures 5.1a,b* respectively. The elastic counts per bin $N_{\text{el}}^{\theta_{\text{lab}}}/\sin\theta_{\text{lab}}$ are shown in the lower panels. Also, overlaid on each

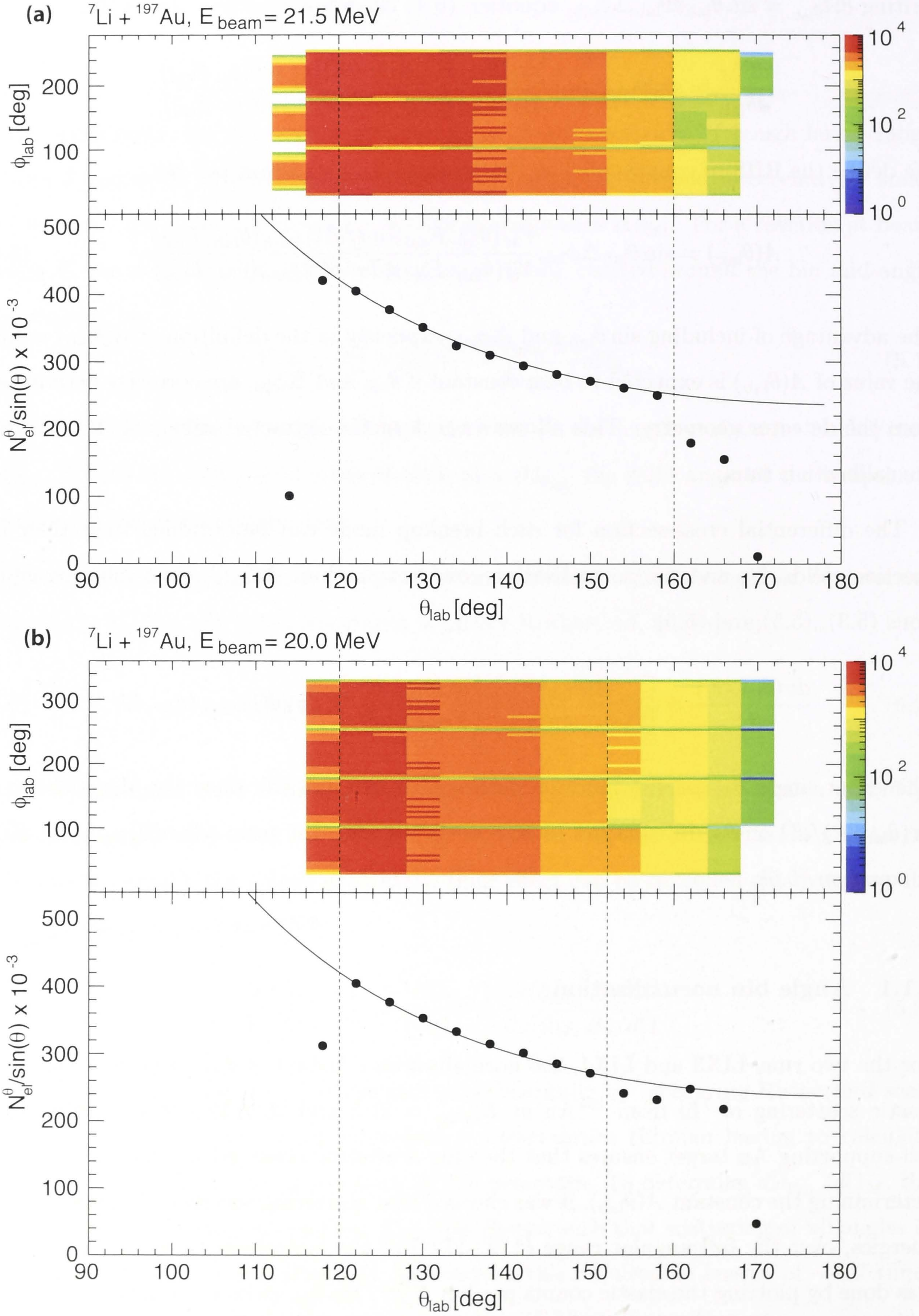

Figure 5.1: (a) The (θ_{lab},ϕ_{lab}) bin yields of elastic scattering from ^{7}Li +^{197}Au at $E_{\mathrm{beam}} = 21.5$ MeV. The lower panel shows the elastic counts per bin, with the expected differential cross-section for Rutherford scattering, as a function of the laboratory angle θ_{lab} and scaled to the counts in the bin centred at $\theta_{\mathrm{lab}} = 122°$, overlaid on top. (b) Same as in (a), but for the reaction of ^{7}Li with ^{197}Au at $E_{\mathrm{beam}} = 20.0$ MeV.

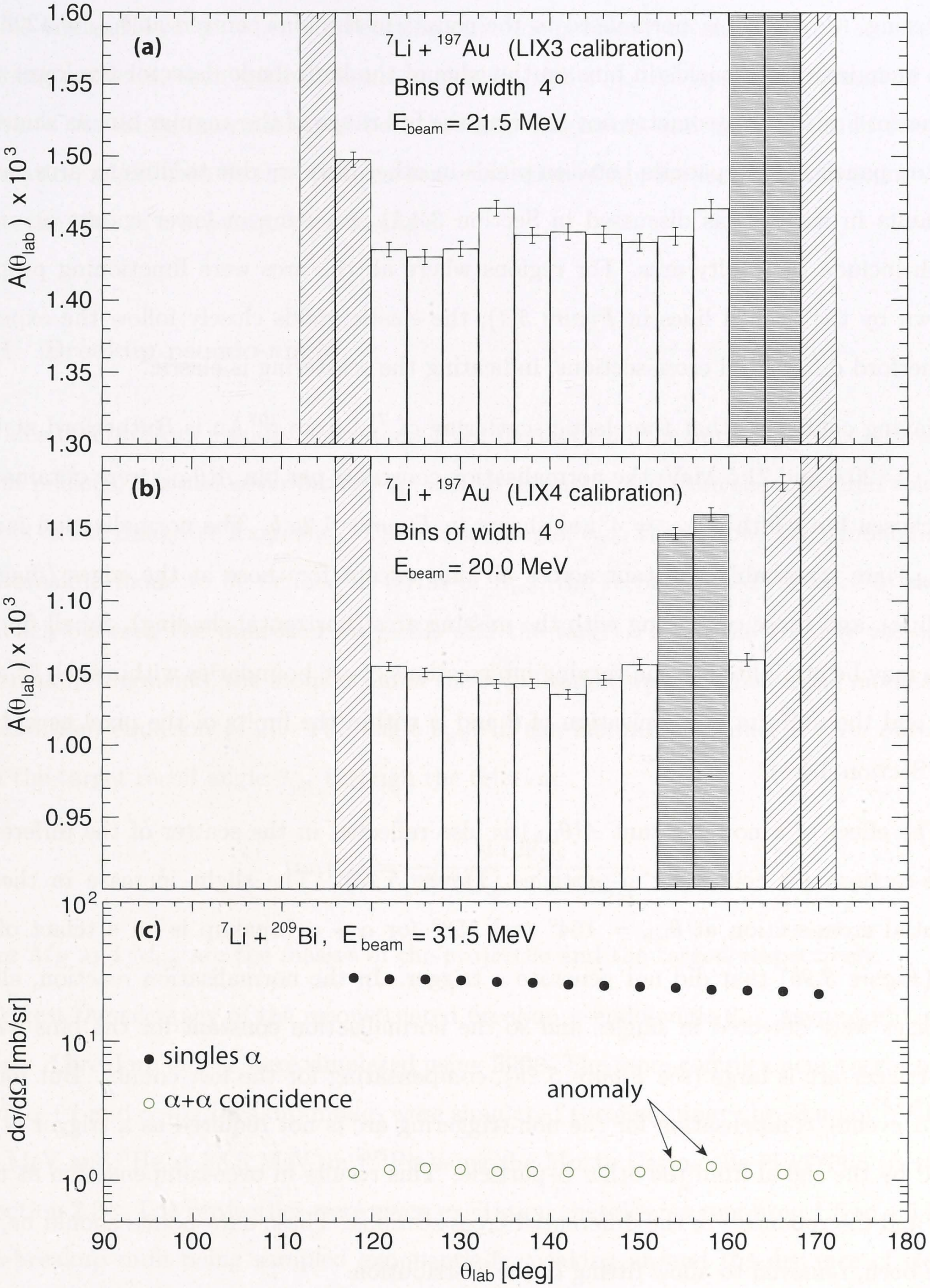

Figure 5.2: (a,b) Bin normalisation constant $A(\theta_{\mathrm{lab}})$ for the indicated runs obtained by measuring elastic scattering of ^{7}Li from ^{197}Au at $E_{\mathrm{beam}} = 21.5$ MeV and 20.0 MeV. (c) Differential cross-sections for α-singles and $\alpha + \alpha$ coincidences, from the reaction of ^{7}Li on ^{209}Bi at $E_{\mathrm{beam}} = 39.0$ MeV, as obtained using the $A(\theta_{\mathrm{lab}})$ values from the LIX4 normalisation. These differential cross-sections are not corrected for efficiency. Structures in the LIX4 normalisation constant cause the indicated anomaly in the distribution, as discussed in the text.

plot are the elastic counts expected from the differential cross-sections for Rutherford scattering, $(d\sigma/d\Omega)_{Ruth}$, normalised to the counts in the bins centred at $\theta_{\text{lab}} = 122°$. At both energies, elastic yields in bins on the edge of the lampshade detector are lower than Rutherford due to its geometry not covering the full range of the angular bin, as shown on the top panels. Discrepancies between yields in other bins are due to missing arcs caused by faults in wirings (as discussed in Section 3.4.1), resulting in lower counts at angles which include the faulty arcs. For regions where all the arcs were functioning properly (shown by the dashed lines in *Figure 5.1*), the elastic yields closely follow the expected Rutherford differential cross-sections, indicating the scattering is elastic.

Having confirmed that the elastic scattering of ^{7}Li from ^{197}Au is Rutherford at both $E_{\text{beam}} = 20.0$ and 21.5 MeV, the normalisation constants per bin $A(\theta_{\text{lab}})$ were obtained for the chosen bin width $\Delta\theta_{\text{lab}} = 4°$, as shown in *Figures 5.2a,b*. The normalisation factors $A(\theta_{\text{lab}})$ are reasonably constant across all bins except for those at the edges (diagonal shading), and those coinciding with the missing arcs (horizontal shading). Small fluctuations may be attributed to the varying intersections of arc boundaries within each 4° angle bin, and the uniform randomisation of θ and ϕ within the limits of the pixel acceptance (see Section 3.4.1).

The effect of a non-constant $A(\theta_{\text{lab}})$ is also reflected in the scatter of the differential cross-sections for coincident α-particles (*Figure 5.2c*). The slight increase in the differential cross-section at $\theta_{\text{lab}} = 154°$ and 158° for $\alpha + \alpha$ breakup is an artefact of the arc (*Figure 3.9b*) that did not generate a trigger. In the normalisation reaction, elastic particles were detected in singles and so the normalisation constant for the bins with a non-trigger arc is large (see *Figure 5.2b*), compensating for the lost counts. But for the $\alpha + \alpha$ events, compensation for the non-triggering arc is not required as a trigger is provided by the signal from the other α-particle. This results in over-compensation at these bins and discrepancies in the differential cross-sections. These data points should be, and have been, removed to allow fitting of the distribution.

5.2 Determination of the distance of closest approach for breakup events

In reactions producing a single projectile-like nucleus, the angular distribution is naturally defined in terms of the detection angle θ_{lab} of that product. Thus the definition of a differential cross-section via equation (5.7) can be achieved in terms of this θ_{lab}. Also, the distance of closest approach of the projectile and target nuclei can be estimated based on this angle. However, when the reaction outcome is binary breakup then there are two outgoing particles, each with different angles $\theta_{i,j}$ and $\phi_{i,j}$. An appropriate angle θ that combines the angle information of both breakup fragments and therefore their reaction kinematics, might then be the optimum representation of $\theta_{\rm lab}$ for each breakup event. This led to the idea of a breakup "pseudo-angle".

5.2.1 Breakup pseudo-angle

The idea of a breakup pseudo-angle stems from the fact that the outgoing trajectory of the parent nucleus, if it had never broken-up, can be reconstructed from the measured velocity vectors of the daughter fragments. The pseudo-angle, $\theta_{\rm rec}$, then allows the probability of each breakup mode to be defined in terms of $R_{\rm rec}$, the reconstructed distance of closest approach between the unbroken projectile and the target. From the velocity vectors of the breakup fragments, the momentum of the recoil target was obtained using momentum conservation, equation (4.2). The angle $\theta_{\rm rec}$, in the laboratory frame, is then obtained from the target recoil angle $\theta_{\rm tgt}$ through the relation

$$\tan\theta_{\rm rec} = \frac{\sin 2\theta_{\rm tgt}}{M_P/M_{tgt} - \cos 2\theta_{\rm tgt}}, \tag{5.8}$$

where M_P and M_{tgt} are the masses of the projectile and the target, respectively.

To test the accuracy of the reconstructed breakup pseudo-angle $\theta_{\rm rec}$, asymptotic $\alpha+\alpha$ and $\alpha+d$ breakup modes were simulated using `BUGS`. The more complex near-target $\alpha+p$, $\alpha+d$, $\alpha+t$ and $\alpha+\alpha$ breakup modes were simulated through binary breakup of ^{5,6,7}Li at 29.0 MeV and ^{8}Be at 38.5 MeV on ^{208}Pb using the Monte Carlo code `PLATYPUS` (detailed in Section 2.3). The projectiles were given excitation energies ranging from 1.5 to 4.5 MeV with breakup radii being sampled exponentially, peaking around the distance of closest approach of each trajectory, both in the entrance and exit channels. Trajectories with impact parameters corresponding to angular momenta up to $50\hbar$ were considered.

From the simulations we know the expected $\theta_{\rm lab}$ for each trajectory, had the projectile not broken up. We also know the angles $\theta_{i,j}$ and $\phi_{i,j}$ of the breakup fragments. Hence we can reconstruct the breakup pseudo-angle $\theta_{\rm rec}$, in the laboratory frame, and compare it to the $\theta_{\rm lab}$ for the unbroken projectile. The deviation between the reconstructed angle $\theta_{\rm rec}$ and

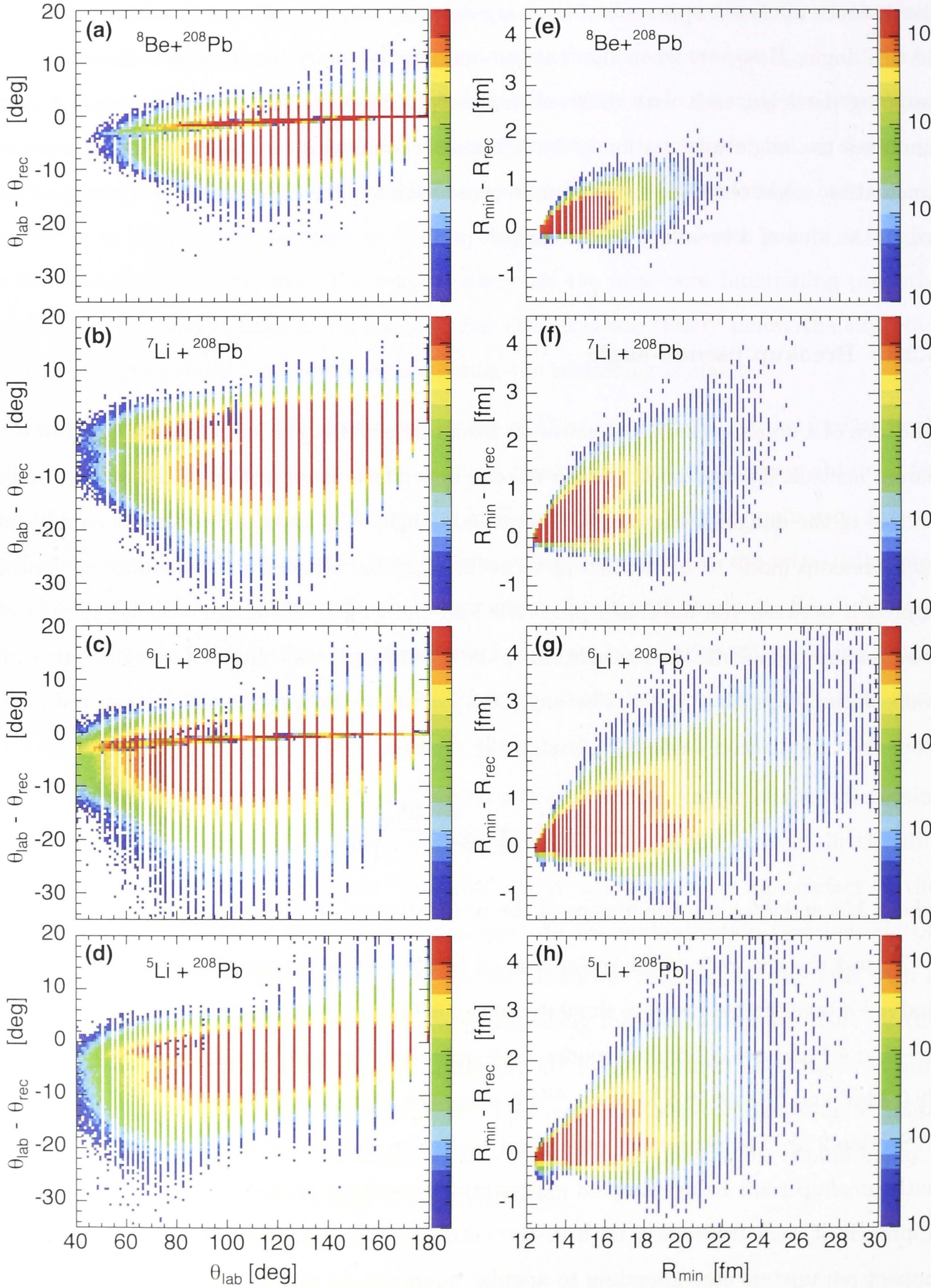

Figure 5.3: Simulated kinematics for breakup of ^{5,6,7}Li at 29.0 MeV, and ^{8}Be at 38.5 MeV, on ^{208}Pb. (left panels) Differences between the reconstructed breakup pseudo-angle θ_{rec} and the laboratory Rutherford scattering angle θ_{lab}, as a function of θ_{lab}. (right panels) Same scatterplots as on the right panel, but with θ_{lab} and θ_{rec} transformed into the associated distance of closest approach R_{min} and R_{rec} respectively.

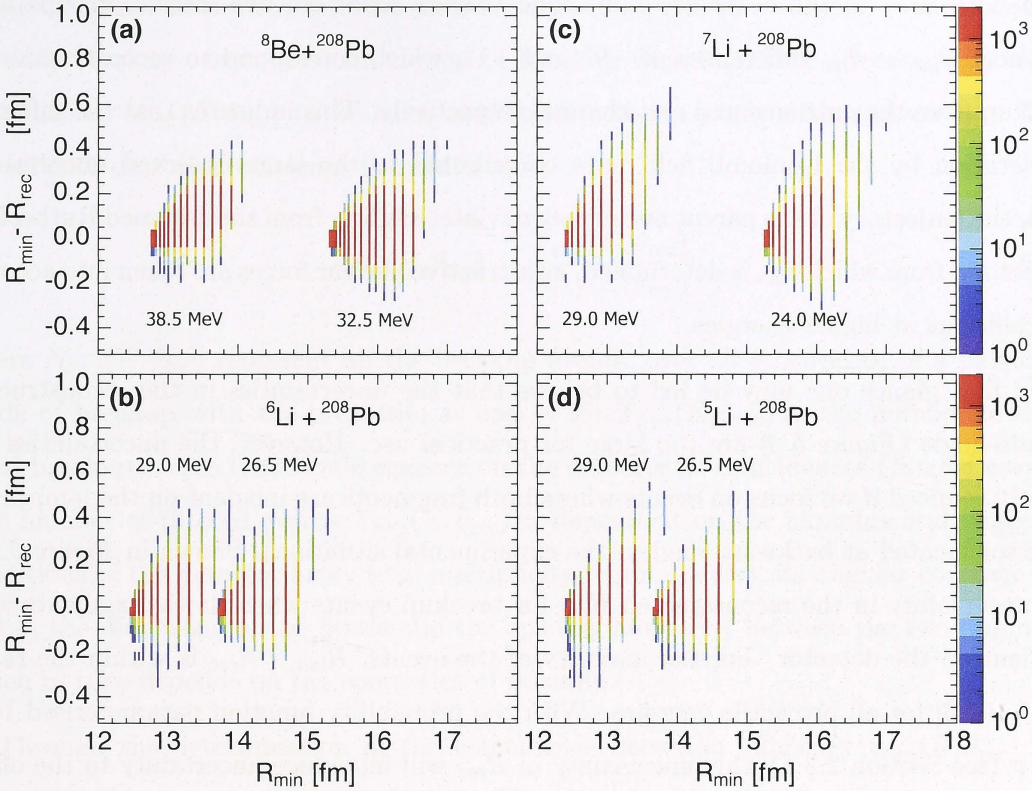

Figure 5.4: Uncertainty in the reconstructed $R_{\rm rec}$ for breakup events where both fragments were incident on the detector at back-angles. Breakup of ^{8}Be on ^{208}Pb was simulated at 32.5 and 38.5 MeV, and ^{5,6,7}Li on ^{208}Pb at 24.0 and 29.0 MeV.

the expected scattering angle $\theta_{\rm lab}$ is shown as a function of $\theta_{\rm lab}$ in *Figure 5.3* (left panel). This $\theta_{\rm rec}$ is transformed into the distance of closest approach $R_{\rm rec}$ between the parent nuclei and the target, had the former never broken up, and is shown in *Figure 5.3* (right panel) as a function of the expected distance $R_{\rm min}$.

For the $\alpha+\alpha$ (*Figure 5.3a*) and $\alpha+d$ (*Figure 5.3c*) breakup modes, the intense lines at $\theta_{\rm lab} - \theta_{\rm rec} \approx 0$ correspond to the reconstruction from asymptotic breakup (simulated by `BUGS`). As there is minimal fragment-target and fragment-fragment Coulomb interactions, the reconstruction of $\theta_{\rm rec}$ is almost perfect with slight overestimations for breakup at more forward angles. The randomisation of the position of the breakup fragments (see Section 3.4.1), however, introduces a ±3° uncertainty in the reconstructed $\theta_{\rm rec}$ for asymptotic breakup.

For all breakup close to the target, $\theta_{\rm rec}$ may be significantly overestimated for breakup at more forward angles. This uncertainty is a result of stochastic sampling of the excitation energy and the initial separation of the breakup fragments at the moment before breakup.

Most noticeably in the $\alpha + t$ breakup mode (*Figure 5.3b*) are two distinct groups with the mean $\theta_{\text{lab}} - \theta_{\text{rec}}$ differences of $-9°$ and $-1°$, which correspond to reconstruction of breakup from the entrance and exit channel respectively. This indicates that the different acceleration by the Coulomb field have contributed to the large observed uncertainty. Also, the trajectory of the parent nuclei may deviate* slightly from the assumed Rutherford trajectory, from which θ_{lab} is determined, as attractive nuclear forces are taken into account for collisions at higher energies.

At first glance one may be led to believe that the uncertainties in the reconstructed pseudo-angle (*Figure 5.3*) are too large for practical use. However, the uncertainties are greatly reduced if we focus on events where both fragments are incident on the lampshade detector located at backward angles (the experimental situation). Shown in *Figure 5.4* is the uncertainty in the reconstructed R_{rec} for breakup events where both fragments were incident on the detector. For the majority of the events, R_{min} - R_{rec} is within the range $[-0.1, +0.3]$ for all projectile energies. With the probability function parameterised by μ and ν (see Section 2.3.1), this uncertainty in R_{rec} will introduce uncertainty to the offset (strength) ν of the probability, but not its slope μ. The overall impact it has on the probability for each breakup mode is insignificant as will be seen in Section 5.5.2.

Using normalisation to Rutherford scattering (see Section 5.1) and the pseudo-angle concept, we obtain breakup yields as a function of R_{min}. To obtain absolute breakup probabilities, however, we need to account for the coincidence detection efficiency.

5.3 Procedures for efficiency determination

In grazing collisions, the probability of a given outcome (i) can be defined as the measured yield for that outcome divided by the yield (Y_{Ruth}) expected for Rutherford scattering at the given energy E and scattering angle θ

$$P_i(E, \theta) = \frac{Y_i(E, \theta)}{Y_{\text{Ruth}}(E, \theta)} \, . \tag{5.9}$$

Where the outcome is breakup, two complications arise. The first is how θ is defined, and the second is due to the fact that the efficiency for coincidence detection of fragments $i + j$ will in general be less than that for detecting an elastically scattered event.

---

*private communication with A. Diaz-Torres, the author of the simulation code `PLATYPUS`.

As discussed in Section 5.2, the pseudo-angle (θ_{rec}) allows a value of θ to be defined for each breakup event. The simulation of breakup with `PLATYPUS` (Section 5.3) allows an efficiency $\epsilon_{i+j}(E, \theta_{\mathrm{rec}})$ to be calculated for a breakup event with a given θ_{rec}. This coincidence detection efficiency is defined as

$$\epsilon_{i+j}(E, \theta_{\mathrm{rec}}) = \frac{\Upsilon_{i+j}(E, \theta_{\mathrm{rec}})}{N_{i+j}(E, \theta_{\mathrm{rec}})}, \tag{5.10}$$

where $N_{i+j}(E, \theta_{\mathrm{rec}})$ represent all the breakup events, over all θ_{rec} and ϕ, of a particular mode of breakup with the projectile at energy E; $\Upsilon_{i+j}(E, \theta_{\mathrm{rec}})$ is the number of simulated breakup events that would register on the detector as coincidences (*filtered events*). The number of filtered events $\Upsilon_{i+j}(E, \theta_{\mathrm{rec}})$ is dependent on the experimental triggering conditions of the detector array (e.g. multiplicity requirements), its angular coverage in θ and ϕ, the dimension of the pixels and the opening angle Θ_{12} between the two fragments which in turn depends on the energetics of breakup.

Through the determination of the coincidence detection efficiency $\epsilon_{i+j}(E, \theta_{\mathrm{rec}})$, the probability for a particular mode $(i + j)$ of breakup can then be obtained from the coincidence yield $Y_{i+j}(E, \theta_{\mathrm{rec}})$ with the equation

$$P_{i+j}(E, \theta_{\mathrm{rec}}) = \frac{1}{\epsilon_{i+j}(E, \theta_{\mathrm{rec}})} \frac{Y_{i+j}(E, \theta_{\mathrm{rec}})}{Y_{\mathrm{Ruth}}(E, \theta_{\mathrm{rec}})}. \tag{5.11}$$

This quantity can then be used to obtain the breakup probability function, required for the prediction of reaction outcomes at above-barrier energies as discussed in Sections 5.5 and 5.6.

This procedure does not distinguish between events with high and low E_{rel}, which is critical in separating prompt breakup from delayed breakup. To separate breakup events based on E_{rel}, we need to obtain the absolute yields also as a function of E_{rel}. We therefore define an efficiency in E_{rel}, called the *E_{rel}-efficiency*, as

$$\eta_{i+j}(E, E_{\mathrm{rel}}) = \frac{\Upsilon_{i+j}(E, E_{\mathrm{rel}})}{N_{i+j}(E, E_{\mathrm{rel}})}, \tag{5.12}$$

which is the ratio between the number of filtered events, at a given E_{rel}, and the total number of breakup events unfiltered by the detector system. This efficiency is effectively integrated over all θ_{rec} and can be used to determine both the prompt and delayed breakup probabilities.

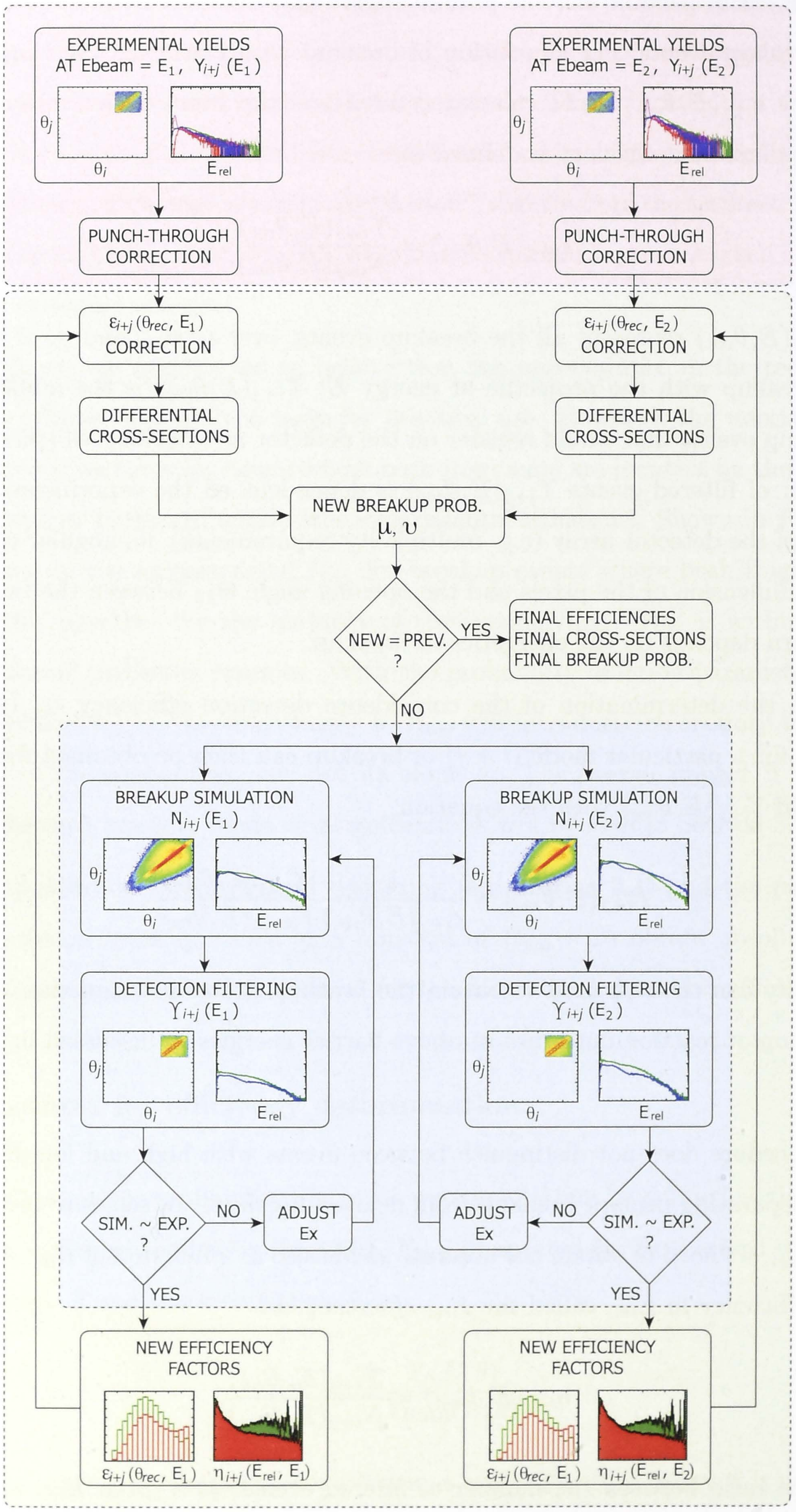

Figure 5.5: Illustration of the iterative processes involved in obtaining the final detection efficiency, and thus the breakup probability functions, for each breakup mode.

Obtaining these efficiency factors experimentally is a "chicken and egg" problem. Determining ϵ_{i+j} and η_{i+j} requires a knowledge of N_{i+j}, the very unknown variable that we wish to obtain. The only possible way to estimate these efficiencies is through iterative Monte Carlo simulation of breakup kinematics, which are as close as possible to the real kinematical conditions. In reality this condition is difficult to achieve as realistic models of breakup do not yet exist. We have therefore taken an empirical approach, where simulations based on the three-dimensional classical trajectory model code `PLATYPUS` are compared with experimentally obtained observables, namely the angles and relative energy of the breakup fragments.

The reliability of `PLATYPUS` has been verified elsewhere [32, 86] through the consistent description of below barrier breakup and above-barrier incomplete fusion for a ^{9}Be projectile. In this work, however, to ensure the simulated breakup kinematics reflects the physical conditions as closely as possible, the energy available for each breakup mode is changed and the simulation are repeated if the simulations do not match the experimental observables. This procedure is carried out for each breakup mode until a good agreement (see *Figure 5.7*) is obtained between the simulations and the experimental observables. This method ensures that we get the best estimate of the efficiency factors.

The steps involved in obtaining the efficiencies are illustrated in *Figure 5.5*. In the *first stage* (red block), the yields for the $\alpha + p$, $\alpha + d$, and $\alpha + t$ breakup modes are corrected for loss due to punch-through of high energy Z=1 particles incident on the non-telescope part of the lampshade detector. This correction process is described in Section 5.3.1. In the *second stage* (green and blue block), the input parameters for the simulation code `PLATYPUS` are optimised as described in Section 5.3.2.

5.3.1 High energy Z=1 punch-through correction

In the LIX3 runs, the lampshade detector was arranged in the A|C-D|B telescopic configuration (see *Figure 3.4b*). For breakup events involving high energy Z=1 particles, only the central C-D telescope registers the correct Q-value for events involving high energy Z=1 particles. Such particles are not stopped in detectors A and B, and they do not have a second detector stacked behind them. Thus, the lampshade detector does not register the full energy of all Z=1 particles, which means we would not get the correct relative energy E_{rel} for events where Z=1 particles punch through detectors A and B. Since the

E_{rel} analysis plays an important part in this work, this fractional loss of events needs to be corrected.

The particles that punch-through detectors A and B are clearly seen in the E_1 vs. E_2 plots (e.g. see *Figure 4.1*), where they appear in arc-like bands that extend from bands comprising of events where full energy is detected. Correction for the Z=1 events that lie in the arc-like bands can be made using 2D-gates in E_1 vs. E_2, but the presence of background makes this method unreliable compared to the method which will be described next.

It is important to note that detectors A and B cover the same θ range as the central C-D telescope, and only differ in that A and B together cover twice the azimuthal angle ϕ compared to that of the C-D telescope. Thus for a breakup mode $\alpha + i$ $(i = p, d, t)$ if both particles are detected and identified in the central C-D telescope, then the same number would be expected to be detected by each of the detectors A and B (had they also been configured as $\Delta E - E$ telescope elements). This correction means:

$$\begin{array}{l}\text{Total } \alpha + i \text{ coincidence pairs}\\ \text{detected by the same detector}\end{array} = 3\times \begin{array}{l}\alpha + i \text{ pairs detected}\\ \text{in the C-D telescope}\end{array} \tag{5.13}$$

An example of the E_{rel}-spectrum for the reaction of ^{6}Li with ^{208}Pb at $E_{\mathrm{beam}} = 29.0$ MeV is shown in *Figure 5.6*. The $\alpha + i$ coincident pairs detected by the C-D telescope are shown by the dashed magenta line.

Corrections are also needed for $\alpha + i$ coincident events where fragment i $(= p, d, t)$ is incident on detector A or B, with the α-particle detected in the C-D telescope. The knowledge of the complementary events where fragment i is detected in the C-D telescope and the α-particle in detector A or B allows the correction:

$$\begin{array}{l}\text{Total } \alpha + i \text{ coincidence pairs}\\ \text{with } \alpha \text{ detected in one detector}\\ \text{and } i \text{ in the other}\end{array} = 2\times \begin{array}{l}\alpha + i \text{ pairs with } \alpha \text{ detected}\\ \text{in A or B and } i \text{ detected in}\\ \text{the C-D telescope}\end{array} \tag{5.14}$$

The E_{rel}-spectrum for $\alpha + d$ coincidence pairs where the particle i incident on the C-D telescope, and the α-particle on either detector A or B, is shown by the full magenta line in *Figure 5.6*. The final E_{rel}-spectrum for the $\alpha + i$ coincidence events (example shown by the full line in *Figure 5.6*) is then the E_{rel}-spectrum where both α,i were stopped in the detectors (dotted black line in *Figure 5.6*) plus that from equations (5.13) and (5.14).

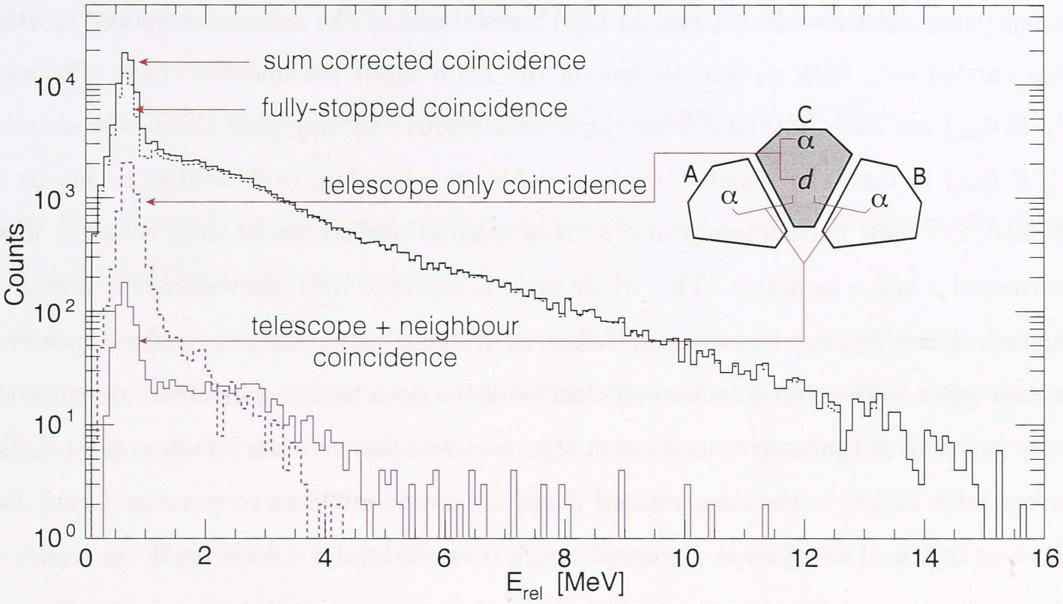

Figure 5.6: E_{rel} spectra for $\alpha + d$ breakup from the reaction of ^{6}Li with ^{208}Pb at $E_{\mathrm{beam}} = 29.0$ MeV. The black dashed line shows kinematically identified $\alpha + d$ coincidences where both fragments are stopped in the detectors. The dashed magenta line shows coincidences where both coincident particles were incident on the same C-D telescope element. The full magenta line shows coincidences where a deuteron is identified in the C-D telescope element, and the α-particle is detected in the neighbouring element A or B. The black solid line is the final corrected E_{rel}-spectrum.

5.3.2 Optimising `PLATYPUS` inputs

The code `PLATYPUS` requires as input the breakup probability as a function of distance of closest approach R_{min} between the projectile and target nucleus for each breakup mode. This is parameterised in form of an exponential function,

$$P_{i+j}(R_{min}) = e^{(\nu - \mu R_{\mathrm{min}})} \,. \tag{5.15}$$

To obtain the parameters ν, μ, the breakup probabilities $P_{i+j}(E, \theta_{\mathrm{rec}})$ were obtained from the yields $Y_{i+j}(E, \theta_{\mathrm{rec}})$ in each $\Delta\theta_{\mathrm{lab}} = 4°$ bin, measured at sub-barrier energies. This energy and pseudo-angle dependent probability $P_{i+j}(E, \theta_{\mathrm{rec}})$ was then converted to the radial-dependent probability $P_{i+j}(R_{\mathrm{min}})$ using equation (2.9). Fitting $P_{i+j}(R_{\mathrm{min}})$ by an exponential function, equation (5.15), result in determination of the two parameters ν and μ.

As shown in *Figure 5.5 (blue block)*, it is assumed initially that nothing is known about the detector response and thus $\epsilon_{i+j}(E, \theta_{\text{rec}})$ was set to 1/3, uniformly across all θ_{rec}, reflecting the ϕ coverage. This leads to an initial set of breakup probability function parameters (μ_0, ν_0) using equations (5.11) and (5.15). Simulations of the detector response are then again carried out, with μ_0 and ν_0 among the main input parameters. New efficiencies $\epsilon_{i+j}(E, \theta_{\text{rec}})$ are then obtained from these simulations. By applying the newly obtained $\epsilon_{i+j}(E, \theta_{\text{rec}})$ to the experimental breakup yields, new breakup probabilities functions are obtained, i.e. new parameters μ and ν. New simulations are performed, with the newly determined μ and ν as inputs. This whole cycle is repeated until convergence of μ and ν is achieved. The efficiency factors $\epsilon_{i+j}(E, \theta_{\text{rec}})$ at which convergence of μ and ν is achieved, are then taken as the true detection efficiencies of the detector for coincidence detection for binary breakup of the parent nuclei at energy E. The other efficiency factor, $\eta_{i+j}(E, E_{\text{rel}})$ (see equation (5.12), is then determined based on the calculations to give the $\epsilon_{i+j}(E, \theta_{\text{rec}})$ efficiency factor. This process discussed above is carried out for each break up mode.

5.3.3 Breakup simulation

The ^{6}Li $\rightarrow \alpha + d$ breakup mode was simulated for incident ^{6}Li at energies of 26.5 and 29.0 MeV, which are the same energies at which measurements were made. Since `PLATYPUS` does not handle transfer leading to breakup, the breakup of ^{6}Li into $\alpha + p$ was simulated using ^{5}Li as a projectile, also at energies 26.5 and 29.0 MeV, which gives the same R_{min} between ^{5}Li and the target as compared to ^{6}Li and the same target. As for the ^{7}Li $\rightarrow \alpha + t$ breakup, simulation were done for the ^{7}Li projectile at 24.0 and 29.0 MeV, matching the experimental beam energies. The $\alpha+\alpha$ breakup that follows p-pickup by ^{7}Li was simulated using ^{8}Be as the parent nuclei. However, it is necessary to keep ^{8}Be on the same trajectory as that of ^{6,7}Li, since `PLATYPUS` samples breakup radii R_{BU} along the trajectory of the parent projectile.

Take for example the ^{208}Pb(^{7}Li,^{7}Li)^{208}Pb reaction at 29.0 MeV where for a head-on collision R_{min} is 12.39 fm. To simulate the $\alpha + \alpha$ breakup following the p-pickup reaction ^{208}Pb(^{7}Li,2α)^{207}Tl, the associated ^{207}Tl(^{8}Be,2α)^{207}Tl reaction requires a projectile energy of 38.5 MeV for $R_{\text{min}} = 12.41$ fm. The extra 9.5 MeV, required for matching R_{min}, coincides with the optimum experimental Q-value (see *Figure 4.10b*).

Samples of $N_{i+j,\ell} = 5000(2\ell+1)P_{\text{BU},\ell}$ breakup events of ^{5,6,7}Li and ^{8}Be projectiles were generated for partial wave ℓ, where $P_{\mathrm{BU},\ell}$ is determined by the input parameters ν, μ as described by the equation (2.16). Partial waves up to $\ell_{max} = 90$ have been included as the probability of breakup $P_{\mathrm{BU},\ell}$ becomes vanishingly small thereafter (10^{-8} of that of the s-wave). The total number of breakup events N_{i+j} included in the simulation is then

$$N_{i+j} = 2\sum_{\ell} 5000(2\ell+1)P_{\mathrm{BU},\ell} = \sum_{\ell} 5000(2\ell+1)\ e^{\nu-\mu R_{\mathrm{min}}}\,. \tag{5.16}$$

where R_{min} depends on the beam energy and partial wave ℓ, and ν, μ continually change after each iteration (until convergence).

Post-processing was then applied to filter these N_{i+j} events through the geometry of the detector, and the detection trigger conditions. Events with either of the $\theta_{1,2}$ and $\phi_{1,2}$ falling outside of the detector angular coverage (geometrical filtering) and events where both particles were incident on the same pixel, or the same arc, (trigger filtering) are all rejected. This results in the filtered Υ_{i+j} events, each with its own θ_{rec} and E_{rel}. Generally $N_{i+j} > 2 \times 10^6$ breakup events were used for most iterations with the number of filtered Υ_{i+j} events greater than 8% of N_{i+j}. The kinematics of these simulated yields are then compared to their experimental counterparts (see *Figure 5.5(blue block)*) for the optimisation of the excitation energy distribution of the parent projectile.

Comparison of experimental and simulated observables

Shown in *Figure 5.7* are comparisons between experimental observables for $\alpha + \alpha$ coincidence from the reaction of ^{7}Li with ^{208}Pb at $E_{\mathrm{beam}} = 29.0$ MeV (*Figures 5.7a,b,c*), and the corresponding simulated observables for $\alpha + \alpha$ breakup of ^{8}Be on ^{207}Tl at 38.4 MeV (*Figures 5.7d,e,f*). The experimental and simulated ϕ_1 vs. ϕ_2 scatterplots agree well with each other (*Figures 5.7a,d*). Agreement in $\theta_{1,2}$ can also be seen between the θ_1 vs. θ_2 scatterplots from experiment and simulation (*Figures 5.7b,e*). These agreements show that `PLATYPUS` describes the trajectories breakup fragments quite well. The distinct diagonal band, where $\theta_1 \approx \theta_2$, comprises ground-state decay of ^{8}Be as simulated using `BUGS`.

For reliable determination of $\eta_{i+j}(E_{\mathrm{rel}})$, discussed in Section 5.4.2, agreement between the experimental (*Figures 5.7c*) and the simulated (*Figures 5.7f*) E_{rel} spectrum is also important. This agreement was achieved by making between 0.9 to 1.5 MeV of energy available during the $\alpha + \alpha$ breakup of ^{8}Be.

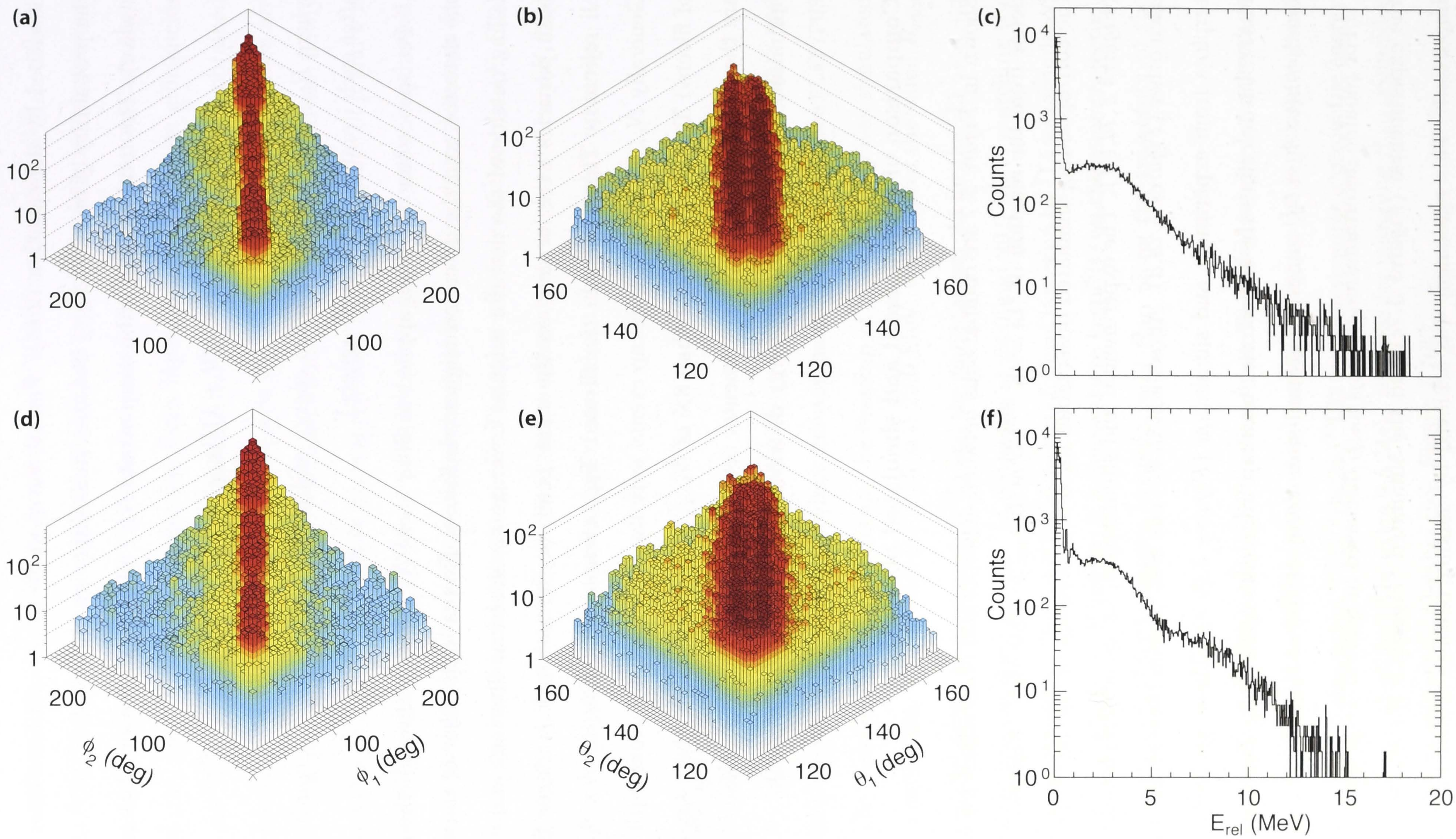

Figure 5.7: Comparisons between experimental observables for $\alpha + \alpha$ coincidence from the reaction of ^{7}Li on ^{208}Pb at $E_{\mathrm{beam}} = 29.0$ MeV (*top panel*), and the corresponding `PLATYPUS` simulation for $\alpha + \alpha$ breakup of ^{8}Be on ^{207}Tl at $E_{\mathrm{beam}} = 38.4$ MeV (*bottom panel*). The distinct diagonal band, where $\phi_1 \approx \phi_2$ or $\theta_1 \approx \theta_2$, comprises asymptotic breakup (ground-state decay) of ^{8}Be as simulated using `BUGS`. (a,d) ϕ_1 vs. ϕ_1 scatterplots. (b,e) θ_1 vs. θ_1 scatterplots. (c,e) E_{rel} spectra.

Angular distribution of breakup fragments

Shown in *Figure 5.8* are θ_1 vs. θ_2 scatterplots for both the experimental and simulated $\alpha + \alpha$ and $\alpha + t$ breakup from the reaction of ^{7}Li with ^{208}Pb at 29.0 MeV. The total N_{i+j} events plotted have contributions from both $N_{\alpha+\alpha}$ and $N_{\alpha+t}$ breakup events, which were determined by the ratio of the experimental yields. The potential parameters for this reaction and all others are taken from Refs. [81, 20], and where not available, from RIPL-2*, and are reproduced in Table A.1. The input files for this reaction and that of ^{6}Li with ^{208}Pb are shown in Appendix A.

In *Figure 5.8a*, the diagonal band comprises ground-state decay of ^{8}Be as simulated using `BUGS`. After post-processing, events comprising this band form the two diagonal bands in the θ_1 vs. θ_2 scatterplot of filtered events Υ_{i+j} (*Figure 5.8b*). The squares arise from pixelation of the detector. A reduction in intensity can be seen for events in the squares lying on the diagonal dashed line. This is because events where two particles are incident on the detector at the same θ_{lab} and ϕ_{lab}, i.e. the same pixel, will be considered as coincidence-one event and will not be registered on the scatterplot. The simulated $\theta_{1,2}$ distribution (*Figure 5.8b*) is very similar to that measured experimentally (*Figure 5.8c*).

From the angular distribution of the breakup fragments (see *Figure 5.8*), the differential cross-section for α-particles and tritons can also be obtained as shown in *Figure 5.9*. The green solid line shows the angular distribution for α-particles produced via the $\alpha + t$ breakup mode, while the blue solid line shows the complementary tritons. The green dashed line denotes the differential cross-section of α-particles produced from the $\alpha + \alpha$ breakup mode. The full black line is the differential cross-section of the total α-particles produced, i.e. two α-particles from $\alpha + \alpha$ breakup plus one from $\alpha + t$ breakup. Overlaid are experimental distributions for singles tritons (filled triangles) and α-particles (filled circles), from the reaction of ^{7}Li with ^{208}Pb at $E_{\text{beam}} = 30.0$ MeV by Häusser *et al.* [46].

At $\theta_{\text{lab}} \geqslant 120^\circ$, the angular distribution of the $N_{\alpha+t}$ simulated tritons is in reasonable agreement with the experimental data. This shows the reliability of the input parameters to the code `PLATYPUS`, and that the simulated data is reliable enough for the determination of the detector efficiency at backward angles. The simulated total α-particles have a different angular distribution to that observed experimentally. Since the simulation only consider α-particles produced through binary breakup, this disagreement indicates that,

---

*RIPL-2 Optical Model Parameter Segment `http://www-nds.iaea.org/ripl-2/optical.html`

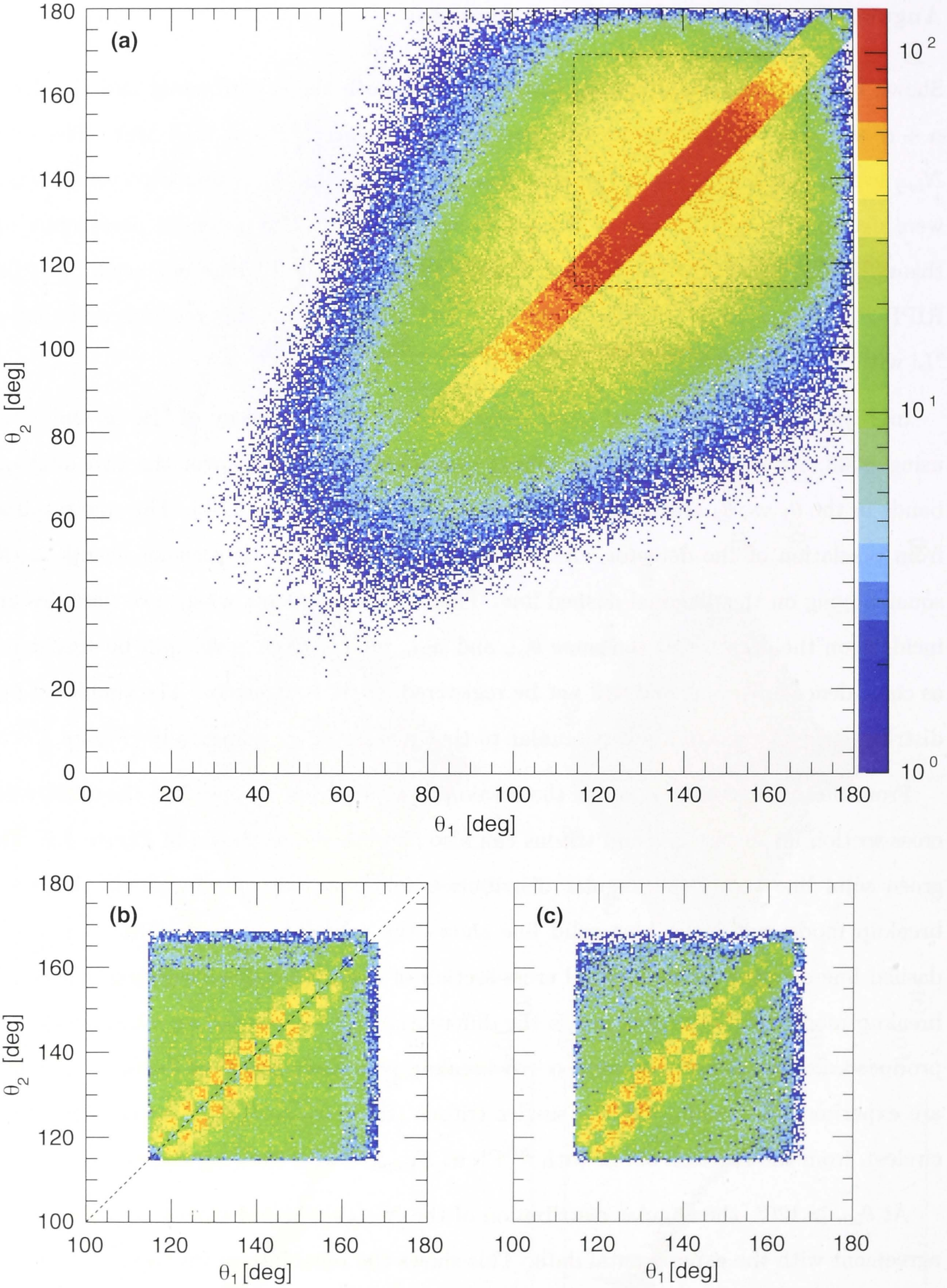

Figure 5.8: (a) θ_1 vs. θ_2 scatterplot for N_{i+j} breakup events simulated for the ^{208}Pb(^{7}Li,$\alpha + t$)^{208}Pb and ^{207}Tl(^{8}Be,$\alpha + \alpha$)^{207}Tl reactions. Dashed black lines outline the θ coverage of the the detector array. Events with correlated $\theta_{1,2}$ forming bands correspond to breakup of projectiles from the same partial wave ℓ. (b) Same plot as in (a) but only for the number of filtered events Υ_{i+j}, as dictated by the detector geometry and trigger conditions. (c) Scatterplot of θ_1 vs. θ_2 from the experimental yield Y_{i+j} of the reaction of ^{7}Li with ^{208}Pb at $E_{\mathrm{beam}} = 29.0$ MeV showing close correspondence with the Υ_{i+j} coincidences filtered from simulated events.

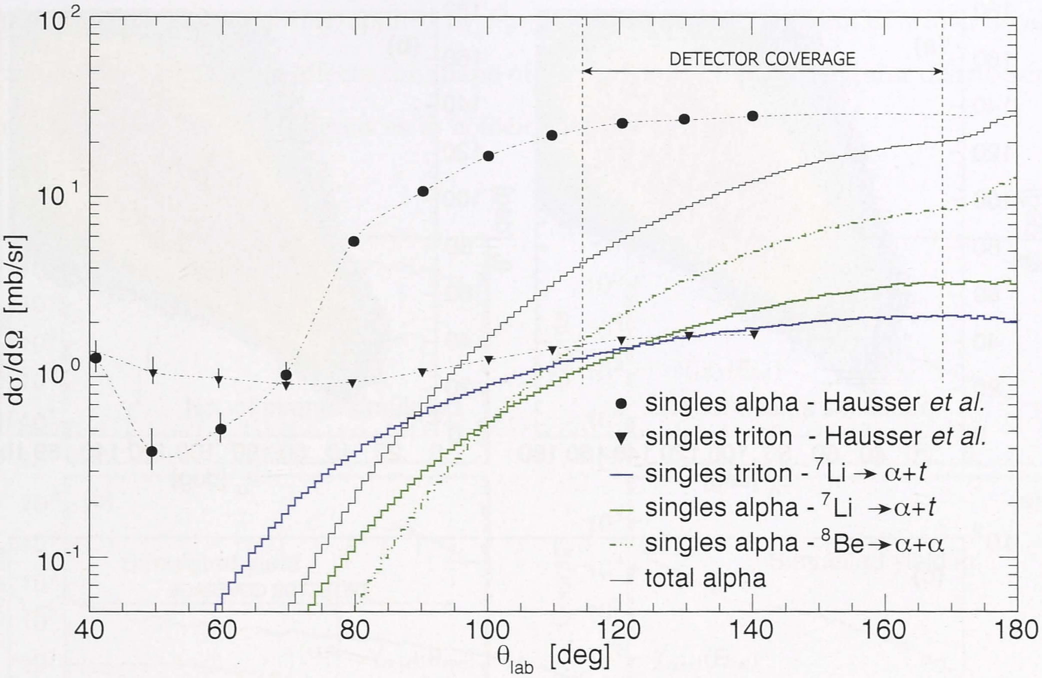

Figure 5.9: Angular distributions of simulated breakup fragments from the breakup reactions of ^{7}Li + ^{208}Pb at $E_{\text{beam}} = 29.0$ MeV and ^{8}Be + ^{207}Tl at $E_{\text{beam}} = 38.5$ MeV. Solid triangles and circles (with black lines to guide the eyes) are experimental angular distributions for singles triton and α-particles from the reaction of ^{7}Li + ^{208}Pb at $E_{\text{beam}} = 30.0$ MeV, from Häusser *et al.* [46].

quite possibly, the experimental yields for α-particles has contributions from other α-particle production mechanisms. It should also be noted that for $^7\text{Li} \to \alpha + t$ breakup, the shape of the angular distributions shows that tritons are more forward-focused than their complementary α-particles. This means coincidence detection for the $\alpha + t$ breakup mode will be less efficient than the $\alpha + \alpha$ breakup mode (which have identical angular distributions due to mass and charge symmetry.)

For the simulated breakup of ^{5,6}Li on ^{209,208}Pb at $E_{\text{beam}} = 29.0$ MeV, *Figure 5.10* shows the θ_1 vs. θ_2 scatterplots and the angular distributions of the breakup fragments. The different mass-to-charge ratios between the the $\alpha + p$ and $\alpha + d$ coincident fragments are reflected in the asymmetry about the 45° diagonal line in the θ_α vs. θ_p scatterplot (*Figure 5.10a*) and the θ_α vs. θ_d scatterplot (*Figure 5.10b*) respectively. Events with correlated $\theta_{1,2}$, forming bands in the scatterplots, correspond to breakup of ^{5,6}Li from the same partial wave ℓ. The differential cross-sections for the $^5\text{Li} \to \alpha + p$ breakup fragments (*Figure 5.10c*) shows that the protons (dashed red line) are more backward-focused compared to the complementary α-particles (dashed green line). For the $^6\text{Li} \to \alpha + d$ breakup, the deuterons are slightly more forward-focused as compared to the heavier complementary

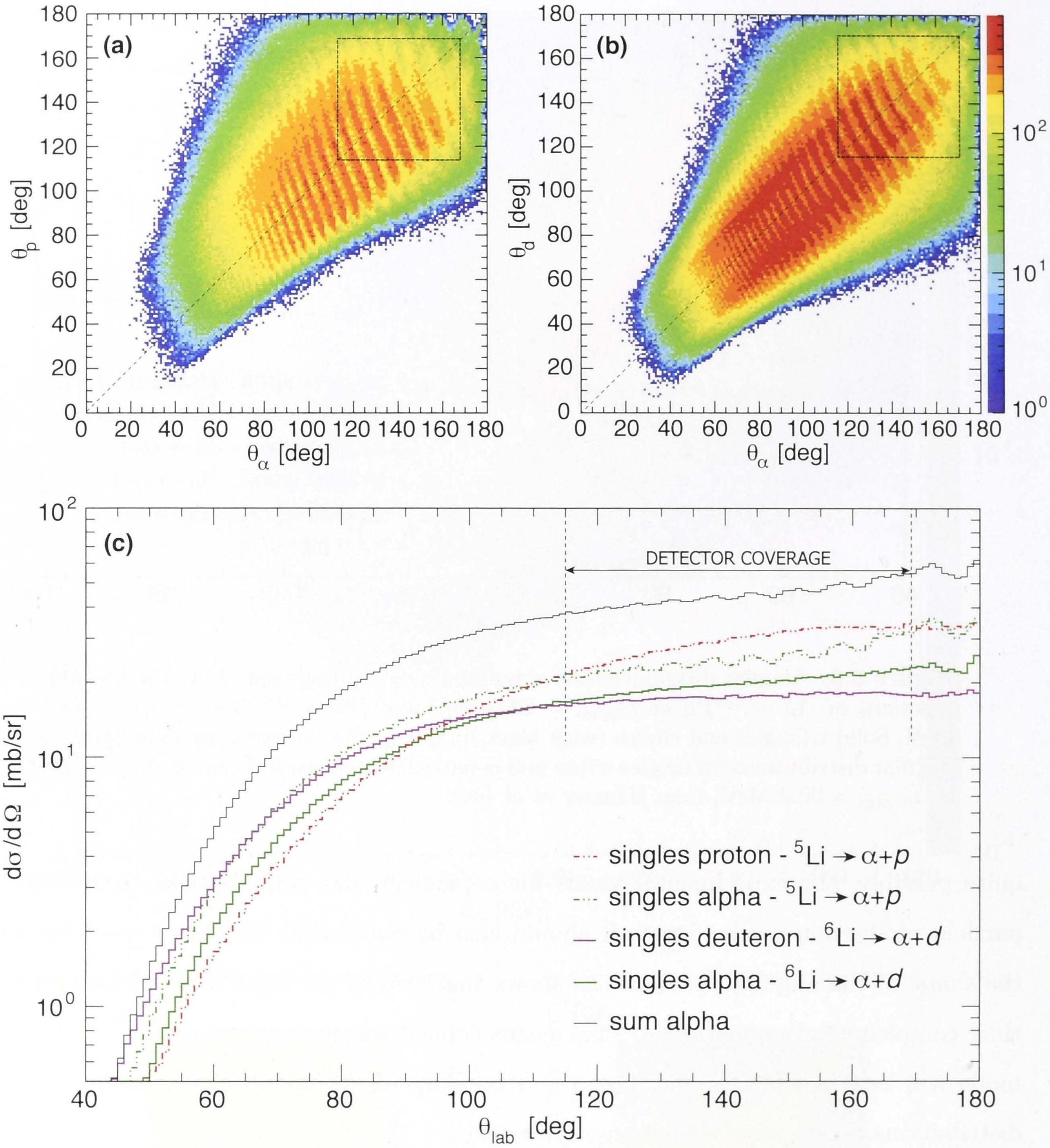

Figure 5.10: (top panel) Scatterplots of θ_α vs. θ_p and θ_α vs. θ_d from simulations of the breakup reactions ^{209}Pb(^{5}Li,$\alpha + p$)^{209}Pb and ^{208}Pb(^{6}Li,$\alpha + p$)^{208}Pb at $E_{\text{beam}} = 29.0$ MeV. The squares outlined by the dashed lines show the θ coverage of the detector array. (bottom panel) Angular distribution for protons (dashed red line), deuterons (magenta) and the total α-particle (black).

α-particles (and note that the tritons from $\alpha + t$ breakup are even more forward-focused compared to the α-particles). This is a result of the mass-assymetry of breakup and the difference in charge-to-mass ratio of the Z=1 breakup fragments. The former leads to different amount of energy being shared between the fragments at breakup (back to back emission), and the latter leads to different post-breakup acceleration in the target

Coulomb field. The weighting applied by $P_{\mathrm{BU},\ell}$ will determine the point at which breakup takes place, which in turn affects the shape of the breakup fragment angular distributions. These factors all lead to differences in coincidence detection efficiency.

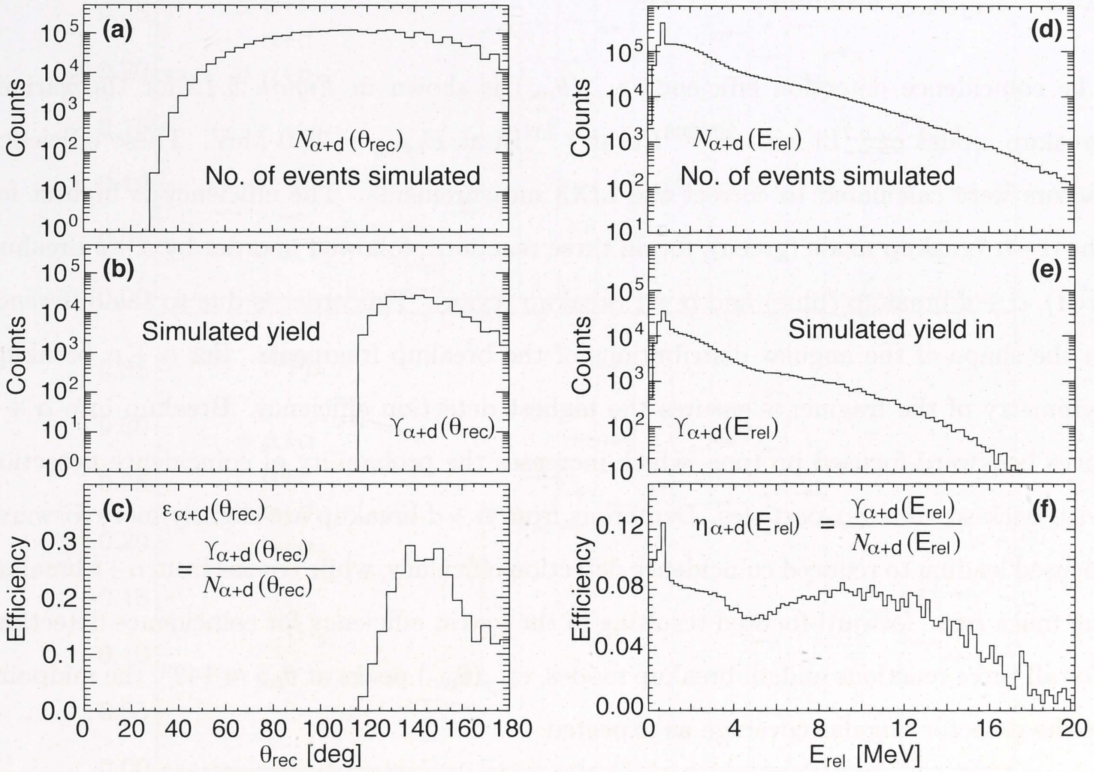

Figure 5.11: Determination of coincidence detection efficiencies the ^{6}Li → $\alpha + d$ breakup on ^{208}Pb at $E_{\mathrm{beam}} = 29.0$ MeV using `PLATYPUS` simulation. (a,d) The θ_{rec} and E_{rel} spectra for the $N_{\alpha+d}$ number of simulated breakup events. (b,e) The θ_{rec} and E_{rel} spectra for the filtered $\Upsilon_{\alpha+d}$ events. (c,f) Coincidence detection efficiencies $\epsilon(\theta_{\mathrm{rec}})$ and $\eta(E_{\mathrm{rel}})$ for the $\alpha + d$ breakup mode.

5.4 Coincidence detection efficiencies

Having ensured that the detailed properties of the simulated events for each breakup mode match those observed experimentally, the `PLATYPUS` simulations were used to obtain the two efficiency factors $\epsilon_{i+j}(E, \theta_{\mathrm{lab}})$ and $\eta_{i+j}(E, E_{\mathrm{rel}})$. These were determined by firstly simulating a total number (N_{i+j}) of $i + j$ breakup events as a function of θ_{rec} and E_{rel}, and then filtering these through the detector geometry and the triggering conditions of the system to obtain Υ_{i+j}, also as a function of θ_{rec} and E_{rel}. The detection efficiency is then Υ_{i+j}/N_{i+j}. These quantities are illustrated in *Figure 5.11* for the case of ^{6}Li → $\alpha + d$

breakup in reaction of ^{6}Li with ^{208}Pb at 29 MeV. The top panel shows the total number of $N_{\alpha+d}$ events simulated, the middle shows the filtered $\Upsilon_{\alpha+d}$ events, and taking their ratio ($\Upsilon_{\alpha+d}/N_{\alpha+d}$) gives the efficiencies shown in the bottom panel.

5.4.1 $\epsilon_{i+j}(\theta_{\text{rec}})$ efficiency

The coincidence detection efficiency $\epsilon_{i+j}(\theta_{\text{rec}})$ is shown in *Figure 5.12* for the various breakup modes of ^{6,7}Li with ^{207,208}Pb and ^{209}Bi at $E_{\text{beam}} = 29.0$ MeV. These efficiency factors were calculated to correct the LIX3 measurements. The efficiency is highest for the $\alpha+\alpha$ breakup mode (green), for all three reactions, followed in order by $\alpha+p$ breakup (red), $\alpha+d$ breakup (blue) and $\alpha+t$ breakup (cyan). This order is due to the difference in the shape of the angular distributions of the breakup fragments. For $\alpha+\alpha$ breakup, symmetry of the fragments ensures the highest detection efficiency. Breakup into $\alpha+p$ gives backward-focused protons, which increases the probability of coincidence detection with back-scattered α-particles. Deuterons from $\alpha+d$ breakup are slightly more forward-focused leading to reduced coincidence detection efficiency, while tritons from $\alpha+t$ breakup are much more forward-focused resulting in the lowest efficiency for coincidence detection. For all three reactions and all breakup modes, $\epsilon_{i+j}(\theta_{\text{rec}})$ peaks at $\theta_{\text{rec}} \approx 142^\circ$, the midpoint of the detector angular coverage as expected.

5.4.2 $\eta_{i+j}(E_{\text{rel}})$ efficiency

The coincidence detection efficiency $\eta_{i+j}(E_{\text{rel}})$ describes the probability of detecting a breakup fragment pair, with a given relative energy E_{rel}, out of all the breakup events producing fragments over all possible angles with that same E_{rel}. For the LIX3 experimental runs, the efficiencies $\eta_{i+j}(E_{\text{rel}})$ for the reactions of ^{6,7}Li with ^{207,208}Pb and ^{209}Bi at $E_{\text{beam}} = 29.0$ MeV are shown in *Figure 5.13.* For all breakup modes, breakup events with low E_{rel}, i.e. breakup from long-lived states, are detected more efficiently than prompt breakup with high E_{rel}. This is due to the fact that fragments from breakup of long-lived states have a smaller opening angle between them (than from short-lived states) and thus both fragments are more likely to be detected. The efficiency however drops for breakup events with $E_{\text{rel}} \approx 0$, since the opening angle between the coincident fragments becomes smaller than that of the size of each pixel – this renders them undetectable as a coincidence event.

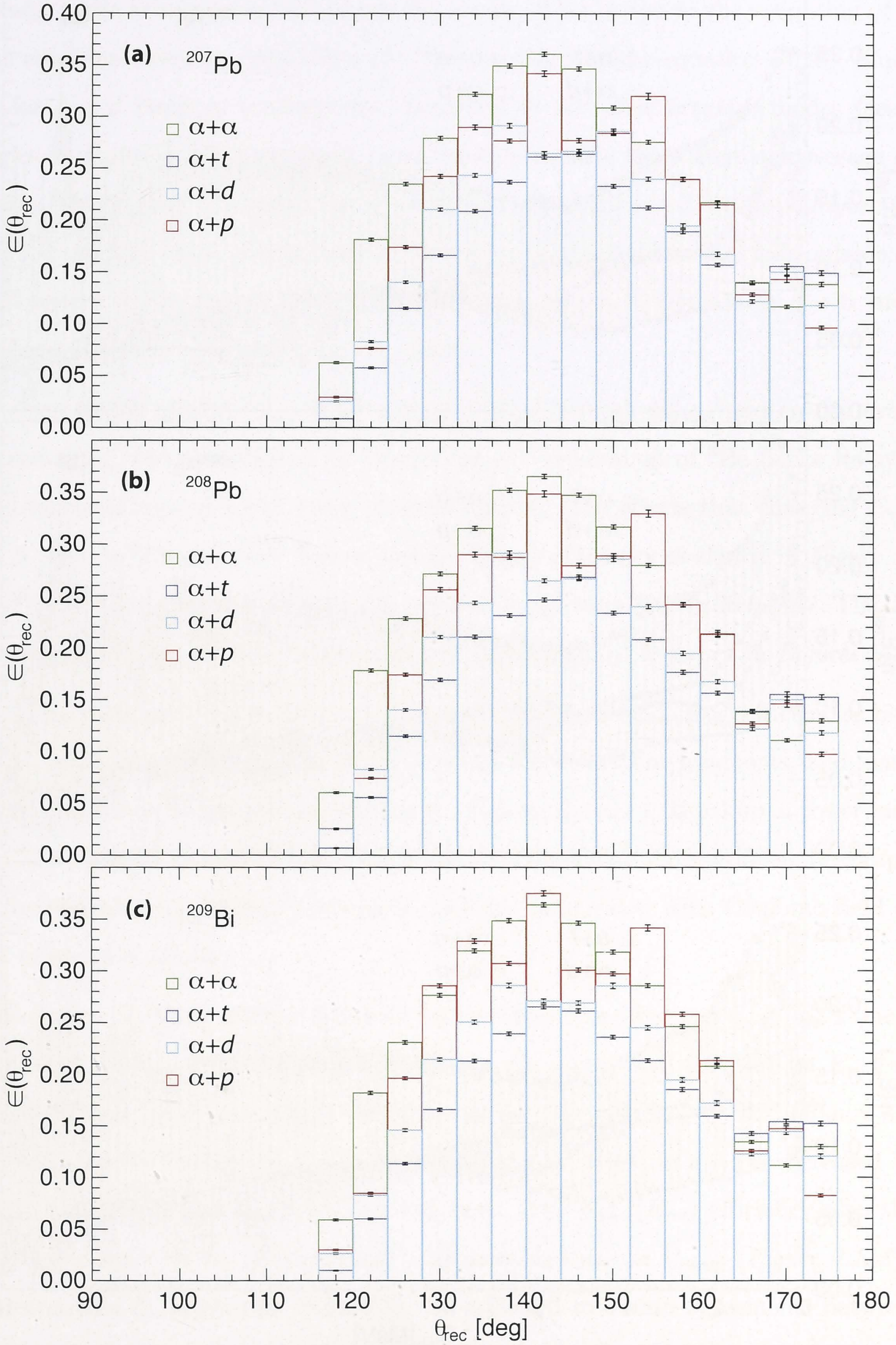

Figure 5.12: Coincidence detection efficiency $\epsilon_{i+j}(\theta_{\rm rec})$ for indicated breakup modes from the reactions of ^{6,7}Li with indicated targets at $E_{\rm beam}$ = 29.0 MeV. These efficiency factors are calculated for the LIX3 experimental runs, which use the A|C-D|B configuration of the lampshade detector. They also combine both the prompt and asymptotic components of breakup.

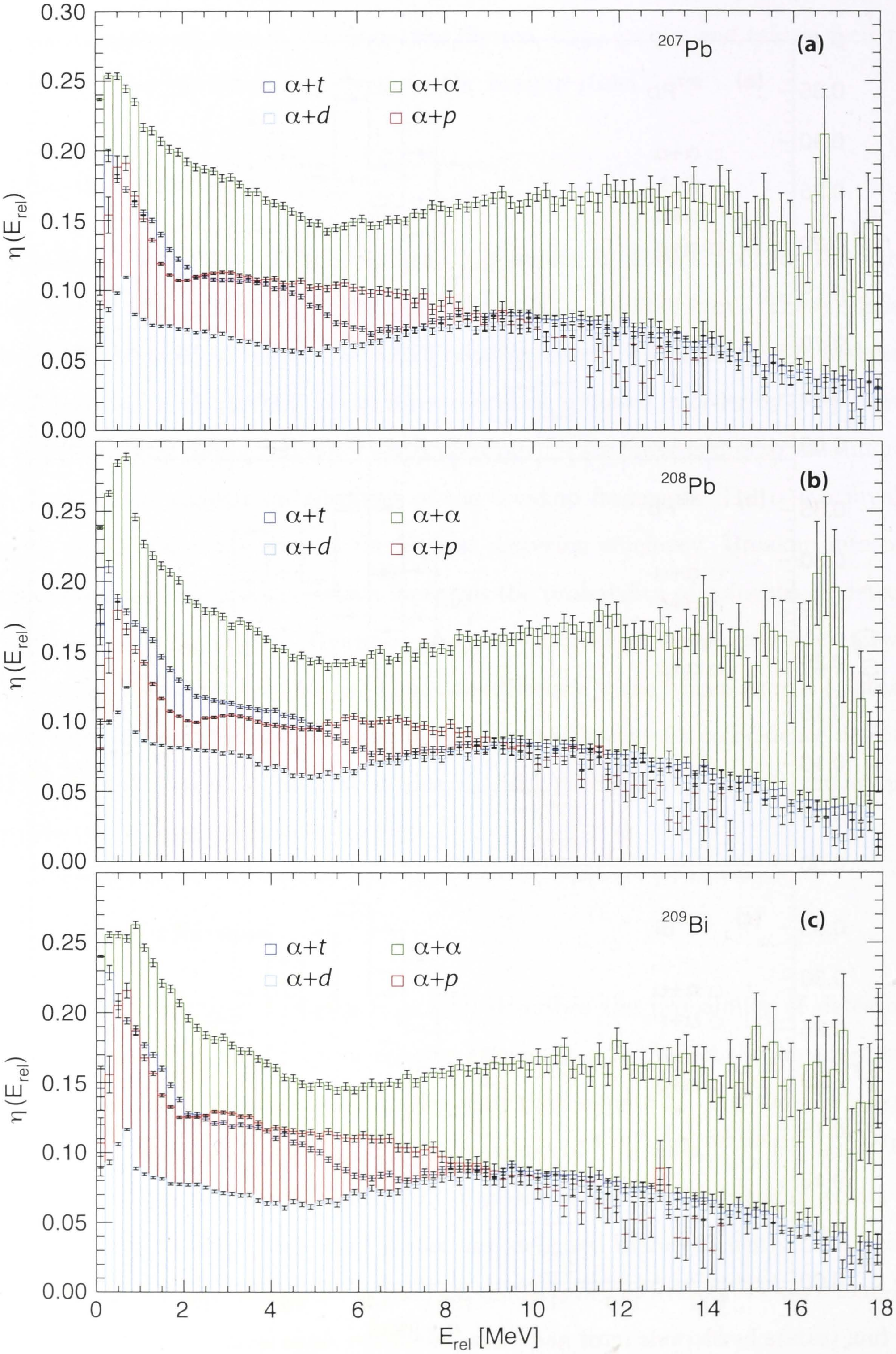

Figure 5.13: $\eta_{i+j}(E_{\rm rel})$ efficiencies for indicated breakup modes from the reactions of ^{6,7}Li with indicated targets at $E_{\rm beam}$ = 29.0 MeV. These efficiency factors are calculated for the LIX3 experimental runs, which use the A|C-D|B telescopic configuration of the lampshade detector. These total efficiency factors combine both the prompt and asymptotic components of breakup.

Among the different breakup modes, breakup into $\alpha + \alpha$ has the highest $\eta_{i+j}(E_{\text{rel}})$ efficiency, while breakup into $\alpha + d$ has the lowest. This is due to the weighting of $N_{\alpha+d}$ by the empirical breakup probability $e^{\nu-\mu R_{\text{min}}}$ as described by equation (5.16). Since the slope for $\alpha + d$ breakup is shallowest compared to all other breakup modes (see pink triangles in *Figure 5.15*), this places most breakup outside the θ angular coverage of the detector. This is most evident in the θ_1 vs. θ_2 scatterplot for $\alpha + d$ breakup (*Figure 5.10b*) and $\alpha + \alpha$ breakup (*Figure 5.8a*), where the majority of $\alpha + d$ breakup falls outside of the dashed square indicating the detector angular coverage in θ, while most $\alpha + \alpha$ breakup events are seen inside the same dashed square.

The sensitivity of both $\epsilon_{\alpha+\alpha}(\theta_{\text{rec}})$ and $\eta_{\alpha+\alpha}(E_{\text{rel}})$ to both E_{beam} and energy available for breakup E_{x} was investigated by simulating $\alpha + \alpha$ breakup of ^{8}Be (since its symmetry allows easier separation of these external effects). The effects that changing E_{x} from 0.9–1.5 MeV to 0.9–6.5 MeV has on the $\epsilon_{\alpha+\alpha}(\theta_{\text{rec}})$ efficiency is shown in *Figure 5.14a*, while *Figure 5.14b* shows the effects of increasing E_{beam} from 32.0 to 38.0 MeV. The dependency of $\eta_{\alpha+\alpha}(E_{\text{rel}})$ on the same variations in E_{x} and E_{beam} is shown in *Figures 5.14c,d*.

Breakup with lower E_{x} results in higher $\epsilon_{\alpha+\alpha}(\theta_{\text{rec}})$ and $\eta_{\alpha+\alpha}(E_{\text{rel}})$ efficiencies because lower E_{x} leads to smaller opening angle between the coincident fragments, and hence increased probability for coincidence detection (*Figures 5.14a,c*). Breakup at lower incident energy also lead to smaller opening angles as lower incident energy means breakup happens further from the target, resulting in minimal interaction with Coulomb field of the target (*Figures 5.14b,d*).

The energy E_{x} has a greater influence on the detection efficiency $\epsilon_{\alpha+\alpha}(\theta_{\text{rec}})$ than that of the energy E_{beam} of the incident projectile. An increase of 5.0 MeV in E_{x} leads to a 10% reduction in the $\epsilon_{\alpha+\alpha}(\theta_{\text{rec}})$ efficiency, at the bin with $\theta_{\text{rec}} = 142^\circ$ (*Figure 5.14b*). An increase of 6.0 MeV in E_{beam} on the onther hand results in a ~1% increased in the $\epsilon_{\alpha+\alpha}(\theta_{\text{rec}})$, for the same θ_{rec} bin (*Figure 5.14a*). The $\eta_{\alpha+\alpha}(E_{\text{rel}})$ efficiency also show a strong dependency on E_{x} (*Figure 5.14c*), far more so than on E_{beam} (*Figure 5.14d*). For this reason, the E_{x} input into `PLATYPUS` was adjusted to obtain agreements between the E_{rel}-spectrum for filtered events Υ_{i+j} and for the experimental yield Y_{i+j}. This ensures the kinematics of the simulated breakup is as close as possible to the real physical conditions.

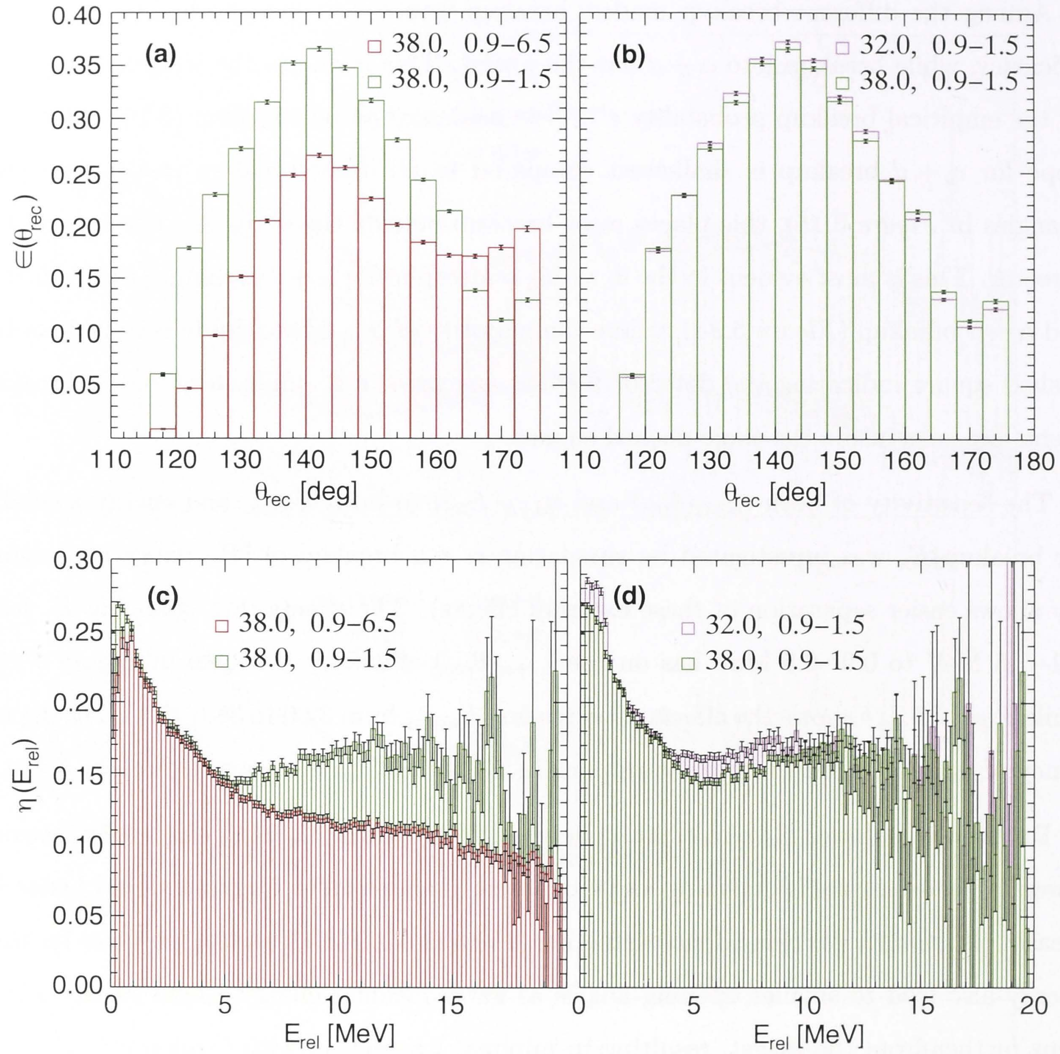

Figure 5.14: (top panel) The sensitivity of $\epsilon_{\alpha+\alpha}(\theta_{\text{rec}})$ to both (a) the energy E_{x} available during the $\alpha + \alpha$ breakup of ^{8}Be at $E_{\text{beam}} = 38.0$ MeV and (b) the energy E_{beam} of the ^{8}Be nucleus when E_{x} is fixed between 0.9 to 1.5 MeV. (bottom panel) The dependency of $\eta_{\alpha+\alpha}(\theta_{\text{rec}})$ on (a) the energy E_{x} and (b) E_{beam}. The kinematics of the $\alpha + \alpha$ breakup of ^{8}Be on ^{208}Tl was calculated using `PLATYPUS`, without contribution from asymptotic breakup.

5.5 Sub-barrier breakup probabilities

The reactions induced by ^{6,7}Li were measured at sub-barrier energies, at $E_{\text{beam}} = 26.5$ and 29.0 MeV for ^{6}Li and 24.0, 26.5 (^{7}Li + ^{207}Pb only) and 29.0 MeV for ^{7}Li. All major breakup modes were identifiable at all measured energies, as shown for example by the breakup yields for the reaction of ^{7}Li with ^{207}Pb in *Figure 4.14*. These measured coincidence yields $Y_{i+j}(E_{\text{beam}}, \theta_{\text{rec}})$ were then corrected for detection efficiencies (see Section 5.4, *Figure 5.12*) to obtain the absolute probabilities for each breakup mode using equation (5.11). Breakup probabilities as a function of the distance of closest approach R_{min} were then obtained by calculating R_{min} values using:

$$R_{\mathrm{min}} = \frac{Z_1 Z_2 e^2}{2E_{\mathrm{c.m.}}} \left(1 + \frac{1}{\sin \frac{\theta_{\mathrm{rec}}^{c.m.}}{2}}\right), \tag{5.17}$$

where Z_{i} are the charges of the projectile and target nuclei, $E_{\mathrm{c.m}}$ is the centre-of-mass energy and $\theta_{\mathrm{rec}}^{c.m.}$ is the breakup pseudo-angle in the centre-of-mass frame. It should be noted that for all the probabilities obtained in this section, the statistical uncertainty is smaller than the symbols used to indicate the data points.

For the ^{6}Li-induced reactions, the probabilities for each breakup mode are shown in *Figure 5.15* as a function of R_{min}. The $\alpha + d$ breakup mode is shown as pink triangles, $\alpha + p$ as red triangles and $\alpha + \alpha$ as green circles. Open symbols indicate the probability for the *prompt* component only, i.e. probability for breakup that can compete directly with complete fusion. The probabilities for each breakup mode are similar across all targets, suggesting that reaction processes are determined more by the properties of the projectile than of the target. Direct $\alpha + d$ breakup has the shallowest slope indicating the long-range Coulomb excitation triggering breakup of the projectile. The steeper slopes for breakup initiated by n-stripping ($\alpha + p$), and d-pickup ($\alpha + \alpha$), are indicative of the short-range nature of the nuclear interaction governing the transfer reactions. The data from the bins nearest to the edge of the detector fall below the fit, and is most prominent in the prompt component. This fall off is due to detector edge effects, where the efficiency decreases rapidly which makes the efficiency sensitive to small uncertainties in the simulations (*Figure 5.12*).

For the ^{7}Li-induced reactions, the probabilities for each breakup mode are shown in *Figure 5.16* as a function of R_{min}. Direct cluster-breakup into $\alpha + t$ is shown by blue triangles. Breakup initiated by n- and $2n$-stripping (leading to $\alpha + d$ and $\alpha + p$ breakup) and p-pickup ($\alpha + \alpha$) are shown as solid pink, red, and green triangles respectively. Open symbols show only the *prompt* component. Breakup into $\alpha + t$ has the shallowest slope, as expected for direct breakup triggered by long-range Coulomb excitation of ^{7}Li. The steep slopes for the $\alpha + \alpha$ and $\alpha + d$ breakup modes show the expected short-range nature of the nuclear interaction.

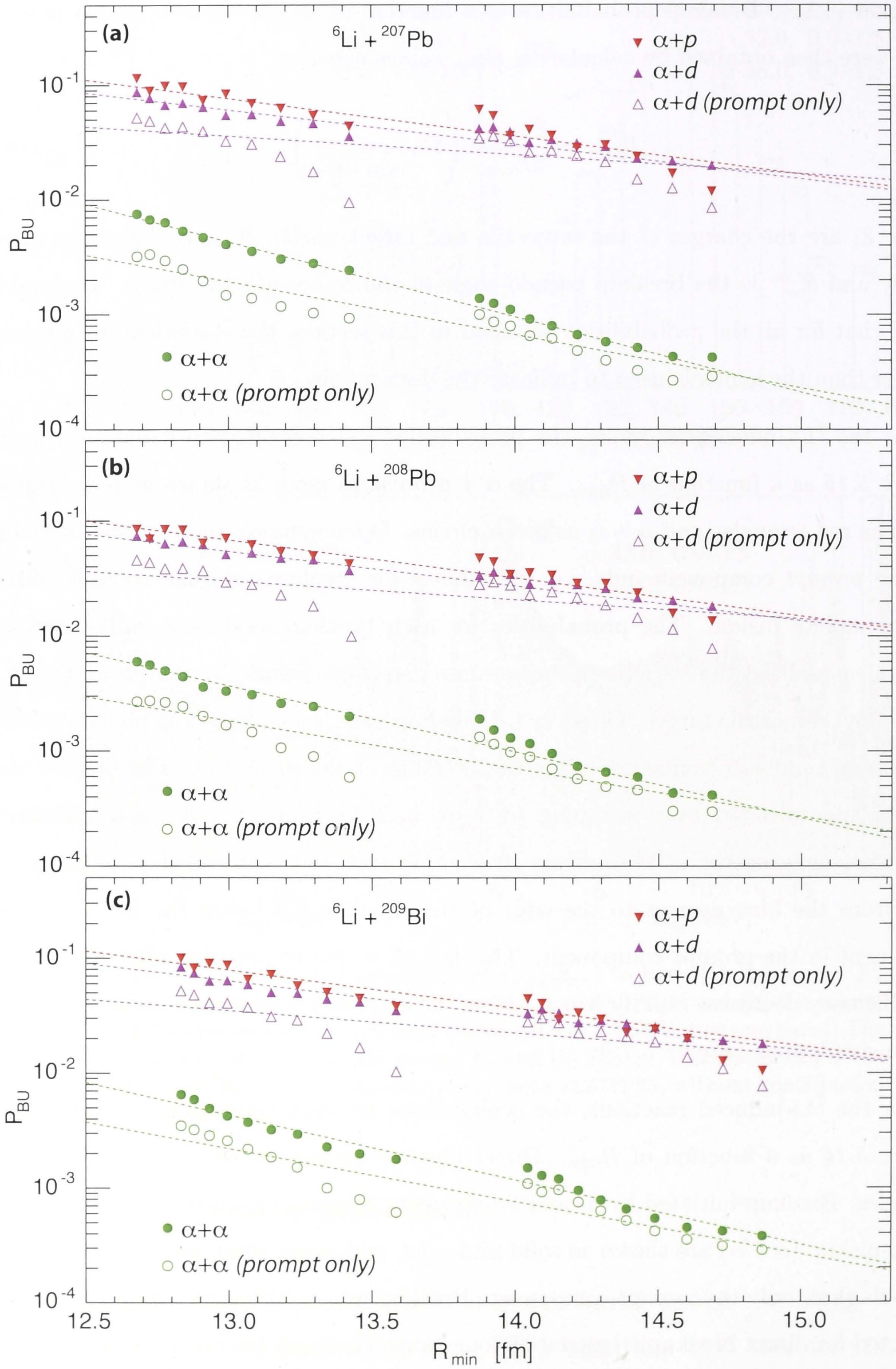

Figure 5.15: Probabilities for different breakup modes, as a function of $R_{\min}$, in the reactions of ^{6}Li with the indicated targets at sub-barrier energies. The dashed lines indicate the exponential line of best fit for each breakup mode.

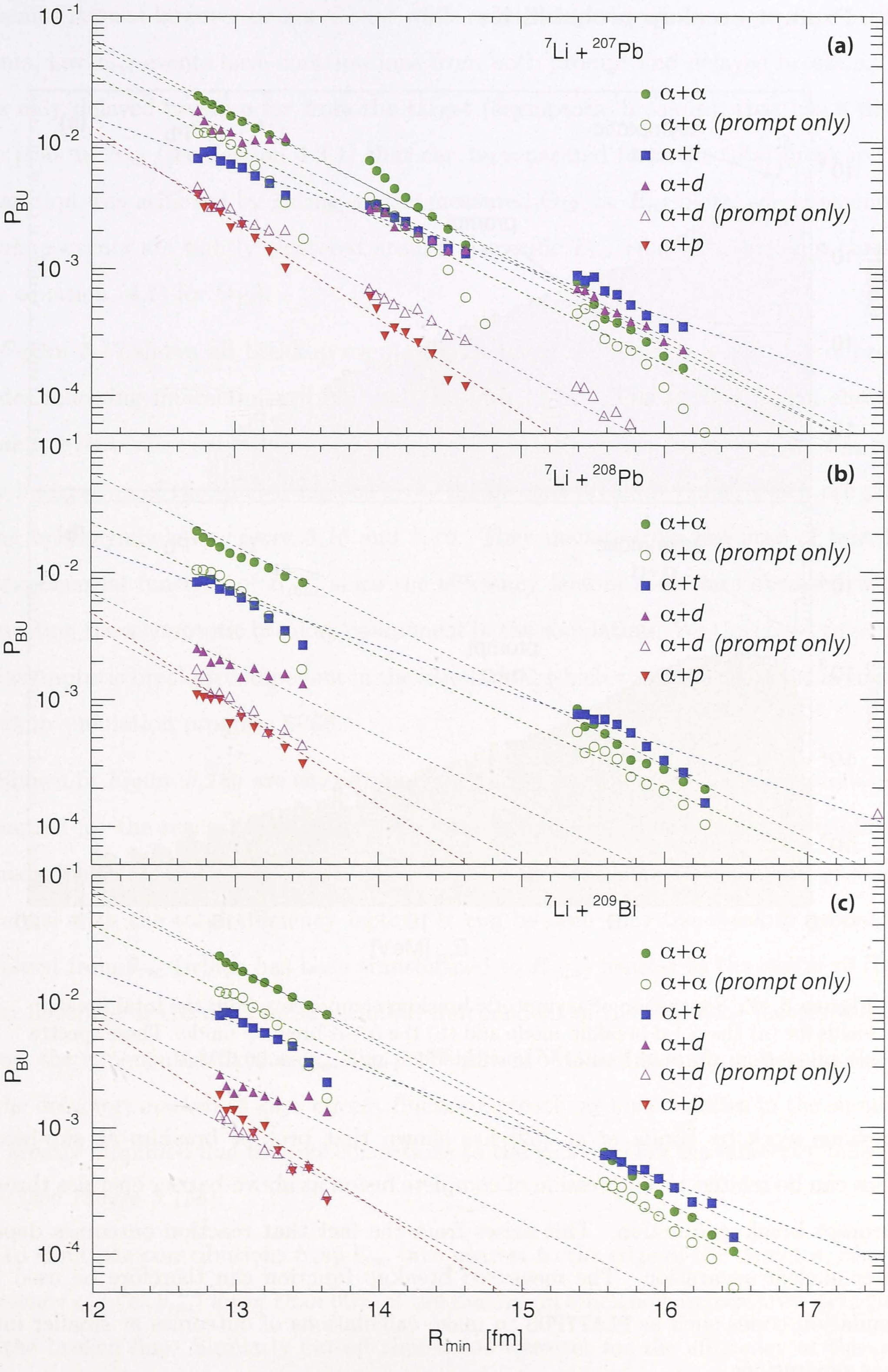

Figure 5.16: Probabilities for different breakup modes, as a function of R_{min}, in the reactions of ^{7}Li with the indicated targets at sub-barrier energies. The dashed lines indicate the exponential line of best fit for each breakup mode.

5.5.1 Prompt breakup probabilities

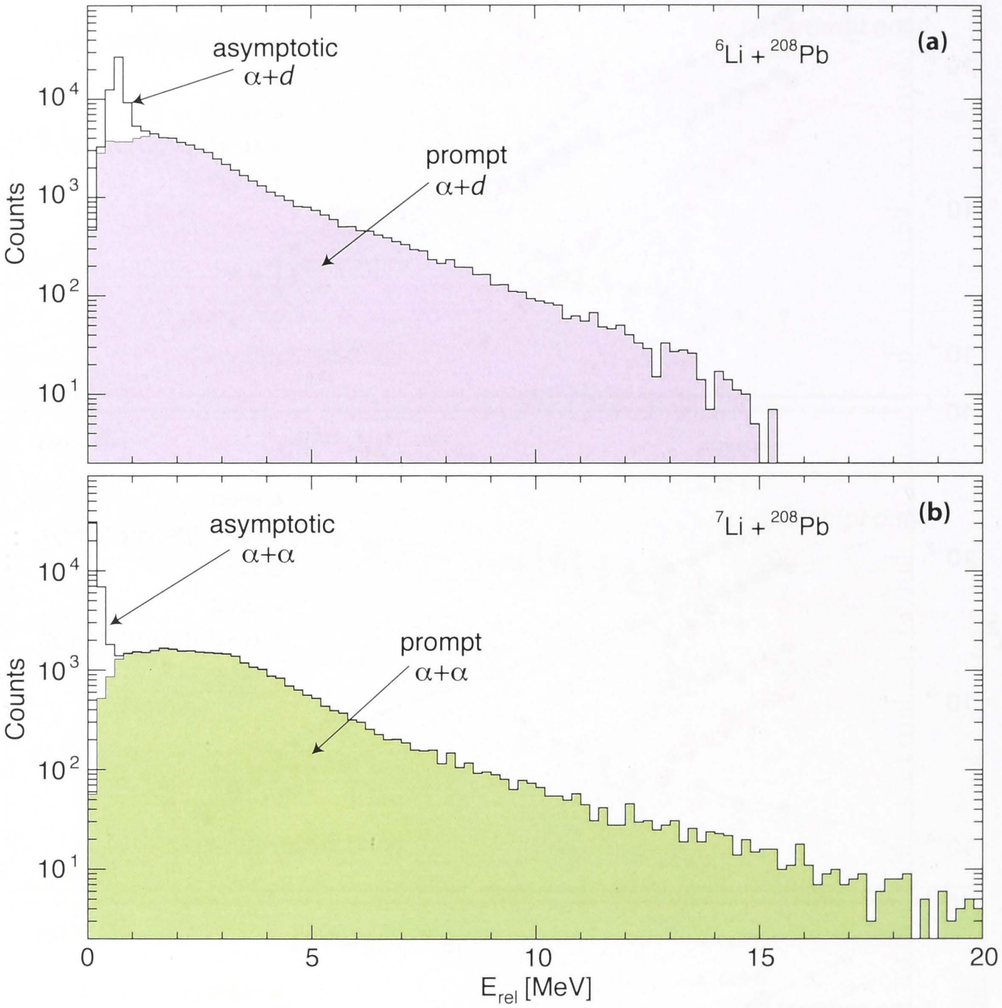

Figure 5.17: Separation of asymptotic breakup components from the total breakup yields for (a) the $\alpha + d$ breakup mode and (b) the $\alpha + \alpha$ breakup mode. These spectra are taken from the reactions of ^{6,7}Li with ^{208}Pb at $E_{\mathrm{beam}} = 29.0$ MeV.

Previous work by Hinde *et al.* [52] has shown that prompt breakup at sub-barrier energies can be related to suppression of complete fusion at above-barrier energies through the prompt breakup function. This arises from the fact that reaction outcomes depend on inter-nuclear separation. The measured breakup function can therefore be used [86] in simulation codes such as `PLATYPUS` to make calculations of outcomes at smaller inter-nuclear separations.

Since we are interested only in the prompt breakup events, we need to remove contributions due to delayed breakup. With prompt breakup having a wider E_{rel} distribution compared to delayed breakup, the quantity E_{rel} can be used for separating the two components. It must however be noted that while only prompt breakup can produce high E_{rel} events, low E_{rel} events have contributions from both prompt and delayed breakup. Thus it is only delayed breakup far from the target (asymptotic breakup), that has a distinctive peak in E_{rel} (see Section 4.3.1) that can be separated from the total breakup. This separation was achieved by gating on the measured Θ_{12} vs. E_{rel} plots, where asymptotic breakup events are tightly clustered around a specific E_{rel} related to breakup threshold (see equation (4.7) for Θ_{12}).

Figure 5.17 shows all breakup events (black lines) for the $\alpha + d$ and $\alpha + \alpha$ breakup modes following interactions of ^{6}Li and ^{7}Li with ^{208}Pb. The shaded region shows the breakup events after subtracting the asymptotic breakup events (using Θ_{12} vs. E_{rel} plots). The integration of the shaded regions gives the prompt breakup yields, which are plotted using open symbols in *Figure 5.15* and *5.16.* They deviate from the lines of best fit to an exponential function of R_{min} since the efficiency factors used were obtained without separating the asymptotic breakup component in the simulation. We thus need to separate the asymptotic breakup component in the simulation, which was done using the asymptotic breakup simulation program `BUGS`.

Shown in *Figure 5.18a* are the efficiency corrected prompt $\alpha + \alpha$ breakup probabilities measured for the reaction ^{7}Li with ^{208}Pb. The green symbols shows the probability obtained with the prompt only efficiency factor, and the blue symbols shows the probability obtained with the total efficiency factor. It can be seen that the breakup probabilities obtained from θ_{rec} (which has been transformed to R_{min}) nearest to the centre of the angular coverage of the detector are similar, independent of the efficiency factors used, and follow the exponential fit closely. The probabilities obtained from θ_{rec} closer to the edge of the detector, marked as *edge effects*, fluctuate greatly as uncertainties in the simulation are greatly amplified due to large corrections to the yields where the efficiency falls below 20% (see *Figure 5.18b*).

To eliminate contributions from θ_{rec} bins nearest to the edge of the detector, bins with efficiency $\epsilon_{i+j}(E, \theta_{\text{rec}})$ lower than 60% of the maximum efficiency are removed as indicated by the broken line. Similarly cut-off thresholds were set for the efficiency of the $\alpha + p$, $\alpha + d$, and $\alpha + t$ breakup modes, resulting in the inclusion of probabilities from only seven central θ_{rec} bins as shown in *Figure 5.18b*.

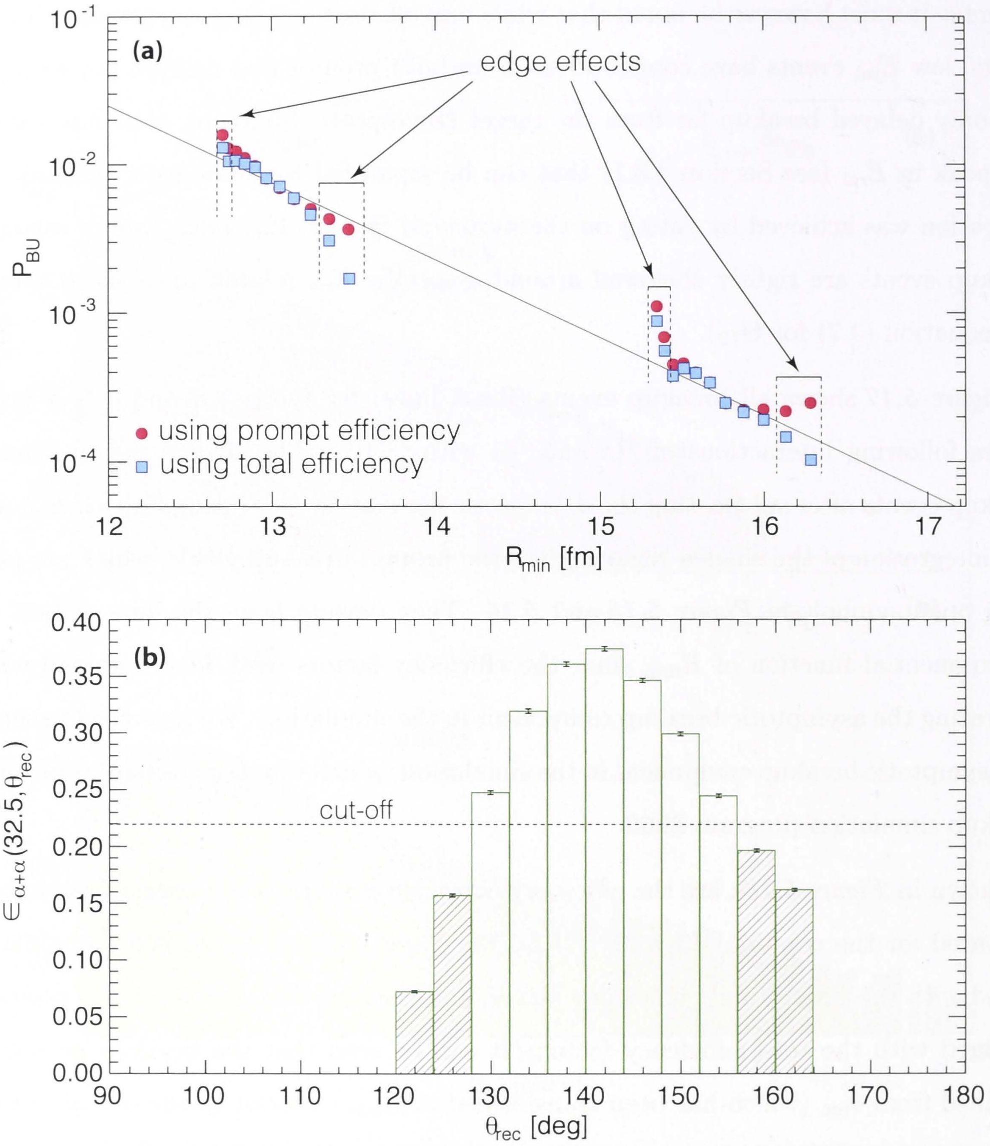

Figure 5.18: (a) Probabilities for the *prompt* component of $\alpha + \alpha$ breakup of ^{7}Li on ^{208}Pb. The efficiency in the $\theta_{\rm rec}$ bin at the edge of the detector is $\lesssim$20%, which cause variation in the efficiency corrected breakup probability as shown by the arrows. (b) Efficiency factors for the $\alpha + \alpha$ breakup mode for ^{8}Be at $E_{\rm beam}$ =32.5 MeV. The edge effect in (a) is caused by the low efficiency factor at $\theta_{\rm rec}$ near the edge of the lampshade detector. The dashed line indicates the cut-off threshold to minimise the dependence on uncertainties in simulations.

5.5.2 Parameterisation of the breakup probabilities

For all breakup modes in the ^{6,7}Li induced reactions, the dependence of the breakup probabilities on $R_{\rm min}$ are parameterised by μ and ν through fitting of the experimentally obtained probabilities to the exponential function defined by equation (5.15). In avoiding the "edge effects", breakup probabilities from $\theta_{\rm rec}$ corresponding to the seven central bins are included in the fitting. For the ^{7}Li-induced reactions, this corresponds to $\theta_{\rm rec}$ from 130° to 154°, and for the ^{6}Li-induced reactions, $\theta_{\rm rec}$ from 134° to 160° are included. For the fitting of the prompt breakup component, three different fitting methods were used resulting in three different μ, ν parameter sets labelled $\mathbb{A}$, $\mathbb{B}$, and $\mathbb{C}$. The reason for this is as follows.

For the ^{6}Li-induced reactions, results from fitting of the $\alpha + p$ breakup mode, triggered by n-stripping from ^{6}Li, and the *prompt* component of the $\alpha + d$ breakup mode are shown in *Figure 5.19.* For the former, scattering of the probabilities (*Figure 5.19a*) means two different sets of μ, ν are obtained per reaction due to two different fitting methods employed. The full lines indicate fitting results obtained by fits that weight each data point according to their statistical uncertainties (set $\mathbb{A}$). The dashed lines indicate results obtained from best fit where all data points have equal weighting, disregarding any statistical uncertainties (set $\mathbb{B}$). Scatter of the probabilities is also observed in the *prompt* $\alpha + d$ breakup mode (*Figure 5.19b*), which also resulted in multiple sets of μ, ν per reaction.

For the ^{7}Li-induced reactions, results from fitting of the $\alpha + t$ breakup mode, and the *prompt* component of the $\alpha + \alpha$ breakup triggered by p-pickup by ^{7}Li, are shown in *Figure 5.20.* Unlike the probabilities for $\alpha + p$ and $\alpha + d$ breakup in the ^{6}Li-induced reactions, the probabilities for breakup into $\alpha + t$ (*Figure 5.20a*) and *prompt* $\alpha + \alpha$ (*Figure 5.20b*) do not scatter greatly. Only the uncertainty from the uncertainty-weighted fitting method was therefore used, with the results indicated by the solid lines.

The systematic uncertainty from the pseudo-angle $\theta_{\rm rec}$ (see Section 5.2 and *Figure 5.3*), when transformed into $R_{\rm min}$, results in uncertainty within -0.1 to $+0.3$ fm (see *Figure 5.4*). By randomly adding this uncertainty to $R_{\rm min}$, as shown in *Figure 5.21*, and fitting with the uncertainty-weighted method results in variations in the parameters μ, ν. The upper limit (indicated by the full black line) corresponds to adding 0.3 fm to all $R_{\rm min}$ bins before fitting. Results from uncertainty-weighted fitting of the upper limit give the third parameter set, set $\mathbb{C}$.

All parameter sets μ, ν obtained from fitting of the probabilities for each breakup mode with different fitting methods are tabulated in Table 5.1. The variation in μ, ν between the different fitting methods is adopted as the uncertainty in the breakup function. This is then is carried through in the determination of the incomplete fusion, resulting in uncertainties in the suppression of complete fusion as seen in *Figure 5.22.*

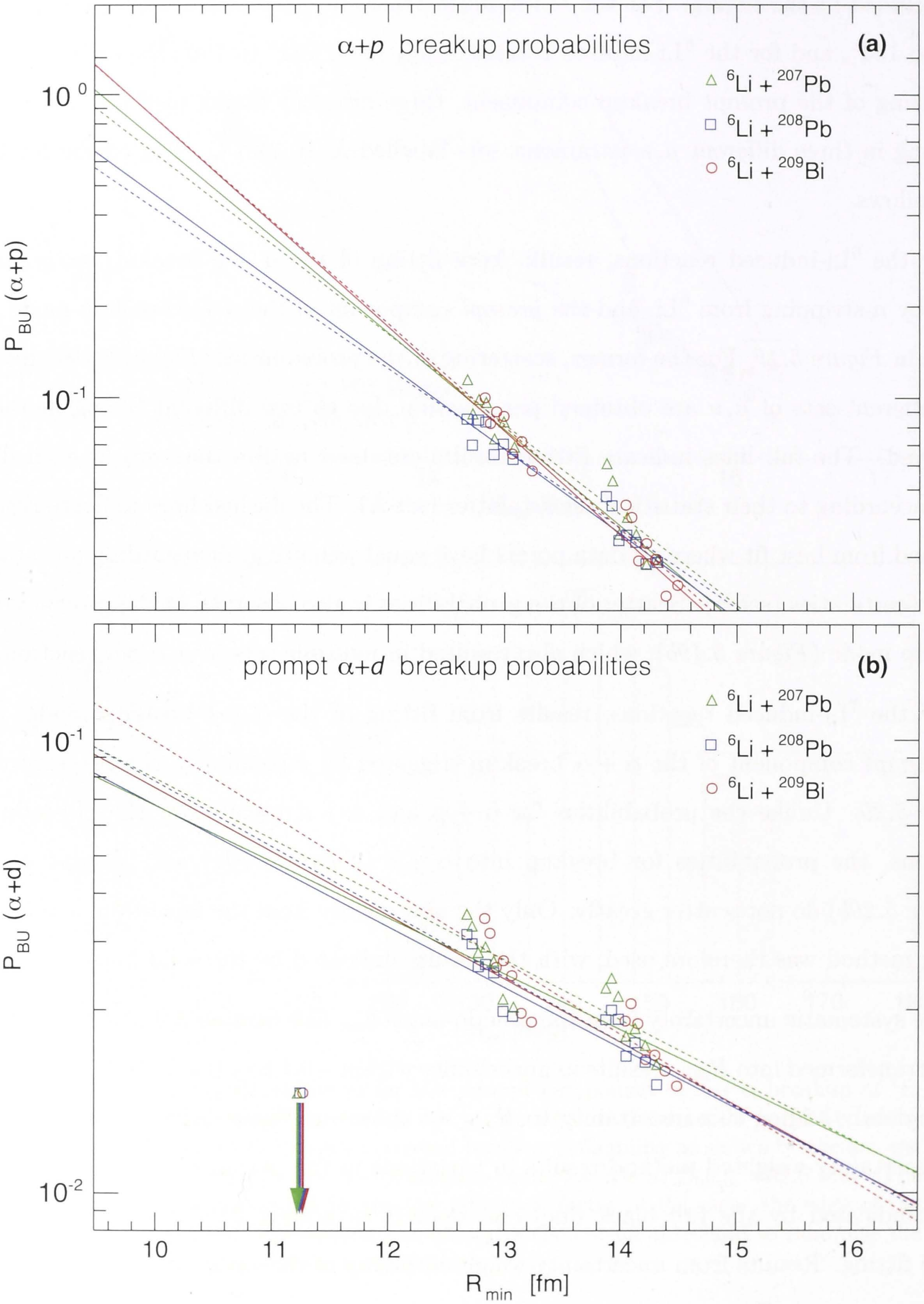

Figure 5.19: Breakup probabilities as a function of distance of closest approach R_{min} between the projectile and target nuclei for the (a) $\alpha + p$ breakup mode and (b) *prompt* $\alpha + d$ breakup in ^{6}Li-induced reactions at sub-barrier energies. The solid lines indicate fitting results obtained when the data points are weighted according to their statistical uncertainties. The dashed lines indicate results obtained from fitting where all data points were considered with equal weighting, with statistical uncertainty disregarded. The arrows indicate the barrier radius of each reaction.

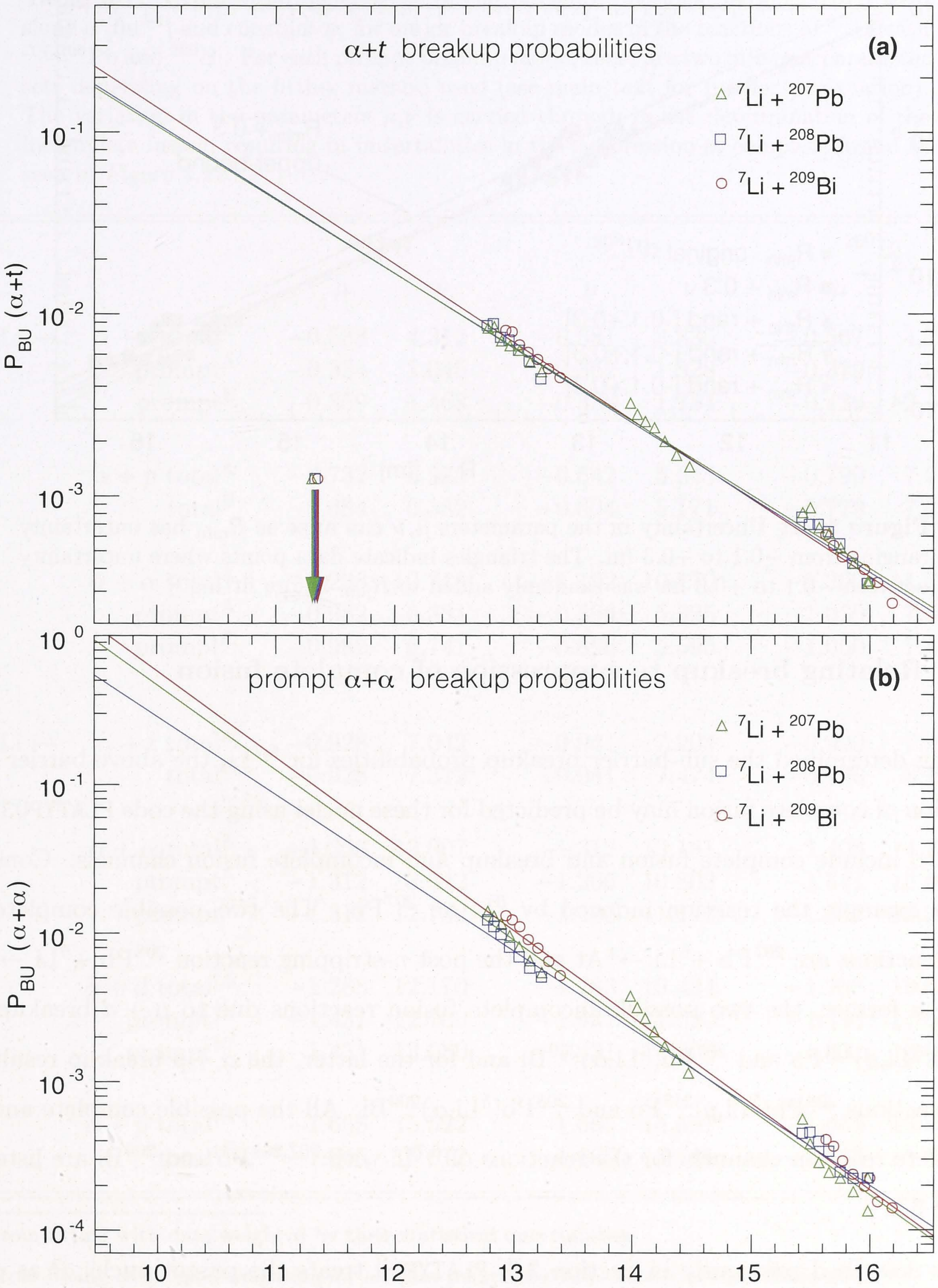

Figure 5.20: Breakup probabilities as a function of distance of closest approach R_{min} between the projectile and target nuclei for the (a) $\alpha + t$ breakup mode and (b) *prompt* $\alpha + \alpha$ breakup in ^{7}Li-induced reactions at sub-barrier energies. The solid lines indicate fitting results obtained when the data points are weighted according to their statistical uncertainties. The arrows indicate the barrier radius of each reaction.

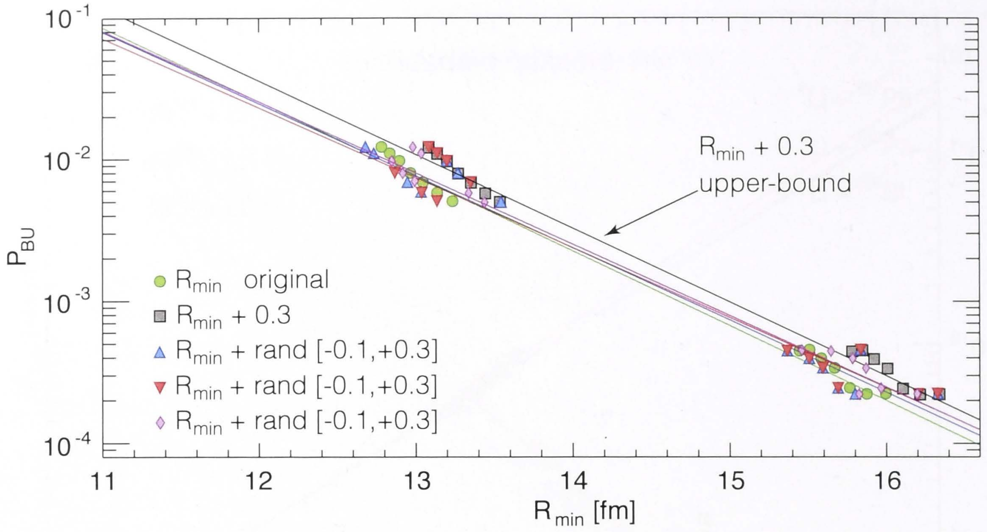

Figure 5.21: Uncertainty in the parameters μ, ν can arise as R_{min} has uncertainty ranging from -0.1 to $+0.3$ fm. The triangles indicate data points where uncertainty between -0.1 to $+0.3$ fm was randomly added to R_{min} before fitting.

5.6 Relating breakup to suppression of complete fusion

Having determined the sub-barrier breakup probabilities for ^{6,7}Li, the above-barrier suppression of complete fusion may be predicted for these nuclei using the code `PLATYPUS`. We need to include complete fusion and breakup and incomplete fusion channels. Consider as an example the reaction induced by ^{6}Li on ^{207}Pb. The two possible complete fusion reactions are $^{207}\mathrm{Pb} + {}^{6}\mathrm{Li} \rightarrow {}^{x}\mathrm{At}$ and the post n-stripping reaction $^{208}\mathrm{Pb} + {}^{5}\mathrm{Li} \rightarrow {}^{x}\mathrm{At}$. For the former, the two possible incomplete fusion reactions due to $\alpha + d$ breakup are ^{207}Pb(^{6}Li,d)^{211}Po and ^{207}Pb(^{6}Li,α)^{209}Bi and for the latter, the $\alpha + p$ breakup results in the reactions ^{208}Pb(^{5}Li,p)^{212}Po and ^{208}Pb(^{5}Li,α)^{209}Bi. All the possible complete and incomplete reaction channels for the reactions of ^{6,7}Li with ^{207,208}Pb and ^{209}Bi are listed in Table 5.2.

As described previously in Section 2.3, `PLATYPUS` treats the parent nuclei P as comprising a core i and a valence cluster j and their interaction is through the Coulomb and nuclear potentials including potentials between all charged participants P-T, i-T, j-T, and i-j, where T is the target. The potential parameters used in the code are given in Table A.1 in the appendix. Through time-step evolution of the system, the projectile that survive breakup, or the breakup fragments that penetrate their respective P, i, j-T barrier radius are said to have undergone fusion with the target. Breakup events with only one fragment captured by the target are termed incomplete fusion events.

Table 5.1: Exponential dependence of the breakup functions, parameterised with slope μ [fm^{-1}] and constant ν, for major breakup modes in the reactions of ^{6,7}Li with ^{207,208}Pb and ^{209}Bi. For each prompt breakup mode, there are two different parameter sets depending on the fitting method used (see main text for further explanation). The variation in the parameters μ,ν is carried through in the determination of the incomplete fusion, resulting in uncertainties in the suppression of complete fusion as seen in *Figure 5.22*.

		^{207}Pb		^{208}Pb		^{209}Bi	
		μ	ν	μ	ν	μ	ν
^{6}Li →	$\alpha + d$ total$^{\mathbb{A}}$	−0.538	4.313	−0.581	4.836	−0.567	4.702
	prompt$^{\mathbb{A}}$	−0.334	1.045	−0.362	1.328	−0.379	1.602
	prompt$^{\mathbb{B}}$	−0.359	1.468	−0.388	1.734	−0.436	2.448
	$\alpha + p$ total$^{\mathbb{A}}$	−0.732	6.975	−0.642	5.645	−0.790	7.720
	total$^{\mathbb{B}}$	−0.684	6.382	−0.604	5.171	−0.779	7.610
	$\alpha + \alpha$ total$^{\mathbb{A}}$	−1.238	10.718	−1.192	10.170	−1.300	11.794
	prompt$^{\mathbb{A}}$	−0.982	6.381	−0.896	5.325	−1.050	7.536
	prompt$^{\mathbb{C}}$	−0.982	6.741	−0.896	5.595	−1.050	7.856
^{7}Li →	$\alpha + t$ total$^{\mathbb{A}}$	−0.928	7.042	−0.941	7.204	−0.990	7.908
	total$^{\mathbb{C}}$	−0.928	7.312	−0.941	7.474	−0.990	8.198
	$\alpha + \alpha$ total$^{\mathbb{A}}$	−1.356	13.907	−1.312	13.181	−1.408	14.738
	prompt$^{\mathbb{A}}$	−1.312	12.342	−1.206	10.802	−1.341	12.866
	prompt$^{\mathbb{C}}$	−1.312	12.732	−1.206	11.172	−1.341	13.276
	$\alpha + d$ total$^{\dagger\mathbb{A}}$	−1.283	12.170	−1.283	10.434	−1.283	10.685
	prompt$^{\dagger\mathbb{A}}$	−1.431	12.700	−1.431	11.520	−1.431	11.653
	prompt$^{\dagger\mathbb{C}}$	−1.431	13.080	−1.431	11.900	−1.431	12.033
	$\alpha + p$ total$^{\dagger\mathbb{A}}$	−1.665	15.522	−1.665	14.681	−1.665	15.032
	total$^{\dagger\mathbb{C}}$	−1.665	16.012	−1.665	15.181	−1.665	15.532

$\mathbb{A}$ From fitting with data weighted by their statistical uncertainties.

$\mathbb{B}$ From fitting with equal weighting for all data points, statistical uncertainties disregarded.

$\mathbb{C}$ An offset of +0.3 fm was added to $R_{\min}$ (due to systematic uncertainty in θ_{rec}, see *Figure 5.21*) before fitting with data weighted by their statistical uncertainties.

† The common slope parameter μ is defined by the reaction with the ^{207}Pb target where measurements were done at three energies.

Table 5.2: Reaction channels considered by `PLATYPUS` for the reactions induced by ^{6,7}Li on ^{207,208}Pb and ^{209}Bi.

	complete fusion	breakup	incomplete fusion	
^{6}Li + ^{207}Pb	^{207}Pb(^{6}Li,γxn)^{x}At	$\alpha + d \rightarrow$	^{207}Pb(^{6}Li,d)^{211}Po	− 7.594 MeV
			^{207}Pb(^{6}Li,α)^{209}Bi	+ 8.942 MeV
	^{208}Pb(^{5}Li,γxn)^{x}At	$\alpha + p \rightarrow$	^{208}Pb(^{5}Li,p)^{212}Po	− 8.954 MeV
			^{208}Pb(^{5}Li,α)^{209}Bi	+ 3.799 MeV
	^{205}Tl(^{8}Be,γxn)^{x}At	$\alpha + \alpha \rightarrow$	^{205}Tl(^{8}Be,α)^{209}Bi	− 3.137 MeV
			^{205}Tl(^{8}Be,α)^{209}Bi	− 3.137 MeV
^{6}Li + ^{208}Pb	^{208}Pb(^{6}Li,γxn)^{x}At	$\alpha + d \rightarrow$	^{208}Pb(^{6}Li,d)^{212}Po	− 8.954 MeV
			^{208}Pb(^{6}Li,α)^{210}Bi	+ 6.179 MeV
	^{209}Pb(^{5}Li,γxn)^{x}At	$\alpha + p \rightarrow$	^{209}Pb(^{5}Li,p)^{213}Po	− 8.536 MeV
			^{209}Pb(^{5}Li,α)^{210}Bi	+ 4.466 MeV
	^{206}Tl(^{8}Be,γxn)^{x}At	$\alpha + \alpha \rightarrow$	^{206}Tl(^{8}Be,α)^{210}Bi	− 5.036 MeV
			^{206}Tl(^{8}Be,α)^{210}Bi	− 5.036 MeV
^{6}Li + ^{209}Bi	^{209}Bi(^{6}Li,γxn)^{x}Rn	$\alpha + d \rightarrow$	^{209}Bi(^{6}Li,d)^{213}At	− 9.254 MeV
			^{209}Bi(^{6}Li,α)^{211}Po	+ 7.309 MeV
	^{210}Bi(^{5}Li,γxn)^{x}Rn	$\alpha + p \rightarrow$	^{209}Bi(^{5}Li,p)^{214}At	− 8.987 MeV
			^{209}Bi(^{5}Li,α)^{211}Po	+ 4.929 MeV
	^{207}Pb(^{8}Be,γxn)^{x}Rn	$\alpha + \alpha \rightarrow$	^{207}Pb(^{8}Be,α)^{211}Po	− 7.594 MeV
			^{207}Pb(^{8}Be,α)^{211}Po	− 7.594 MeV
^{7}Li + ^{207}Pb	^{207}Pb(^{7}Li,γxn)^{x}At	$\alpha + t \rightarrow$	^{207}Pb(^{7}Li,t)^{211}Po	− 7.594 MeV
			^{207}Pb(^{7}Li,α)^{210}Bi	+ 7.289 MeV
	^{206}Tl(^{8}Be,γxn)^{x}At	$\alpha + \alpha \rightarrow$	^{206}Tl(^{8}Be,α)^{210}Bi	− 5.036 MeV
			^{206}Tl(^{8}Be,α)^{210}Bi	− 5.036 MeV
	^{208}Pb(^{6}Li,γxn)^{x}At	$\alpha + d \rightarrow$	^{208}Pb(^{6}Li,d)^{212}Po	− 8.954 MeV
			^{208}Pb(^{6}Li,α)^{210}Bi	+ 6.179 MeV
^{7}Li + ^{208}Pb	^{208}Pb(^{7}Li,γxn)^{x}At	$\alpha + t \rightarrow$	^{208}Pb(^{7}Li,t)^{212}Po	− 8.954 MeV
			^{208}Pb(^{7}Li,α)^{211}Bi	+ 5.060 MeV
	^{207}Tl(^{8}Be,γxn)^{x}At	$\alpha + \alpha \rightarrow$	^{207}Tl(^{8}Be,α)^{211}Bi	− 6.750 MeV
			^{207}Tl(^{8}Be,α)^{211}Bi	− 6.750 MeV
	^{209}Pb(^{6}Li,γxn)^{x}At	$\alpha + d \rightarrow$	^{209}Pb(^{6}Li,d)^{213}Po	− 8.536 MeV
			^{209}Pb(^{6}Li,α)^{211}Bi	+ 7.379 MeV
^{7}Li + ^{209}Bi	^{209}Bi(^{7}Li,γxn)^{x}Rn	$\alpha + t \rightarrow$	^{209}Bi(^{6}Li,t)^{213}At	− 9.254 MeV
			^{209}Bi(^{6}Li,α)^{212}Po	+ 7.060 MeV
	^{208}Pb(^{8}Be,γxn)^{x}Rn	$\alpha + \alpha \rightarrow$	^{208}Pb(^{8}Be,α)^{212}Po	− 8.954 MeV
			^{208}Pb(^{8}Be,α)^{212}Po	− 8.954 MeV
	^{210}Bi(^{6}Li,γxn)^{x}Rn	$\alpha + d \rightarrow$	^{210}Bi(^{6}Li,d)^{214}At	− 8.987 MeV
			^{210}Bi(^{6}Li,α)^{212}Po	+ 8.713 MeV

Simulations of complete and incomplete fusion of ^{6,7}Li were carried at energies >10% above the fusion-barrier energy. 4000 incident projectiles per partial wave were followed in the calculations. Partial waves of angular moment up to $70\hbar$ were included, with partial waves with angular momentum up to $60\hbar$ observed contributing to the cross-sections. The suppression of complete fusion for reactions with ^{6,7}Li is shown in *Figure 5.22*. The experimentally observed suppression of complete fusion are also shown for comparison. Contribution from individual breakup modes are shown in Table 5.3.

At above-barrier energies, a 52% suppression of complete fusion is predicted for the reaction of ^{6}Li with ^{207}Pb. A suppression factor of 40% and 56% is also predicted for reactions with the ^{208}Pb and ^{209}Bi targets respectively (*Figure 5.22b*). For the latter, this prediction is significantly larger than the 36% observed experimentally for the same reaction. When the contribution from the $\alpha+p$ breakup is halved (red circles), the "reduced total" amounts to 33%, agreeing very well with the experimentally observed suppression of complete fusion. There are three possible explanations for this. Firstly, ^{5}Li has a lifetime of 5.3×10^{-22} s [112], and thus not all ^{5}Li may decay into $\alpha + d$ before fusion, i.e. not all $\alpha + p$ breakup would compete with complete fusion. Secondly, during the separation of $\alpha+p$ breakup from the overlapping $\alpha+d$ breakup (see Section 4.2.1), the former may have been over-compensated. The uncertainty contributed from this gating method is small, however, and would not be able to explain such large differences. The third possible cause comes from the simulation of ^{5}Li and the $\alpha+p$ breakup kinematics. As there is no reliable phenomenological potential for ^{5}Li, the addition and average method used to obtain its potential parameters is a crude approximation at best. This is further complicated by the fact that the proton is small enough that its motion may not be well-described by classical mechanics, the basis of `PLATYPUS` trajectories simulations.

By halving the contributions from the $\alpha + p$ breakup across all targets, the predicted suppression of complete fusion in the reactions of ^{6}Li with ^{207}Pb and ^{208}Pb reduces to 31% and 24% respectively. For the latter, this figure is somewhat lower than the 33% found to agree reasonably well with experimental observations [128], but perhaps within estimated uncertainties, which were not quoted in that work.

For the ^{7}Li induced reactions (*Figure 5.22b*), complete fusion with ^{208}Pb is predicted to be suppressed by 12%, with a 25% and 32% suppression predicted for ^{207}Pb and ^{209}Bi respectively. The observed 32% suppression in ^{209}Bi agrees, within uncertainty, with the

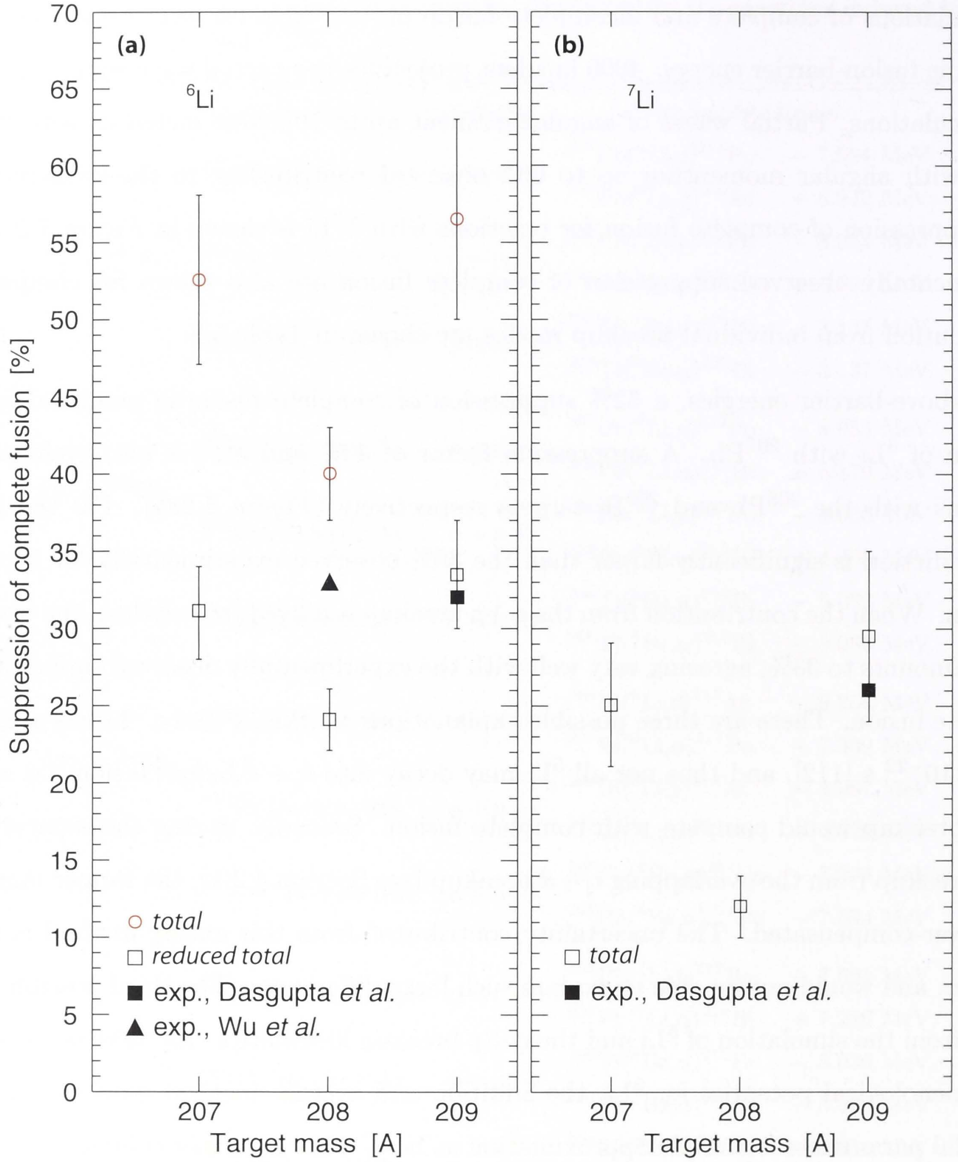

Figure 5.22: Predictions for the suppression of complete fusion in reactions induced by ^{6,7}Li on ^{207}Pb, ^{208}Pb and ^{209}Bi targets. The experimental suppression factors are taken from Dasgupta *et al.* [26] (solid square) and Wu *et al.* [128] (solid triangles). For the ^{6}Li-induced reactions, contribution from the $\alpha + p$ breakup mode have been halved in the "reduced total" (see text). The uncertainties are due to the uncertainty in the breakup functions.

26% observed experimentally. This reaffirms that something is definitely amiss with the $\alpha + p$ breakup mode in ^{6}Li. With the $\alpha + \alpha$ breakup mode, triggered by p-pickup, being the major contributor to the suppression of complete fusion in ^{7}Li (see Table 5.3), the 12% suppression in ^{208}Pb, which arises from differences in experimental breakup function, may indicate that the doubly magic nature of ^{208}Pb inhibits nucleon exchange with ^{7}Li

Table 5.3: Percentage of suppression of complete fusion as contributed by the major breakup modes in reactions induced by ^{6,7}Li on each target nucleus.

		^{207}Pb	^{208}Pb	^{209}Bi
^{6}Li	$\alpha + d$ †	7–8	6–7	8–9
	$\alpha + p$	39–48	30–36	40–51
	$\alpha + \alpha$ †	1–2	1–2	2–3
	Total	**52 ±5**	**40 ±3**	**56 ±7**
	$*$	**31 ±3**	**24 ±2**	**33 ±4**
^{7}Li	$\alpha + t$	4–5	3–4	5–6
	$\alpha + \alpha$ †	10–14	6–8	17–26
	$\alpha + d$ †	7–10	1–2	2–3
	Total	**25 ±4**	**12 ±2**	**29 ±6**

† *Prompt* breakup component only.

$*$ Contribution from the $\alpha + p$ breakup mode have been halved.

leading to less suppression of complete fusion. Further experimental investigation into the complete and incomplete fusion of ^{7}Li with ^{208}Pb is thus required.

The prediction for the suppression of complete fusion in ^{6,7}Li-induced reactions, while in reasonable agreements with experimental observations, take into account only the contributions from binary breakup of the projectile-like nuclei. Other reaction channels such as cluster-transfer may also be competing with complete fusion at energies near and above the barrier energy. Cluster-transfer was observed by Castaneda *et al.* [18] from 75 MeV ^{6}Li bombardment of ^{197}Au, using the particle-γ coincidences technique. Triton transfer have also been mentioned by Häusser *et al.* [46] as a possible reaction channel in ^{7}Li.

5.7 Summary and discussion

Breakup kinematics for the reactions induced by ^{6,7}Li were simulated using `PLATYPUS`, allowing the estimation of coincidence detection efficiency of the detector for all the major breakup modes. The concept of a pseudo-angle for breakup was introduced, allowing the breakup probability to be expressed as a function of the distance of closest approach between the projectile and target nuclei. Bin normalisation of the detector then allows for the determination of the absolute probabilities for each breakup mode.

The sub-barrier breakup probabilities, as a function of distance of closest approach between the projectile and target nuclei, were used to predict the above-barrier suppression of complete fusion in ^{6,7}Li-induced reactions using the classical trajectory code `PLATYPUS`. For the reactions induced by ^{6}Li, contribution from the $\alpha + p$ breakup mode was over-predicted, leading to major over-prediction of suppression of complete fusion in ^{6}Li-induced reactions. When the contribution from $\alpha + p$ breakup was halved, the predicted total suppression agreed well with experimental observation for reaction with ^{209}Bi. The necessity to reduce the $\alpha + p$ contribution is likely to be due to the lifetime of ^{5}Li being comparable to fusion time-scales, and thus there is a significant probability that ^{5}Li can fuse before breakup.

For the ^{7}Li-induced reactions, prompt $\alpha + \alpha$ breakup was predicted to be the major contributor to the suppression of complete fusion. Taking into account all prompt breakup modes, complete fusion of ^{7}Li with ^{208}Pb was predicted to have a 12% suppression, which is much lower than the 25% and 29% predicted for reactions with ^{207}Pb and ^{209}Bi respectively. The 29% suppression predicted for reaction with ^{209}Bi agrees, within uncertainty, with experimental observations. This gives credence to the low suppression factor predicted for the reaction with ^{208}Pb. Further investigation into the reaction of ^{7}Li with ^{208}Pb should prove interesting.

A great discovery is not a terminus, but an avenue leading to regions hitherto unknown. We climb to the top of the peak and find that it reveals to us another higher than any we have yet seen, and so it goes on.

J. J. Thompson (1856 - 1940)

6

Conclusions and future outlook

As a testbed for relating nuclear structure of weakly-bound and unstable nuclei to nuclear reaction outcomes within a coherent framework, the reactions of ^{6}Li and ^{7}Li were studied at sub-barrier energies. Charged fragments were detected at backward angles, both in singles and in coincidence, using a highly pixelated detector array. Reconstruction of the reaction Q-values together with isotopic identification for a subset of Z=1 breakup fragments allowed the determination of all the mechanisms that trigger binary breakup of ^{6}Li and ^{7}Li. The time-scales for these breakup processes were also investigated through the relative energy of the coincidence fragments. The results obtained allow many unresolved questions regarding reactions induced by ^{6}Li and ^{7}Li to be answered and allow the sub-barrier breakup to be related to the above-barrier suppression of complete fusion for reactions of these nuclei.

Summary

For the reactions with ^{6}Li, binary coincidences revealed that breakup triggered by n-transfer ($^{6}\text{Li} \to {}^{5}\text{Li} \to \alpha + p$) is more probable than direct cluster breakup ($^{6}\text{Li} \to \alpha + d$). This predominance is rather target independent, as similar results were observed on all three targets ^{207}Pb, ^{208}Pb and ^{209}Bi. Based on the relative energy of the two fragments, about half of all sub-barrier $\alpha + d$ breakup was determined to come from $\alpha + d$ decay from the 2.18 MeV (3^{+}) resonant state in ^{6}Li. This state has a lifetime of 2.7×10^{-20} s, orders of magnitude slower than the 10^{-22} s time-scale for direct nuclear reactions. Therefore breakup from this 3^{+} resonance cannot lead to incomplete fusion at above-barrier energies.

The remaining half of all sub-barrier $\alpha + d$ breakup is prompt breakup, with time-scales comparable to that of direct reactions. Capture of these breakup fragments by the target is possible at above-barrier energies leading to incomplete fusion, which leads to suppression of complete fusion.

Using a classical model, the sub-barrier breakup probability for the $\alpha + d$ breakup mode is predicted to contribute as much as 9% to the above-barrier suppression of complete fusion in reactions with ^{6}Li. From the probability for neutron-stripping ($^{6}\mathrm{Li} \rightarrow {}^{5}\mathrm{Li} \rightarrow \alpha + p$), the same classical model predicts a 50% above-barrier suppression of complete fusion for $^{6}\mathrm{Li} + {}^{209}\mathrm{Bi}$. This figure is larger than the experimentally observed 34% suppression [26] for the same reaction, indicating that even the 5.3×10^{-22} s ground-state lifetime of ^{5}Li is long enough to allow significant fusion before breakup.

For the reactions induced by ^{7}Li, p-pickup by the projectile leading to the $\alpha + \alpha$ breakup mode ($^{7}\mathrm{Li} \rightarrow {}^{8}\mathrm{Be} \rightarrow \alpha + \alpha$) was observed to be a major reaction channel, along with direct cluster breakup ($^{7}\mathrm{Li} \rightarrow \alpha + t$). For the former, about half of the breakup yield came from ground-state decay of ^{8}Be, with a long lifetime of $\sim 10^{-16}$ s. These projectile-like ^{8}Be nuclei would thus survive long enough to participate in complete fusion with the target, at above-barrier energies, and thus will not affect complete fusion in reaction with ^{7}Li. Breakup triggered by n-stripping ($^{7}\mathrm{Li} \rightarrow {}^{6}\mathrm{Li} \rightarrow \alpha + d$) was also observed to be prominent in the reaction with ^{207}Pb.

From the sub-barrier probability for the $\alpha + t$ breakup mode, a maximum of 6% suppression of complete fusion was predicted for reactions of ^{7}Li at above-barrier energies using a classical model. The same model also predicted a further 26% suppression, due to the prompt component of the $\alpha + \alpha$ breakup of ^{8}Be, in above-barrier complete fusion of ^{7}Li. This prediction is in reasonable agreement with the observed 26% suppression of complete fusion [26] in reactions with ^{7}Li.

For both the ^{6}Li and ^{7}Li reactions, prompt breakup following transfer is more likely than prompt direct breakup into the projectile cluster constituents. The short time-scale of prompt breakup ($\sim 10^{-22}$ s), which gives rise to high E_{rel} components, can only be quantitatively interpreted by quantal reaction models [58, 89, 110]. This will be a major challenge for the quantum theory of low energy nuclear reactions, requiring new theoretical developments to allow calculation of relative energy spectra outside the initial mass-partition.

Future outlook

Measurements presented in this work demonstrated that the reaction dynamics and outcomes are determined not only by the properties of the two colliding nuclei, but also by the ground-state and excited state properties of their neighbours. This is a key insight for understanding and predicting reactions of weakly-bound nuclei near the limits of nuclear existence. Furthermore, these results suggest that in sub-barrier collisions of ^{6}Li and ^{7}Li with all but the lightest nuclei, the most likely nuclear reactions will lead to breakup of the projectile-like nucleus, forming elements lighter than Li. This needs to be tested experimentally for reactions with much lighter nuclei, and possible implications for lithium abundances in cosmological processes [23, 103, 118] investigated.

Initial analyses of experiments investigating breakup of ^{6}Li and ^{7}Li on ^{58}Ni, and ^{64}Ni and ^{64}Zn showed the same outcomes, with breakup triggered predominantly by transfer of a neutron or a proton, i.e. a two-step process. Further experiments, on a wide range of target nuclei, will provide important input to developing a complete model of reactions involving both α-cluster nuclei and exotic nuclei at the limits of existence, with potential applications in nuclear astrophysics.

Future outlook.

Measurements presented in this work demonstrated that the reaction dynamics and outcomes are determined not only by the properties of the two colliding nuclei, but also by the ground-state and excited state properties of their neighbours. This is a key insight for understanding and predicting reactions of weakly-bound nuclei near the limits of nuclear existence. Furthermore, these results suggest that in sub-barrier collisions of ^{6}Li and ^{7}Li with all but the lightest nuclei, the most likely nuclear reactions will lead to breakup of the projectile-like nucleus, forming nuclei lighter than Li. This needs to be tested experimentally, particularly for reactions with much lighter nuclei, and possible implications for lithium abundances in cosmological processes [23, 193, 328] investigated.

Initial analysis of experiments investigating breakup of ^{6}Li and ^{7}Li on ^{58}Ni and ^{64}Ni and ^{64}Zn showed the same outcomes, with breakup triggered predominantly by transfer of a neutron or a proton, i.e. a two-step process. Further experiments, on a wide range of target nuclei, will provide important input to developing a complete model of reactions involving both α-cluster nuclei and exotic nuclei at the limits of existence, with potential applications in nuclear astrophysics.

A

PLATYPUS input files

PLATYPUS input file for the reaction ^{5}Li + ^{209}Pb with potential given in Table A.1.

```
0,0,0,0,1,0
0,70,3000
0
29.0
4.5,0.000
1.5,0.000
0   ,0.922
1.800,1.00
0.604,5.171
50.
0
########POTENTIALS##################
209.,82.
5.,3.
4.,2.
1.,1.
-156.7,1.357,0.550,1.255
-103.0,1.483,0.500,1.297
-53.70,1.230,0.600,1.213
-48.80,1.200,0.280,1.100
-51.90,1.172,0.800,1.105,-8.536
-103.1,1.480,0.500,1.295,+4.466
```

`PLATYPUS` input file for the reaction ^{6}Li + ^{208}Pb with potential given in Table A.1.

```
0,0,0,0,1,0
0,70,3000
0
29.0
4.5,0.000
1.5,0.000
0   ,0.922
1.80,1.00
0.362,1.328
50.
0
#######POTENTIALS################
208.,82.
6.,3.
4.,2.
2.,1.
-183.0,1.380,0.620,1.400
-155.0,1.282,0.677,1.350
-100.0,1.130,0.890,1.100
-73.20,1.250,0.614,1.300
-91.10,1.157,0.800,1.308,-8.954
-103.1,1.480,0.500,1.295,+6.179
```

`PLATYPUS` input file for the reaction ^{7}Li + ^{208}Pb with potential given in Table A.1.

```
0,0,0,0,1,0
0,70,3000
0
29.0
4.5,0.000
1.5,0.000
0   ,0.922
1.80,0.50
0.941,7.474
50.
0
```

```
#######POTENTIALS#################
208.,82.
7.,3.
4.,2.
3.,1.
-293.8,1.250,0.790,1.400
-155.0,1.282,0.677,1.350
-148.7,1.240,0.697,1.250
-164.0,1.200,0.720,1.300
-217.2,1.090,0.800,1.425,-8.954
-176.7,1.245,0.800,1.245,+5.560
```

PLATYPUS input file for the reaction ^{8}Be + ^{207}Tl with potential given in Table A.1.

```
0,0,0,0,1,0
0,70,3000
0
38.20
4.5,0.000
1.5,0.000
0   ,1.13336
1.800,1.000
1.312,13.181
50.
0
#######POTENTIALS#################
207.,81.
8.,4.
4.,2.
4.,2.
-348.0,1.250,0.800,1.250
-174.0,1.250,0.800,1.250
-174.0,1.250,0.800,1.250
-92.00,1.140,0.600,1.140
-175.6,1.243,0.800,1.243,-6.750
-175.6,1.243,0.800,1.243,-6.750
```

Table A.1: Wood-Saxon potential parameters for all reaction system with $R_0 = r_0\ A_{\mathrm{T}}\ ^{1/3}$ and $R_{\mathrm{c}} = r_{\mathrm{c}}\ A_{\mathrm{T}}\ ^{1/3}$.

	p				d				t				α			
	V_0 [MeV]	r_0 [fm]	a_0 [fm]	r_{c} [fm]	V_0 [MeV]	r_0 [fm]	a_0 [fm]	r_{c} [fm]	V_0 [MeV]	r_0 [fm]	a_0 [fm]	r_{c} [fm]	V_0 [MeV]	r_0 [fm]	a_0 [fm]	r_{c} [fm]
α	48.80	1.200	0.284	1.100	73.20	1.250	0.614	1.300	164.0	1.200	0.720	1.300	92.00	1.140	0.600	1.140
^{206}Tl	53.60	1.236	0.600	1.219									174.2	1.245	0.767	1.245
^{207}Tl	53.60	1.234	0.600	1.217									174.0	1.245	0.767	1.245
^{207}Pb	58.38	1.230	0.720	1.190	121.5	1.050	0.860	1.300	150.0	1.240	0.675	1.250	135.0	1.380	0.577	1.300
^{208}Pb	58.92	1.230	0.720	1.190	100.0	1.130	0.890	1.300	148.7	1.240	0.697	1.250	155.0	1.282	0.677	1.300
^{209}Pb	53.70	1.230	0.600	1.213									174.8	1.245	0.767	1.245
^{209}Bi	58.76	1.230	0.720	1.190	112.2	1.060	0.960	1.300	161.6	1.200	0.720	1.300	100.4	1.444	0.542	1.200
^{210}Bi	53.70	1.178	0.800	1.093									175.7	1.245	0.766	1.245
^{211}Bi													175.5	1.245	0.766	1.245
^{210}Po	53.70	1.178	0.800	1.094									175.7	1.245	0.766	1.245
^{211}Po	53.70	1.176	0.800	1.092	91.10	1.159	0.800	1.310	217.2	1.092	0.800	1.428	176.6	1.245	0.766	1.245
^{212}Po	53.70	1.174	0.800	1.107	91.10	1.157	0.800	1.308	217.2	1.090	0.800	1.425	176.4	1.245	0.766	1.245
^{213}Po	53.70	1.172	0.800	1.105												
^{213}At	53.70	1.172	0.800	1.105	91.20	1.155	0.800	1.306	217.3	1.088	0.800	1.423	177.3	1.245	0.766	1.245
^{214}At	53.70	1.170	0.800	1.103												
	^{5}Li *				^{6}Li				^{7}Li				^{8}Be *			
	V_0	r_0	a_0	r_{c}	V_0	r_0	a_0	r_{c}	V_0	r_0	a_0	r_{c}	V_0	r_0	a_0	r_{c}
^{206}Tl													348.3	1.245	0.767	1.245
^{207}Tl													348.1	1.245	0.767	1.245
^{207}Pb	193.4	1.305	0.649	1.245	256.5	1.215	0.719	1.250	285.0	1.310	0.626	1.275	270.0	1.380	0.577	1.300
^{208}Pb	213.9	1.256	0.699	1.270	183.0	1.380	0.620	1.400	293.8	1.250	0.790	1.300	310.0	1.282	0.677	1.300
^{209}Pb	228.5	1.238	0.683	1.229												
^{209}Bi	159.2	1.337	0.631	1.195	176.6	1.180	0.880	1.150	262.0	1.322	0.631	1.250	200.8	1.444	0.542	1.200
^{210}Bi	229.4	1.211	0.783	1.169												

---

* V_0 is approximated by sum of V_0 from p-T and α-T while r_0, a_0, and r_{c} is averaged.

* V_0 is approximated by twice V_0 from α-T.

Bibliography

[1] Ajzenberge-Selove F. and Lauritsen T., *Energy levels of light nuclei A = 5-10*, Nuc. Phys. A **227** (1974), 1.

[2] Asplund M., Lambert D., Nissen P. E., Primas F., and Smith V., *Lithium isotopic abundances in metal-poor halo stars*, Astrophys. J. **644** (2006), 229.

[3] Austern N., Iseri Y., Kamimura M., Kawai M., Rawitscher G., and Yahiro M., *Continuum-discretized coupled-channels calculations for three-body models of deuteron-nucleus reactions*, Phys. Rep. **154** (1987), 125.

[4] Bass R., *Fusion of heavy nuclei in a classical model*, Nuc. Phys. A **231** (1974), 45–63.

[5] Bass R., *Nuclear reactions with heavy ions*, Springer-verlag, New York, 1979.

[6] Baur G., Bertulani C. A., and Rebel H., *Coulomb dissociation as a source of information on radiative capture processes of astrophysical interest*, Nuc. Phys. A **458** (1986), 188.

[7] Baur G. and Weber M., *The angular correlation in the Coulomb dissociation method for radiative capture processes of astrophysical interest*, Nuc. Phys. A **504** (1989), 352–366.

[8] Bernas R., Gradsztajn E., Reeves H., and Schatzman E., *On the nucleosynthesis of lithium, beryllium and boron*, Ann. Phys. **44** (1967), 426.

[9] Bertulani C. A., *The astrophysical reactions* $^{12}C(\alpha,\gamma)^{16}O$ *and* $^{7}Be(p,\gamma)^{8}B$ *and Coulomb dissociation experiments*, Phys. Rev. C **49** (1994), 2688.

[10] Bethe H. and Ashkin J., *Experimental nuclear physics*, J. Wiley, New York, 1953.

[11] Birkelund J. R. and Huizenga J. R., *Fusion reactions between heavy nuclei*, Annu. Rev. Nucl. Part. Sci. **33** (1983), 265.

[12] Blair J. M. and Hobbie R. K., *Differential cross section for the reaction* $^{12}C(^{6}Li,p)^{17}O$ *and* $^{12}C(^{6}Li,d)^{16}O$, Phys. Rev. **128** (1962), 2282.

[13] Brink B. M., *Kinetmatical effects in heavy-ion reactions*, Phys. Lett. B **40** (1972), 37.

[14] Bromley D. A., *The development of electrostatic accelerators*, Nucl. Instrum. Methods **122** (1974), 1.

[15] Brun R. and Rademakers F., *ROOT - An object oriented data analysis framework*, Nucl. Instrum. Methods **A389** (1997), 81.

[16] Buck B., Merchant A. C., and Perez S. M., *Favoured alpha decays of odd-mass nuclei*, J. Phys. G: Nucl. Part. Phys. **18** (1992), 143.

[17] Canto L. F., Gomes P. R. S., Donangelo R., and Hussien M. S., *Fusion and breakup of weakly bound nuclei*, Phys. Rep. **424** (2006), 1.

[18] Castaneda C. M., Jr. H. A. S., Singh P. P., Jastrzebski J., Karwowski H., and Gaigalas A. K., *Gamma-rays from the transfer of* α *and d fragments in* ^{6}Li *induced reactions far above the Coulomb barrier*, Phys. Lett. B **77** (1978), 371.

[19] Cobern M. E., Pisano D. J., and Parker P. D., *Alpha-transfer reactions in light nuclei. III.* $(^{7}Li,t)$ *stripping reaction**, Phys. Rev. C **14** (1976), 491.

[20] Cook J., $^{6,7}Li$ *optical-model parameters*, At. Data Nucl. Data Tables **26** (1981), 19.

[21] Csótó A., *Three-body resonances in* ^{6}He, ^{6}Li, *and* ^{6}Be, *and the soft dipole mode problem of neutron halo nuclei*, Phys. Rev. C **49** (1994), 3035.

[22] Csótó A. and Lovas R. G., *Dynamical microsopic three-cluster description of* ^{6}Li, Phys. Rev. C **46** (1992), 576.

[23] Cyburt R. H., Fields B. D., and Olive K. A., *An update on the big bang nucleonsynthesis prediction for* ^{7}Li*: the problem worsen*, J. Cosmo. Part. Phys. **11** (2008), 012.

[24] Dasgupta M., Gomes P., Hinde D. J., Moraes S. B., Anjos R. M., Berriman A., Butt R. D., Carlin N., Lubian J., Morton C. R., Newton J. O., and de Toledo A. S., *Effect of breakup on the fusion of* ^{6}*Li,* ^{7}*Li, and* ^{9}*Be with heavy nuclei*, Phys. Rev. C **70** (2004), 024606.

[25] Dasgupta M., Hinde D. J., Butt R. D., Anjos R. M., Berriman A. C., Carlin N., Gomes P. R. S., Morton C. R., Newton J. O., de Toledo A. S., and Hagino K., *Fusion versus breakup: Observation of large fusion suppression for* $^{9}Be + {}^{208}Pb$, Phys. Rev. Lett. **82** (1999), 1395.

[26] Dasgupta M., Hinde D. J., Hagino K., Moraes S. B., Gomes P. R. S., Anjos R. M., Butt R. D., Berriman A., Carlin N., Morton C. R., Newton J. O., and de Toledo A. S., *Fusion and breakup in the reactions of* ^{6}*Li and* ^{7}*Li nuclei with* ^{209}*Bi*, Phys. Rev. C **66** (2002), 041602(R).

[27] Dasgupta M., Hinde D. J., Rowley N., and Stefanini A. M., *Measuring barriers to fusion*, Annu. Rev. Nucl. Part. Sci. **48** (1998), 401.

[28] Dasso C. H. and Donangelo R., *Fusion enhancement via the soft dipole mode in neutron-rich nuclei*, Phys. Lett. B **276** (1992), 1.

[29] Davinson T., Rapp R., Shotter A. C., Branford D., Nagarajan M. A., Thompson I. J., and Sanderson N. E., *Coublomb and nuclear contribution to the excitation of* ^{7}*Li incident on heavy nuclei*, Phys. Lett. **139B** (1984), 150.

[30] Diaz-Torres A., *PLATYPUS: a code for fusion and breakup in reactions induced by weakly-bound nuclei within a classical trajectory model with stochastic breakup*, arXiv: 0712.2275v1 (2007).

[31] Diaz-Torres A., *Platypus: A code for reaction dynamics of weakly-bound nuclei at near-barrier energies within a classical dynamical model*, Comput. Phys. Rep. **182** (2011), 110.

[32] Diaz-Torres A., Hinde D. J., Tostevin J. A., Dasgupta M., and Gasques L. R., *Relating breakup and incomplete fusion of weakly bound nuclei through a classical trajectory model with stochastic breakup*, Phys. Rev. Lett. **98** (2007), 152701.

[33] Diaz-Torres A. and Thompson I. J., *Effect of contimuum couplings in fusion of halo* ^{11}*Be on* ^{208}*Pb around the Coulomb barrier*, Phys. Rev. C **65** (2002), 024606.

[34] Disdier D. L., Ball G. C., Häusser O., and Warner R. E., *Projectile polarization in the Coulomb breakup of* ^6Li, Phys. Rev. Lett. **27** (1971), 1391.

[35] Elad E., Inskeep C. N., Sareen R. A., and Nestor P., *Dead layers in charged-particle detectors*, IEEE Trans. Nucl. Sci. **20** (1973), 534.

[36] Evers M., Hinde D. J., Dasgupta M., Luong D. H., Rafiei R., and du Rietz R., *Coulomb nuclear interference as a tool to investigate the nuclear potential*, Phys. Rev. C **81** (2010), 014602.

[37] Fowler W. A., Greenstein J. L., and Hoyle F., *Nucleosynthesis during the early history of the solar system*, Geophys. J. Roy. Astron. Soc. **6** (1962), 148.

[38] Freer M., *The clustered nucleus - cluster structures in stable and unstable nuclei*, Rep. Pro. Phys. **70** (2007), 2149.

[39] Freer M. and Merchant A. C., *Developments in the study of nuclear clustering in light even-even nuclei*, J. Phys. G: Nucl. Part. Phys. **23** (1997), 261.

[40] Gammel J. L., Hill B. J., and Thaler R. M., *Elastic scattering of deuterons by* He^4, Phys. Rev. **119** (1960), 267.

[41] Gamow G., *Consitution of atomic nuclei and radioactivity*, Oxford: Clarendon Press, 1931.

[42] Gasques L. R., Hinde D. J., Dasgupta M., Mukherjee A., and Thomas R. G., *Suppression of complete fusion due to breakup in the reactions* $^{10,11}B + {}^{209}Bi$, Phys. Rev. C **79** (2009), 034605.

[43] Gontchar I. I., Hinde D. J., Dasguptas M., and Newton J. O., *Double folding nucleus-nucleus potential applied to heavy-ion fusion reactions*, Phys. Rev. C (2004), 024610.

[44] Hafstad L. R. and Teller E., *The alpha-particle model of the nucleus*, Phys. Rev. **54** (1938), 681.

[45] Hansteen J. M. and Wittern H. W., *Coulomb disintegration of* ^6Li, Phys. Rev. **137** (1965), B524.

[46] Häusser O., McDonald A., Alexander T., and Ferguson A. J., *Nuclear polarizability of* ^7Li *from Coulomb excitation*, Phys. Lett. B **38** (1972), 75.

[47] Herbig G. H., *Lithium abundances in F5-G8 dwarfs*, Astrophys. J. **141** (1965), 588.

[48] Hesselbarth J., Khan S., Kihm T., and Knöpfle K. T., *Forward-backward asymmetries in the direct breakup of* ^6Li, Z. Phys. A **331** (1988), 365.

[49] Hesselbarth J. and Knöpfle K. T., *Pb(*$^6Li,\alpha d$*)Pb breakup experiment to test feasibility of extracting the astrophysically relevant* $\alpha+d$ *capture cross section*, Phys. Rev. Lett. **67** (1991), 2773.

[50] Hinde D. J. and Dasgupta M., *Neutron halo slips*, Nature **431** (2004), 748.

[51] Hinde D. J. and Dasgupta M., *Systematics analysis of above-barrier fusion of* $^{9,10,11}Be+^{209}Bi$, Phys. Rev. C **81** (2010), 064611.

[52] Hinde D. J., Dasgupta M., Fulton B. R., Morton C. R., Wooliscroft R. J., Berriman A. C., and Hagino K., *Fusion suppression and sub-barrier breakup of weakly bound nuclei*, Phys. Rev. Lett. **89** (2002), 272701.

[53] Hobbie R. K. and Forbes F. F., *Differential cross section for the reaction* $^{12}C(^6Li,\alpha)^{14}N$ *and* $^{12}C(^7Li,\alpha)^{15}N$, Phys. Rev. **126** (1962), 2137.

[54] Horn D. and Ferguson A. J., *Compound-nucleus cross sections from nuclear chage-density distribution*, Phys. Rev. Lett. **41** (1978), 1529.

[55] Hussein M. S., Lichtenthäler R., Nunes F. M., and Thompson I. J., *Scaling and interference in the dissociation of halo nuclei*, Phys. Lett. B **640** (2006), 91.

[56] Hussein M. S., Pato M. P., Canto L. F., and Donangelo R., *Near-barrier fusion of* ^{11}li *with heavy spherical and deformed targets*, Phys. Rev. C **46** (1992), 377.

[57] Keeley N., Kemper K. W., and Rusek K., *Fusion calculation for the* $^{6,7}Li+^{16}O$ *systems*, Phys. Rev. C **65** (2001), 014601.

[58] Keeley N., Raabe R., Alamanos N., and Sida J. L., *Fusion and direct reactions of halo nuclei at energies around the Coulomb barrier*, Prog. Part. Nucl. Phys. **59** (2007), 579.

[59] Lanford W. A. and Crawley G. M., $^{207}Pb(p,d)^{206}Pb$ *reaction and some matrix elements of the effective interactions*, Phys. Rev. C **9** (1974), 646.

[60] Langanke K. and Martinez-Pinedo G., *Nuclear weak-interaction processes in stars*, Rev. Mod. Phys. **75** (2003), 819.

[61] Leigh J. R., Dasgupta M., Hinde D. J., Mein J. C., Morton C. R., Lemmon R. C., Lestone J. P., Newton J. O., Timmers H., Wei J. X., and Rowley N., *Barrier distributions from the fusion of oxygen ions with* $^{144,148,154}Sm$ *and* ^{186}W, Phys. Rev. C **52** (1995), 52.

[62] Mason J. E., Gazes S. B., Roberts R. B., and Teichmann S. G., *Coulomb and nuclear effects in direct breakup of 54-MeV* ^{7}Li+^{12}C,^{197}Au, Phys. Rev. C **45** (1992), 2870.

[63] Matsuse T., Arima A., and Lee S. M., *Critical distance in fusion reactions*, Phys. Rev. C **26** (1982), 2338.

[64] Michel F., Albinski J., Belery P., Delbar T., Grégoire G., Tasiaux B., and Reidemeister G., *Optical model description of* α+^{16}O *elastic scattering and alpha-cluster structure in* ^{20}Ne, Phys. Rev. C **28** (1983), 1904.

[65] Morrison G. C., *Cluster model interpretation of the isotopic spin selection rule in certain nuclear reactions*, Phys. Rev. Lett. **5** (1960), 565.

[66] Mukherjee A., Dasgupta M., Hinde D. J., Morton C. R., Berriman A. C., Butt R. D., Newton J. O., and Timmers H., *Fusion around the barrier for* ^{7}Li + ^{12}C, Pramana J. Phys. **57** (2001), 195.

[67] Mukherjee A., Pramanik U. D., Chattopadhyay S., Sarkar M. S., Goswami A., Basu P., Bhattacharya S., Chatterjee M. L., and Dasmahapatra B., *Fusion cross sections for* ^{6}Li+^{12}C *and* ^{6}Li+^{13}C *reactions at low energies*, Nuc. Phys. A **635** (1998), 305.

[68] Mukherjee A., Pramanik U. D., Chattopadhyay S., Sarkar M. S., Goswami A., Basu P., Bhattacharya S., Chatterjee M. L., and Dasmahapatra B., *Investigation of* ^{6}Li + ^{16}O *and* ^{7}Li + ^{16}O *reactions at low energies*, Nuc. Phys. A **645** (1999), 13.

[69] Mukherjee A., Pramanik U. D., Sarkar M. S., Goswami A., Basu P., Bhattacharya S., Sen S., Chatterjee M. L., and Dasmahapatra B., ^{7}Li+^{12}C *and* ^{7}Li+^{13}C *fusion reactions at subbarrier energies*, Nuc. Phys. A **596** (1996), 299.

[70] Nakamura S., *Theory of coulomb disintegration of complex nuclei*, Phys. Rev. **152** (1966), 955.

[71] Nguyen N. B., Nunes F. M., Thompson I. J., and Brown E. F., *Low-temperature triple-alpha rate in a full three-body nuclear model*, Phys. Rev. Lett. **109** (2012), 141101.

[72] Nikolaev V. and Dmitriev I. S., *On the equilibrium charge distribution in heavy element ion beams*, Phys. Lett. **28A** (1968), 277.

[73] Nörenberg W., *Relaxation phenomena in and microscopic transport theories of deeply inelastic collisions between heavy ions*, J. Phys. (Paris) (Colloq. C5) **37** (1976), C5–141.

[74] Ohkubo S. and Ishikawa Y., *Higher nodal states of alpha+^{15}N cluster structure in ^{19}F*, Phys. Rev. C **31** (1985), 1560.

[75] Ohlsen G. G., *Kinematic relations in reactions of the form $a+ b \to c + d + e$*, Nucl. Instrum. Methods **37** (1965), 240.

[76] Ollerhead R. W., Chasman C., and Bromley D. A., *Dissociation of ^{6}Li*, Phys. Rev. **134** (1963), B74.

[77] Ophel T. R., Harrison J. S., Newton J. O., Spear R. H., Titterton E. W., and Weisser D. C., *The 14UD Pelletron accelerator at the Australian National University*, Nucl. Instrum. Methods **122** (1974), 227.

[78] Ost R., Bethge K., Gemmeke H., Lassen L., and Scholz D., *Three-particle correlations from ^{208}Pb + ^{6}Li*, Z. Phys. **266** (1974), 369.

[79] Ost R., Speth E., Pfeiffer K. O., and Bethge K., *Coulomb breakup of ^{6}Li*, Phys. Rev. C **5** (1972), 5.

[80] Parkar V. V., Mahata K., Santra A., Kailas S., Shrivastava A., Ramachandran K., Chatterjee A., Jha V., and Singh P., *Fusion cross sections for ^{7}Li+^{12}C system at near barrier energies*, Nuc. Phys. A **792** (2007), 187.

[81] Perey C. M. and Perey F. G., *Compilation of phenomenological optimal-model parameters 1954-1975*, At. Data Nucl. Data Tables **17** (1976), 1.

[82] Perring J. K. and Skyrme T. H. R., *The alpha-particle and shell model of the nucleus*, Proc. Phys. Soc. A **69** (1956), 600.

[83] Pfeiffer K. O., Speth E., and Bethge K., *Break-up of* ^{6}Li *and* ^{7}Li *on tin and nickel nuclei*, Nuc. Phys. A **206** (1973), 545.

[84] Pham-Dinh-Lien and Marquez L., *Étude de la réaction* $^{12}C(^{6}Li,\alpha)^{14}N$, Nuc. Phys. **33** (1962), 202.

[85] Québert J. L., Frois B., Marquez L., and Sousbie G., *Search for* ^{7}Li *breakup in* $^{7}Li + {}^{197}Au$ *near grazing incidence*, Phys. Rev. Lett. **32** (1974), 1136.

[86] Rafiei R., du Rietz R., Luong D. H., Hinde D. J., Dasgupta M., Evers M., and Diaz-Torres A., *Mechanism and systematics of breakup in reactions of* ^{9}Be *at near-barrier energies*, Phys. Rev. C **81** (2010), 024601.

[87] Ruhla C., Riou M., Gusakow M., Jacmart J. C., Liu M., and Valentin L., *Etude des reactions* $^{6}Li(p,pd)$ *et* $(p,p\alpha)$ *et* $^{9}Be(p,p\alpha)$ *at 155 MeV*, Phys. Lett. **6** (1963), 282.

[88] Rutherford E. and Chadwick J., *The artificial disintegration of light elements*, Phil. Mag. **42** (1921), 809.

[89] Sakuragi Y., Yahiro M., and Kamimura M., *Microscopic coupled-channels study of scattering and breakup of light heavy-ions*, Prog. Theor. Phys. Suppl. **89** (1986), 136.

[90] Santra S., Parkar V. V., Ramachandran K., Pal U. K., Shrivastava A., Roy B. J., Nayak B. K., and Chatterjee A., *Resonant breakup of* ^{6}Li *by* ^{209}Be, Phys. Lett. B **677** (2009), 139.

[91] Satchler G. R., Nagarajan M. A., Lilley J. S., and Thompson I. J., *Heavy-ion fusion: Channel-coupling effects, the barrier penetration model, and the threshold anomaly for heavy-ion potential*, Ann. Phys. **178** (1987), 110.

[92] Scholz D., Gemmeke H., Lassen L., Ost R., and Bethge K., *Angular correlations from* ^{6}Li *break-up near the Coulomb barrier of* ^{118}Sn *and* ^{208}Pb, Nuc. Phys. A **288** (1977), 351.

[93] Shotter A. C., Bice A. N., Wouters J. M., Rae W. D., and Cerny J., *Observation of the direct and sequential breakup of* ^{7}Li *from* ^{12}C *and* ^{208}Pb, Phys. Rev. Lett. **46** (1981), 12.

[94] Shotter A. C., Rapp V., Davinson T., and Branford D., *Projectile energy and target dependence of the yield for* ^7Li *direct break-up reactions*, J. Phys. G: Nucl. Part. Phys. **14** (1988), L169.

[95] Shotter A. C., Rapp V., Davinson T., Branford D., Sanderson N. E., and Nagarajan M. A., *Direct coulomb breakup of* ^7Li, Phys. Rev. Lett. **53** (1984), 1539.

[96] Shrivastava A., Navin A., Keeley N., Mahata K., Ramachandran K., Nanal V., Parkar V. V., Chatterjee A., and Kailas S., *Evidence for transfer followed by breakup in* $^7Li + {}^{65}Cu$, Phys. Lett. B **633** (2006), 463.

[97] Signorini C., *Fusion at the barrier with light radioactive ion beams*, Nuc. Phys. A **693** (2001), 190.

[98] Signorini C., *Interaction at the barrier in the system* $^{9,10,11}Be + {}^{209}Bi$*: Well-established facts and open questions*, Eur. Phys. J. A **13** (2002), 129.

[99] Signorini C., Edifizi A., Mazzocco M., Lunardon M., Fabris D., Vitturi A., Scopel P., Soramel F., Stroe L., Prete G., Fioretto E., Cinausero M., Trotta M., Brondi A., Moro R., Rana G. L., Vardaci E., Ordine A., Inglima G., Commara M. L., Pierroutsakou D., Romoli M., Sandoli M., Diaz-Torres A., Thompson I. J., and Liu Z. H., *Exclusive breakup of* ^6Li *by* ^{208}Pb *at Coulomb barrier energies*, Phys. Rev. C **67** (2003), 044607.

[100] Signorini C., Liu Z. H., Yoshida A., Fukuda T., Li Z. C., Löbner K. E. G., Müller L., Pu Y. H., Rudolph K., Soramel F., Zotti C., and Sida J. L., *Fusion around the barrier in* $^{11,9}Be + {}^{209}Bi$, Eur. Phys. J. A **2** (1998), 227.

[101] Spiger R. J. and Tombrello T. A., *Scattering of* He^3 *by* He^4 *and of* He^4 *by tritium*, Phys. Rev. C **163** (1967), 964.

[102] Spite F. and Spite M., *Abundance of lithium in unevolved halo stars and old disk stars: Interpretation and consequences*, Astron. Astrophys. **115** (1982), 357.

[103] Spite M. and Spite F., *Lithium abundance at the formation of the Galaxy*, Nature **297** (1982), 483.

[104] Takahashi J., Munhoz M., Szanto E. M., Carlin N., Added N., Suaide A. A. P., de Moura M. M., Neto R. L., and de Toledo A. S., *Is fusion inhibited for weakly bound nuclei?*, Phys. Rev. Lett. **78** (1997), 30.

[105] Takigawa N., Kuratani M., and Sagawa H., *Effect of breakup reactions on the fusion of a halo nucleus*, Phys. Rev. C **47** (1993), R2470.

[106] Takigawa N. and Sagawa H., *Interaction potential and fusion of a halo nucleus*, Phys. Lett. B **265** (1991), 23.

[107] Tamura T., *Coupled-channel approach to nuclear reactions*, Annu. Rev. Nucl. Part. Sci. (1969), 99–138.

[108] Tanihata I., Hamagaki H., Hashimoto O., Nagamiya S., Shida Y., Yoshikawa N., Yamakawa O., Sugimoto K., Kobayashi T., Greiner D. E., Takahashi N., and Nojiri Y., *Measurements of the interaction cross sections and radii of He isotopes*, Phys. Lett. **160B** (1985), 380.

[109] Tanihata I., Hamagaki H., Hashimoto O., Shida Y., Yoshikawa N., Sugimoto K., Yamakawa O., Kobayashi T., and Takahashi N., *Measurements of the interaction cross sections and nuclear radii in the light p-shell region*, Phys. Rev. Lett. **55** (1985), 2676.

[110] Thompson I. J., *Coupled reaction channels calculations in nuclear physics*, Comput. Phys. Rep. **7** (1988), 167.

[111] Thompson I. J. and Nagarajan M. A., *Elastic breakup of 70MeV ^7Li ions on lead*, Phys. Lett. B **123** (1983), 379.

[112] Tilley D. R., Cheves C. M., Godwin J. L., Hale G. M., Hofmann H. M., Kelley J. H., Sheu C. G., and Weller H. R., *Energy levels of light nuclei $A = 5, 6, 7$*, Nuc. Phys. A **708** (2002), 3.

[113] Tilley D. R., Kelley J. H., Godwin J. L., Millener D. J., Purcell J. E., Sheu C. G., and Weller H. R., *Energy levels of light nuclei $A = 8, 9, 10$*, Nuc. Phys. A **745** (2004), 155.

[114] Tombrello T. A. and Phillips G. C., *A two-body cluster model of the nucleus*, Nuc. Phys. **20** (1960), 648.

[115] Tombrello T. A. and Phillips G. C., *Cluster nature of ^7Li and ^7Be*, Phys. Rev. **122** (1961), 224.

[116] Tostevin J. A., Nunes F. M., and Thompson I. J., *Calculations of three-body observables in ^8Be breakup*, Phys. Rev. C **63** (2001), 024617.

[117] Utsunomiya H., Lui Y. W., Haenni D. R., Dejbakhsh H., Cooke L., Srivastava B. K., Turmel W., O'Kelly D., Schmitt R. P., Shapira D., del Campo J. G., Ray A., and Udagawa T., *Breakup of ^7Li near the $\alpha-t$ threshold and a possible probe of radiative-capture processes*, Phys. Rev. Lett. **65** (1990), 847.

[118] Utsunomiya H., Tokimoto Y., Mabuchi H., Osada K., Yamagata T., Ohta M., Aoki Y., Hirota K., Ieki K., Iwata K., Katori K., Hamada S., Lui Y. W., and Schmitt R. P., *Strongly-suppressed post-Coulomb acceleration in non-resonant breakup of ^7Li*, Phys. Lett. B **416** (1998), 43.

[119] Valkovic V., Joseph C., Emerson S. T., and Phillips G. C., *Two-particles coincidence spectra from the $p+^6Li \rightarrow p+d+\alpha$ reaction*, Nuc. Phys. A **106** (1968), 138.

[120] Varner R. L., Thompson W. J., McAbee T. L., Ludwig E. J., and Clegg T. B., *A global nucleon optical model potential*, Phys. Rep. **201** (1991), 57.

[121] Vold P. B., Andreassen J. O., Lien J. R., Graue A., Cosman E. R., Dünnweber W., Schmitt D., and Nüsslin F., *The $^{207}Pb(d,p)^{208}Pb$ reaction with high resolution*, Nuc. Phys. A **215** (1973), 61.

[122] von Oertzen W., Bohlen H. G., and Gebauer B., *Enhancement of two-proton transfer in $N = 82$ nuclei: A study of 1p, 2p and (2p+2n) transfer reactions induced by ^{16}O on ^{140}Ce, ^{142}Nd and ^{144}Sm near the Coulomb barrier*, Nuc. Phys. A **207** (1973), 91.

[123] von Oertzen W., Freer M., and Kanada-En'yo Y., *Nuclear clusters and nuclear molecules*, Phys. Rep. **432** (2006), 43.

[124] Wei J. X., Leigh J. R., Hinde D. J., Newton J. O., Lemmon R. C., Elfstrom S., and Chen J. X., *Experimental determination of the fusion-barrier distribution for the $^{154}Sm+$ ^{16}O reaction*, Phys. Rev. Lett. **67** (1991), 3368.

[125] Wheeler J. A., *Molecular viewpoints in nuclear structure*, Phys. Rev. **52** (1937), 1083.

[126] Wildermuth K. and Kanellopoulos T., *The "cluster model" of the atomic nuclei*, Nuc. Phys. **7** (1958), 150.

[127] Woods R. D. and Saxon D. S., *Diffuse surface optical model for nucleon-nuclei scattering*, Phys. Rev. Lett. **95** (1954), 577.

[128] Wu Y. W., Liu Z. H., Lin C. J., Zhang H. Q., Ruan M., Yang F., Li Z. C., Trotta M., and Hagino K., *Near barrier fusion excitation function of* ^{6}Li + ^{208}Pb, Phys. Rev. C **68** (2003), 044605.

[129] Ziegler J. F., Biersack J. P., and Ziegler M. D., *SRIM-2003*, Nucl. Instrum. Methods **B219-220** (2004), 1027.